ISSN 0503-1540

Tome 30 *Août* *1992* Numéro 3

La mer

うみ

Proceedings of the Sixth Japan and
East China Seas Study Workshop,
22-27 April 1991, Fukuoka, Japan

1992 年 8 月

日 仏 海 洋 学 会

La Société franco-japonaise
d'océanographie
Tokyo, Japon

Note pour la présentation des manuscrits

La mer, organe de la Société franco-japonaise d'océanographie, publie des articles et notes originaux, des articles de synthèse, des analyses d'ouvrages et des informations intéressant les membres de la société. Les sujets traités doivent avoir un rapport direct avec l'océanographie générale, ainsi qu'avec les sciences halieutiques.

Les manuscrits doivent être présentés avec un double, et dactylographiés, en *double interligne*, et au recto exclusivement, sur du papier blanc de format A4 (21×29,7 cm). Les tableaux et les légendes des figures seront regroupés respectivement sur des feuilles séparées à la fin du manuscrit.

Le manuscrit devra être présenté sous la forme suivante:

1° Il sera écrit en japonais, français ou anglais. Dans le cadre des articles originaux, il comprendra toujours le résumé en anglais ou français de *200 mots* environs. Pour les textes en langues européennes, il faudra joindre en plus le résumé en japonais de *500 lettres* environs. Si le manuscrit est envoyé par un non-japonophone, le comité sera responsable de la rédaction de ce résumé.

2° La présentation des articles devra être la même que dans les numéros récents; le nom de l'auteur précédé du prénom *en entier*, en minuscules; les symboles et abréviations standards autorisés par le comité; les citations bibliographiques seront faites selon le mode de publication: article dans une revue, partie d'un livre, livre entier, etc.

3° Les figures ou dessins originaux devront être parfaitement nettes en vue de la réduction nécessaire. La réduction sera faite dans le format 14,5×20,0 cm.

La première épreuve seule sera envoyée à l'auteur pour la correction.

Les membres de la Société peuvent publier 7 pages imprimées sans frais d'impression dans la mesure à leur manuscrit qui ne demande pas de frais d'impression excessifs (pour des photos couleurs, par exemple). Dans les autres cas, y compris la présentation d'un non-membre, tous les frais seront à la charge de l'auteur.

Cinquante tirés-à-part peuvent être fournis par article aux auteurs à titre gratuit. On peut en fournir aussi un plus grand nombre sur demande, par 50 exemplaires.

Les manuscrits devront être adressés directement au directeur de publication de la Société: M. MURANO, Université des Pêches de Tokyo, Konan 4-5-7, Minato-ku, Tokyo, 108 Japon; ou bien au rédacteur étranger le plus proche: H. J. CECCALDI, EPHE, Station marine d'Endoume, rue Batterie-des-Lions, 13007 Marseille, France; E. D. GOLDBERG, Scripps Institution of Oceanography, La Jolla, California 92093, Etats-Unis; T. ICHIYE, Department of Oceanography, Texas A & M University, College Station, Texas 77843, Etats-Unis; ou T. R. PARSONS, Department of Oceanography, University of British Columbia, Vancouver, B. C. V6T 1W5, Canada.

Proceedings of the Sixth Japan and East China Seas Study Workshop, 22–27 April 1991, Fukuoka, Japan

Dedicated

to

Prof. Kenzo TAKANO

Preface

Kuh KIM

This Proceedings contains selected papers given at the Sixth JECSS (Japan and East China Seas Study) Workshop held in Fukuoka, Japan on April 22–27, 1991. The workshop was convened by Prof. K. TAKANO (University of Tsukuba) and organized by Profs. H. MITSUYASU (Chairman), K. KAWATATE (Secretary), M. TAKEMATUS, H. HONJI, S. MIZUNO, T. KUSABA, T. YAMAGATA, J.-H. YOON and A. KANEKO at Kyushu University. The workshop was sponsored by the Regional Committee for the Western Pacific Ocean (WESTPAC) of the Intergovernmental Oceanographic Commission (IOC), the American Geophysical Union, the Oceanographic Society of Japan, La Société franco-japonaise d'océnographie and Kyushu University with supports by Ministry of Education, Science and Culture of Japan, Fukuoka Science and Technology Foundation, Fukuoka Convention Bureau, Yokatopia Foundation and other volunatary companies. Efforts of the local committee in successfully organizing both the scientific and social programmes were greatly appreciated by all participants.

Eighty-nine papers, the largest ever presented at the JECSS workshop, reflect the growing interests in physical oceanography of the Japan Sea, the East China Sea and adjacent waters, and also the intensity of research activities in these seas initiated through previous five workshops. It is exciting that JECSS itself is growing to cover important subjects such as the air-sea interactions and exchange processes between margional seas and the Pacific Ocean. Participants at the sixth workshop submitted forty-one papers to this Proceedings and nineteen papers were finally accepted after reviews. I am very thankful to forty five referees, whose comments and criticisms were so helpful to improve most of papers in this volume.

Prof. K. TAKANO, who have worked so hard to convene six workshops ever since JECSS began in 1981, made an arrangement with Prof. Y. ARUGA, the president of Société franco-japonaise d'océanographie, to publish this Proceedings in La mer. I am most grateful to Profs. TAKANO and ARUGA for their cooperations. Also I am deeply indebted to Prof. B. H. CHOI for his unlimited helps and am encouraged by Prof. K. KAWATATE to complete the long and difficult task of editing this Proceedings.

(Guest Editor, Seoul National University)

La mer 30: 95–103, 1992
Société franco-japonaise d'océanographie, Tokyo

Meanders of the Tsushima Current

Takashi ICHIYE* and Matthew HOWARD*

Abstract: The Tsushima Current in the Japan Sea is treated as a thin jet in a reduced gravity field with the beta effect, including dissipation and entrainment. Integration with the latitude of a cross-jet momentum equation leads to the path equation together with the along jet momentum equation and with a simplified conservation equation of volume transport. The non-dissipative and transport conserved solution corresponds to the one derived by C.G.ROSSBY and R.O.REID earlier. The linear friction and a given entrainment function are incorporated in a linearized form. Those effects tend to cause crossings of the streamlines, suggesting that these processes may be a cause of pinch-off of mesoscale eddies frequently observed in the Japan Sea. As preliminary applications, several computed paths are fitted to the 100m isotherms of the Japan Sea collected in August 1990. An example of meso-scale eddies formation by streamline crossing is inferred from a series of IR images taken in spring of 1984 west of Oki Island.

1. Introduction

Meandering of the Tsushima Current (TC) can be seen in charts of isotherms both at the surface and subsurface published routinely by the Japan Meteorological Agency, Hydrographic Department of the Maritime Safety Agency and the Japan Fisheries Agency. The 100m isotherms are particularly useful to interpret the meander from ocean dynamics, because they are relatively free from short-term interactions by the atmospheric heating. They represent to a degree geostrophic flow in the upper layer (ICHIYE and TAKANO, 1988) and the data are relatively abundant.

Many Japanese authors noticed that in the Japan Sea the water below 200–300 meters is almost uniform both in temperature and salinity with a sharp thermocline and pycnocline at these levels (MORIYASU, 1972; KAWABE, 1982). This feature suggests that we can handle dynamics of the TC that mainly flows in the upper 200m as a process in a two-layer ocean with an inactive lower layer. This does not imply that effects of the lower layer or bottom topography are unimportant to the TC. On the contrary, these effects could become important for long-term behaviors of the TC and their effects on heat and mass transports in the Japan Sea.

In this paper we only deal with a short-term or synoptic process with the duration of, say several weeks but after achieving geostrophic adjustment. A basic approach is to start from momentum equations with natural coordinates, incorporating the conservation of volume in a simple scheme with an assumption that the TC is a jet-like flow with almost uniform across the flow. Emphasis is put on paths of the flow as it meanders in the upper layer.

2. Basic equations

The natural coordinates (s, n) are taken with s along the flow and n across it to the left, as indicated in Fig. 1. The momentum conservation equations along s and n are given by

$$v\frac{\partial v}{\partial s}=-g'\frac{\partial h}{\partial s}-F \qquad (1)$$

$$\kappa v^2+fv=-g'\frac{\partial h}{\partial n} \qquad (2)$$

respectively, where v, h, κ, f, g', and F are velocity, thickness of the upper layer, curvature of streamlines, Coriolis parameter, reduced gravity and dissipation force, respectively.

Conservation of volume transport is expressed by

* Department of Oceanography, Texas A & M University, College Station, Texas 77843 USA

$$vh=v_0h_0+S \tag{3}$$

S is the entrainment (or detrainment) along the flow and the suffix o indicates the values at the starting point (for the TC at the Korean Strait). More exactly, both sides should be averaged across the flow over an unspecified width, but this analytical subtlety is forsaken for conceptual simplicity of (3). If we assume that the velocity vanishes outside a narrow band of the flow and that there is no dissipation and entrainment then equation (1) yields

$$\frac{1}{2}v^2+g'h=\frac{1}{2}v_0^2+g'h_0-G \tag{4}$$

This equation represents the energy conservation along a streamline and this equation with $G=0$ and equation (3) with $S=0$ leads to a solution

$$v=v_0, \quad h=h_0 \tag{5}$$

Therefore, both v and h are constant along the streamline, equaling their initial values, though they may be variable across the flow. By solving equations (3) and (4) as algebraic equations about v and h, these two quantities can be determined in terms of v_0, h_0, S and G, where v_0 and h_0 are dependent on n only but S and G are dependent on both n and s. Equations (3) and (4) lead to a cubic equation about v or h which has three roots. One of the roots is positive and equivalent to (5) even when G and S do not vanish. When there is a root which is real and positive, two or three roots can represent real flows. In ICHIYE (1990), it was speculated that transition from one flow regime represented by one root to other regime represented by another root could be occurred analogous to hydraulic jumps in a channel flow when the streamlines crossed each other. Such processes seem to be a cause of mushroom-like flows, particularly of multiple structures which had been observed commonly along the edge of a jet-like flow of warm water or fresher water over heavier stagnant water of a great depth below (FEBROV and GINSBURG, 1989).

In other manifests of streamline crossings and transitions in flow regimes can be seen in IR images of the Tsushima Current west of Oki Island. KITANI *et al.* (1986) analyzed IR data from March 28 to April 24, 1984 and reported formation and change of warm water belts of 10 to 20 km wide and 100 to 200 km long at about 132° E to 133° E and 36° N to 38° N. The location of these belts corresponds to the west leg of the second penetration of the meander (west of a portion designated C in Fig. 8). The tip of the warm belts indicated anti-cyclonic vorticity. The formation took only 12 hours in the beginning but for full development it took several days.

Since the location of formation of the warm belts or ribbons could be determined with IR imagery and its time scales are within range of shipboard measurements, it is possible to determine dynamical processes accompanying with streamline crossing and the transition of flow regimes corresponding to different roots of equation (3) and (4). The results of further studies on this problem will be reported elsewhere.

Since the TC flows from 35° N to 45° N, the beta effect cannot be neglected as in ICHIYE (1990) , where G and S are assumed to vanish. The $x-y$ coordinates are taken as eastward and northward (Fig. 1). Then the curvature can be expressed by

$$\kappa = \frac{\partial \theta}{\partial s} \tag{6}$$

where θ is the angle of the streamline with the x-axis. When the effects of dissipation and entrainment are small, deviation of v and h from v_0 and h_0 are also small. Thus

$$v=v_0+a, \quad h=h_0+b \tag{7}$$

When at the starting point ($s=0$ and $y=0$) the flow is geostrophic,

$$f_0=-\left(\frac{g'}{v_0}\right)\frac{\partial h_0}{\partial n} \tag{8}$$

Using a relation $\partial y/\partial s=\sin\theta$ in (6), equation (2) can be integrated with θ and y, leading to

$$\cos\theta-\cos\theta_0=\int_0^y\left(fv^{-1}+g'v^{-2}\frac{\partial h}{\partial n}\right)dy \tag{9}$$

Anomalies a and b can be determined by substituting (7) into (3) and (4). When only the first order terms of a and b are retained,

$$a=(v_0G+g'S)\,q^{-1} \tag{10a}$$
$$b=-(h_0G+v_0S)\,q^{-1} \tag{10b}$$

where

$$q=g'h_0-v_0^2 \tag{11}$$

When (7) is substituted into (9), retaining only the first order terms of a and b and relation (8) is used, (9) becomes

$$\cos\theta=\int_0^y\left[\beta y v_0^{-1}+a(f_0-\beta y)v_0^{-2}+g'\left(\frac{\partial b}{\partial n}\right)v_0^{-2}\right]dy \tag{12}$$

where the relation $f=f_0+\beta y$ is used, v_0 is constant and the flow at the starting point is assumed northward ($\theta_0=\pi/2$).

The dissipation term G is an integration of frictional force F along the path. In a simple parameterzaion, we assume Rayleigh-type frictional force and also the path mainly of meridional direction. Then

$$G=kv_0y \tag{13}$$

where k is a friction coefficient including a factor of deviation of the path from the strictly meridional direction. Substitution of (10) and (13) into (12) leads to

$$\cos\theta=g'f_0Sq^{-1}(v_0^{-2}-q^{-1})y+\frac{1}{2}(v_0^{-1}\beta+2kf_0q^{-1}-g'kf_0h_0q^{-2}v_0^{-1}-g'Sq^{-1}\beta v_0^{-2})\,y^2-\frac{k\beta}{qv_0}\frac{y^3}{3} \tag{14}$$

As expected the terms with S represent the effects of entrainment and those with k indicate effects of friction. Since only the first order term of a and b are retained, the friction and the entrainment are affecting the path independently. A case of $k=0$ and $S=0$ corresponds to a path obtained by REID (1968) as it should be. In the present derivation, we do not use the rule of conservation of potential vorticity. In ICHIYE (1990) this rule is derived from equations (2) and (3) with $S=0$ and (4) with $G=0$.

Admittedly the assumption that the entrainment function S and a frictional force F are independent on s is very crude indeed, though S and k could be assigned functions of n. (It is unwarranted to assume S as a linear function of y similar to (13) as suggested by a, reviewer, because relation (3) specifies volume transport at each section represented by s, unlike G that is an integral of F along the path.) Of course, S could be taken as an arbitrary function on both n and s in equation (14) and determined the path or, by fitting the path to the observed path and determine S as a function of n and s. But in the present stage of uncertainties in the information on various parameters, these exercises seem to complicate modelling unnecessarily.

3. Numerical calculation

The path can be determined from the relation

$$dx/dy=\cot\theta \tag{15}$$

where the r.h.s. can be obtained from (14). Although v_0 is assumed constant, h_0 and S are variable with n; therefore θ is dependent on n. Thus the streamlines are not necessarily parallel to each other and they may diverge, or converge and even cross each other, particularly when S is not zero.

For numerical calculation, the r.h.s. of equation (14) is scaled with characteristic values. l_h, h_b, h_m, and v_1 which are horizontal distance, right hand side depth and mean depth of the flow at the starting point, and speed, respectively. For simplicity, the initial speed is constant; thus from (8)

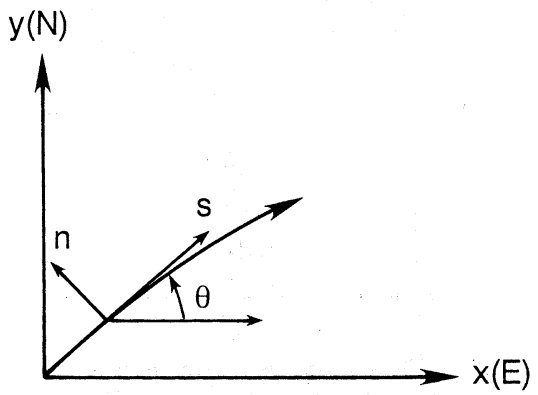

Fig. 1. Natural coordinate system with Cartesian coordinates.

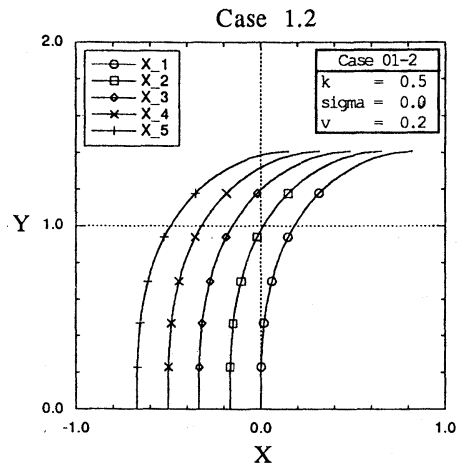

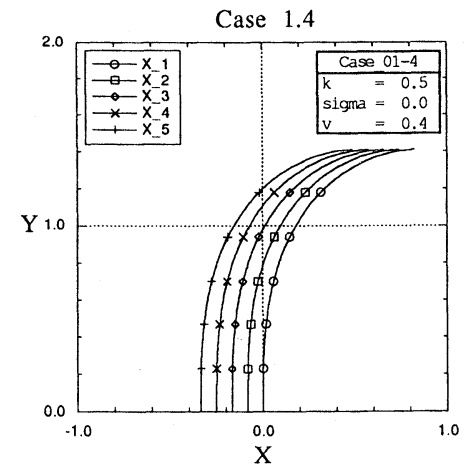

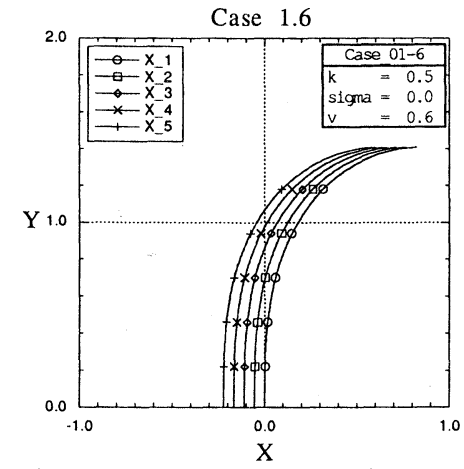

Fig. 2. Three examples of streamlines computed from equations (18) to (20). For K=0.5 and V=0.2 to 0.6. The streamlines converge but not cross each other.

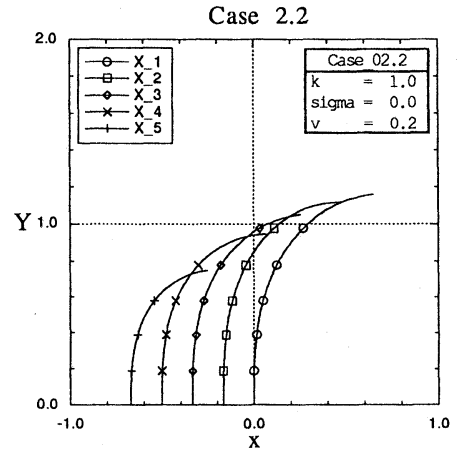

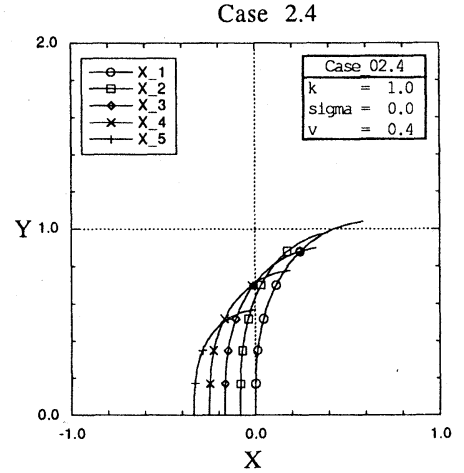

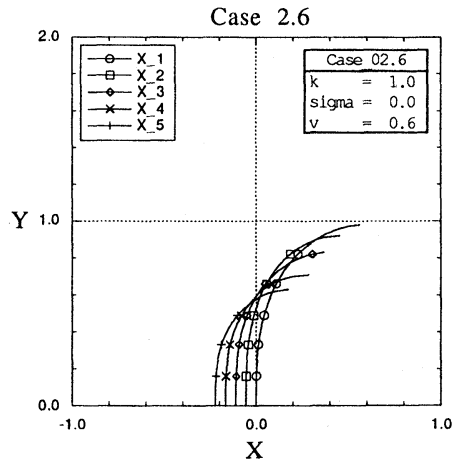

Fig. 3. Three examples of computed streamlines, for K=1.0 and V=0.2 to 0.6. The streamlines cross each other.

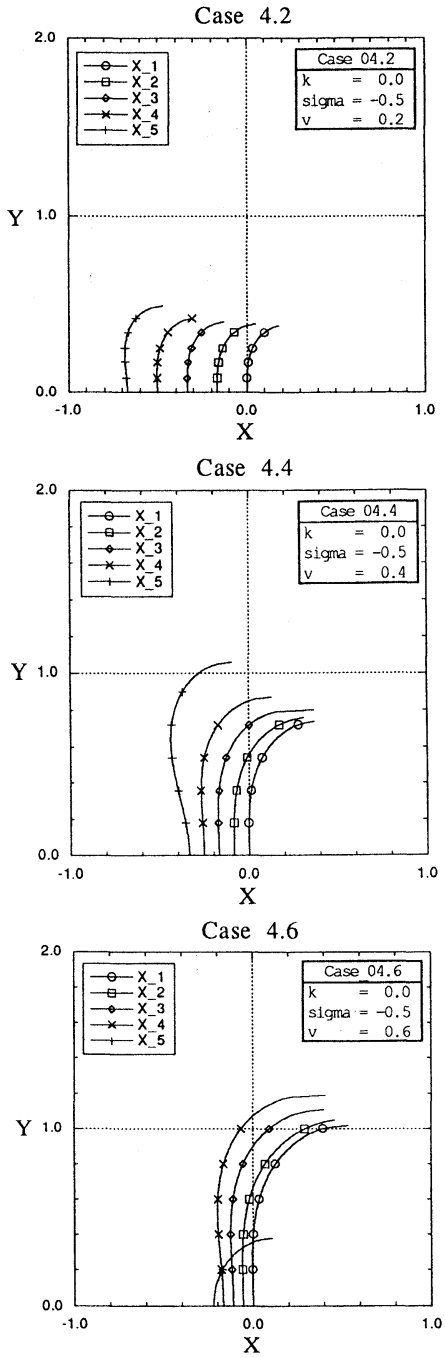

Fig. 4. Three examples of computed streamlines, for $\sigma = -0.5$, corresponding detrainment along the path. The streamlines do not reach as cases of no entrainment or detrainment. Some streamlines cross near the starting point in case for V=0.6

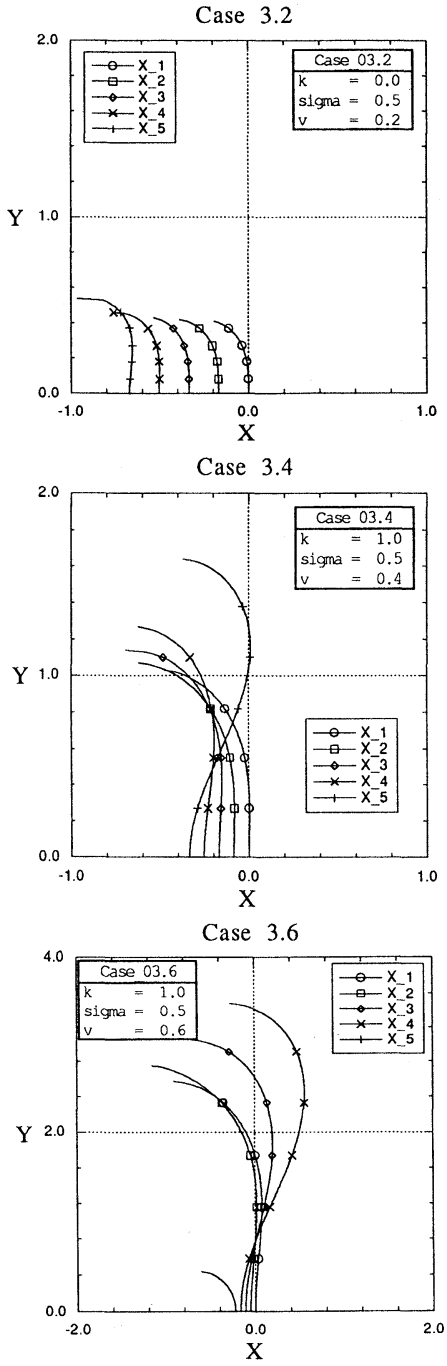

Fig. 5. Three examples of computed streamlines for $\sigma = 0.5$, corresponding to entrainment. Entrainment cause streamlines becoming cyclonic and also crossing each other for faster speed.

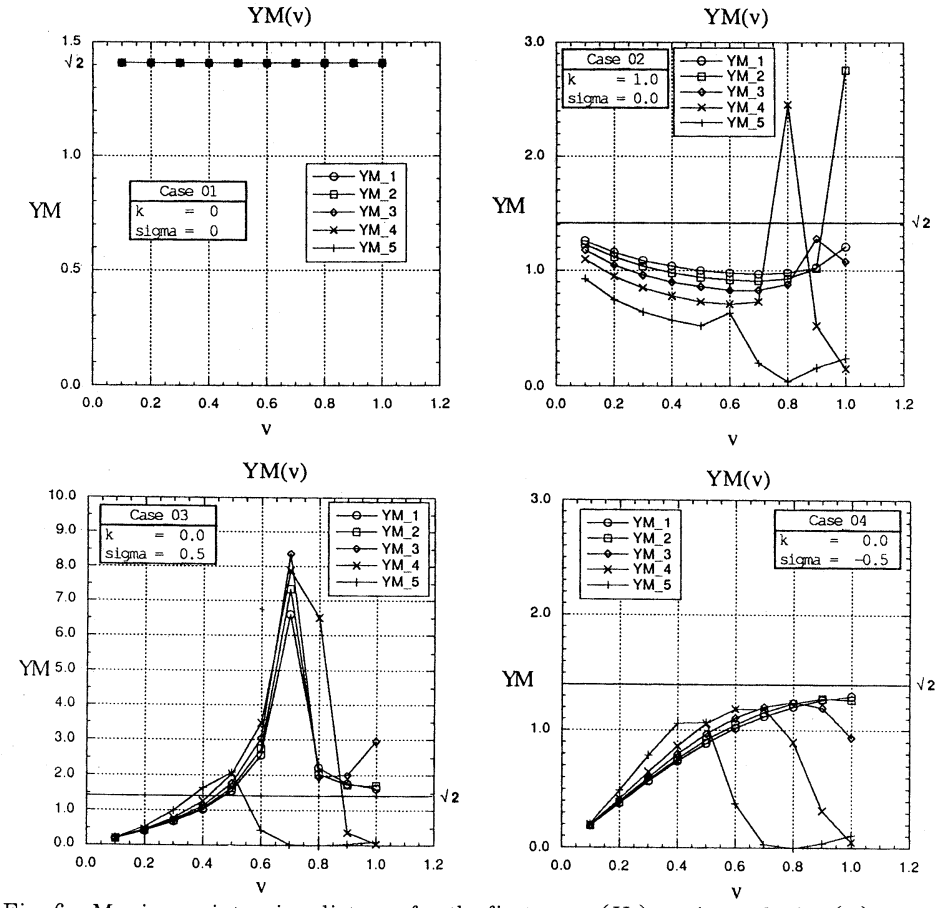

Fig. 6. Maximum intrusion distance for the first wave (Y_m) against velocity (V) for different streamlines with different combinations of K and sigma. YM-1 etc. correspond to streamlines at different starting points denoted as X-1 etc. in Figs. 2 to 5. Crossings of Y_m versus V curve indicate crossings of the streamlines for which Y_m is computed. The figure shows that with non-zero sigma values (entrainment) streamlines tend to cross each other for smaller V than for cases with dissipation only.

$$h_0 = h_b + (f_0 v_0 / g')x \tag{16}$$

Then

$$l_h = (v_0/\beta)^{1/2},\ v_0 = v_1 V,\ h_0 = h_b H,\ x = l_h X,$$
$$y = l_h Y,\ q = v_0^2 Q,\ k = k_0 K,\ S = \sigma v_1 h_m \tag{17}$$

where H, V, Q, X, K, and σ are dimensionless parameters and variables.

When the following values are used for characteristic parameters, $v_0 = 1\,\mathrm{ms}^{-1}$; $\beta = 2 \times 10^{-11}\,\mathrm{m}^{-1}\mathrm{s}^{-1}$; $f_0 = 8 \times 10^{-5}\,\mathrm{s}^{-1}$; $h_m = 75\mathrm{m}$; $h_b = 150\mathrm{m}$; $k_0 = 10^{-6}\,\mathrm{s}^{-1}$, equations (14) and (16) can be expressed by

$$\cos\theta = 2.0035 Q^{-1}(1-Q^{-1})\,\sigma V^{-5/2} Y + (1 + 8Q^{-1}KV^{-1} - 12HKV^{-2}Q^{-2} - 1.12\,\sigma V^{-2})\frac{1}{2}Y^2 - 0.0527\,Q^{-1}Y^3 KV^{-1/2} \tag{18}$$

and

$$H = 1 + 5.963\,V^{3/2}X_0 \tag{19}$$

where

$$Q = V^{-2}(3H - V^2) \tag{20}$$

In equation (19), X_0 indicates the starting

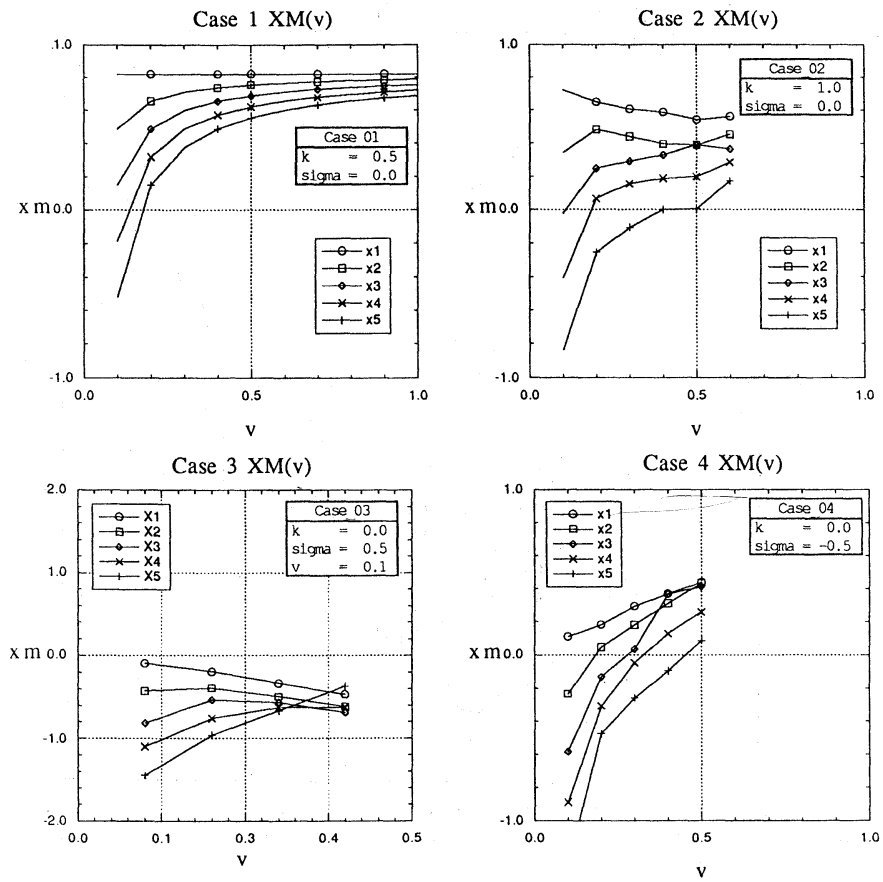

Fig. 7. X_m corresponding to Y_m as determined in Fig. 6. The X_m values indicate those on the X coordinate as in Figs. 2 to 5. The distance of the quarter wave length in zonal direction of each streamline can be determined by subtracting the initial X coordinate denoted as X-1, X-2 etc. in Figs. 2 to 5 from curves of X_m (V) in this figure. (For example streamline X-5 at $V=0.2$ $K=1$ has $X_m=-0.3$ and the starting point X coordinate is $=-0.7$. Thus the quarter wave length is about 0.4).

position of each streamline and thus can be treated as a parameter for integrating equation (15) with Y by replacing $\partial x/\partial y$ with $\partial X/\partial Y$. The mean value h_m is taken for an initial flow in which the thermocline surfaces at the left hand side.

Several examples of the path determined from (18) to (20) are shown in the X-Y coordinates in Fig. 2 to 5 for different value of σ and K. With inclusion of small entrainment or detrainment (σ is non-zero), the path sometimes changes drastically.

Equations (14) or (20) indicate that the path determined from(15)or its equivalent expression with X and Y shows a wave form extending eastward as expressed in general with elliptic integrals on y or Y. The northernmost intrusion of the first wave denoted as Y_m can be determined as the first Y satisfying $\cos\theta=1$. The value X_m corresponding to Y_m on the path is equivalent to a quarter of the wavelength. Figures 6 and 7 show values of Y_m and X_m for different values of V at different values of K and σ.

4. Application to the Tsushima Current paths

Isotherms at 100 m are plotted in Fig.8 from data collected by about a dozen research vessels and patrol boats from August 1 through August 15, 1990 (Japan Fisheries Agency, 1990).

For a non-dissipation non-entrainment case,

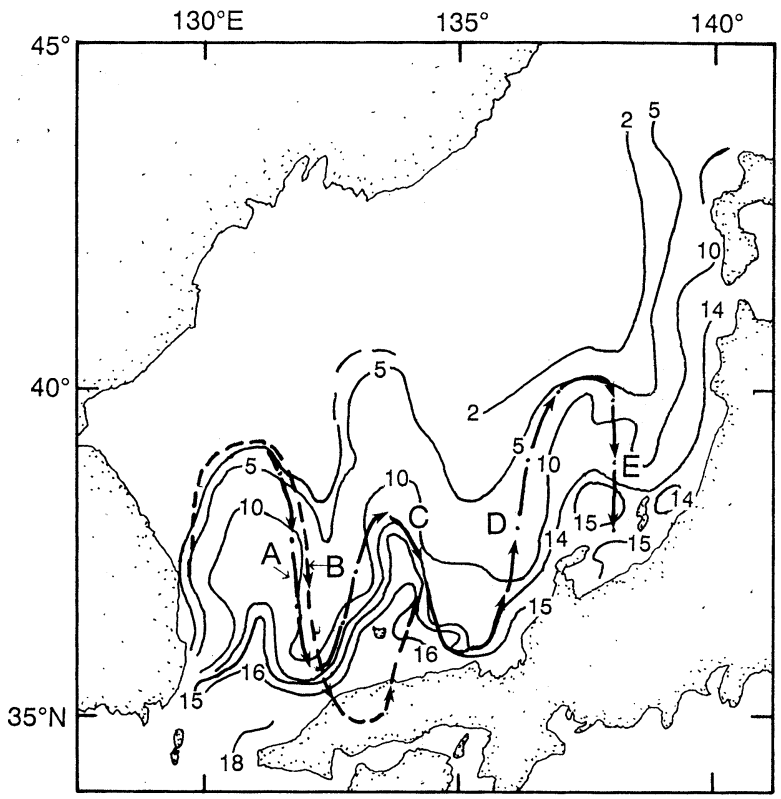

Fig. 8. Example of comparison of 100 m isotherms and computed paths in the Japan Sea. Isotherms are labeled in ℃ and based on data of Fishing Ground Oceanography Charts for August 1990. (Japan Fisheries Agency).

Dashed line denoted B represents the path for no dissipation, no entrainment case with $V=0.5$. Dash-dot line represents the path including non-zero K or σ. Different segments of the dash-dot line are labeled according the the following specifications: A, $\sigma=0.2$; C, $K=0.5$; D, $\sigma=0.5$; E, $\sigma=-0.2$.

the speed $V=0.5$ or $v_0=0.5\text{ms}^{-1}$ seems to be best fit to the first wave of the northward intrusion of the observed isotherm meander. However, the theoretical curve does not fit the second wave crest around 133° E. Third wave is completely out of phase from the theoretical curve. This is due to the condition that the second trough (or southward retreat) interacts strongly with the shelf or the coastline as seen from the figure.

5. Concluding remarks

This is a preliminary study of dynamics of meanders of the Tsushima Current. As shown in Fig.8 modelled paths of the meander are deviated after the first intrusion approaches the coast on its retreat. This suggests both dissipative and entrainment processes are admittedly parameterized inadequately.

This could be improved substantially with help of field experiments that are to be addressed to the dissipative processes in shallow water areas less than 200m and to the entrainment processes in similar areas from coastal water. These experiments may be made successfully with conventional hydrographic techniques if the experimental cruises are planned carefully.

Crossings of the streamlines occur for the flow with v_0 and h_0 that are not uniform across the section (dependent on n) as shown in the case of S and $G=0$ (ICHIYE, 1990). When S and G do not vanish, further upstream these crossings are apt to occur in the path of the flow than when $S=G=0$, since finite S or G makes h and v

deviate from uniform and become dependent on n.

Crossings with or without dissipation or entrainment suggest formation of mesoscale eddies in the Japan Sea as pointed out by ICHIYE and TAKANO (1988). Influence of dissipation and entrainment on crossings indicates necessity to parameterize these processes more adequately particularly upstream of the crossings or eddy formation. Since locations of the latter processes manifested as warm water ribbons were known at least west of Oki Island, it is not difficult to conduct field experiments with drifters, closely spaced CTD measurements and moored current meters by coordinating ongoing studies of the Tsushima Current by several agencies and institution. Then the results might shed light on dynamics of crossings of streamlines, transition of flow regimes caused by different roots of (3) and (4) as well as mechanism of formation of mesoscale eddies from a jet-like ocean current, that is so ubiquitous in the world ocean but yet to be understood its physics.

Acknowledgement

The second author is supported by U.S.W.O.C.E. program. Typing by Susan MAHAN is appreciated.

References

FEDROV, K.N. and A.I. GINSBURG (1989): "Mushroom like" currents: one of the most widespread forms of non-stationary motion in the oceans. Geophysical Turbulence, Proc. 20th Liege Colloq. on Ocean Hydrodynamics. (edited by J.C.J. NIHOUL and B.M. JAMART) 1–14, Elsevier Publishers, 844pp.

ICHIYE, T. (1990) : A simple model of mushroom-like flows. Tribute to Prof. K.N.FEDROV, Pacific Annual, 1989–1990 (Far Eastern Branch, USSR Academy of Sciences, Vladivostok), 131–145.

ICHIYE, T. and K. TAKANO (1988): Mesoscale eddies in the Japan Sea. La mer, **26**, 69–79.

KAWABE, M., (1982): Branching of the Tsuhima Current in the Japan Sea I and II. J. Oceanogr. Soc. of Japan, **38**, 95–107, 183–192.

KITANI, K., H. NAGATA and K. MUNEYAMA (1986): An explanation of the sea condition off San-In District based on infrared images. Sora To Umi (in Japanese) No. 8, 15–25.

MORIYASU, S. (1972): The Tsushima Current. Chapt. 9, 353–369. *In* The Kuroshio, Its Physical Aspect, (Edited by H. STOMMEL and K. YOSHIDA), Univ. of Tokyo Press, 517p.

REID, R.O. (1972): A simple dynamic model of the Loop Current. 157–159, Contributions on the Physical Oceanography of the Gulf of Mexico, (edited by L.R.A. CAPURRO and J.L. REID), Gulf Publishing Co., Houston, Texas, 288p.

ROSSBY, C.G. (1945): On the propagation of frequencies and energy in certain types of oceanic and atmospheric waves. J. Meteorol. **2**, 187–204. Also *in* Handbook of Meteorology (edited by F.A. BERRY, E. BOLLAY and N.R. BEERS), McGRAW Hill Inc., New York, (1945).

La mer 30: 105–118, 1992
Société franco-japonaise d'océanographie, Tokyo

Influence of surface water circulations on the sea bottom in the southern Japan Sea

Ken IKEHARA*

Abstract: Influences of surface water circulation on the sea bottom are discussed on the basis of the distribution of surface sediments and bedform morphology. Spatial distribution of surface sediments and bedform morphology suggest a northeastward sediment transport in and around the Tsushima Strait. Transport of sandy sediments and prevention of mud deposition occur at the shelf edge of north of Kita-Kyushu and at the marginal terrace edge between Mishima Island and Oki Islands, indicative of bottom currents along the edge of shelf or marginal terrace. A second branch of the Tsushima Current or surface water circulation seems to form eddies that are related to cold water mass influencing the sea bottom and controling modern sedimentation along the shelf or marginal terrace edge. On the other hand, muddy sediments are deposited on the marginal terrace, though located just beneath the current path of the first branch of the Tsushima Current at the north of Hamada. This means that the effects of the first branch are too small to prevent the deposition of mud.

1. Introduction

The Japan Sea is a northeast-southwest trending marginal sea between the Asian Continent and the Japanese Islands. The oceanography of the Japan Sea has been investigated by many institutes. Among these studies, the behavior of the Tsushima Current has been a main target. The Tsushima Current has high temperature, high salinity and relatively low oxygen content and is derived from the Kuroshio (NITANI, 1972). It flows northeastward, after entering the Japan Sea through the Tsushima Strait. The current path exhibits a complicated figure. Some workers have recognized three branches (e.g. SUDA and HIDAKA, 1932; UDA, 1934; KAWABE, 1982), whereas others have recognized a meandering path (MORIYASU, 1972). This conflict results from the considerable variability in the spatial location of the Current.

Many studies on the water movements in the Japan Sea have been carried out on the basis of oceanographic data such as temperature, salinity and dissolved oxygen (e.g. ICHIYE, 1954; KANO, 1980; KOLPACK, 1982). However, precise figure of the thickness of the water movement or bottom current behavior such as direction and velocity is not clear yet. On the other hand, sedimentological, paleontological and marine geological investigations in the southern Japan Sea have clarified sediment distribution (e. g. MARITIME SAFETY AGENCY, 1949; IWABUCHI, 1968; TANIMURA, 1981; YAMAMOTO *et al.*, 1989; IKEHARA, 1989, 1991). Modern sedimentation, however, has not been discussed enough. As the sediment grain is transported and deposited according to flow velocity (KIMURA, 1956; SUNDBORG, 1956), spatial distribution of the sediments is influenced by the vector distribution of current. In addition, surface sediments record long-term, averaged current conditions near the sea bottom, because they have been exposed on the sea bottom for a long time. Sedimentological information is, therefore, important not only to geological problems such as Quaternary sea level changes but also to modern oceanographic considerations.

In this paper, the influence of the Tsushima Current and surface water circulation on the sea bottom will be examined on the basis of sedimentological and marine geological data obtained during survey cruises by the Geological

* Marine Gelogy Department, Geological Survey of Japan, Tsukuba, Ibaraki, 305 Japan

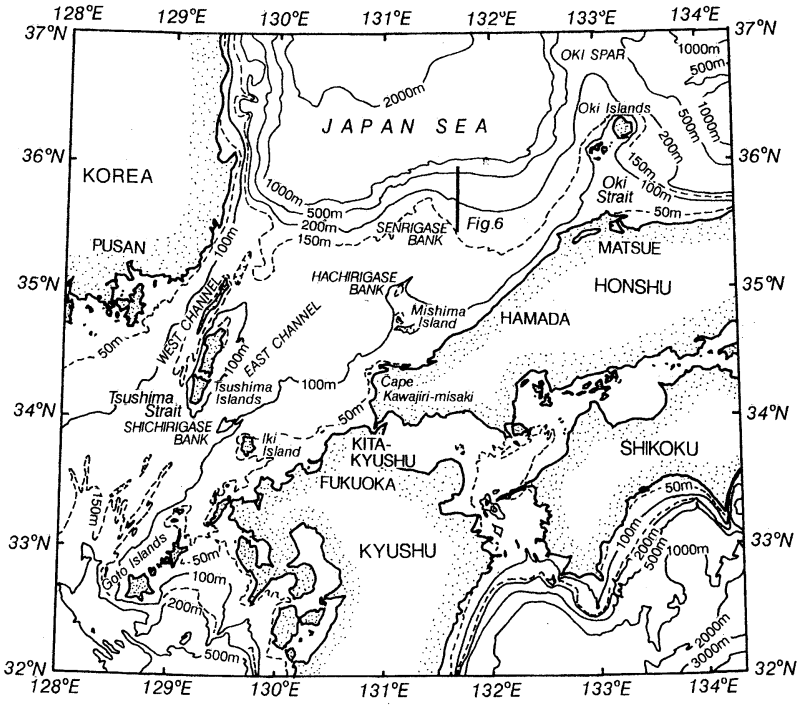

Fig. 1. Area and bathymetry of study in the southern Japan Sea.

Survey of Japan. I will describe spatial distribution of surface sediments and bedforms in the southern Japan Sea and will discuss the influence of water movements in the Tsushima Strait and off Kita-Kyushu to San'in district.

2. Methods

Sedimentological and marine geological data were obtained during the survey cruises GH85-2 (May–July, 1985) and GH 86-2 (June–July, 1986) of the R/V Hakurei-Maru by the Geological Survey of Japan. A bathymetric survey using 12 kHz echosounder and 3. 5 kHz sub-bottom profiler was conducted throughout the survey area. Surface sediment sampling was carried out using a Smith-McIntyre type grab sampler or a K (Kinoshita)-type grab sampler which is newly designed by the Geological Survey of Japan (KINOSHITA, 1987); sea bottom photography was carried out at 536 locations.

Grain-size distributions of surface sediments were determined by sieve analysis for the sand component (coarser than 4.5 phi) and by hydrometer analysis for the mud component (finer than 4.5 phi). Median diameters and sorting values were calculated using Inman's method (INMAN, 1952).

3. Physiography and oceanography

Major submarine topographic features in the study area are a wide shelf in the west, a wide marginal terrace and narrow shelf in the east and two topographic highs extending in the north-south direction (Fig. 1). These highs are the Oki Spar, a relief from the Shimane Peninsula through the Oki Islands to further north, and a relief from Cape Kawajiri-misaki through the Mishima Island and Hachirigase Bank to Senrigase Bank. The eastern and western areas are bounded by topographic high through Mishima Island. The shelf is widely developed in the western area (Fig. 1) and some submarine terraces are recognized (MOGI, 1981; OHSHIMA *et al.*, 1982). On the other hand, the shelf is narrow in the eastern area. The shelf edge is about 110–175 m deep and is shallowest at the eastern exit of the Oki Strait (110–120 m deep) and is deepest at the north of Hamada (160–175m deep) (JAPAN ASSOCIATION for QUATERNARY RESEARCH, 1987). The marginal terrace is a

wide terrace 200–400 m deep (IWABUCHI, 1968; IWABUCHI and KATO, 1988) and is developed at the east of Mishima Island. The distinct slope of 2–10° occurs between the edge of shelf or marginal terrace and the Tsushima Basin.

Water masses in the southern Japan Sea can be divided into two parts: surface water (above 200m isobath) and deep water (Japan Sea Proper Water; below 200 m isobath). The surface water is characterized by high temperature, high salinity and low oxygen concentration and originates from the Tsushima Current (ASAOKA *et al.*, 1985; MURAYAMA *et al.*, 1990). The Tsushima Current flows into the Japan Sea through the Tsushima Strait and generally flows eastward (NAGANUMA, 1972; KAWABE, 1982). As mentined earlier, the Tsushima Current shows a very complicated flow pattern. According to SUDA and HIDAKA (1932) and UDA (1934), three branches are recognized. The first branch (the nearshore branch along the Japanese coast) flows eastward from the East Channel of the Tsushima Strait over the Japanese shelf. The second branch (the offshore branch) flows along the edge of the shelf or marginal terracetoward east and is seasonally variable and appears only in summer time. The third branch (the Eastern Korean Current) splits at the exit of the Tsushima Strait and flows northward. The third branch exists in all seasons and forms a polar front against northern cold water mass. Schematic representation of surface currents indicates that many warm and cold water masses are developed among the branches and form eddies (NAGANUMA, 1972).

4. General descriptions of surface sediments

Surface sediments distributed in the study area are mainly composed of sand and silt (MARITIME SAFETY AGENCY, 1949; UJIIÉ and MITSUOKA, 1969; OHSHIMA *et al.*, 1982; IKEHARA and KAWAHATA, 1986 ; IKEHARA *et al.*, 1987; KAMADA *et al.*, 1988). Sandy sediments are widely distributed on the shelf. In the Tsushima Strait and on Hachirigase and Senrigase banks, both located at the north of Mishima Island, gravelly sediments and rocky bottoms are recognized. Silty sediments cover the marginal terrace at the north of Hamada and the shelf at the northeast of the Tsushima Islands. Clayey sediments are deposited on the slope between the marginal terrace and the basin and in the basin.

The assemblages of planktonic remains of diatoms (TANIMURA, 1981), silicoflagellates (SHIMONAKA *et al.*, 1970), planktonic foraminifers (ODA and IKEHARA, 1987) and calcareous nannoplanktons (TANAKA, 1986, 1987) are composed of warm-water species and indicate that all of the study area is under the realm of influence of the warm Tsushima Current.

5. Influences of the water movements at the selected area

5-1. The Tsushima Strait

In and around the Tsushima Strait, the effects of the Tsushima Current are recorded on the sediment distributions and bedform morphology. Sediment distribution in and around the Tsushima Strait (Fig. 2) has been reported by many workers (UJIIÉ and MITSUOKA, 1969; MARITIME SAFETY AGENCY, 1978a, 1978b, 1979, 1980, 1981a, 1981b, 1982, 1983; OHSHIMA *et al.*, 1982; IKEHARA and KAWAHATA, 1987; KAMADA *et al.*, 1988). Surface sediments in the Strait are sand except northeast of the Tsushima Islands and offshore of the Korean coast where muddy sediments are deposited. In general, sediment grain size becomes finer from the central part of the Strait toward the northeast (Fig. 2). For example, in the East Channel, the coarsest sediments (coarse to very coarse sand) are distributed in the central part, that is, at the north of the Shichirigase Bank. The grain size becomes finer northeastward and the fine to very fine sand is widely distributed around the exit of the East Channel. Because sediment grains become finer with decreasing flow velocity and these trends are in harmony with the direction of sediment transport (KIMURA, 1956; IKEHARA, 1988), the sediment distribution in the Tsushima Strait indicates northeastward sediment transport.

MOGI (1981) showed the distribution of submarine linear sand ridges more than 10m in waveheight in the East Channel, which are arranged in current-parallel direction, trending NE-SW. This trend is the same as the direction of sediment transport. Although these sand ridges were formed by tidal currents under lower

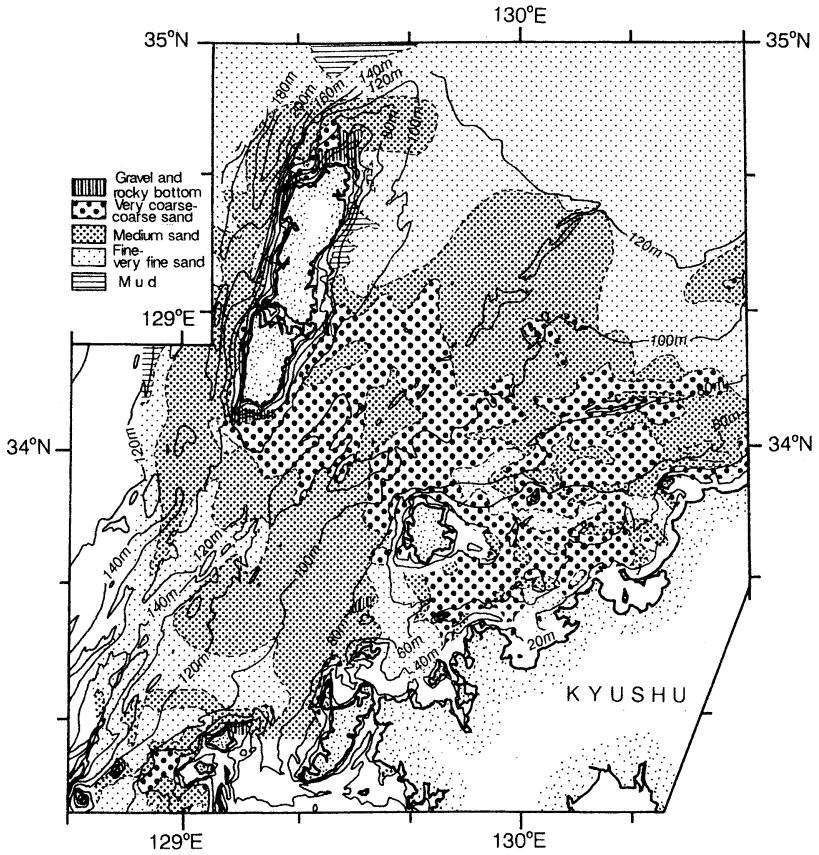

Fig. 2. Sediment distribution in and around the Tsushima Strait. Data are compiled from UJIIÉ and MITSUOKA (1969), MARITIME SAFETY AGENCY (1978a, b, 1979, 1980, 1981a, b, 1982, 1983), OHSHIMA *et al.* (1982), IKEHARA and KAWAHATA (1987), KAMADA *et al.* (1988) and the navigational charts (No.173, 179, 1228) by MARITIME SAFETY AGENCY.

sea level stage (80 m below present sea level) (MOGI, 1981), it is thought that the sand ridges have maintained their morphology after their formation because of no critical change in the direction of sediment transport in the East Channel. KATSURA and NAGANO (1982) showed the distribution and morphology of subaqueous dunes near the shelf edge of the northwestern Goto-Islands, southwest of the Tsushima Strait. On the basis of profiles of these subaqueous dunes, sandy sediments are transported northeastward. Tidal currents are also important to flow condition in the Tsushima Strait. As grain size of surface sediments does not become finer gradually toward the southwest in the East Channel (Fig. 2) and morphology of subaqueous dunes in and around the Strait (MARITIME SAFETY AGENCY, 1978b; KATSURA and NAGANO, 1982) does not indicate the southwestward sediment transport, sediment transport in the Strait is controlled by uni-directional current (Tsushima Current) rather than bi-directional tidal currents.

It is considered that mud deposition on the east of the Tsushima Islands (Fig.2) results from hydrographically more stagnant zone than the surroundings where the northeastward current from the East Channel flows at the south and the east to east-northeastward current from the West Channel flows at the north. Muddy sediments in the northern side of the West Channel are derived from Korea (SUK, 1986, 1989; CHOUGH *et al.*, 1991) and are deposited in the area of the Korea Coastal Water (SUK, 1989).

These sediment distribution and bedform data indicate that the bottom sediments in and

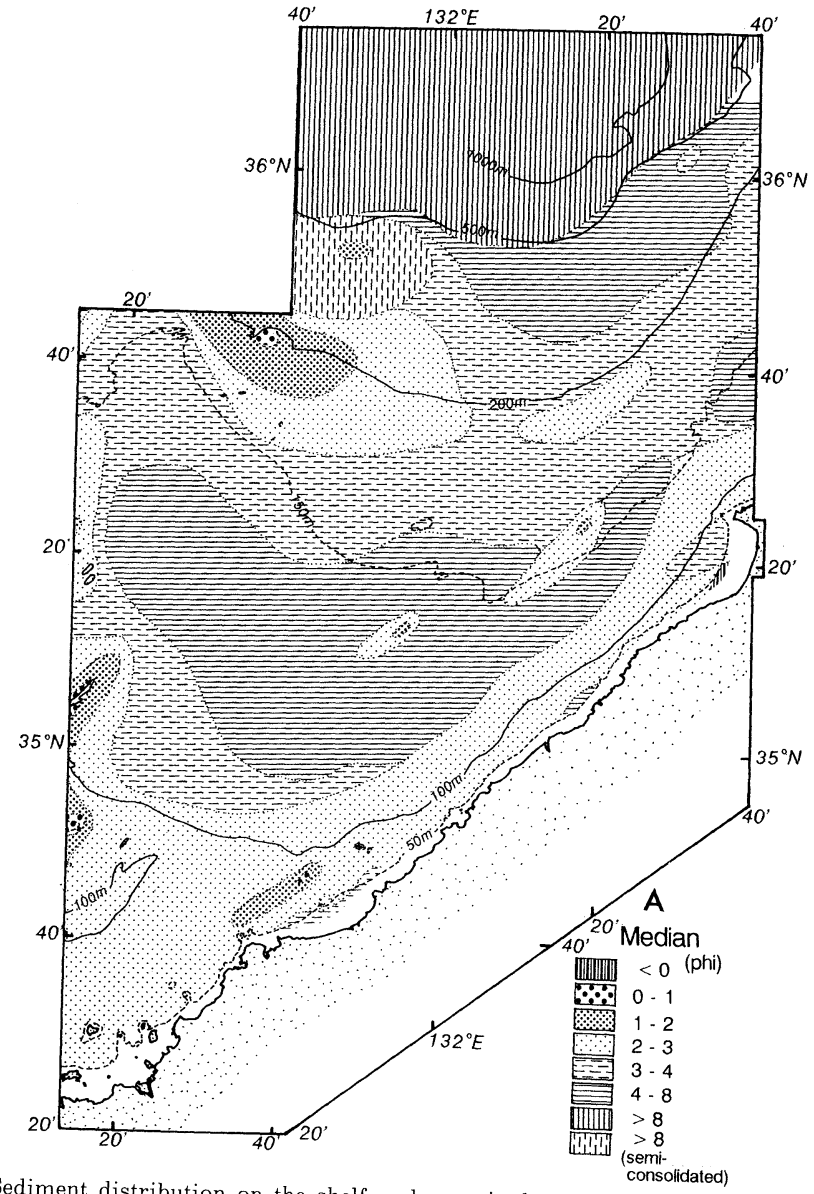

Fig. 3-1. Sediment distribution on the shelf and marginal terrace at the north of Hamada.

around the Tsushima Strait have been affected by a current flowing northeast to east-northeastward, that is, the Tsushima Current.

5-2. Shelf area along the Japanese coast; effects of the first branch on the sea bottom

The first branch of the Tsushima Current flows over the Japanese shelf from the East Channel of the Tsushima Strait. In this area, it is thought that the effects of the current on sediment transport and deposition are very small under modern conditions.

On the shelf under the current path of the first branch, muddy sediments are widely distributed, although sandy sediments are distributed at the north of Kyushu shelf and around the Oki Strait (IKEHARA and KAWAHATA, 1986; IKEHARA *et al.*, 1987; KAMADA *et al.*, 1988). In general, deposition of muddy sediments occurs where the amounts of mud supply are greater

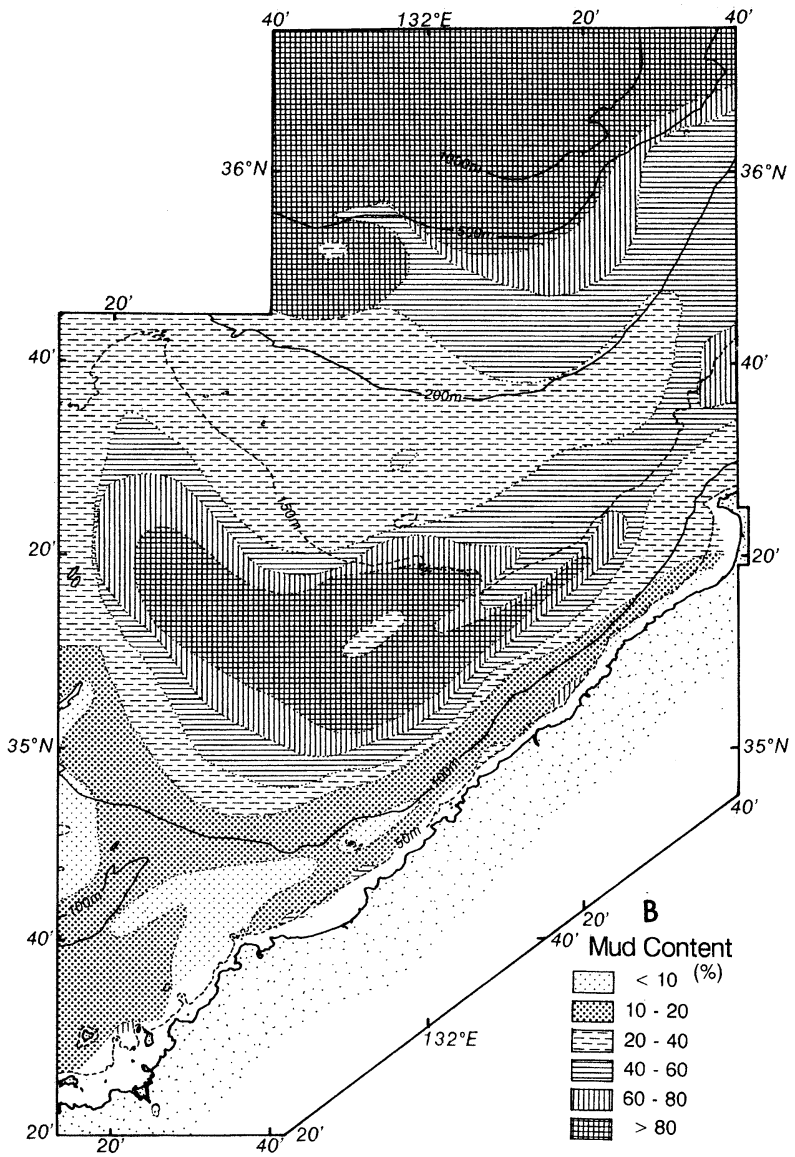

Fig. 3–2.

than that reworked by water movements (SAITO, 1989), generally inhibited by water movements such as currents and waves (IKEHARA, 1991). On the marginal terrace with a water depth of 200 –300 m at the north of Hamada, modern muddy sediments are deposited, though just beneath the path of the first branch of Tsushima Current (Fig.3). This suggests that the current activities are too weak to prevent the deposition of mud. As the boundary between the surface water and the deep water is located around 200 m deep, the first branch has no effect on the movement of deep water mass.

On the shelf under the path of the first branch off Kyushu, no large bedforms such as large subaqueous dunes are observed. On the other hand, in the Oki Strait, which is located between the Shimane Peninsula and the Oki Islands, smaller ripple marks are not distributed widely, although larger bedforms such as large–very

Table 1. Composition of pollen and spores in the semiconsolidated mud at Station 862 63 (for location see Fig.5)

Arboreal Pollen (AP)			Nonarboreal Pollen (NAP)		
Taxa	Counts	Percentage	Taxa	Counts	Percentage
Picea	18	5.6	Typha	2	0.6
Abies	38	11.9	Umbelliferae	2	0.6
Pinus	72	22.6	Chenopodiaceae	2	0.6
Tsuga	67	21.0	Rosaceae	1	0.3
Cryptomeria	1	0.3	Caryophyllaceae	2	0.6
Larix	1	0.3	Artemisia	11	3.4
Cupressaceae	1	0.3	Liliaceae	1	0.3
Fagus	1	0.3	Poligonium	1	0.3
Carpinus	5	1.6	Carduoideae	1	0.3
Castanea	1	0.3	Cyperaceae	2	0.6
Quercus	31	9.7	Gramineae	4	1.3
Celtis	1	0.3	Lycopodiaceae	2	0.6
Betula	13	4.1	Tricolporate	5	1.6
Alnus	10	3.1	Trilete type	1	0.3
Carya	2	0.6	Monolete type	20	6.3
AP Total	262	82.1	NAP Total	57	17.9

large (50–490m in wavelength) and medium–large subaqueous dunes (8–20 m in wavelength) are found (IKEHARA, 1991). Because ripple marks are formed under lower velocity condition than subaqueous dunes, modern sand transport is too small to create or activate tha large bedforms (IKEHARA, 1991).

5-3. The edge of shelf or marginal terrace from the north of Kita-Kyushu to the Oki Islands; effects of the second branch or surface water circulations (eddies) on the sea bottom

Along the edge of shelf or marginal terrace from the northern offshore of Kita-Kyushu to the Oki Islands many indicators of bottm water movements are recognized.

Well-sorted sandy sediments with low mud content and ripple marks are found on the surface along the shelf edge of the north of Kita-Kyushu at a water depth of around 120-200m (Fig. 4). It suggests the occurrence of bottom currents which transport sandy sediments and prevent mud deposition. Surface sediments become finer in grain size, greater in mud content and more poorly sorted northeastward. This direction indicates the direction of decreasing current velocity as well as decreasing sediment transport. Plan morphologies of ripple marks show a relatively complicated flow pattern dominated by currents moving east to northeastward (Fig.4-2D), that is, almost parallel to the direction of shelf edge. It is considered that the direction of the long-term, averaged sediment transport is northeastward, inferred from the spatial distribution of surface sediments and ripple mark morphology.

The current velocity near the bottom can be inferred from sedimentological data, because bedform type is primarily controlled by the interaction between hydraulic conditions of the flow such as current velocity and flow depth, and sediment properties (e.g. SIMONS *et al.*, 1965; RUBIN and MCCULLOCH, 1980). The ranges of flow conditions necessary to create bedforms such as ripple marks are estimated from experimental and field observations (SIMONS *et al.*, 1965; SOUTHARD, 1971, 1975; RUBIN and MCCULLOCH, 1980). It is estimated that the current velocity necessary to move the sand grain is about 25 cm/s, and the transition from ripple marks to subaqueous dunes is about 70 cm/s at 1 m above the sea bottom, using the relationship shown by RUBIN and MCCULLOCH (1980, Fig. 8). As ripple marks are forming and subaqueous

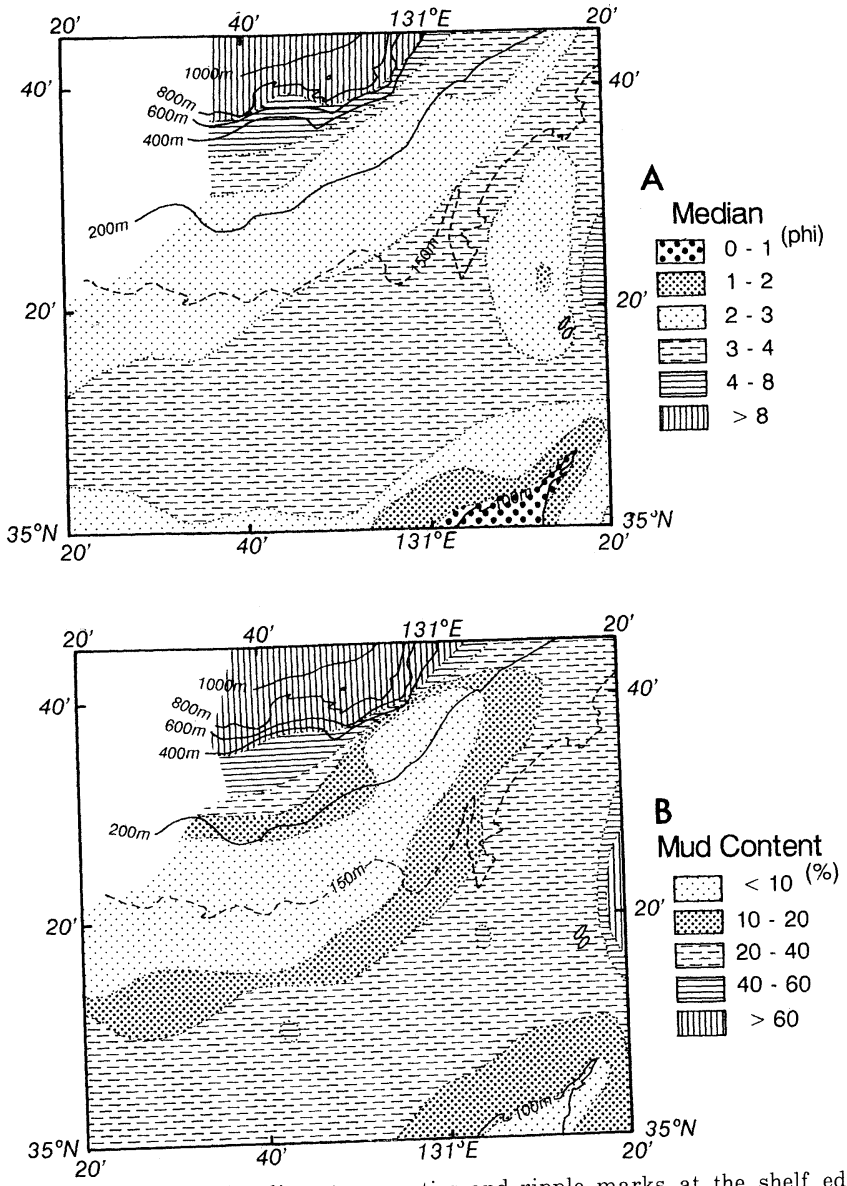

Fig. 4-1. Distribution of sediment properties and ripple marks at the shelf edge of the north of Kita-Kyushu.

dunes are not forming on the fine sand bed at the shelf edge off Kita-Kyushu, it is inferred that the bottom currents have the velocity between 25–70 cm/s at 1 m above the sea bottom.

At the edge of marginal terrace between Mishima Island and the Oki Islands, which has a water depth around 200–500 m, semiconsolidated muddy sediments are exposed on the sea bottm (Fig.5). Some of them are covered by thin sheet of very fine sand with rounded granules. Old and reworked foraminiferal species are contained in the very fine sand (ODA and IKEHARA, 1987; NOMURA and IKEHARA, 1987). Calcareous nannoplankton assemblages in the semiconsolidated mud are different from those in modern mud distributed on both the inner marginal terrace and outer basin, containing cold water species and reworked older fossils of the Cretaceous age (TANAKA, 1986, 1987). Pollen fossils in a semiconsolidated mud collected at Station 862–

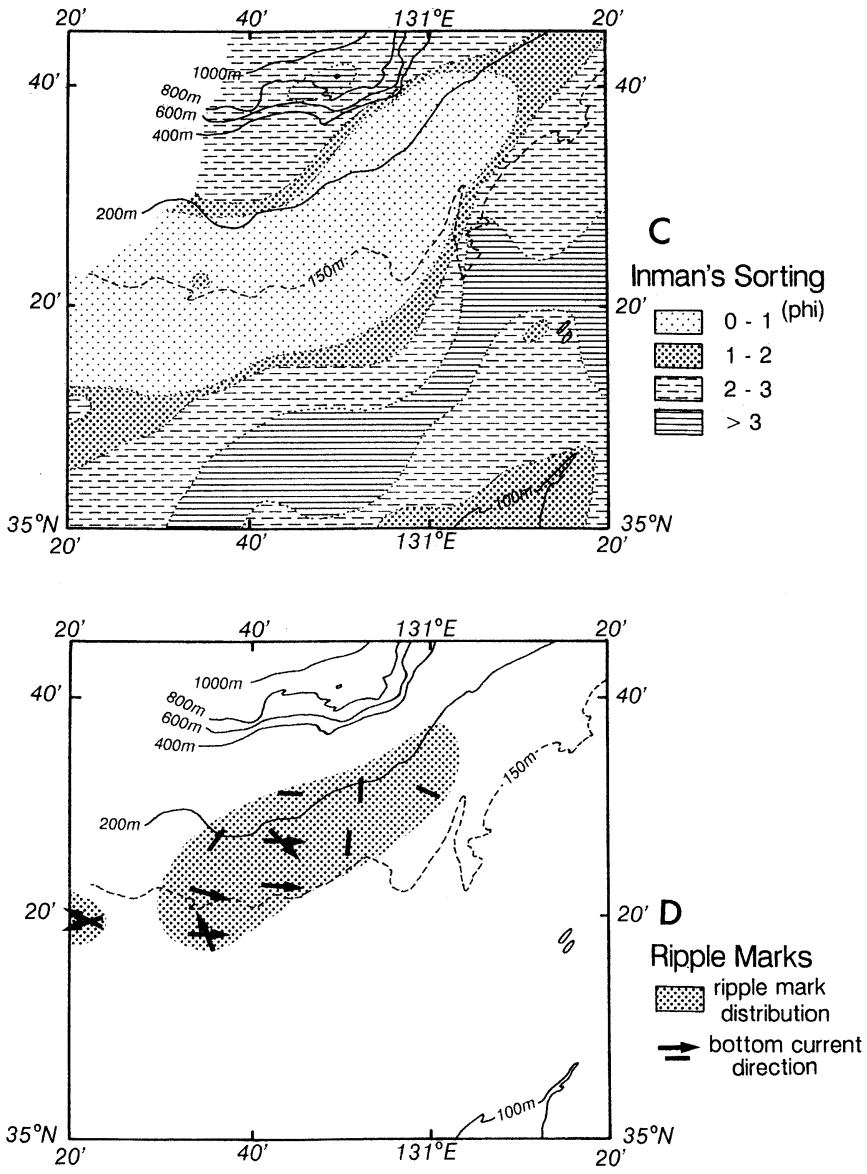

Fig. 4-2.

63 (shown in Fig. 5) with a water depth of 311 m indicate a colder climate (glacial period). That is, it has a high percentage of subarctic flora containing Haploxyon-type Pinus which has five needled leaves and a lower percentage of temperate broad-leaved trees than present (Table 1). Very rough profiles in bathymetric records are found along the southern boundary of the semi-consolidated mud at the north of Mishima Island (OGAWA *et al.*, 1986). Uplift and exposure of older basement are recognized in sub-bottom profiler records (Fig.6), and rocky bottoms are observed at the north of Mishima Island (Fig. 5). In addition, teeth of older elephants (*Palaeoloxodon naumanni* MAKIYAMA) of the Pleistocene age (about 30000–40000 years B.P.; HOSIMI and MORIOKA, 1987; AKIYAMA *et al.*, 1988) have been collected from this area (KAMEI, 1967; AKAGI, 1981; KAMEI *et al.*, 1986). These facts show that the sedimentation rate in this

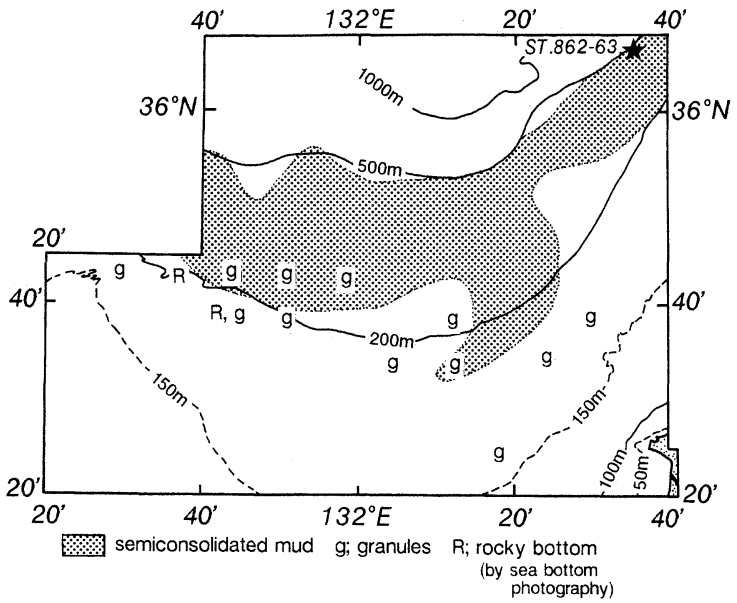

Fig. 5. Distribution of sediment properties at the edge of marginal terrace between Mishima Island and the Oki Islands. Star (upper-right) shows the location of Station 862-63.

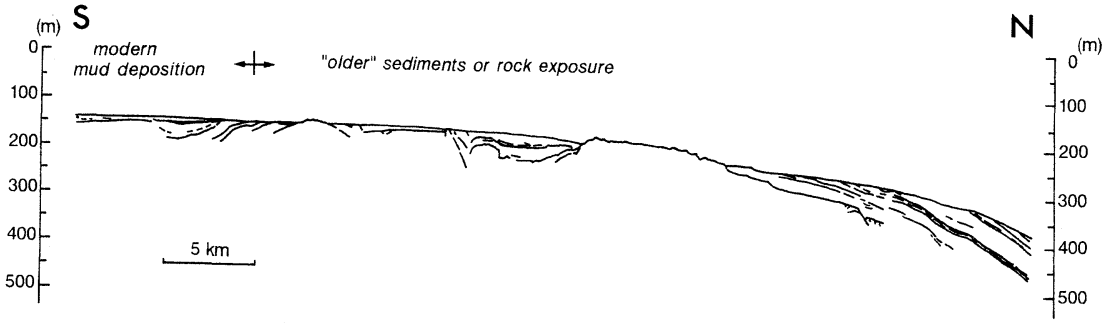

Fig. 6. Seismic (3.5 kHz) profiler record near the edge of marginal terrace at the north of Mishima Island.

area is very small. The occurrence of current lineations on the sea bottom around the rocky area indicates the presence of a bottom current. Therefore, it is considered that this area is now under non-depositional or erosional conditions by the effects of bottom currents.

These sedimentological data show the occurrenct of bottom current along the edge of shelf or marginal terrace. There are some possibilities for the generating force of the bottom currents. One is that the current is caused by the second branch of the Tsushima Current. It is shown from the coincidences of the current path of the second branch with the area where the occurrence of bottom current is inferred, and of the direction of sediment transport at the north of Kita-Kyushu shelf edge with that of the second branch. The second branch is not a permanent flow, present only in summer time (KAWABE, 1982). Therefore, it is difficult to make bottom currents transport the sandy sediments and prevent modern mud deposition throughout the year. Another possibility is the surface water circulations (eddies) formed among the branches or meandering path of the Tsushima Current. These eddies are recognized at both of the north of Kita-Kyushu shelf edge and north of Hamada marginal terrace edge (NAGANUMA, 1972). There is a possibility that the complicated figure in the bottom current

pattern inferred from ripple mark morphology at Kita-Kyushu shelf edge (Fig. 4–2) is caused by the complicated bottom water movements near the edge of eddies. Another possibility is the contour currents which flow along depth contour. Although ISODA and MURAYAMA (1991) reported the occurrence of the contour current which flows eastward with the fluctuation of a period of 13.7 days at the shelf edge off Hamada, precise figure of the contour currents is still unclear. Therefore, it is difficult to describe the relationship between the contour currents and the sediment transport. Although there are no data to decide the original force generat the bottom currents at present, bottom currents are controlling the modern sedimentation at the shelf or marginal terrace edge.

6. Summary

Effects of surface water circulation on the sea bottom in the southern Japan Sea are recognized in and around the Tsushima Strait and along the edge of shelf or marginal terrace. At the edge of marginal terrace of north of Hamada, the water circulations influence the sea bottom of 200–500 m deep. Because IKEHARA (1991) showed the current effects on sediment transport and deposition at the western Oki Ridge with a water depth of around 500 m, the bottom current occurs up to 500 m deep. On the other hand, there is no evidence of active bottom current on the shelf and marginal terrace in the eastern part of study area. This suggests that the first branch of the Tsushima Current does not affect the sea bottom in the north of San'in coast.

Acknowledgements

I express my hearty thanks to officers, crew and scientists of the R/V Hakurei-Maru for their kind help throughout the surveys. I am grateful to Drs.Masafumi ARITA and P.A. JARVIS of the Geological Survey of Japan for their critical readings of an early version of the manuscript. Acknowledgements are due to, Drsa. Hodaka KAWAHATA, Yuichiro TANAKA and Mr.Hajime KATAYAMA of the Geological Survey of Japan for their cooperations in field and laboratory works and fruitful discussions. Thanks are also due to Dr.S.K. CHOUGH for his valuable suggestions on the manuscript. This work was supported by the special research program, geological mapping on the continental shelf areas in Japan, of the Geological Survey of Japan.

References

AKAGI, S. (1981): *Palaeoloxodon naumanni* (MAKIYAMA) from the sea bottom off the coast of San'in. J. Faculty of Education, Tottori Uni., Natural Science, **30**, 57–64.

AKIYAMA, M., T. KAMEI and N. NAKAI (1988): ^{14}C ages of Naumann's elephant *Palaeoloxodon naumanni* (MAKIYAMA) from the sea bottom off the San'in district in the Sea of Japan by accelerator mass spectrometry. ^{14}C age of the Quaternary deposits in Japan (168), Earth Science (Chikyu-Kagaku), **42**, 29–31.

ASAOKA, O., Y. HASHIMOTO and K. KATAYAMA (1985): Physical oceanography in the Wakasa Bay. *In*: Coastal Oceanography of Japanese Islands, Coastal Oceanogr. Res. Committee, Oceanogra. Soc. Japan, Tokai Univ. Press, Tokyo, 958–968.

CHOUGH, S.K., H.J. LEE and S.J. HAN (1991): Sedimentological and geotechnical properties of fine-grained sediments in part of the South Sea, Korea. Continental Shelf Research, **11**, 183–195.

HOSIMI, K. and H. MORIOKA (1987) ^{14}C age of *Palaeoloxodon naumanni* (MAKIYAMA) from the sea bottom off the coast of San'in. ^{14}C age of the Quaternary deposits in Japan (165). Earth Science (Chikyu-Kagaku), **41**, 248–250.

ICHIYE, T. (1954): On the distribution of oxygen and its seasonal variation in the adjacent seas of Japan. Oceanogr. Mag., **6**, 41–66.

IKEHARA, K. (1988): Ocean current generated sedimentary facies in the Osumi Strait, south of Kyushu, Japan. Progress in Oceanography, **21**, 515–524.

IKEHARA, K. (1989): Some physical properties of shelf to basin deposits off San'in and Hokuriku district, southern part of Japan Sea. Bull. Geol. Survey of Japan, **40**, 239–250.

IKEHARA, K. (1991): Modern sedimentation off San'in district in the southern Japan Sea. *In*: Oceanography of Asian Marginal Seas, ed. K. TAKANO, Elesevier Oceanography Series, **57**, Elesevier, Amsterdam, 143–161.

IKEHRA, K., H.KATAYAMA and M. ARITA (1987): Surface sediments off San'in district. *In*: Prel. Reports of Geological Mapping Program of the Continental Shelf Areas in Japan in 1986. eds. M. ARITA, Y. OKUDA and T. MORITANI,

Geol. Survey of Japan, Tsukuba, 121–152.

IKEHARA, K. and H. KAWAHATA (1986): Surface sediments off Kita-Kyushu. *In*: Prel. Reports of Geological Mapping Program of the Continental Shelf Areas in Japan in 1985, eds. S. NAKAO, K. TAMAKI and T. MORITANI, Geological Survey of Japan, Tsukuba, 68–102.

INMAN, D. L. (1952): Measures for describing the size distribution of sediments. J. Sedimentary Petrology, **22**, 125–145.

ISODA, Y. and T. MURAYAMA (1991): Mesoscale (three-fifteen days) fluctuation off Hamada. Abstracts of the 50 years memorial meeting of the Oceanogr. Soc. of Japan, 182–183.

IWABUCHI, Y. (1968): Submarine geology of the southeastern part of the Japan Sea. Contributions of Institute of Geology and Palaeontology, Tohoku University, **66**, 1–76.

IWABUCHI, Y. and S. KATO (1988): Some features of the continental shelf around the Japanese Islands on compilation of the Quaternary Map. The Quaternary Research (Daiyonki-kenkyu), **26**, 217–225.

JAPAN ASSOCIATION for QUATERNARY RESEARCH (1987): Quaternary Maps of Japan I, Land forms, Geology and Tectonics, C. southwest Japan. *In*: Quaternary Maps of Japan (with explanatory text), Japan Association for Quaternary Reserch, Univ. of Tokyo Press, Tokyo.

KAMADA, Y., H. KONDO and T. MIITA (1988): Bottom sediments in the Genkainada, off Fukuoka Prefecture, Kyushu, Japan. Science Bull. Fac. Education, Nagasaki Univ., **39**, 73–82.

KAMEI, T. (1967): *Elephas naumanni* MAKIYAMA from the sea bottom of the southern Sea of Japan. Earth Science Report of College of Liberal Arts and Science, Kyoto Univ. (Tsukumo Earth Science), **2**, 24–31.

KAMEI, T., S. AKAGI, H. OTHUKA, N. OKADA and H. SHIBATA (1986): Elephant fossils collected from the sea bottom around the Japanese Islands. Abstr. 93rd annual meeting of the Geol. Soc. of Japan, 135.

KANO, Y. (1980): The annual variation of the temperature, salinity and oxygen content in the Japan Sea. Oceanogr. Mag., **31**, 15–26.

KATSURA, T. and M. NAGANO (1982): Geomorphology of Goto shelf channels off northern Kyushu, Japan. Report of Hydrogr. Res., **17**, 71–92.

KAWABE, M. (1982): Branching of the Tsushima Current in the Japan Sea, Part I. Data analysis. J. Oceanogr. Soc. Japan, **38**, 95–107.

KIMURA, H. (1956): Mechanism of sorting–a fundamental study of sedimentation (Part 7). J. Geol. Soc. of Japan, **62**, 472–489.

KINOSHITA, Y. (1987): K (Kinoshita) -type grab sampler and its results for practical use. *In*: Preliminary Reports of Geological Mapping Program of the Continental Shelf Areas in Japan in 1986, eds. M. ARITA, Y. OKUDA and T. MORITANI, Geological Survey of Japan, Tsukuba, 232–233.

KOLPACK, R. L. (1982): Temperature and salinity changes in the Tsushima Current. La mer, **20**, 199–209.

MARITIME SAFETY AGENCY (1949): Bottom sediment chart of the adjacent seas of Japan. sheet 1-4. Chart No. 7051–7054, Maritime Safety Agency, Tokyo.

MARITIME SAFETY AGENCY (1978a): Basic Map of the Sea in Coastal Waters (1:50,000) Tutu (with report of survey). Maritime Safety Agency, Tokyo, 39p.

MARITIME SAFETY AGENCY (1978b): Basic Map of the Sea in Coastal Waters (1:50,000) Northern part of Iki (with report of survey). Maritime Safety Agency, Tokyo, 39p.

MARITIME SAFETY AGENCY (1979): Basic Map of the Sea in Coastal Waters (1:50,000) Siro-se (with report of survey). Maritime Safety Agency, Tokyo, 39p.

MARITIME SAFETY AGENCY (1980): Basic Map of the Sea in Coastal Waters (1:50,000) Hukue-sima (with report of survey). Maritime Safety Agency, Tokyo, 37p.

MARITIME SAFETY AGENCY (1981a): Basic Map of the Sea in Coastal Waters (1:50,000) Northern part of Tusima-East Coast (with report of survey). Maritime Safety Agency, Tokyo, 41p.

MARITIME SAFETY AGENCY (1981b): Basic Map of the Sea in Coastal Waters (1:50,000) Southern part of Tusima-East Coast (with report of survey). Maritime Safety Agency, Tokyo, 39p.

MARITIME SAFETY AGENCY (1982): Basic Map of the Sea in Coastal Waters (1:50,000) Southern part of Iki (with report of survey). Maritime Safety Agency, Tokyo, 51p.

MARITIME SAFETY AGENCY (1982): Basic Map of the Sea in Coastal Waters (1:50,000) Western part of Nakadori-sima (with report of survey). Maritime Safety Agency, Tokyo, 39p.

MOGI, A. (1981): Geomorphological evolution of continental shelves of Tsushima Strait–with reference to the Tsushima land bridge–. Quaternary Res. (Daiyonki-kenkyu), **29**, 243–256.

MORIYASU, S. (1972): The Tsushima Current. *In*: Kuroshio, eds. H. STOMMEL and K. YOSHIDA,

Univ. Washington Press, Seattle, 353–369.

MURAYAMA, T., A. KUWABARA and Y. OGAWA (1990): Physical oceanography off San'in coast. *In*: Coastal Oceanography of Japanese Islands, Supplementary Volume. Coastal Oceanogr. Res. Committee, Oceanogr. Soc. Japan, Tokai Univ. Press, Tokyo, 755–767.

NAGANUMA, K. (1972): The oceanographical conditions in the Japan Sea. Gyokaikyo Handobukku (Handbook of Fishery Oceanography), Zengyoren Gyokaikyo Center, 32–38.

NITANI, H. (1972): Beginning of the Kuroshio. *In*: Kuroshio, its physical aspects. eds. H. STOMMEL and K. YOSHIDA, Univ. Tokyo Press, Tokyo, 129–163.

NOMURA, R. and K. IKEHARA (1987): Benthic foraminiferal assemblage off San'in district. *In*: Preliminary Reports of Geological Mapping Program of the Continental Shelf Areas in Japan in 1986, eds. M. ARITA, Y. OKUDA and T. MORITANI, Geological Survey of Japan, Tsukuba, 165–176.

ODA, M. and K. IKEHARA (1987): Preliminary reports on the planktonic foraminiferal assemblage off San'in district. *In*: Preliminary Reports of Geological Mapping Program of the Continental Shelf Areas in Japan in 1986. eds. M. ARITA, Y. OKUDA and T. MORITANI, Geological Survey of Japan, Tsukuba, 162–164.

OGAWA, T., K. IKEHARA and H. KAWAHATA (1986): Preliminary report on the unconformity found around the water depth of 200 m, off Mishima Island, Yamaguchi Prefecture. *In*: Preliminary Reports of Geological Mapping Programs of the Continental Shelf Areas in Japan in 1985, eds. S. NAKAO, K. TAMAKI and T. MORITANI, Geological Survey of Japan, Tsukuba, 137–145.

OHSHIMA, K., E. INOUE, K. ONODERA, M. YUASA and K. KURODA (1982): Sediments of the Tsushima Strait and Goto-nada Sea, northwestern Kyushu. Bull. Geological Survey of Japan, **33**, 321–350.

RUBIN, D. M. and D. S. MCCULLOCH (1980): Single and superimposed bedforms: a synthesis of San Francisco Bay and flume observations. Sedimentary Geology, **26**, 207–231.

SAITO, Y. (1988): Relationships between coastal topography and sediments, and wave base. Earth Monthly (Gekkan Chikyu), **10**, 458–466.

SHIMONAKA, M., F. OGAWA and W. ICHIKAWA (1970): Silicoflagellatae remains in the deep-sea sediments from the Sea of Japan. Nihonkai (Japan Sea), **4**, 1–14.

SIMONS, D.B., E.V. RICHARDSON and C.F. NORDIN, Jr. (1965): Sedimentary structures generated by flow in alluvial channels. *In*: Primary Sedimentary Structures and Their Hydrodynamic Interpretation, ed. G.V. MIDDLETON, SEPM Special Publication, **12**, 34–52.

SOUTHARD, J.B. (1971): Representation of bed configurations in depth-velocity-size diagrams. J. Sedimentary Petrology, **41**, 903–915.

SOUTHARD, J.B. (1975): Bed configurations. *In*: Depositional Environments as Interpreted from Primary Sedimentary Structure and Stratification Sequences. SEPM Short Course Notes, **2**, 5–43.

SUDO, K. and K. HIDAKA (1932): The results of the oceanographical observations on board R. M. S. "Syunpu Maru" in the southern part of the Japan Sea in the summer of 1929, Part 1. J. Oceanogr., **3**, 291–375.

SUK, B.-C. (1986): Depositional environment of late Quaternary sediments and suspended particulate matter on the southeastern continental shelf, Korea. J. Geol. Soc. Korea, **22**, 10–20.

SUK, B.-C. (1989): Sedimentology and history of sea level changes in the East China Sea and adjacent seas. *In*: Sedimentary Facies in the Active Plate Margin, eds. A. TAIRA and F. MASUDA, editors, Terra Scientific Publishing Company (TERRAPUB), Tokyo, 215–231.

SUNDBORG, Å. (1956): The river Klaralven. A study of fluvial processes. Geografiska Annaler, **38**, 127–316.

TANAKA, Y. (1986): Calcareous nannofossils in the surface sediments around the Tsushima Strait. *In*: Preliminary Reports of Geological Mapping Program of the Continental Shelf Areas in Japan in 1985, eds. S.NAKANO, K. TAMAKI and T. MORITNI, Geological Survey of Japan, Tsukuba, 128–136.

TANAKA, Y.(1987): Calcareous nannofossil assemblages in the surface sediments around the Oki Islands. *In*: Preliminary Reports of Geological Mapping Program of the Continental Shelf Areas in Japan in 1986, eds. M. ARITA, Y. OKUDA and T. MORITANI, Geological Survey of Japan, Tsukuba, 177–185.

TANIMURA, Y. (1981): Late Quaternary diatoms of the Sea of Japan. Science Reports of Tohoku University, 2nd series (Geology), **51**, 1–37.

UDA, M. (1934): The results of simultaneous oceanographical investigations in the Japan Sea and its adjacent water in May and June, 1932. J. Imperial Fishery Experimental Station, **5**, 57–190.

UJIIÉ, H. and T. MITUOKA (1969): Preliminary

report on the topography and sediments of the Tsushima Straits, southern entrance to the Sea of Japan. Memoirs of the National Science Museum, **2**, 29–38.

YAMAMOTO, H., M. JOSHIMA and K. KISIMOTO (1989): Geological map offshore of Tottori (with explanatory notes). Marine Geology Map Series, **35**, Geological Survey of Japan, Tsukuba, 27p.

La mer 30: 119–125, 1992
Société franco-japonaise d'océanographie, Tokyo

A laboratory model of thermally-driven marginal seas

Masaki TAKEMATSU*

Abstract: Here we describe a new laboratory experiment which has been designed to study the possible effects of the differential cooling of the Japan Sea on the Tsushima Current system. The laboratory model consists of a cylindrical basin of uniform depth placed centrally in a lager tank; the inner basin ('the Japan Sea') is connected to the outer tank through two shallow passages on the western and eastern side of the basin. The fluid motion in the model is driven by cooling the northern portion of the basin's sidewall. By means of a dye technique it is observed that the localized sinking of cold water along the northern sidewall, combined with (constant) Coriolis forces and damping effects, gives rise to not only an intense western boundary current in the inner basin but also an inflow through the western passage (the 'Korea/Tsushima Strait') and a compensating outflow through the eastern passage (the 'Tsugaru Strait'). A feature of the buoyancy-driven inflow through the 'Korea/Tsushima Strait' is that its volume transport tends to concentrate in the northern part of the Strait.

In some experimental runs the eastern passage is closed to model the Mediterranean Sea with the Strait of Gibraltar. In this case the differential cooling of the inner basin induces a surface inflow through the single western passage; the surface inflow is replaced by a compensating lower-layer outflow from the inner basin.

1. Introduction

A major feature of the current system in the Japan Sea is the inflow of the Tsushima Current through the Korea/Tsushima Strait and the outflow through the Tsugaru Strait. This in- and outflow phenomenon in the Japan Sea is generally thought to be caused by the pressure (sea-level) difference associated with the Kuroshio current system in the North Pacific Ocean (cf. Minato and KIMURA, 1980; TOBA *et al.*, 1982; SEKINE, 1988; FANG et al., 1991). As noted by MINATO and KIMURA (1980), however, the pressure difference in the open ocean is merely one of possible factors causing the in- and outflow of the marginal sea: Other relevant factors include the differential cooling and the wind forcing over the Japan Sea. Indeed, a previous laboratory study of TAKEMATSU (1991) suggested that a localized sinking of cold water due to differential cooling of an ocean basin might strongly affect the in- and outflow process through openings (or an opening) of the basin. The objective of the present study is to confirm this suggestion in a suitable laboratory model.

The laboratory model employed is a conceptually simple one on an f-plane, consisting of a cylindrical basin of uniform depth which is connected to an 'open ocean' through two shallow passages. The fluid motion is driven by applying a uniform cooling at a portion (1/4) of the basin's vertical sidewall. The sidewall cooling is much easier to control than the more realistic way of cooling from above, and that it can produce a localized sinking of cold (dense) water which is an essential part of the oceanic buoyancy forcing. The resultant convective circulations in the model are observed by means of a dye technique over a period of 'stratification time scale'.

On an f-plane, unlike on a β-plane, there is no definite rule for introducing cardinal points to the system. One natural and meaningful way of doing so is to regard the cooled portion of the basin as "north" ("south") for the northern (southern) hemisphere basic rotation; other directions are then automatically determined. In what follows, we will follow this rule and

* Research Institute for Applied Mechanics, Kyushu University, Kasuga 816, Japan.

directions thus introduced will be distinguished by attaching a quotation mark " "as "west" or "western". In most experiments o ne passage is made on the "west" side of the inner basin and the other is on the "east" side to model the basic configuration of the Japan Sea. If the "eastern" passage is closed, the model mimics the Mediterranean Sea with the Strait of Gibraltar. Experiments are carried out also for this version with a single passage to see the possible effect of the northern sinking in the Mediterranean Sea on the water exchange processes through the Strait of Gibraltar.

2. Description of experiments

A top view of the laboratory model is schematically shown in Fig. 1. The model consists of a plexiglass cylindrical container (40 cm in diameter) placed centrally in another container (60 cm in diameter). The inner basin is connected to the outer one (an 'open ocean') through two shallow passages with a width of 5 cm (about 5 times the internal radius of deformation). A portion (1/4) of the annulus region between the two cylindrical containers is partitioned by two *insulated* vertical plates so that the water temperature in this portion can be varied independently of the remainder. The working fluid then occupies the remaining portion (3/4) of the annulus region and the inner basin to a constant depth (mostly 8 cm). These working basins are further set in a larger water tank (80 cm in diameter) to minimize the effect of the change in room temperature on the working fluid; otherwise, the sidewall of the outer basin is directly exposed to the temperature change, which readily gives rise to unwanted convective motions in the annulus region and then in the inner basin. Initially all the water temperatures in the apparatus were set at a fixed value, say T_0, and the top of the working basin was covered with a lucite plate to prevent the air from exerting a stress on the free surface of the working fluid (the gap between the top cover and the free surface was less than 1 cm). The whole apparatus was mounted on a turntable and set rotating in the counter-clockwise direction about its vertical axis of symmetry. After the working fluid attained a complete solid-body rotation (this was checked by releasing dye-lines), the water temperature in the partitioned (1/4) portion of the annulus region was lowered by ΔT_0 by adding chilled water to the "northern" cooling zone and was kept at the lowered value ($T_0 - \Delta T_0$) throughout the duration of each experimental run, while the water temperature in the outermost tank was kept constant at the initial value T_0. This allowed us to impose a well-controlled local cooling on the vertical sidewall of the inner basin. Experiments were conducted only when the room temperature was slightly (by less than 0.5℃) higher than the basin water temperature; otherwise, the top cover of the working basin would be dimmed with water vapor. Hence the working fluid was subject to heating from above. Repeated checks by dye lines showed that the uniform heating from above alone induced no appreciable motion in the basin.

The convective motion thus induced in the basin was observed by a dye technique. For this purpose, a diluted solution of thymol blue (a pH indicator) was used as the working fluid and several electrodes of 0.005 cm platinum wire were stretched horizontally at desired locations and depths. A standard arrangement of dye wires is sketched in Fig. 1, where the lower dye wire is at 1.5 cm above the bottom plate and others are at the mid-depths of the inner basin and the passages. A movable vertical electrode

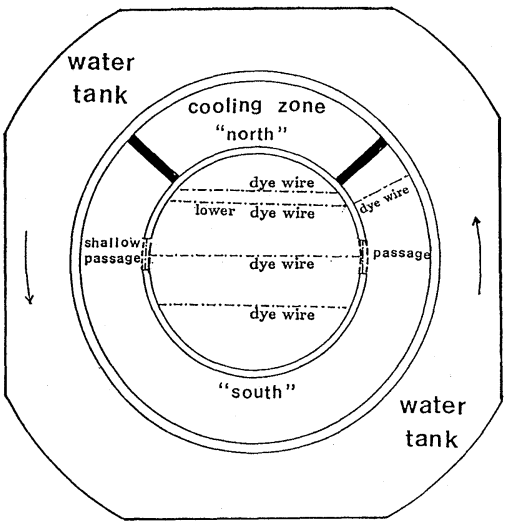

Fig. 1. Top view of the experimental set-up on a turntable.

of 0.05 cm copper wire was also used to survey the vertical profile of the flow. When a d.c. potential (~15v) was applied across the electrodes, blue dye was swept off each electrode by flow. Resulting dye patterns were photographed by a camera mounted on the turntable. The temperature of the working fluid was measured by a thermister at the foot of the cooled ("northern") sidewall where the coldest water mass was found.

The controllable external parameters are the basic rotation rate Ω, the applied temperature difference ΔT_0 and the height of the working fluid H. Values of these parameters were

$$\Omega = 0.1 \sim 0.5 \text{ rad/s}, \quad H = 8 \text{ cm},$$
$$\Delta T_0 = 0.5 \sim 1.5℃ \text{ (for } T_0 = 15℃ \text{ typically)}.$$

The depth of the passages was set to be $H/2$ (=4 cm). It shoud be noted here that the effective temperature difference imposed on the working fluid was much smaller than ΔT_0 due to highly insulating nature of the sidewall material (0.8 cm-thick plexiglass); temperature measurements showed that it was about one third of ΔT_0. Then we will use $\Delta T = \Delta T_0/3$, rather rhen ΔT_0 itself, as a measure of the thermal forcing. In terms of these external parameters, a propagation speed of the density difference, the internal radius of deformation and the buoyancy frequency are given respectively as

$$c = \sqrt{g \cdot \alpha \cdot \Delta T \cdot H}, \quad \lambda = c/2\Omega$$
$$\text{and } N = \sqrt{g \cdot \alpha \cdot \Delta T/H},$$

where g is the gravitational acceleration and α the thermal expansion coefficient (which depends on the fluid temperature). Values of these basic quantities were typically (e.g., for $\Delta T_0 = 1.0°C$, $T_0 = 15°C$, $\Omega = 0.3$ rad/s)

$$c = 0.6\text{cm/s}, \quad \lambda = 1\text{cm}, \quad N = 0.08\text{s}^{-1}.$$

Related non-dimensional quantities are the Ekman number E, the Burger number S and the Rayleigh number Ra, which are respectively defined as

$$E = \nu/2\Omega H^2, \quad S = (N/2\Omega)^2 \cdot (H/L)^2 = (\lambda/L)^2,$$
$$\text{and} \quad Ra = g\alpha\Delta T H^3/\nu\kappa,$$

where L is the diameter of the inner working basin and κ the thermal diffusivity. Most experiments were conducted under the following conditions:

$$E = 10^{-4} \sim 10^{-3}, \quad S = 10^{-4} \sim 10^{-3}, \quad Ra = 10^6 \sim 10^7.$$

Before describing the experimental results, we will refer to the time scales relevant to the thermal motion. The shortest one is the time for the density difference to propagate (as Kelvin waves) over a significant distance of the working basin, which may be given as $\tau_1 = L/c$. The phenomenon under consideration is a typical 'filling box' process (TURNER, 1979). As is well known (see, e.g., WORSTER, and LEITCH, 1985; CONDIE, 1989), the most important time scale for general 'filling box' problems is the time to pump all the working fluid through vertical boundary layers along cooled (or heated) sidewalls. This so-called 'stratification time scale' is defined for the present configuration as

$$\tau_2 = L \cdot H/\kappa Ra^{1/4}.$$

The longest time scale is the thermal diffusion time $\tau_3 = H^2/\kappa$. The momentum diffusion time $\tau'_3 = H_2/\nu$ is much smaller than τ_3 since $\nu \gg \kappa$ for the working fluid. Another diffusive time worth noting is a damping time of the Kelvin wave, $\tau_d = \lambda^2/\nu$. Values of these time scales were typically $\tau_1 \sim 1$ min, $\tau_d \sim 2$ min, $\tau_2 \sim 1$ hour, $\tau'_3 \sim 2$ hours and $\tau_3 \sim 12$ hours. The duration ofeach experimental run was about 3 hours, i.e. $3\tau_2$.

3. Experimetal results

When the differential cooling is applied, working fluid adjacent to the cooled ("northern") portion of the basin's sidewall sinks to the bottom through a thin vertical boundary layer and flows away from the source region in a density current. Under the rotational constraint (the basic rotation is anti-clockwise), the density current is deflected to the right (facing downstream) to form a narrow boundary current flowing anti-clockwise along the periphery of the bottom layer. Because of damping effect the density-driven deep current is stronger on the "western" side than on the downstream "eastern" side, exhibiting an "east-west" asymmetry. The object of major interest here is the compensatory circulation in the upper-layer and the associated in- and outflow phenomena between the

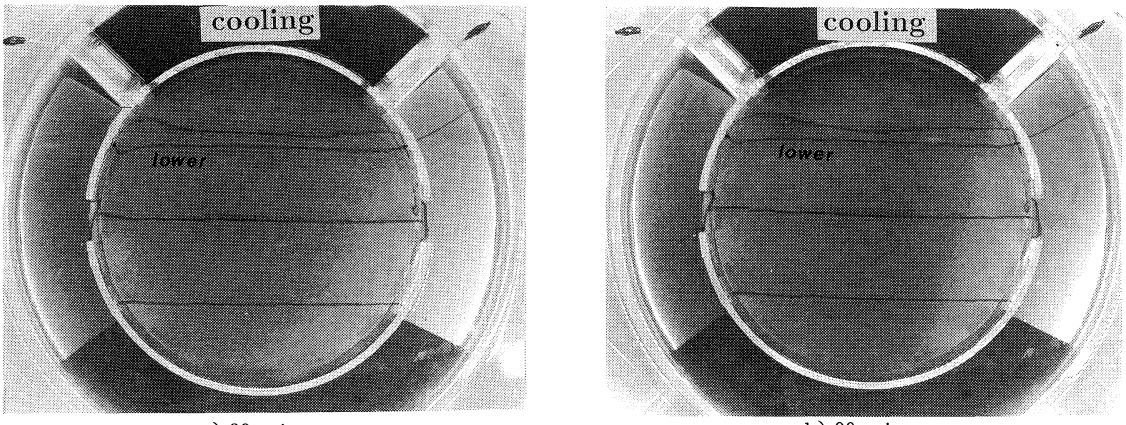

a) 30 min b) 90 min.

Fig. 2. A basin-wide circulation and an in- and outflow through the two passages induced by the sidewall colloing: $\Omega=0.140$ rad/s, $\alpha\,\Delta T=0.30\times10^{-4}$. The lower dye wire is at 1.5 cm above the bottom and others are at the mid-depths of the basin and the passages. Interval between dye pulses is 1 min.

inner basin and the surrounding basin.

Figures. 2a), b) are typical examples of the convective circulation as visualized by horizontal dye lines at two different times after the onset of the differential cooling. The basin-wide circulation in the inner basin is essentially similar to the one in the absence of the passages which has been described in some detail in a previous paper (TAKEMATSU, 1991). It consists of an anti-cyclonic major gyre with a "westward" intensified boundary current and a "western" deep counter-current from the sinking region. [The deep boundary current is not visible on the "eastern" side due to a relatively large damping ($\tau_d/\tau_1\sim O(1)$).] Note in particular that the compensating surface boundary current is much stronger and wider than the underlying boundary current of "northern" origin. The net horizontal transport in the "western" boundary region is apparently "northward". It is also worth nothing that the surface "western" boundary current naturally separates from the side boundary in the "northern" region where sinking is produced. A new and important feature demonstrated in Fig. 2 is the marked inflow through the "western" shallow passage. Survey by a vertical (movable) electrode showed that the inflow at the passage was almost barotropic although it had a slight vertical shear decreasing downwards. [If the passage were fully open to the bottom, the cold deep water of "northern" origin would spill out of the inner basin through the passage and this would alter the entire flow pattern.] It is remarkable that the buoyancy-driven inflow is not uniform across the "western" passage; the inflow is much stronger in the "northern" part of the passage than in the "southern" part, having the maximum speed near the "northern" end of the passage. The maximum speed of the inflow is comparable to that of the surface "western" boundary current towards the sinking region. The net inflow through the "western" passage is balanced by the same amount of outflow through the "eastern" passage. This exchange of fluid in the inner basin is accompanied with a recirculating flow from the "eastern" to "western" passage in the annulus region (this was confirmed in prelimiary experiments). It should be noted that the cooling of the inner basin had no *direct* influence on the fluid in the annulus region: Indeed the "northern" ends of the annulus near the cooling zone were always motionless as may be seen from the dye line across the annulus.

Figure. 3 shows a horizontal circulation pattern for a different rotation rate $\Omega=0.419$ rad /s. The general features are similar to those in Fig. 2 for $\Omega=0.140$ rad/s except that the widths of the "western" boundary current, deep counter-current and the inflow are all smaller than the corresponding widths in Fig. 2. These

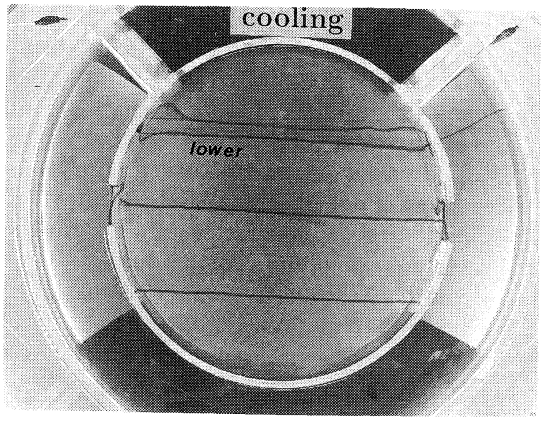

Fig. 3. A basin-wide circulation and an in- and outflow at 150 min for a different rotation rate: $\Omega = 0.419$ rad/s, $\alpha \Delta T = 0.30 \times 10^{-4}$. Dye interval, 1.5 min.

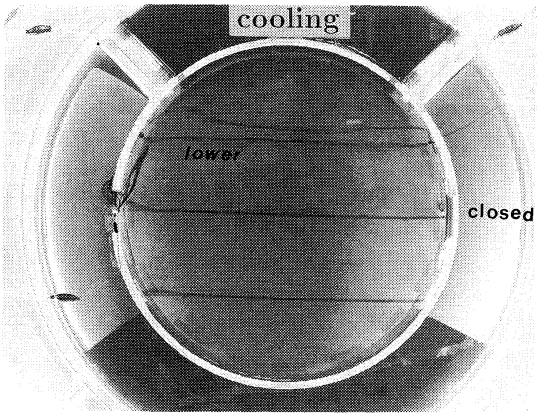

Fig. 4. A surface inflow and a compensatory outflow in the lower layer through the single "western" opening: $\Omega = 0.140$ rad/s, $\alpha \Delta T = 0.67 \times 10^{-4}$.

current widths seem to vary in proportion to the radius of deformation λ : Indeed, values of λ in Figs. 2 and 3 are 1.7 cm and 0.7 cm respectively, and the corresponding widths of the inflow are 5 cm and 2 cm (about 3λ).

Experiments for the case of a single passage are also suggestive. Figure 4 illustrates a feature of the flow through the "western" passage when the "eastern" one is closed (a configuration relevant to the Mediterranean Sea). The dye pattern released from a vertical electrode at the center of the "western" passage shows that an inflow occurs only in the upper layer of the passage and this surface inflow is replaced by a

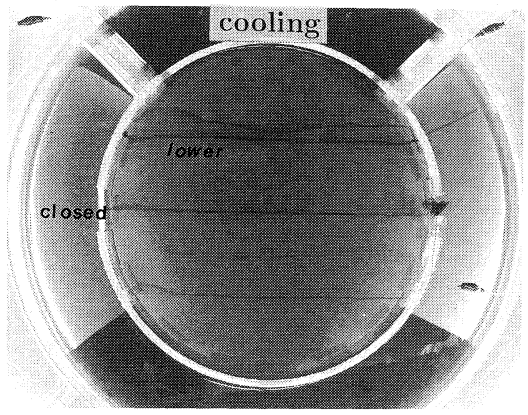

Fig. 5. A photograph illustrating the absence of an in- and outflow through the single "eastern" opening. The experimental conditious are the same as those in Fig. 4.

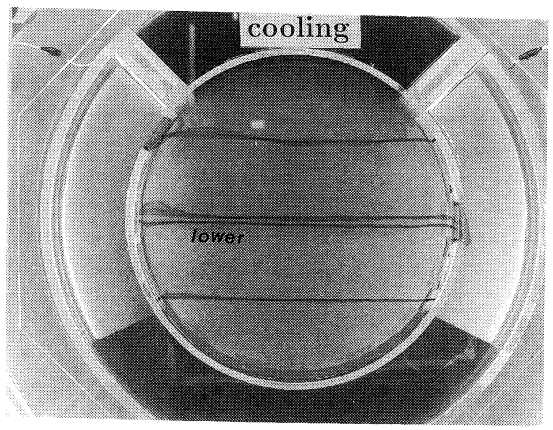

Fig. 6. An intense inflow through a "western" pssage opening located very near to the sinking region. The experimental conditions are almost the same as those in Fig. 2b). Interval between dye pulses is 0.75 min (45 sec).

lower-layer outflow from the inner basin. For comparison, a typical example of flow patterns in the basin with a single "eastern" passage is shown in Fig. 5. The dye released at the passage is only lingering around the source region, indicating that there is no appreciable in- and outflow through the single "eastern" passage. This feature contrasts with the prominent in- and outflow through the single "western" passage. These experiments with a single passage indicate that the "eastern" passage plays only a passive role in the buoyancy-driven in- and outflow

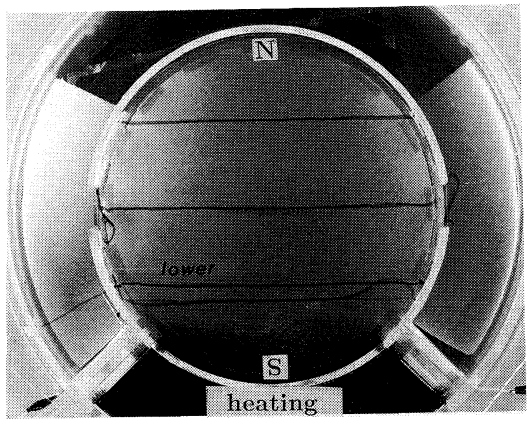

Fig. 7. An in- and outflow through the two openings induced by heating a "southern" portion of the basin's sidewall: $\Omega = 0.419$ rad/s, $\alpha \Delta T = 0.63 \times 10^{-4}$ (heating). Dye interval, 1.5 min.

processes. This is presumably because the effects of "northern" cooling which propagate anticlockwise effectively damp out before reaching the "eastern" side of the basin. The "northern" sinking, affected by Coriolis forces and damping effects, appears to act as a non-isotropic sink (biased towards "west") for the upper layer of the basin. It may be this "westward" intensified sink-effect that drives the surface inflow in Fig. 4 as well as the nearly barotropic inflow in Figs. 2 and 3. In this respect the inflow feature illustrated in Fig. 6 is noteworthy, where the passage on the "west" side has been approached to the sinking region. It can be seen that the inflow through the "north-west" passage is stronger than that through the due "west" passage in Fig. 2b).

In an additional experiment the water temperature of the cooling zone was raised, rather than lowered. A resulting horizontal circulation pattern is shown in Fig. 7, where the heating zone is regarded as "south". The localized rising of warm fluid along the heated sidewall causes a basin-wide cyclonic gyre in the inner basin and an in- and outflow through its two passages. It is remarkable that the inflow occurs again through the "western" passge as in the case of "northern" cooling. In another additonal experiment, the working fluid was subjected to a uniform cooling from above (by lowering the room temperature) as the Japan Sea would be during the last Ice Age, and it was confirmed that uniform cooling from above induces no appreciable mean currents eigher in the inner basin or around the passages.

Evolution characteristics of the buoyancy-driven motion are also worth noting. Dye observations carried out at specially short intervals (5~10 min) showed that the basin-wide circulation including the in- and outflow develops very rapidly during about 20 min after the onset of the thermal forcing. An apparent inflow was seen even at the first 5 min ($\sim 5\,\tau_1$); the convective motion at this earliest stage was still weak, but it possessed all essential features of the fully developed one. The in- and outflow as well as the circulation in the inner basin then gradully evolve over a period of 90 min ($\sim \tau_2$). Evolution of the convective motion at this second stage is illustrated in Figs. 2a) and 2b). Note in particular that the flow field at 30 min (Fig.2 a)) is already very similar to the fully developed one at 90 min (Fig. 2b)). During the subsequent 90 min no appreciable change was observed in the flow features. After a period of the longest time-scale τ_3, however, the density field as well as the velocity field in the basin are supposed to approach gradually a final steady state that depends on the room temperature and the thermal boundary conditions of the basin (insulated or isothermal).

4. Summary and concluding remarks

The laboratory experiments on an f-plane with the northernhemisphere rotation have revealed some new aspects of a convective motion in a rotating basin which is connected to an open ocen through shallow passages. An important finding is that a localized sinking in a "northern" area of the basin produces not only a basin-wide circulation with a "western" boundary current but also an inflow from an open ocean if there is a shallow passage on the "west" side of the basin. The buoyancy-driven inflow is characterized by a marked "north-south" asymmetry across the passage; it is concentrated in the "northern" portion of the passage. The entire convective motion manifests itself very soon ($\sim 5\,\tau_1$) after the onset of the differential cooling and gradually evolves on longer time scales (τ_2 and τ_3). The experiments have been conducted

only within the laminar-flow regime and rather restricted ranges of parameters, but the major flow features are expected to be similar for wider ranges of flow conditions. More detailed study of the quantitative aspects of the buoyancy-driven in- and outflow is now under way and will be published elsewhere.

The buoyancy-driven inflow process demonstrated herein may be oceanically relevant. We have in mind the winter-time sinking of dense water in the northern part of the Japan Sea or of the Mediterranean Sea. The present study suggests that such a localized sinking may induce a nearly barotropic inflow through the Korea/Tsushima Strait and a surface inflow through the Gibraltar Strait. Since sinking phenomena in reality are intermittent, the resultant inflow and the compensatory outflow would also be intermittent. In this respect it should be recalled that the basin-wide circulation as well as the inflow appear very soon (within a period of 5 τ_1 or so) after the onset of sinking. In real marginal seas τ_1 is of the order of 10 days. Then it seems likely that the in- and outflow processes can feel the seasonal change in the rate of sinking.

References

CONDIE, S.A. (1989): A Laboratory Model of a Convectively Driven Ocean. Dyn. Atmos. Ocean, **13**, 77–93.

FANG, G., B. ZHAO and Y. ZHU (1991): Water Volume Transport through the Taiwan Strait and the Continental Shelf of the East China Sea Measured with Current Meters. *In* Oceanography of Asian Marginal Seas (Proc. 5th JECSS workshop), ed. K. TAKANO, Elsevier Oceanogr. Ser., **54**, 345–358.

MINATO, S. and R. KIMURA (1980): Volume Transport of the Western Boundary Current Penetrating into a Marginal Sea. J. Oceanog. Soc. Japan. **36**, 185–195.

SEKINE, Y. (1988): On the Seasonal Variation in In- and Outflow Volume Transport of the Japan Sea. Prog. Oceanog., **21**, 269–279.

TAKEMATSU, M. (1991): Western Intesification of Buoyancy-Driven Ocean Currents. Rep. Res. Inst. Appl. Mech., Kyushu Univ., **38**, No. 108, 37–47.

TOBA, Y., K. TOMIZAWA, Y. KURASAWA and K. HANAWA (1982): Seasonal and Year-to-Year Variability of the Tsuhima-Tsugaru Warm Current System with its Possible Cause. La mer, **20**, 40–51.

TURNER, J.S. (1979): Buoyancy Effects in Fluids. Cambridge Univ. Press.

WORSTER, M.G. and A.L. Leitch (1985): Laminar Free Convection in Confined Regions. J. Fluid Mech., **156**, 301–319.

La mer 30: 127–138, 1992
Société franco-japonaise d'océanographie, Tokyo

Dynamics of deep sea surface buoy system for ocean mixed layer experiment

W. KOTERAYAMA*, S. MIZUNO**, K. MARUBAYASHI* and M. ISHIBASHI*

Abstract: A deep sea surface buoy system for measuring the water temperature and current velocity in the upper mixed layer has been developed. On-site, long-term experiments were carried out at 29°N, 133°E, south of Japan in the Pacific Ocean from 1987 to 1991, and provided useful data in the study of heat and momentum transfer between the ocean and the atmosphere. To evaluate the accuracy of the measurements and improve the data quality, motions of the surface buoy and instruments fixed to the mooring line were analyzed by numerical simulation.

1. Introduction

Studies of ocean-atmosphere coupling require knowledge of the water temperature and current velocity. This necessitates long- term observation, and until the artificial satellite system has a device for underwater measurements, the moored buoy offers the best measuring method to study an ocean mixed layer. The area of ocean mixed layer experiments (OMLET) must be far remote from the land mass so that the effects of land on the data are eliminated. Sea depth at such a location is usually between 3000m and 5000m. The buoy system should be light and small in size so that researchers can handle it by themselves; it is important for them to continue the study for a long time under the restricted economical condition. In this report the dynamics of a comparatively small surface buoy system moored in mid-ocean at a depth of 5000m is reported, and the effects of the motions of the system on the accuracy of the data obtained are discussed.

2. Design of the buoy system

Since the authors previously reported details of the method of calculating the dynamics of the surface buoy system (KOTERAYAMA *et al.*,1986), the design scheme is explained here briefly. The environmental conditions must first be determined. The sea area for the experiment was decided as 29° N, 133° E. Water depth is about 5000m. The maximum values of wave height and wind velocity used in designing an ocean structure to be moored in mid-ocean are generally 30m and 50m/s respectively. These were values used in our design. The system had to be safe under these conditions (survival condition). The wind load acting on a small surface buoy directly is minimal and negligible, but the drag force due to the surface current induced by wind must be considered in the calculation. The magnitude of the wind induced surface current was estimated by assuming Ekman drift current (FKMAN, 1905). The wave-making force can be neglected compared with the viscous drag force because the wave length is much larger than the diameter of the surface buoy. The effects of the ocean current are dominant on deep sea mooring because the line is very long. In this study the highest value of the current profile proposed by Woods Hole Oceanographic Institution was adopted (Fig. 1; CLAY, 1983) for the design of the system. The force due to current acts on the mooring line as a drag force. The Lumped Mass Method used to estimate the data accuracy is explained here briefly.

As shown in the concept of the Lumped Mass Method (Fig. 2), the cable is modeled as N-discrete masses interconnected by springs of which the spring-constants are equal to those of

* Research Institute for Applied Mechanics, Kyushu University, Kasuga, 816 Japan
**Department of Civil Engineering Hiroshima Institute of Technology, Hiroshima, 731–51 Japan

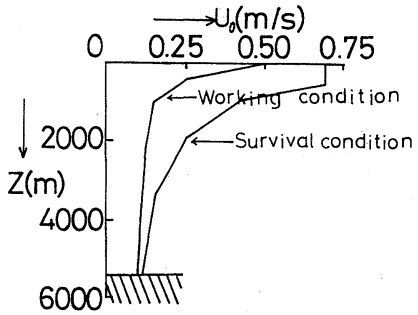

Fig. 1. Vertical velocity profiles of ocean current used for buoy design.

the mooring rope. All force such as the drag force, the added mass force, the inertia force, the buoyancy and weight acting on the cable are considered to be concentrated on each mass, so that the motions of the cable can be represented by simultaneous differential equations. The point of lumped masses in the calculation model is selected to coincide with the massive points in the real system; buoy, floats, current meters, which enables us to get a realistic model. In this study two-dimensional numerical simulations are adopted, so that the motion of each mass is described by two simultaneous equations. Finally, the motions of N-lumped masses can be written by 2N-simultaneous equations. These equations cannot be solved analytically but numerically because they include strong nonlinear terms.

Fig. 3 shows a schematic view of the buoy system which was designed on the basis of these numerical simulations and improved through on-site experiments. Since most accidents with the surface buoy system such as the severance of the mooring line occur near the buoy, the floats were distributed in such a way that the entire system except the surface buoy is retrievable through the buoyancy of the floats and activation of the acoustic release even if the surface buoy is lost. Under extremely severe conditions the line tension becomes very great. The surface buoy is pulled down to the subsurface when the tension becomes greater than the excess buoyancy of the surface buoy. To prevent this the surface buoy must be very large, which is not practical. The maximum value of the line tension nearly equals the smaller value of the sinker

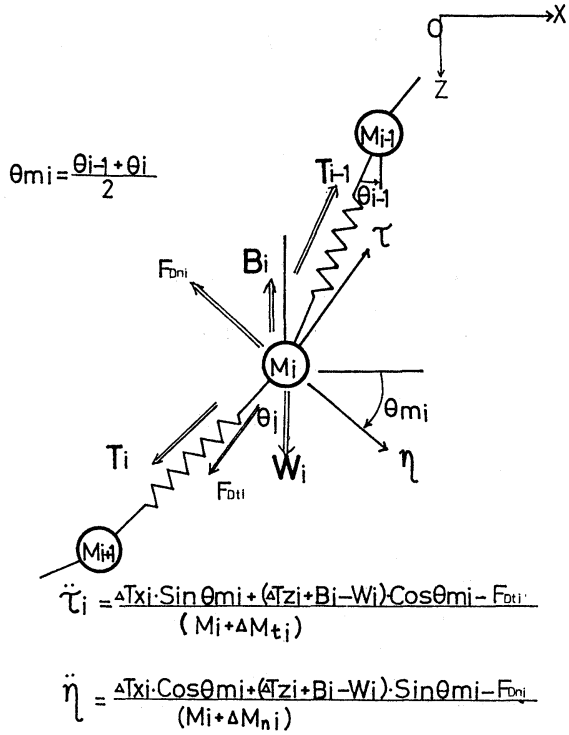

Fig. 2. Concept of Lumped Mass Method.

weight in water and the excess buoyancy of the surface buoy. The sinker is raised when the vertical component of the line tension becomes greater than its weight. The line tension does not become much greater than the weight of the sinker. We had to decide to make the surface buoy submerge or the sinker to be raised under severe conditions in order to avoid making the system very large. We finally selected a light sinker weighing less than the excess buoyancy of the surface buoy, because otherwise the buoy must be very strong to endure the water pressure. We anticipated that the sinker would lift and the entire system would drift under severe conditions. To compensate for this eventuality we installed a satellite positioning system (ARGOS SYSTEM) to locate the system when it moved from the initial point. For safety, floats should be positioned between the buoy and the depth of 1000m, but these floats increase the vertical displacement of the instrument and deteriorate data, so the floats concentrated at 1000m depth in the final design. The mooring

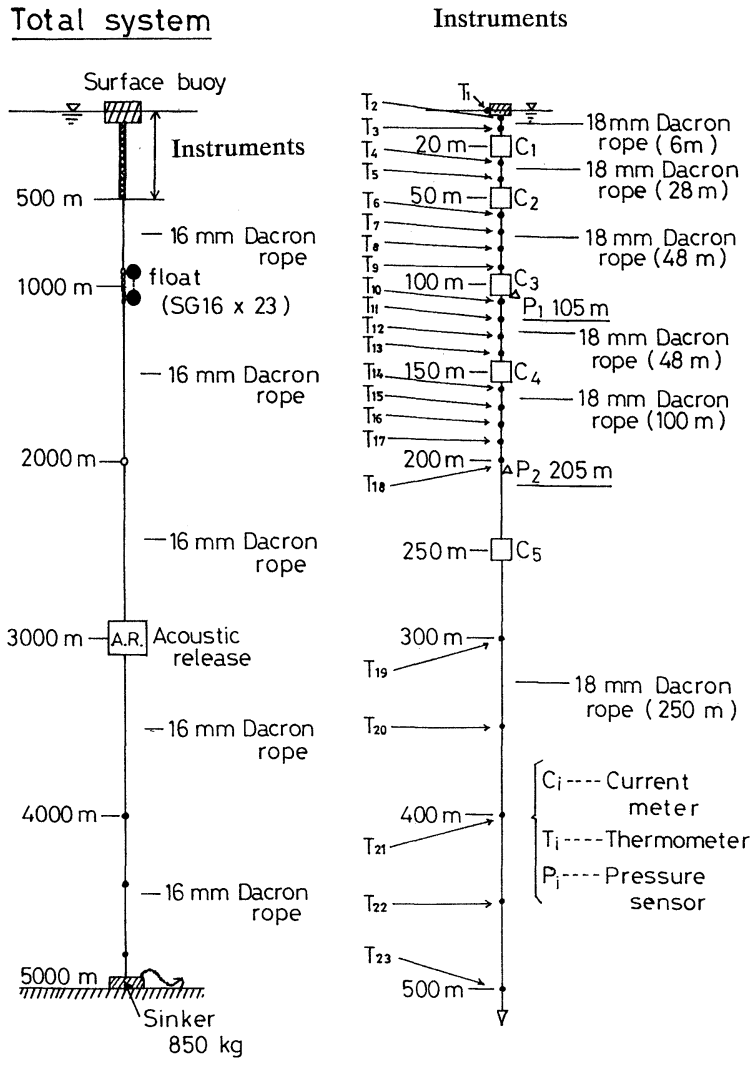

Fig. 3. Schematic view of buoy system designed for ocean mixed layer experiment.

line is of DACRON, because of its high strength and good chemical characteristics under the high pressure environment of the deep sea. The surface buoy is of rubber because of its toughness in potential collisions with ships, and its deployment and retrieval is fairly easy on the mother ship. The buoyancy of the surface buoy is 1500kg and its weight in air is 440kg.

Thus, we were able to design a light and compact buoy system for very deep sea experiment using accurate calculations for the buoy dynamics.

3. On-site experiments

This buoy system was used in on-site experiments carried out in 1987, 1988, 1989 and 1990. The results of the 1990 experiment are reported here. It was moored 133°16′ E, 29°09′ N by university ships; Keiten Maru of Kagoshima University, and recovered by Hakuho Maru of Tokyo University. Photo 1 shows scenes of the deployment. Difficult steps in this action would usually be the launching of the surface buoy and deployment of the sinker, because surface buoy is fragile and the sinker is heavy. However, those steps were fairly easy because the surface

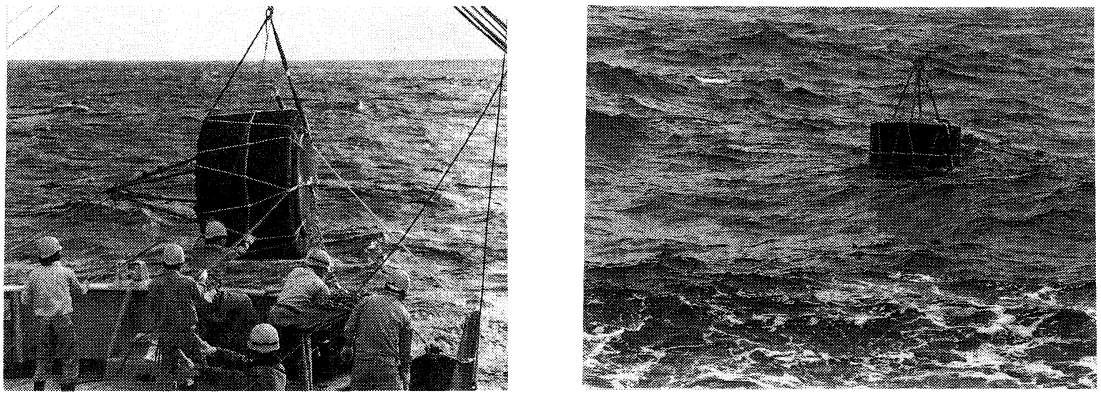

Photo. 1. Scenes of an experiment.

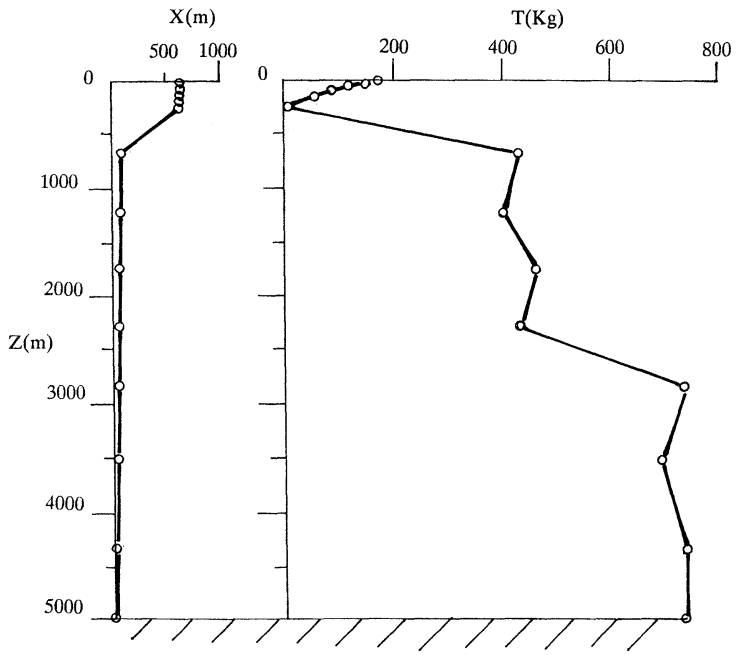

Fig. 4. Statical configuration of mooring line and tension distribution obtained by calculation.

buoy can withstand collisions or bumping and the sinker is comparatively light.

The statical configuration of the mooring line and tension distribution are shown in Fig. 4. The instruments are between the sea surface and 250m depth in order to collect data in the mixed layer, and the figure shows that the vertical displacements of the instruments are very small in this design. The current velocity used in the calculation is 0.1m/s (measured value) from 0 to 200m depth and 0.05m/s (estimated) below 200m. The current velocity is minimal in this case, so there is little statical tension. The shape of the statical configuration suggests that the spindle rod of the current meter C_5 at 250m depth is subjected to not only the tension but the bending moment. The spindle rod of C_5 was broken by its fatigue failure due to the action of the bending moment caused by waves and current so that the upper system including the surface buoy drifted though found with the help of the satellite positioning system. This weakness will be

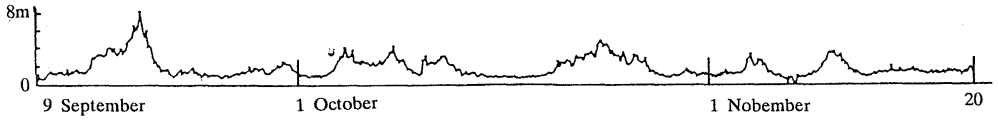

Fig. 5. Wave record by weather observation buoy of Meteological Agency.

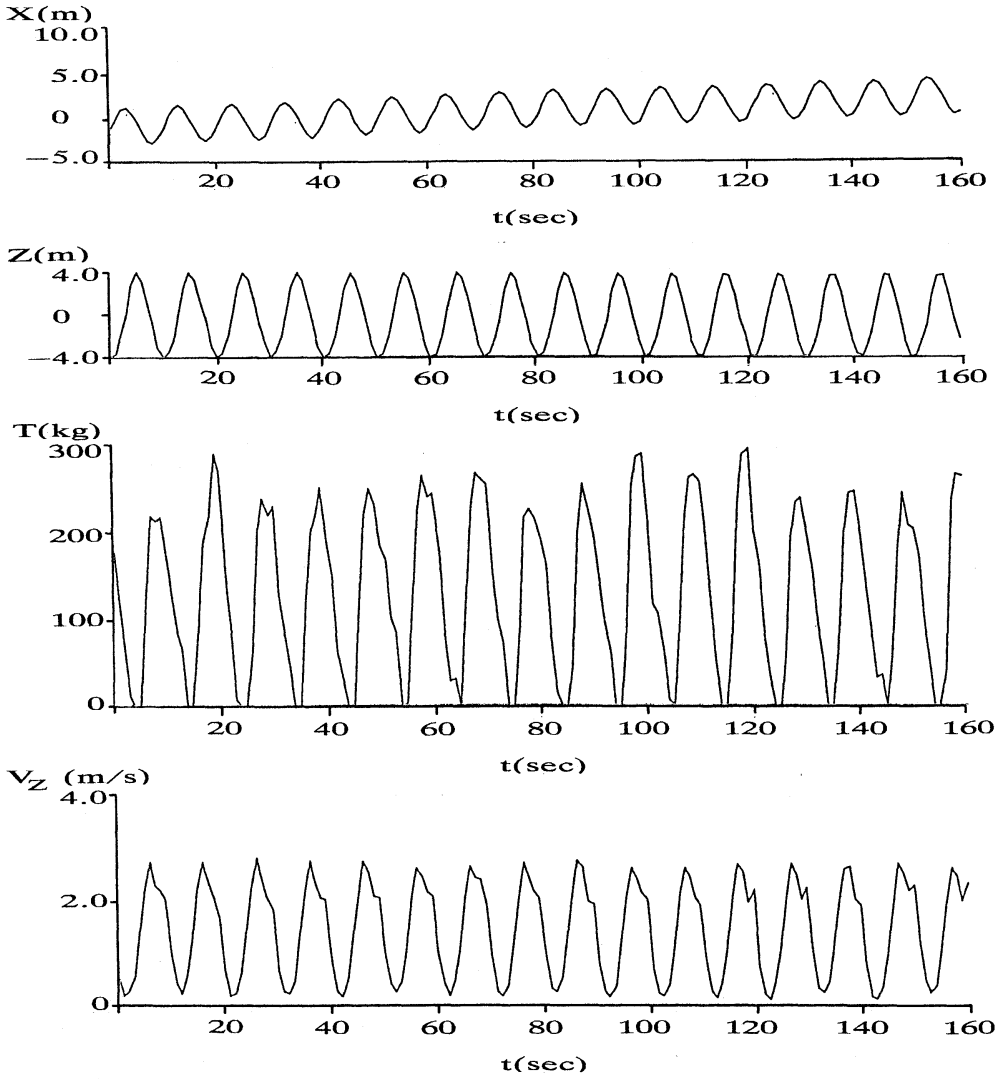

Fig. 6. Motions of surface buoy and dynamic tension of mooring line in waves (Hw=8m, Tw=10 sec).

improved by fixing a mass or drag just below the current meter.

The wave records shown in Fig. 5 were obtained with the weather observation buoy of the JAPAN Meteorological Agency located at 29° N, 135° E. The maximum wave height was 8m. Quality of the current data obtained by the surface buoy system is generally believed not as good as that by the submerged buoy system because of the motion of the surface buoy induced by waves and surface currents. It is thus important to evaluate the motions of the instruments

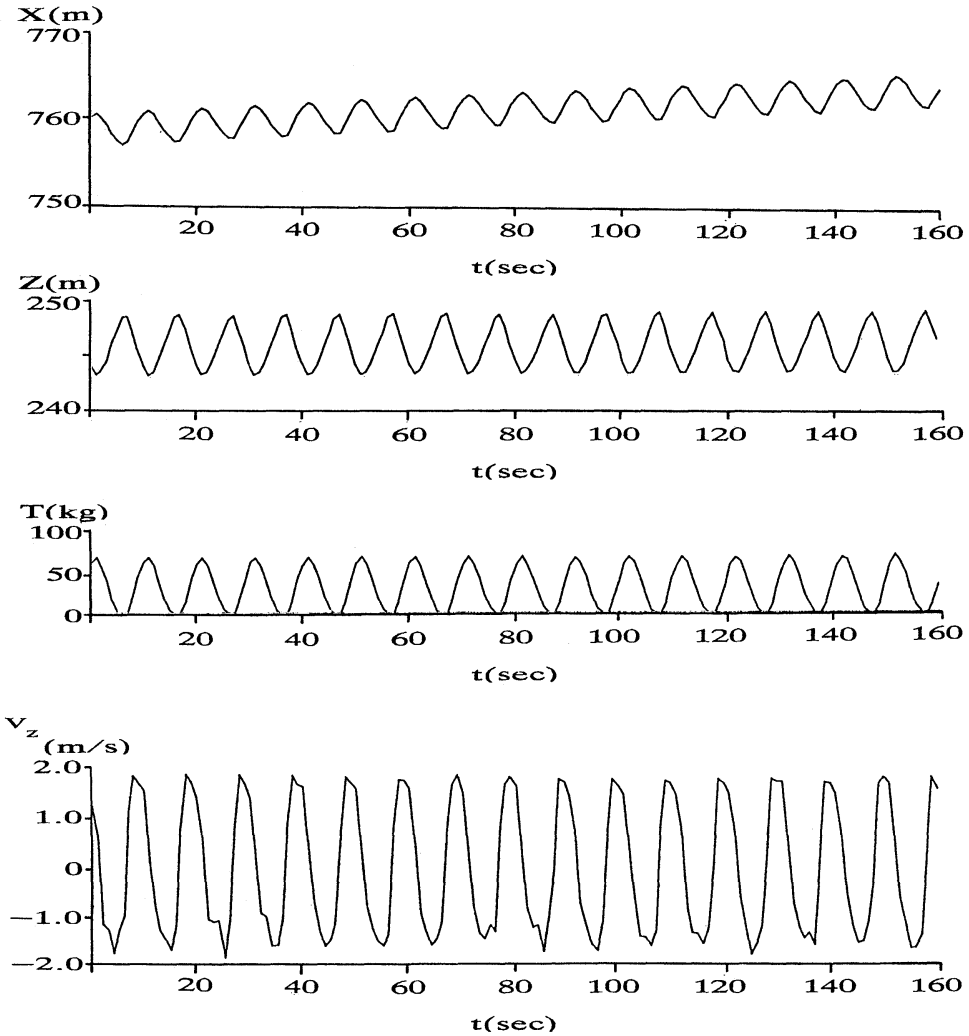

Fig. 7. Motions of C_5 and dynamic tension of mooring line at C_5.

fixed to the mooring line.

Figure 6 shows calculation results of the motions of the surface buoy and dynamic tension of the mooring line for regular waves of 8m height and 10 sec period. The current is also taken into the consideration, but details of the current measurements will be explained later. From top to bottom in the figure are shown horizontal displacement X and vertical displacement Z of the surface buoy, line tension T at the surface buoy and the vertical velocity V_z of the surface buoy. The theory of floating body dynamics shows that the motion amplitudes of a small body compared with wave length are almost the same as the wave amplitude when the restriction of the mooring line is not strong, which is confirmed by our calculations. The phase difference between the vertical displacement Z and wave surface is almost zero and the surface buoy follows the wave surface with fidelity. Under survival conditions such as current, wind and waves, the surface buoy occasionally submerges (KOTERAYAMA *et al.*, 1986). But it did not occur because of weak current. As the figure shows, the buoy drifts gradually from the initial point of the static balance, which is shown in Fig. 4.

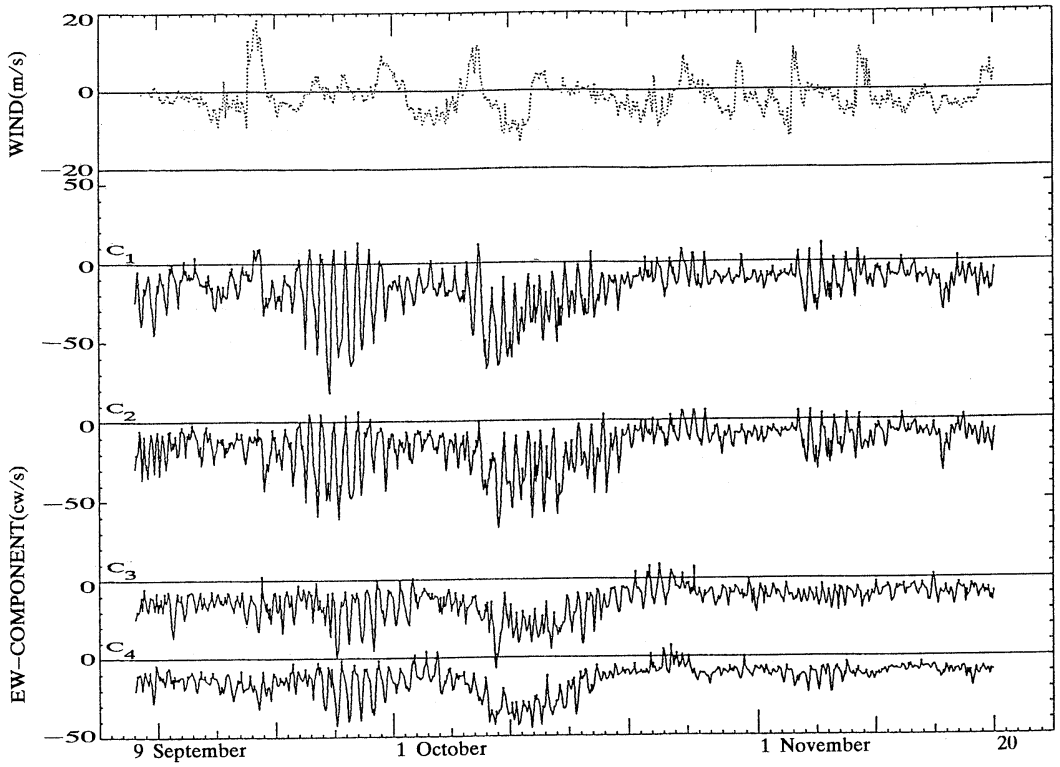

Fig. 8. Time series of wind velocity and current velocities measured with C_1~C_4.

It is a result of the increase of the steady drag force generated by the interaction between waves and current, and a kind of transient motion. At a glance, the tension variation is irregular. The variation of phase difference between the waves and mooring line motions causes this irregularity and the variation may be a numerical error. The maximum tension is about 300kg, small enough as compared with the breaking tension of the mooring line (7 tons). It is undesirable from a safety standpoint that the tension becomes zero, which may kink the line. For this reason a wire rope was not used in this system. A kink is fatal for wire rope. Even a syntactic rope might cling to the instruments at zero tension. The zero tension occurs when the static tension of a line is smaller than the amplitude of dynamic tension. A large static tension is thus desirable, but requires that the surface buoy be large and is therefore contrary to the design philosophy.

The motions of the deepest current meter C_5 and the tension variation of the line at that point are shown in Fig. 7 using the coordinate system X and Z shown in Fig. 4. The motion amplitude is 3.7m horizontally and 5.6m vertically. The maximum tension is about 60 kg and the tension variation induced by waves is very small, but the vertical velocity V_z varies between −1.5m/s and 1.5m/s. The horizontal velocity of C_5 is estimated 1.0m/s~−1.0m/s from the amplitude of the displacement and its period. Under these conditions it is difficult to measure a small current velocity accurately with this type of the current meter (Savonius rotor with a vane) because the vane can not follow the direction change in high frequency velocity, and the oscillating component due to waves can not be measured properly. The steady component is affected by the error. The accuracy of current velocity measurement in a storm is therefore dubious. Another type of meter should be adopted if measurement of current velocity in a storm is desired.

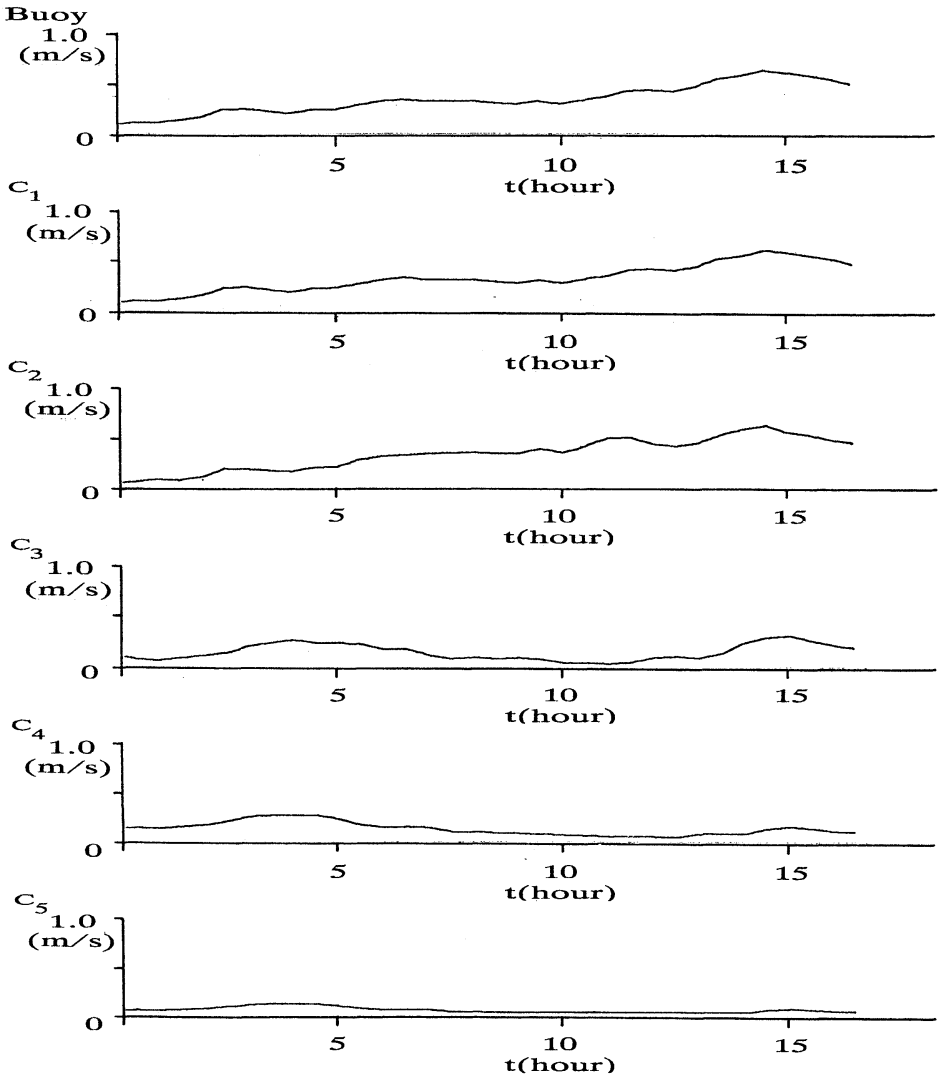

Fig. 9. Time series of current velocities used in calculation.

Fig. 8 shows the time series of the current velocity measured with C_1 to C_4 at the locations shown in Fig. 3. The current velocities oscillated violently during September 22–30, October 6–16, and November 3–9. The oceanographical discussion of these phenomena will appear in a later paper, and here the reliability of the measured data is investigated. We consider that the oscillations in the current record were not the result of buoy motion due to changes in wind velocity, because the wind data shown at the top of the figure (which was obtained by the weather observation buoy of the Japan Meteorological Agency) does not reflect oscillations of the same frequency, and the natural frequency of the buoy system is much higher than that of the oscillation. We therefore guess that the oscillations must be those of current velocity. The recorded current velocity is that from the moving current meter, and the absolute velocity must be obtained by adding the horizontal velocity of the current meter induced by the current oscillation and mooring line motion. The motion of the buoy system is calculated for 16 hours from

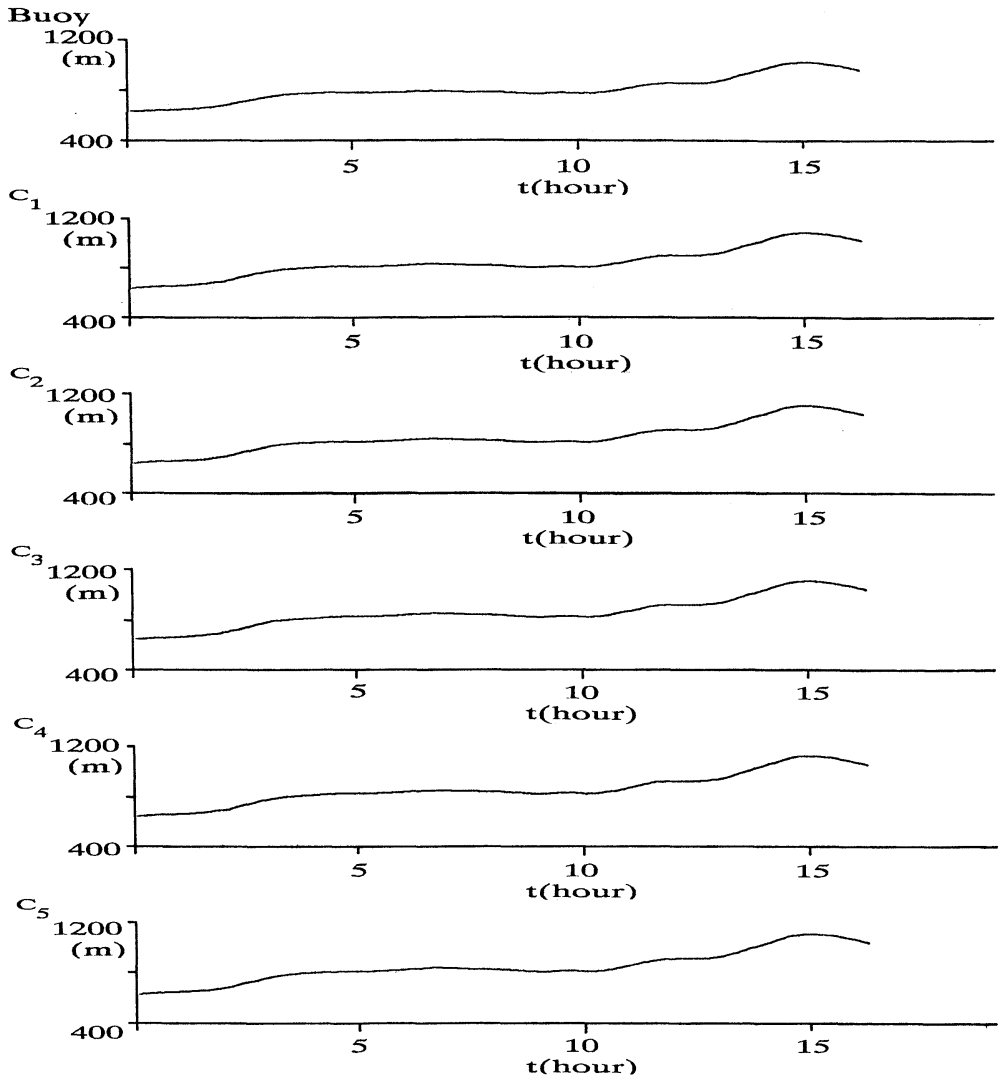

Fig. 10. Horizontal displacement of buoy and current meters obtained by calculation.

22:00 of September 23 to 14:00 of the next day when the current oscillation was strongest. The current velocities at each of the lumped masses used in the calculation are shown in Fig. 9. As a first approximation these absolute velocities are assumed to be equal to the relative ones measured by the current meters, where the current velocity at the surface buoy is assumed to be equal to that at C_1, and all the other values are measured ones. The velocities at lumped masses deeper than C_5 are assumed to be 0.05 m/s.

The calculated horizontal displacement of each current meter is shown in Fig. 10, where the time lag of the motion from the current variation is about 30 minutes. This fact means that the system goes on moving for 30 minutes after the peak of the current. The maximum displacement of the surface buoy is 480 m and that of C_5 is 380 m.

Fig. 11 shows the horizontal motion velocity of each current meter. The maximum drifting velocities (3.6 cm/s) are those of the surface buoy and C_1 at11:30 on September 24. The

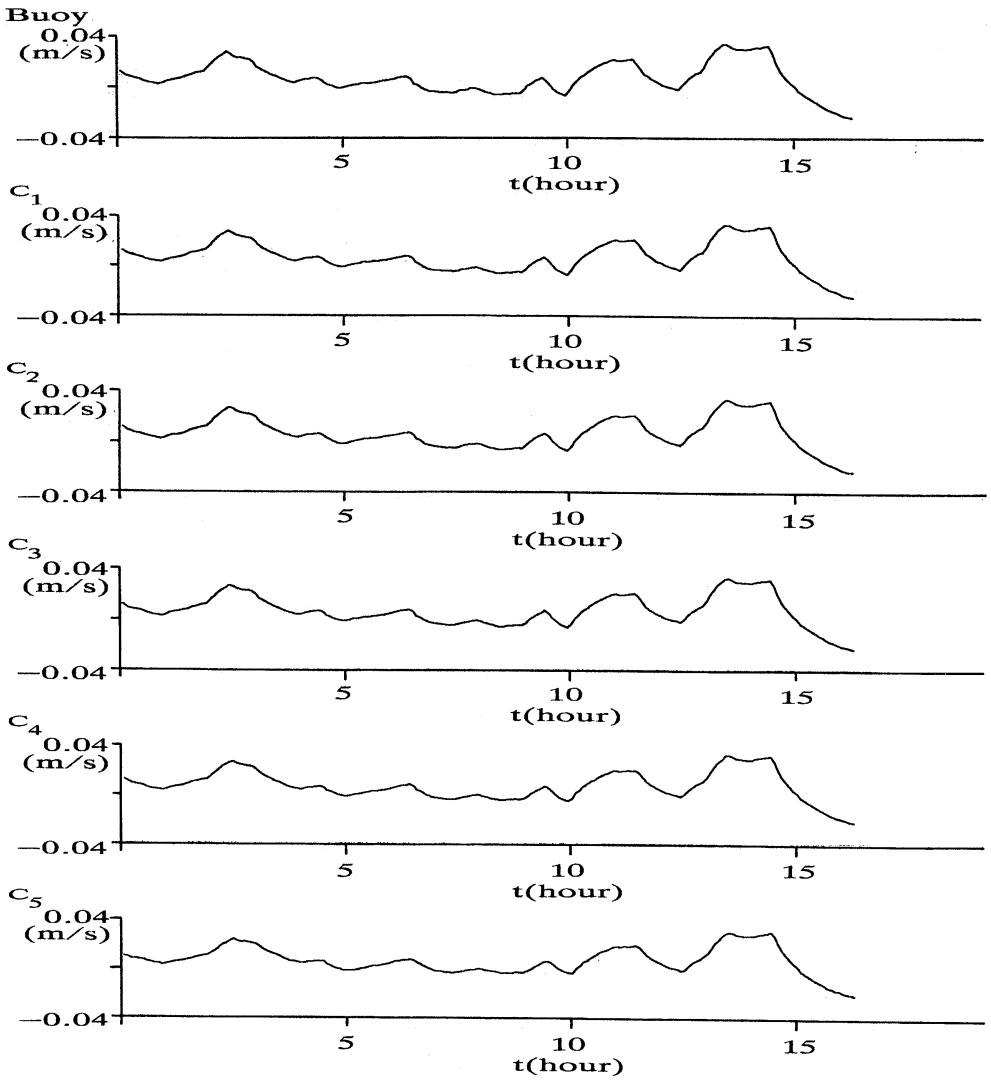

Fig. 11. Horizontal drifting velocities of current meters obtained by calculation.

maximum velocity was continued for one hour. After 12:30 when the maximum current velocity was recorded, their drifting velocities became vanishingly small. After 13:00 the drifting velocities became negative and the system began to return to original levels. The tendency of the drift of C_5 was the same as C_1 and finally the maximum drifting velocity throughout the entire system was estimated as 3.6 cm/s. Therefore, the drifting velocities of the current meters were less than 5.5% of the maximum current velocity of 65cm/s recorded by C_1. We may assume that this ratio does not vary remarkably with the current velocity. We can obtain the second approximation for the absolute velocity by adding the drifting velocities to those recorded by the current meters, and through the iterative procedure, can obtain higher approximate values. This iteration procedure is convergent when it is a linear system or the ratio does not increase suddenly. In case the mooring system has a resonant frequency in the horizontal motion, the ratio increases suddenly at the resonant frequency and the iteration might be divergent, but

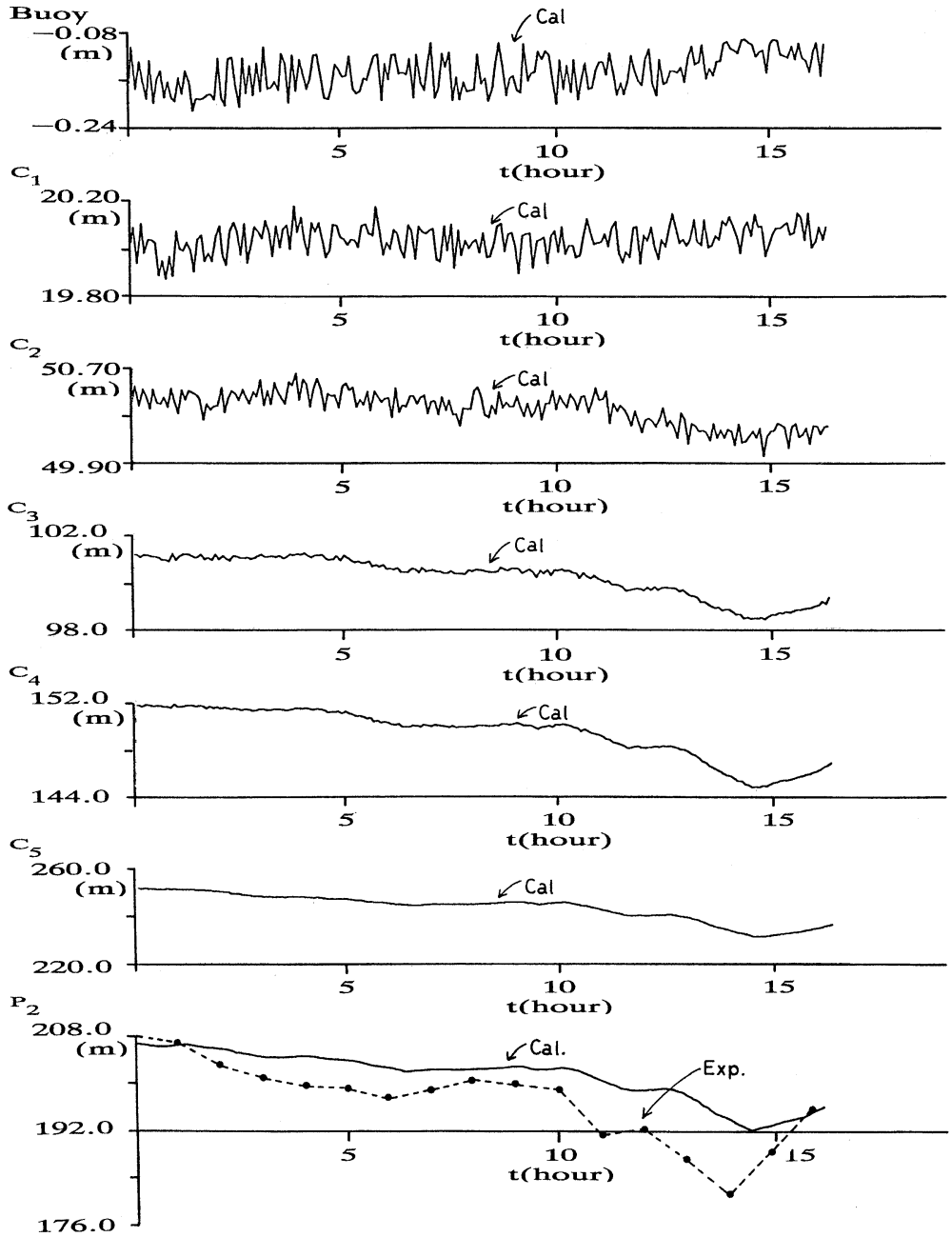

Fig. 12. Vertical displacement of current meters and pressure sensor.

generally the viscous damping is very large in case of the buoy mooring and the ratio does not increase remarkably even at the resonant frequency. The iteration is therefore convergent in usual surface buoy system. In the present buoy system the drifting velocity was so small, compared with the measured current velocity that we confine ourselves into first approximation. It depends on the research object whether the iterative procedure is continued.

To analyze the data recorded by current meters and thermometers we need vertical displacements of the instruments. As an example, the time series of the vertical displacements during the current oscillation are shown in Fig. 12. Calculations indicate that the vertical displacement of the surface buoy is about 0.1m and that of C_1 is 0.2m. Both are very small. The value of C_5 (16m) is fairly large. When the data collected by thermometers and current meters are analyzed, the vertical displacement of the instruments should be taken into consideration, especially for the lower instruments. We set two pressure sensors, P_1 and P_2 at depths of 105m and 205m (Fig. 3) to measure the vertical displacements, but in the present experiment P_1 did not work well. In Fig. 12 the calculated result (solid line) is compared with the measured value of vertical displacement by pressure sensor P_2 (black circles and broken line). Both are in good agreement.

4. Conclusions

A deep sea surface buoy system for ocean mixed layer experiments was designed and manufactured. On-site experiments were carried out and the accuracy of collected data was discussed using numerical simulations. The main conclusions are as follows:

1. The drifting velocity of surface buoy system induced by the current oscillation is much smaller than the current velocity.
2. The motion velocities of the buoy system induced by surface waves are large and the accuracy of current measurement is questionable in a severe storm unless a vector-average type current meter is used.
3. From conclusions 1 and 2, the accuracy of the current data with the surface buoy system would be much improved by using a vector-average type current meter and can be compared with that of the submerged buoy system.
4. The accuracy of calculations using the Lumped Mass Method was confirmed by experiments.

Acknowledgments

The authors thank the crews of the Hakuho Maru of the Ocean Research Institue of Tokyo University, the Keiten Maru and the Kagoshima Maru of Kagoshima University for their contributions in the on-site experiments and the staff of the Japan Meteorological Agency for providing us the valuable data of meteorological buoys around Japan. The authors also express their appreciation to Miss Aki YOSHIDA for preparing the manuscript.

References

CLAY, P.R. (1983): The LOTUS discus mooring. Woods Hole Oceanogr. Inst. Contr. No. 5354, 1–6.

EKMAN, V.W. (1905): On the influence of the earth's rotation on ocean currents. Ark. F. Math. Astr. Och. Fysik.

KOTERAYAMA, W., S. MIZUNO and H. MITSUYASU (1986): Preliminary design of deep-sea surface buoy system for ocean mixed layer experiments. La mer, **24**, 139–149.

La mer 30: 139–147, 1992
Société franco-japonaise d'océanographie, Tokyo

A numerical study on the barotropic transport of the Tsushima Warm Current*

Young Ho SEUNG** and Soo Yong NAM**

Abstract: A barotropic numerical model is run over the N.W. Pacific Ocean to examine the formation of the Tsushima Warm current. Analysis of the results with various different parameter values indicate that the Tsushima Current is a downstream extension of Taiwan Warm Current. The parameters determining the transport of Tsushima Current are friction (mostly bottom friction), the depth difference across the East China Sea continental slope and the total transport of Kuroshio. Local wind does not change the transport much but changes the flow pattern such that for southerly wind, the transport is through the Taiwan Strait and for northerly wind, it is through the eastern side of Taiwan.

1. Introduction

The Tsushima Warm Current (TSWC) is defined as the current entering the East (Japan) Sea through the Korea Strait, between Korea and Japan, and joins the Kuroshio through the northern straits, north of Japan (Fig. 1). Based on dynamic computation, the amount of volume transport of TSWC is known to be less than 2 Sv. (c.f. MORIYASU, 1972; YI, 1966), equivalent to a few percent of the Kuroshio transport. The TSWC water is generally considered as a mixture of Kuroshio and East China Sea (ECS) shelf waters (e.g., LIM, 1971).

The Kuroshio water flows along the ECS continental slope (Fig. 1) and part of it crosses the slope to form the TSWC. Up to present, there are a few different views on the formation of TSWC. These consist of one or a combination of the following components: First, it may be a broad northward transport of the Kuroshio and the ECS shelf waters along the shelf edge (LIM, 1971; NAGATA, 1981). Secondly, it may be a contribution from periodic intrusions of Kuroshio water, especially in summer near the northern end of slope, southwest of Japan (HUH, 1982). And finally, it may be a direct branch of the Kuroshio. The branch may occur either at the southwestern end of the slope, near Taiwan, or at the northeastern end of it, southwest of Japan. The latter one is alluded by the schematic chart of NITANI (1972, see Fig. 2) and the former one, by GUAN (1986). Actually, this former one is verified and termed Taiwan Warm Current which may feed the TSWC according to GUO *et al.* (1987). According to these observations (GUO *et al.*, 1987), the Taiwan Warm Current consists of two components: one is the current through the Taiwan Strait, between Taiwan and mainland China, and the other is the current through the northeastern tip of Taiwan.

Many numerical models perfomed in this region are not suitable for the study of TSWC because they eigher exclude the Korea Strait (e.g. CHAO, 1990) or treat it as an open boundary (HSUEH *et al.*, 1986; WANG and SU, 1987). TAKANO and MISUMI's (1990) 3-dimensional model comprises the whole North Pacific Ocean and may be appropriate to examine the TSWC if their grids are further refined. A simple analytic model is also proposed by MINATO and KIMURA (1980) to explain the dependence of TSWC transport on external parameters. According to their model, the bottom friction and the shelf depth relative to the Kuroshio depth are major factors controlling the transport; the transport increases with decrease of friction and increase of shelf depth. However, they assumed narrow openings where the current is uniformly geostrophic. In reality, the continental slope of

* This is partially supported by Inha University.
** Department of Oceanography, Inha Univ., Inchon 402-751, Korea

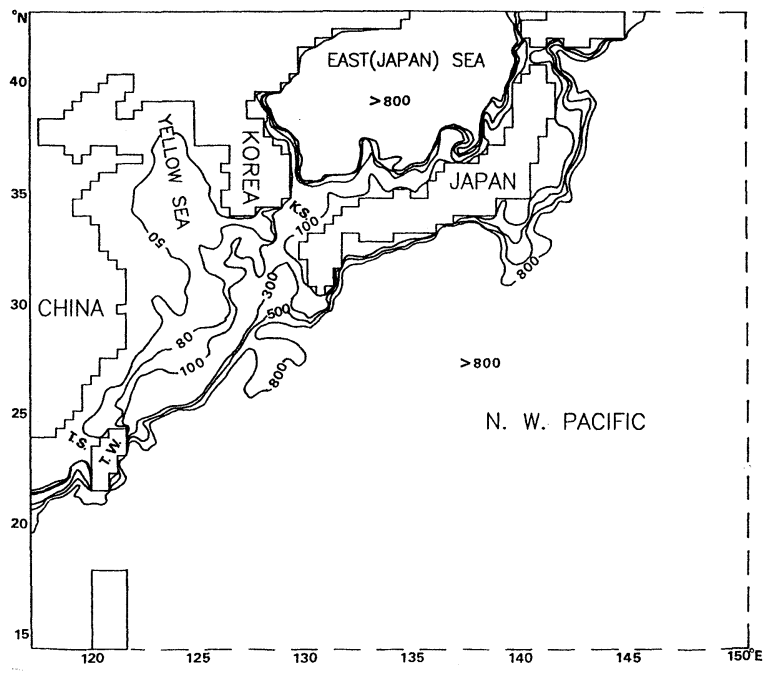

Fig. 1 Model domain with bottom topography (depth in meters). Solid lines are closed boundaries and dotted lines are open boundaries. T.W. means Taiwan. K.S. and T.S. mean Korea and Taiwan Straits, respectively.

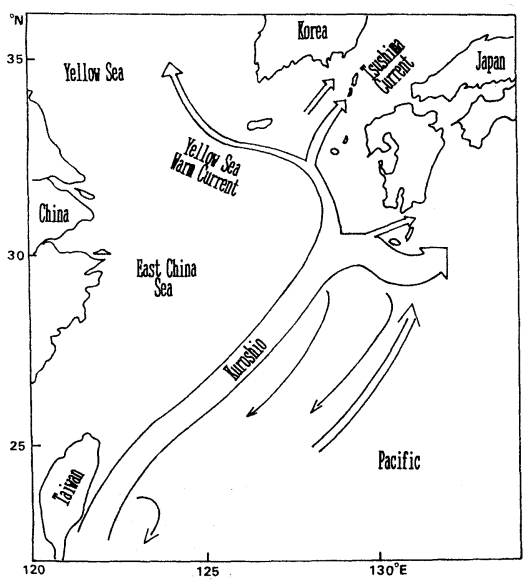

Fig. 2. Schematic diagram of the Kuroshio system in the East China Sea region.

the East China Sea, which is the inflow opening of the TSWC, is so wide that this assumption does not seem appropriate.

The aim of this study is to answer the question how the Kuroshio Water crosses the continental slope to form the TSWC. This question arises especially because the theory of potential vorticity predicts only the flows parallel to the depth discontinuity. The whole N.W. Pacific is taken as the model domain, thus making the TSWC free of open boundary condition, with acceptably small grid for examining the formation of TSWC. Only barotropic component is considered though it does not seem adequate especially in summer when the baroclinicity increases. Nevertheless, the barotropic dynamics seems to be helpful in understanding the process that goes on because most of the Kuroshio water brought up onto the shelf area more or less experiences the topographic changes (UDA and KISHI, 1974; FAN, 1980). To check the importance of factors determining the transport of TSWC, the model is run for various external parameters.

2. Model

The model domain roughly corresponds to the western half of the North Pacific Substropical Gyre, ranging 15°N–43°N and 117°E–150°E

Table 1. Description of experiments

Parameter / EXP. NO.	Coeff. of Horizontal Viscosity Am (cm^2/sec)	Kuroshio Depth He (cm)	Bottom Drag Coef. Cd	Wind Stress Magnitude τ (dyne/cm^2)	Wind Direction * α (°)	Total WBC Transport Ψ_{max} (Sv.)
EXP. 1	1.E7	3.E4	0.002	0	0	60
EXP. 2	1.E7	3.E4	0.002	1	0	60
EXP. 3	1.E7	3.E4	0.002	1	45	60
EXP. 4	1.E7	3.E4	0.002	1	90	60
EXP. 5	1.E7	3.E4	0.002	1	135	60
EXP. 6	1.E7	3.E4	0.002	1	180	60
EXP. 7	1.E7	3.E4	0.002	1	225	60
EXP. 8	1.E7	3.E4	0.002	1	315	60
EXP. 9	1.E7	3.E4	0.002	0.5	45	60
EXP.10	1.E7	3.E4	0.002	2	45	60
EXP.11	1.E7	1.5E4	0.002	0	0	60
EXP.12	1.E7	5.E4	0.002	0	0	60
EXP.13	1.E7	8.E4	0.002	0	0	60
EXP.14	1.E6	3.E4	0.002	0	0	60
EXP.15	1.E8	3.E4	0.002	0	0	60
EXP.16	1.E7	3.E4	0.0005	0	0	60
EXP.17	1.E7	3.E4	0.008	0	0	60
EXP.18	1.E7	3.E4	0.002	0	0	30
EXP.19	1.E7	3.E4	0.002	0	0	90
EXP.20	1.E7	3.E4	0.002	0	0	120

* Wind direction is measured clockwise from north.

(Fig. 1). It has a continental slope separating the deep Kuroshio region from the shallow ECS shelf area. Since the model is barotropic, the deep Kuroshio region is assumed to have uniform depth. The depth is normally taken as 300m but different values are also used to examine its effect. The model ocean is homogeneous and assumed to have a rigid-lid surface.

The usual GCM model described by SEMTNER (1974) is used and the barotropic circulation expressed by stream function is obtained. The ocean is spun up not by direct wind forcing but by imposing an open boundary condition along the eastern boundary. In terms of stream function, this reads

$$\Psi = \Psi_{max} \sin (\pi y/L)$$

where Ψ is the transport stream function with total Western Boundary Current (WBC) transport Ψ_{max}; L, fixed in this study, is the meridional dimension of the model basin; and y is the meridional position measured from the southern boundary. Twenty experiments with different conditions are performed (Table 1). For each experiment, steady state is reached after 150 days of integration (see Fig. 3 for example). In the above expression, Ψ_{max} is normally taken as 60sv. (NITANI, 1972), but different values are also used in experiments 18 –20. Along the coastal boundary, no-slip condition is applied but along the southern and northern open boundary, slip boundary condition is assumed. At the ocean surface, no wind stress is usually assumed but uniform wind stresses are sometimes applied, in experiments 2–10, to examine the effect of local monsoon. At the ocean bottom, a quadratic bottom stress is imposed with various drag coefficient, such as those given in experiments 16 and 17. Stream functions over islands are obtained using the Hole Relaxation Method (TAKANO, 1974).

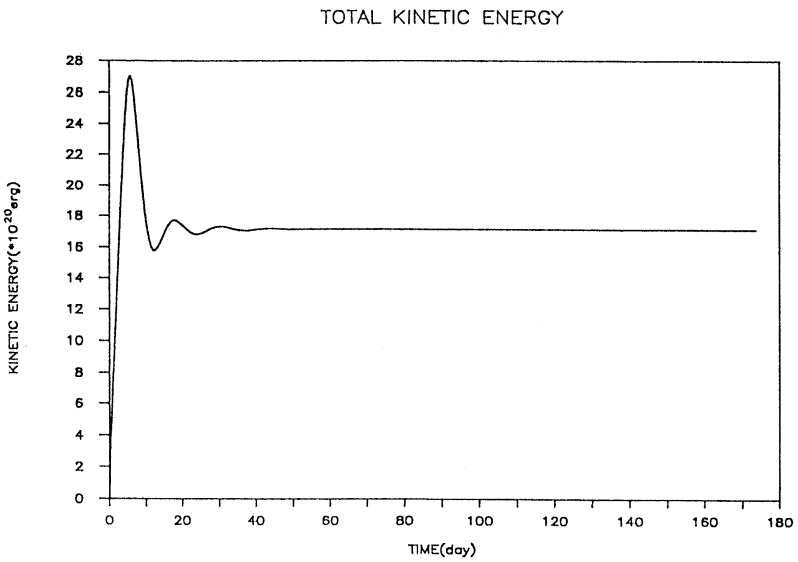

Fig. 3. Time variation of total kinetic energy for experiment 1 (see Table 1).

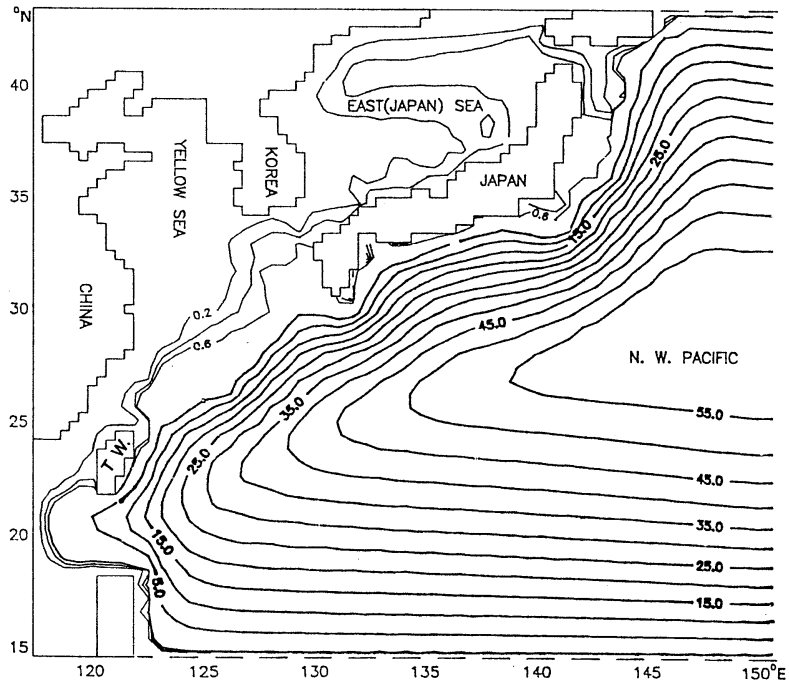

Fig. 4. Distribution of transport stream function (in Sv.) for experiment 1.

3. General flow pattern

Experiment 1 is taken as a standard case (Table 1) and its result is shown in Fig. 4. The Kuroshio water crosses the continental slope through the western and eastern sides of Taiwan and flows approximately along the isobath toward the East (Japan) Sea through the Korea Strait. The flow pattern around Taiwan is exactly the same as what is known as the Taiwan Warm Current (Guo *et al.*, 1987). This flow pattern indicates that the TSWC is the downstream extension of the Taiwan Warm Current.

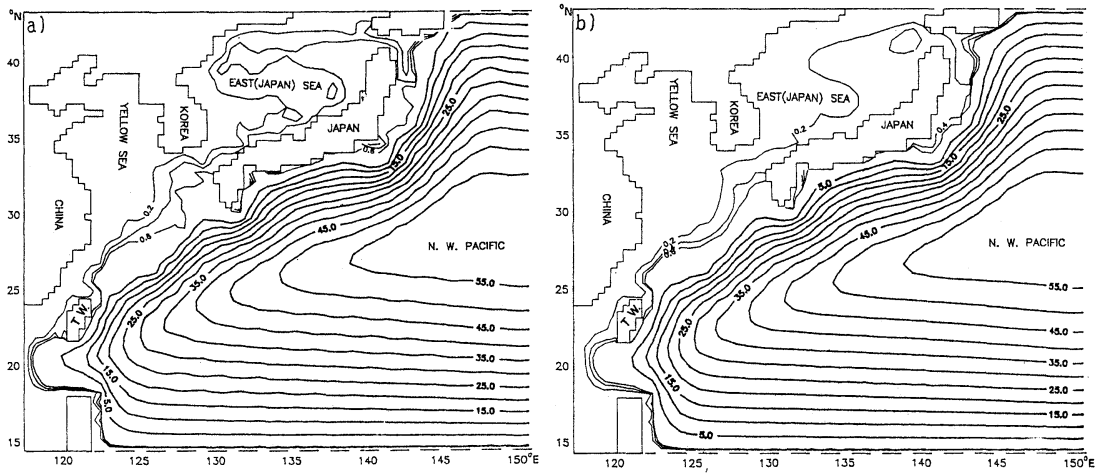

Fig. 5. Distributions of the transport stream function for experiments a) 14 and b) 15 of different eddy viscosity coefficients.

A part of it seems to return back to the Kuroshio along the coast, southwest of Japan. These are the general features throughout all experiments though some changes occur by local wind. The transport of TSWC amounts to 0.43 Sv. which is smaller than the known values, 1～2 Sv. (YI, 1966; MORIYASU, 1972). The discrepancy might come mostly from the neglect of baroclinicity. As seen later, large part of the total transport (TT) comes from the transport through Taiwan Strait (TST).

The result shown here indicates that all transports of Kuroshio water onto the shallow ECS take place through the southwestern end of the slope, i.e. by Taiwan Warm Current. A Rossby wave interpretation of this fact may be possible. Barotropic disturbances generated in mid-ocean propagate westward as the form of Rossby waves. The energy of these waves are normally trapped along the western boundary forming the Western Boundary Current. If the western boundary of the ocean borders a shallow marginal sea with large depth discontinuity, these waves become topographic waves and propagate southward along the discontinuity with the shallower part on their right of propagation direction in the northern hemisphere. When they reach to the coast, their energy is trapped at the coast by reflection in exactly the same way as the planetary waves are trapped along the western boundary. So, the penetration of western boundary current into the shallow marginal sea should take place within narrow region near the southern end of the slope.

4. Effect of viscosity coefficient

Experiments 1, 14 and 15 have different coefficients of eddy viscosity while other parameters are held the same. There is no remarkable difference in flow pattern among the three cases. However, a slight intensification of WBC (or thining of boundary layer) occurs at small coefficient (Fig. 5), as a linear theory predicts (MUNK, 1950). The TT and TST do not change much within the range of values considered (Fig. 6a); they seem to slightly decrease with the magnitude of coefficient. As noted previously, TST contributes to a large part of TT. The remaining contribution comes from the transport through the northeastern tip of Taiwan.

5. Effect of bottom drag coefficient

Experiments 1,16 and 17 have different drag coefficients with other parameters held the same. Comparision of these three experiments shows that small friction intensifies the WBC (thining of boundary layer) in agreement with STOMMEL's (1948) theory (Fig. 7). Both TT and TST decrease with increase of drag coefficient (Fig. 6b). This tendency is in agreement with MINATO and KIMURA's (1980) results. For small friction, TT is entirely from TST but for large friction, TST becomes small. The

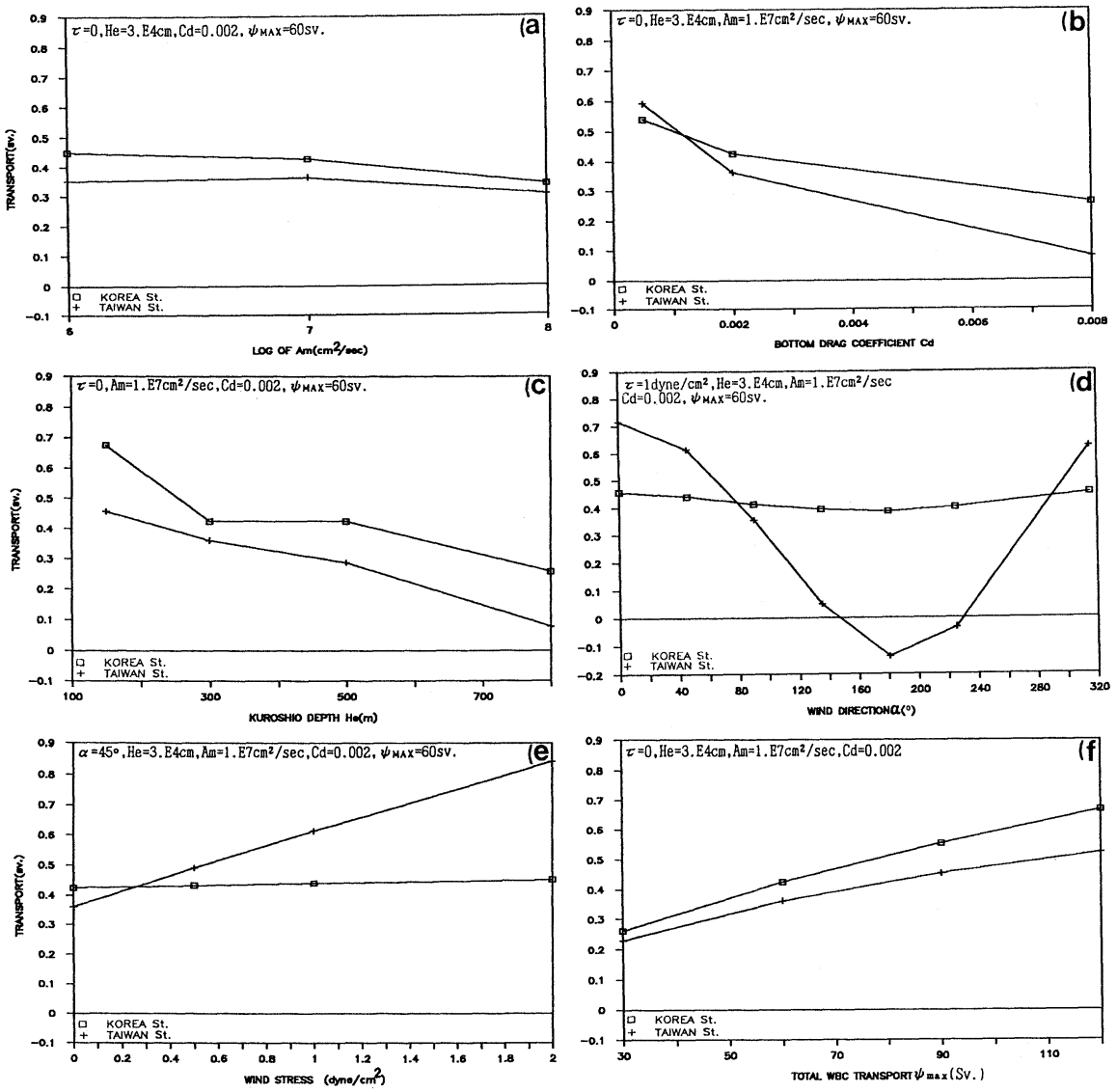

Fig. 6. Dependence of transports through the Korea and Taiwan Straits on the a) eddy viscosity coefficient, b) bottom drag coefficient, c) Kuroshio depth, d) wind direction, e) wind stress magnitude and f) the total WBC transport.

dependence of TST on the drag coefficient is thus larger than that of TT.

6. Effect of Kuroshio depth

Experiments 1, 11 and 13 have three different Kuroshio depths with other parameters held the same. Results of three experiments show that large Kuroshio depth intensifies the WBC (Fig. 8). It is conceivable that large depth diminishes the bottom friction, which then intensifies the WBC as explained previously. Both TT and TST decrease with increase of Kuroshio depth (Fig. 6c) in agreement with MINATO and KIMURA's (1980) results. In fact, large topographic change may hinder the transport of Kuroshio water across the steep slope. This tendancy seems more pronounced in TST than in TT because the proportion of the former to the latter becomes much reduced as the depth increases.

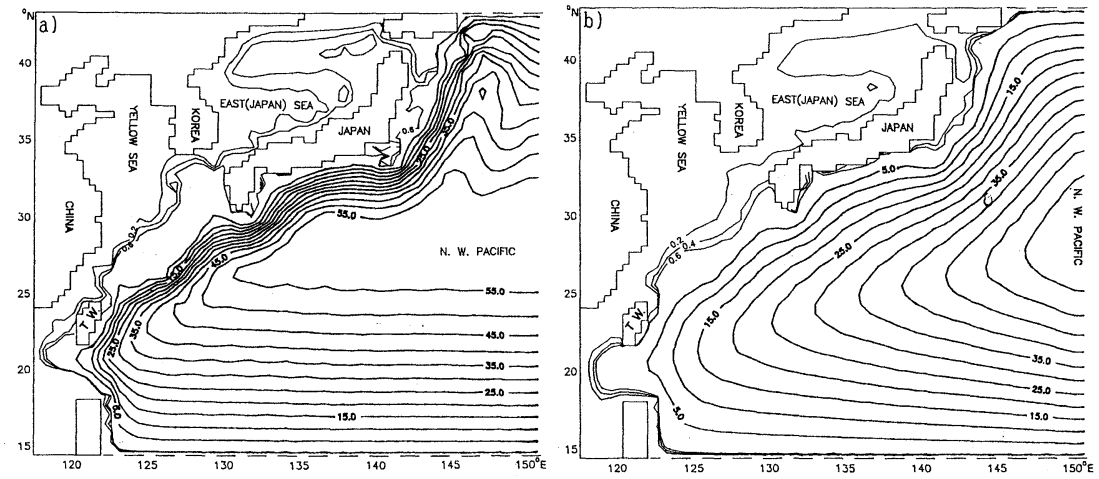

Fig. 7. Distributions of the transport stream function for experiments a) 16 and b) 17 of different bottom drag coefficients.

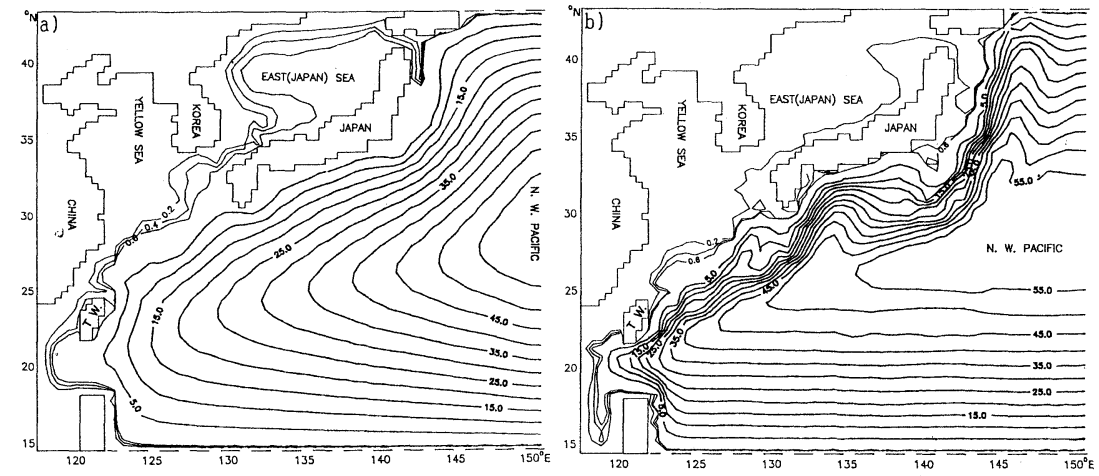

Fig. 8. Distributions of transport stream function for experiments a) 11 and b) 13 of different Kuroshio depths.

7. Effect of local monsoon

Experiments 1 through 10 have different wind fields with other parameters held the same. Among these 10 experiments, the largest contrast in flow pattern occurs between the cases of northerly and southerly winds (Fig. 9). The WBC is nearly the same but the transport pattern crossing the continental slope is quite different. For southerly wind, the transport is by TST whereas for northerly wind, it is by the transport through the northeastern tip of Taiwan. This fact is further clear in Fig.6d where TT and TST are given as functions of wind direction. The amount of TT does not vary much whereas that of TST largely fluctuates depending on wind direction. Under the southerly wind prevailing in summer, TST is larger than TT and the excess of the former over the latter returns back to the Kuroshio along the coast, southwest of Japan. Under the northerly wind prevailing in winter, TT is through the northeastern tip of Taiwan and TST reverses. The TST increases with, while the TT remains independent of, the magnitude of wind stress as shown for the case of southwesterly wind (Fig. 6e). This tendency is in good qualitative agreement with obsevations (Guo *et al.*, 1987) and numerical model (Chao, 1990) performed in local area

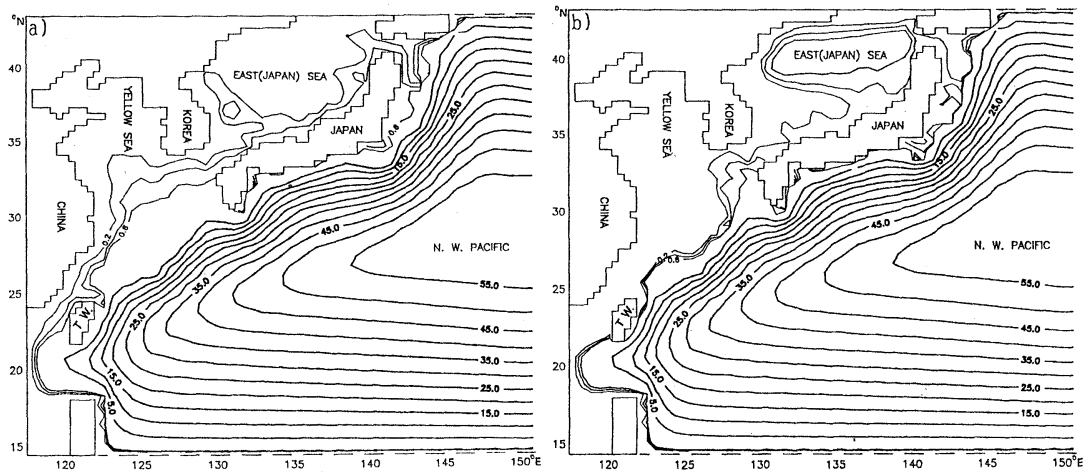

Fig. 9. Distributions of transport stream function for experiments a) 2 and b) 6 of southerly and northerly wind stresses, respectively.

though the transport through the northeastern tip of Taiwan appears more dependent on the seasonal monsoon.

8. Effect of total WBC transport

Experiments 1, 18, 19 and 20 have different total WBC transports with other paramenters held the same. Results of these experiments show the nearly same distribution pattern of stream functions (not shown) although they have different magnitudes. Both TT and TST increase monotonically with increase of the total WBC transport (Fig. 6 f) ; the former increases slightly more than the latter. The proportion of these transports to the total WBC transport, however, decreases slightly with increase of the WBC transport.

9. Concluding remarks

Results obtained in this study can be summarized as follows:

1) The so-called Taiwan Warm Current is confirmed to pass through both sides of Taiwan and the TSWC is just the downstream extension of it. A small part of Taiwan Warm Current Water returns back to the Kuroshio along the coast, southwest of Japan though it does not seem quite significant. It is shown that the western boundary current penetrates into the bordering shallow marginal sea through the narrow region near the southern end of the continental slope.

2) The transport of TSWC depends on the friction (both bottom and lateral, with the former to much larger extent), the depth difference across the continental slope and the total WBC transport. Smaller friction, smaller depth difference and larger WBC transport tend to increase the TSWC transport.

3) Transports through Taiwan Strait, through eastern side of Taiwan and back to the Kuroshio fluctuate depending on the local wind. However, the total transport of TSWC does not change significantly. It is fed by the transport through Taiwan Strait under the southerly wind in summer but by the transport through the eastern side of Taiwan under the northerly wind in winter.

This study is not complete in some respects. The results given above should be more fundamentally explained. Furthermore, the present model dose not include baroclinicity and neglects the buoyancy input from large fresh water sources along the Chinese coast. Also, a part of the transport through the Taiwan Strait may be originated from the South China Sea. These problems may be able to be resolved in near future.

Acknowledegements

This study is supported by the 1990 research fund from the Ministry of Education, Republic of Korea.

References

CHAO, S.-Y. (1991): Circulation of the East China Sea, A Numerical Study. J. Oceanogr. Soc. Japan, **46**, 273–295.

FAN, K.-L. (1980): On Upwelling off northeastern shore of Taiwan. Acta Oceanographical Taiwanica, **11**, 105–117.

GUAN, B. (1986): On the Circulation in the East China Sea. Studia Marina Sinica, **27**, 1–21.

GUO, B.K., Lin, H.Z. and J.Lu (1987): Some features on the circulation in the East China Sea. In: Essays on the Investigation of Kuroshio, X.Sun, (ed), Ocean Press, Beijing. (in China)

HSUEH.Y., R.D. ROMEA and P.W. DEWITT (1986): Wintertime winds and coastal sea level fluctuations in the northeast China Sea. Part III: Numerical model. J. Phys. Oceanogr., **16**, 241–261.

HUH, L.K. (1982): Spring season flow of the Tsushima Current and its separation from the Kuroshio: satellite evidence, J. Geophys. Res., **87**C, 9687–9693.

LIM, D.B. (1971): On the origin of the Tsushima Current Water. J. Oceanogr. Soc. Korea, **6**, 85–91.

MINATO, S. and R. KIMURA (1980): Volume transport of the western boundary current penetrating into a marginal sea. J. Oceanogr. Soc. Japan, **36**, 185–195.

MORIYASU, S. (1972): The Tsushima Current. In: Kuroshio: Its Physical Aspects, H. STOMMEL and K. YOSHIDA, (eds.), Univ. of Tokyo Press, 353–369.

MUNK, W.H. (1950): On the wind-driven ocean circulation. J. Meteorol., **7**, 79-93.

NAGATA, Y. (1981): Oceanic circulation in the East China Sea. Proc. Japan-China Study Symp. Kuroshio, 25–41.

NITANI, H. (1972): Beginning of the Kuroshio. In: Kuroshio: Its Physical Aspects, H. STOMMEL and K. YOSHIDA, (eds.), Univ. of Tokyo Press, 129–156.

SEMTNER, A.J. (1974): An oceanic general circulation model with bottom topography: Numerical Simulation of Weather and Climate, Technical Report No.9, Department of Meteorology, UCLA, 99pp.

STOMMEL, H. (1948): The westward intensification of wind-driven currents. Trans., Amer. Geophys. Union, **29**, 202–206.

TAKANO, K. (1974): A general circulation model for the world ocean. Numerical simulation of Weather and Climate, Technical Report No.8, Department of Meteorology, UCLA, 47pp.

TAKANO, K. and A. MISUMI (1990): Numerical simulation of the North Pacific circulation as a fundamental study on the Kuroshio power harnessing. Proc. Japan-China Joint Symp. Kuroshio, Sci. Techuol. Agency, Japan, State Oceanic Administr. Chine, 146–156.

UDA, M. and A., KISHI (1974): Cyclonic cold eddies along the edge of the Kuroshio Current in relation to the genesis and passage of cyclones, I.Waters north of Taiwan, In: The Kuroshio III, Proc. 3rd Symp., Bankok, 199–218.

WANG, W. and J. SU (1987): A barotropic model of the Kuroshio system and eddy phenomena in the East China Sea. Acta Oceanolog. Sinica, **6**, suppliment, 21–35.

YI, S.-U. (1966): Seasonal and secular variations of the water volume transport across the Korea Strait. J. Oceanogr. Soc. Korea, **1**, 7–13.

La mer 30: 149–155, 1992
Société franco-japonaise d'océanographie, Tokyo

A note on initial nitrate and initial phosphate as tracers for the origin of East Sea (Japan Sea) Proper Water

Kyung-Ryul KIM*, Tae Siek RHEE* and Kuh KIM*

Abstract: The East Sea (Japan Sea) is a mid-latitude marginal sea with average depth over 1,500 meters in the North Western Pacific. The deep waters below several hundred meters over the entire basins, as generally known as the East Sea Proper Water (ESPW), show extreme homogeneous characteristics with relatively large concentration of dissolved oxygen over 230 μM, reflecting rather rapid replenishment of these waters in the basins. Even though ESPW, consisting over 84% of the total volume of the East Sea, may not be a single homogeneous water mass, further analysis imposes serious difficulties due to homogeneous nature of these waters.

We explored the possibility of utilizing initial nutrients as tracers for these waters, providing further constraints on their origins. With respiration coefficients of 76 and 6.5 for phosphate and nitrate, respectively, the initial analysis indicates that ESPW consists of two components; one with larger initial nutrients (11 μM of NO_3^0 and 0.6 μM of PO_4^0) and the other with smaller values (3 μM of NO_3^0 and 0.1 μM of PO_4^0), possibly corresponding to upper portion and deep water of ESPW, respectively.

The lack of data, especially over northernmost region in winter time, prevents further analysis at the present moment. The future study in this direction appears to be of significant importance in understanding and clarifying major oceanographic problems regarding the origin of rapidly replenishing deep waters in the East Sea.

1. Introduction

The East Sea (Japan Sea) is a typical mid-latitude marginal sea in the North Western Pacific. With an average depth of more than 1,500 meters, the topography of the East Sea shows three major basins (Fig. 1). The Japan Basin with a depth of more than 3,500 meters occupied most of the northern part of the East Sea, and the Ulleung and Yamato basins consist of the major part of the southern East Sea to the west and east of the Yamato Rise, respectively.

Though the shallow waters of the East Sea are continually exchanged with the Pacific waters through narrow straits with depth of less than 150 m, it is generally believed that deep convection is occurring within the East Sea (e.g., SUDA, 1932; NITANI, 1972), with the relatively rapid replenishment of the deep waters in the basins. The high concentrations of dissolved oxygen over 230 μM in deep waters of the entire basins reflect the above circulation; the average residence time of 300 to 400 years for the deep waters has been suggested (HARADA and TSUNOGAI, 1986; GAMO and HORIBE, 1983).

The waters below several hundred meters to the bottom in the East Sea show extremely homogeneous characteristics; temperature of 0~1℃ and salinity of 33.96~34.14‰ (e.g., MORIYASU, 1972), which are rather in contrast with the characteristics of deep waters observed in Northwest Pacific; 1~2℃ in temperature and 34.6~34.7‰ in salinity (e.g., SVERDRUP *et al.*, 1942; ROEMMICH *et al.*, 1991). YASUI *et al.* (1967) calculated by T-S analysis that this homogeneous water mass, generally known as the East Sea (Japan Sea) Proper Water (hereafter ESPW), consists of more than 84% of the total volume of the East Sea waters. Though ESPW may not be a single homogeneous water mass, further analysis and identification of source regions of these waters with temperature and

* Department of Oceanography, Seoul National University, Seoul 151-742, Korea

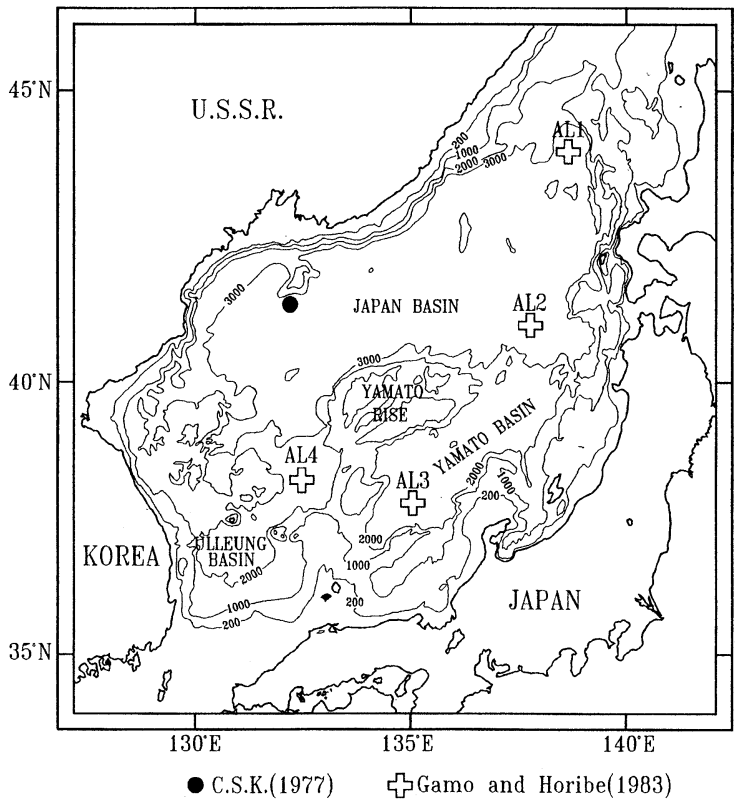

Fig. 1. The topographic map of the East Sea (Japan Sea) showing three major basins: Japan Basin, Ulleung Basin and Yamato Basin. The stations by CSK (Japan Oceanographic Data Center, 1977) and Gamo and Horibe (1983) are also shown in the map.

salinity distributions impose serious difficulties due to extremely narrow ranges of their variation. SUDO (1986) recently reviewed these problems extensively, as discussed further in the later section.

Initial phosphate and initial nitrate are typical examples of chemical parameters applied in water mass analysis in recent years (e.g., BROECKER *et al.*, 1985; BIGG and KILLWORTH, 1990). The terms, initial nitrate and initial phosphate, are identical to the terms, preformed nitrate and preformed phosphate used by some earlier investigators (e.g., REDFIELD *et al.*, 1963; PYTKOWICZ, 1971). Furthermore, the information carried by these initial nutrients is essentially the same as that conveyed by "NO" (BROECKER, 1974) and "PO" (BROECKER *et al.*, 1985). These quantities are the concentrations of nitrate and phoshate generally observed in surface waters at high latitude regions, especially in winter time. When the surface waters sink and start their deep-sea circulation, these quantities are preserved in the waters along their journey in the deep sea as conservative components. The fact that these quantities in surface waters vary geographically, provides the possibility of using these quantities as tracers for the deep waters in the ocean.

Figure 2 shows distribution patterns of 20-year-average phosphate concentrations in surface waters of the East Sea in winter time, collected by Maizuru Marine Observatory (1985). Two important points can be made:

(1) there are relatively large amounts of phosphate present in surface waters in winter, and
(2) significant geographical variations in phosphate concentration exist in the area with relatively small values in southern regions and along the coast.

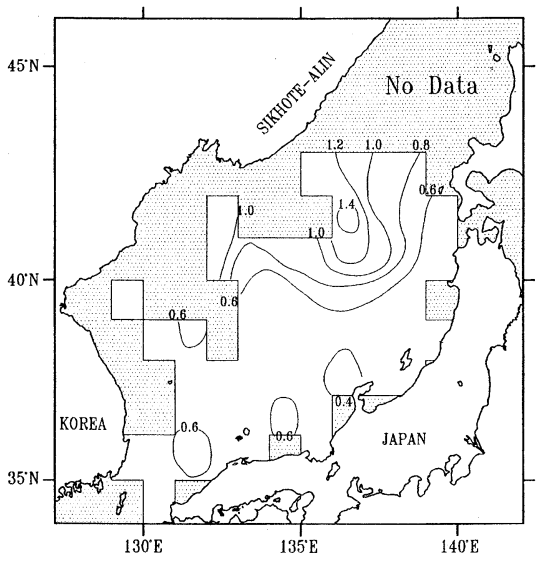

Fig. 2. The distribution pattern of 20-year-average phosphate concentrations in surface waters in winter time, collected by Maizuru Marine Observatory (1985). The large geographical variation ranging from below 0.4 μM to above 1.4 μM with northward increase with relatively lower concentrations along the coast, in general, is clearly seen. However, the lack of data over the northernmost regions along the coast and at north of 43° N in particular, the most critical area for deep water formation in the East Sea, typically represent the present status of data base available in the area.

However, the lack of data over the northernmost regions along the coast and above 43°N in particular, the most critical areas for possible deep water formation, typifies the present status of data base available in the area. With this limitation in mind, if the source region of the deep waters in the East Sea, ESPW, is confined in relatively small areas, then, the initial nutrient concentrations of these waters, if any, may provide additional constraints on the origin of these waters.

In this paper, we explore the possibility of utilizing these excess nutrients for tracing and extracting information on the source regions of ESPW, present in deep layers of the East Sea.

2. Data set and analysis

Oceanographic data with complete nutrient analysis for deep waters in the northern East Sea are rather scarce, especially in winter time. Two sets of data are selected in the analysis: data from CSK survey during February, 1976 (Japan Oceanographic Data Center, 1977) and data from GAMO and HORIBE (1983). Though the data from Gamo and Horibe do not cover the upper 1,000 meters of the water columns, these data represent deep waters in all major basins in the East Sea as shown in Figure 1.

The vertical profiles of potential temperature, salinity, DO (Dissolved Oxygen), AOU (Apparent Oxygen Utilization), nitrate, and phosphate are shown in Figure 3. The homogeneity of all properties for the waters below several hundred meters over the entire basins is remarkable as mentioned earlier. There appears a slight difference in salinity profiles between CSK data and those by GAMO and HORIBE (1983). The difference may be real or simply reflect the calibration difference.

Initial phosphate, PO_4^0 and initial nitrate, NO_3^0 are calculated from the relationships as follows:

$$PO_4^\circ = PO_4 - \frac{DO_{sat} - DO}{76} = PO_4 - \frac{AOU}{76}$$

$$NO_3^\circ = NO_3 - \frac{DO_{sat} - DO}{6.5} = NO_3 - \frac{AOU}{6.5}$$

where PO_4, NO_3 and DO are the observed concentrations, DO_{sat} is the saturation concentration of dissolved oxygen at the potential temperature and salinity of water samples and AOU is the apparent oxygen utilization.

The respiration coefficients, 76 and 6.5 in the above formulae are calculated from CSK data (Japan Oceanographic Data Center, 1977) for waters in upper 400 meters layer as shown in Figure 4.

These coefficients are rather different from the values observed in open oceans: 175 for phosphate (BROECKER *et al.*, 1985) and 9 for nitrate (BROECKER, 1974), possibly reflecting different ecology, especially different chemical characteristics of DOC and POC in the East Sea compared to those in open oceans. The lack of available data especially over northern part of the East Sea prevents any further discussions on the validity of these values at the present time: further careful and extensive analysis on this

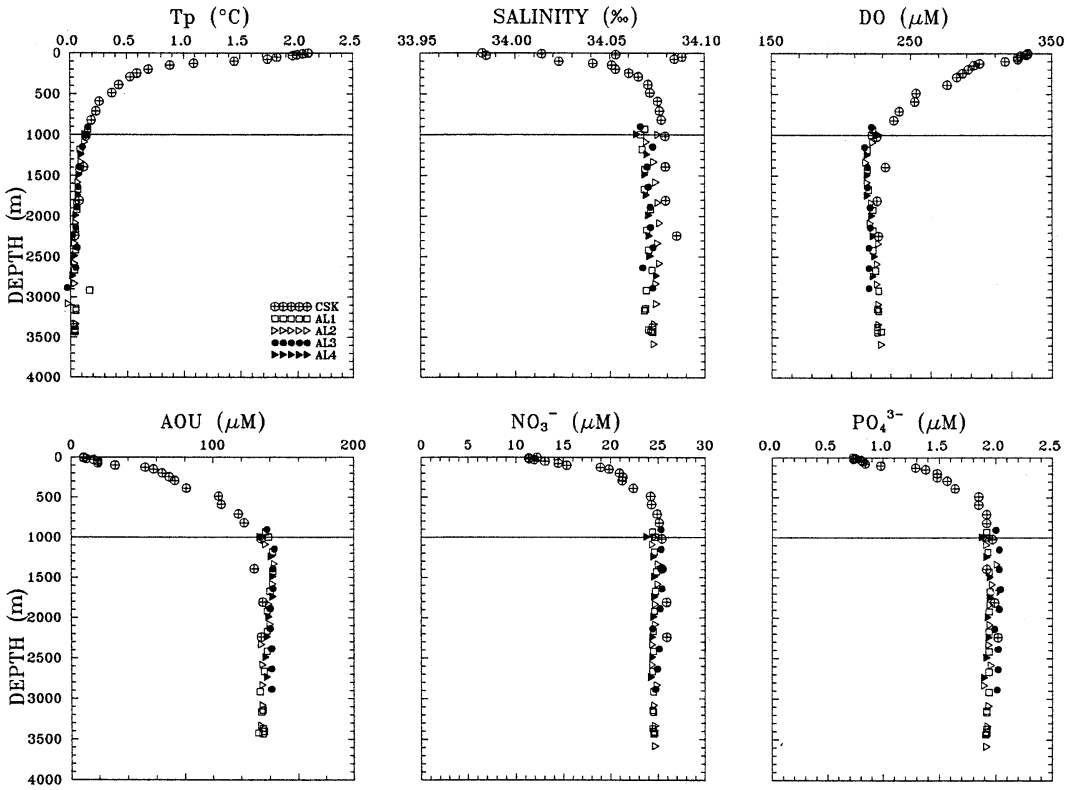

Fig. 3. The vertical profiles of potential temperature, salinity, dissolved oxygen (DO), apparent oxygen utilization (AOU), nitrate and phosphate at CSK and Gamo and Horibe stations. No data at depths shallower than 1,000 meters were available at Gamo and Horibe stations, unfortunately. The extremely homogeneous nature of these properties below 1,000 meters over the most of the basins in the East Sea is clearly seen, especially considering the location of these stations as shown in Fig. 1.

subject is needed in the future.

3. Results and Discussion

Figure 5 shows the vertical profiles of initial nitrate and initial phosphate. While the waters in surface 400 meters show about 10~11 μM of NO_3^0 and about 0.6 μM of PO_4^0, these values decrease with depth to about 1,000 meters and then remain fairly constant to the bottom at about 3~4 μM of NO_3^0 and about 0.1~0.2 μM of PO_4^0. There appears to be a minimum at about 1,000 meters for these initial nutrients, and the significance of it, if any, is not clear at this point.

It is also noted that waters below 1,000 meters over the most of the deep basins in the East Sea, as covered by the stations from Gamo and Horibe, show remarkably similar concentrations of initial nutrients. The exception is the result from CSK station in the northwestern East Sea, where the initial nutrients appear to be higher than in other areas; a possible mechanism producing this difference is discussed in the later section.

Figure 6 shows the correlation between initial phosphate and initial nitrate. A rather well-defined linear relationship is clear, indicating a possibility of mixing between two components: one component with about 11 μM of NO_3^0 and 0.6 μM of PO_4^0, observed in upper 400 meters at CSK station, and the other with about 3 μM of NO_3^0 and 0.1 μM of PO_4^0, observed over most of the basins below 1,000 meters. It is also important to observe that the thermocline waters and deep waters at CSK station lie on the mixing line between these two components.

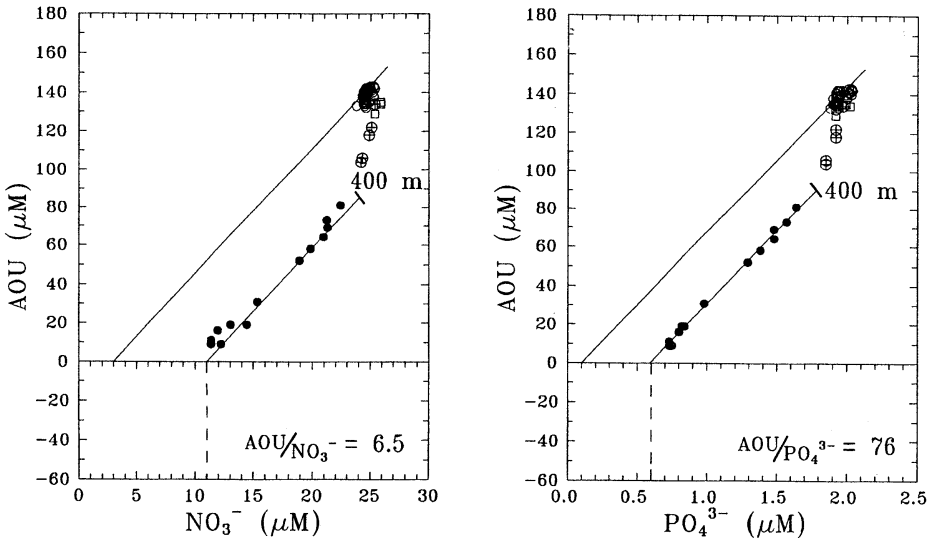

Fig. 4. The plot of AOU vs. nitrate and phosphate. The data at depths shallower than 400 meters at CSK station show respiration coefficients of 6. 5 and 76 for nitrate and phosphate, respectively, with about 11 μM of initial nitrate and about 0. 6 μM of initial phosphate concentrations. The deep waters below 1,000 meters show about 3 μM of initial nitrate and about 0. 1 μM of initial phosphate concentrations, if assuming respiration coefficents in these deep waters as the same as those observed in shallow waters at CSK station; this has to be verified with further investigations in the future.

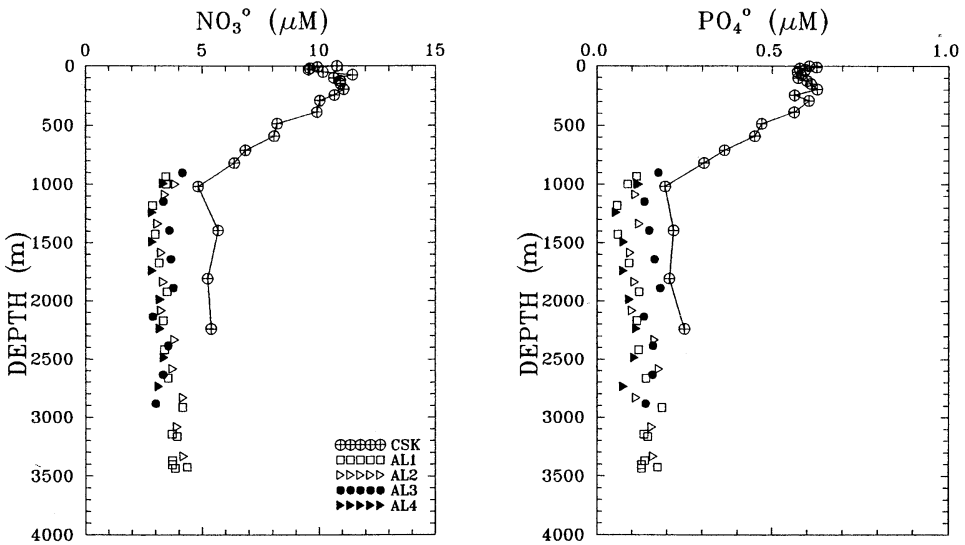

Fig. 5. The vertical profiles of initial nitrate and phosphate at CSK and Gamo and Horibe stations, calculated with respiration coefficients of 6. 5 and 76 for nitrate and phosphate, respectively. The necessity of profiles in shallow waters are most urgent. The initial nutrients in deep waters at CSK station are clearly larger than those in deep waters over all other major basins; a possible cause for this difference is discussed in the text.

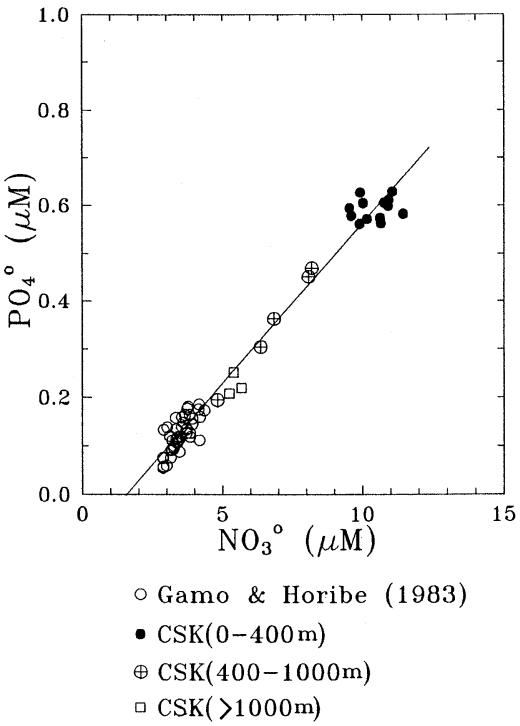

Fig. 6. The initial nitrate-initial phosphate plot at CSK and Gamo and Horibe stations.

In his lengthy analysis of temperature, salinity and dissolved oxygen distributions, SUDO (1986) concluded that ESPW can be further divided into two groups: the upper portion and the deep water with the boundary at the depth of potential temperature ca 0.1℃ (typically at 800 ~1,000 meters in northern East Sea). He proposed, furthermore, that the upper portion of ESPW originates from the northwestern area, west of 134°E and north of 41°N, and the most of the deep water has been formed in northern area, probably north of 43° N. The apparent two-component mixing trend observed in Figure 6 may be consistent with the Sudo's above conclusion: the upper portion of ESPW corresponding to a component with higher initial nutrient concentrations (11 μM of NO_3° and 0.6 μM of PO_4°) and the deep water to the other end member with lower initial concentrations (3 μM of NO_3° and 0.1 μM of PO_4°). In this regard, it is very interesting to note as mentioned earlier that the initial nutrient concentrations in deep waters below 1,000 meters at CSK station, the closest station from the proposed source region of the upper portion of ESPW in northwestern section of the East Sea, are rather higher than those at all the other stations, quite possibly reflecting the effect of proximity to the source region of higher initial nutrients in upper waters.

The magnitude of these initial nutrients, especially in upper waters, are rather significant. This observation clearly indicates that the sinking waters in the East Sea contain enough of these initial nutrients, which can be later calculated and used as tags for the particular water masses. It is interesting, however, to observe that deep waters of ESPW show much smaller concentrations of NO_3° and PO_4° than the upper portion of ESPW, especially considering the possibility of further northern origin of deep waters as discussed above.

First of all, it has to be verified in the future that respiration coefficients for the deep waters are similar to the values in shallow waters as used here. In fact, the very limited amounts of data available at NODC indicate that the chemistry of waters in the area as north as 43° N in winter time does not seem to show any significant differences compared to that at CSK station, discussed in this paper, suggesting that the respiration coefficients in the northernmost region may not be drastically different from the values used in the paper. Therefore, it could be also possible that phosphate concentrations in surface waters over northernmost region may, indeed be very low, due to fresh water inputs, resulting in lower initial nutrient concentrations in deep waters.

As shown in Figure 2, as an example of best data set available at present, concentrations of nutrients in surface waters over northernmost regions of the East Sea are poorly known at the present time. The information on these chemical components over possible source regions of ESPW, expecially in winter time, appears to be of paramount importance in understanding and clarifying major oceanographic problems, regarding the origin of rapidly replenishing deep waters in the East Sea.

4. Conclusion

In order for these initial phosphate and nitrate to be applied successfully in distinguishing

water types, two conditions must be met as summarized by BROECKER *et al.* (1985):

(1) the respiration coefficients must be fairly constant over water depth and geographic location of interest, and
(2) the average value of these coefficients must be precisely known.

Both of the above conditions in the East Sea could not be verified yet due to lack of data available at the present time. The respiration coefficients used in this paper, 76 for PO_4^0 and 6.5 for NO_3^0, are rather different from those used in the open ocean, 175 for PO_4^0 and 9 for NO_3^0. All these points are the subjects for the close examination with new data in the future. However, the present preliminary analysis of nutrient results over northern part of the East Sea does show that ESPW may contain significant amounts of initial nitrate and initial phosphate. The application of these apparent conservative parameters, initial phosphate and initial nitrate, will be a very important addition in investigating the sources and dynamics of the deep waters present in the East Sea, especially considering the difficulties encountered in conventional approaches, which are originating from the extreme homogeneous nature of deep waters in the area.

Acknowledgments

The critical review by Prof. GIESKES at the Scripps Institution of Oceanography (SIO) improved the paper very much. Profs. REID and TALLEY at SIO kindly permitted us to use NODC data and helped to retrieve appropriate data for the study. Prof. HORIBE at Tokai University also provided many productive comments and criticism. Miss J.S. Cho prepared the final manuscript. This work was supported in part by the Basic Sciences Research Institute Program, Ministry of Education, Korea, 1990.

References

BIGG, G.R. and P.D. KILLWORTH (1990): Conservative tracers and the ocean circulation. *In*: Tracers in the ocean (eds., H. CHARNOCK, J.E. LOVELOCK, P.S. LISS and M. WHITFIELD), Princeton University Press, 177–187.

BROECKER, W.S. (1974): "NO", a conservative water-mass tracer. Earth Planet. Sci. Let., **23**, 100–107.

BROECKER, W.S., T. TAKAHASHI and T. TAKAHASHI (1985): Sources and flow patterns of deep ocean waters as deduced from potential temperature, salinity, and initial phosphate concentration. J. Geophys. Res., **90**, 6925–6939.

GAMO, T. and Y. HORIBE (1983): Abyssal circulation in the Japan Sea. J. Oceanogr. Soc. Japan, **39**, 220–230.

HARADA, K. and S. TSUNOGAI (1986): Ra-226 in the Japan Sea and the residence time of the Japan Sea waters. Earth Planet. Sci. Let., **77**,: 236–244.

Japan Oceanographic Data Center (1977): Data Report of CSK. No. 419, 13 pp.

Maizuru Marine Observatory (1985): Climatology of hydrographic and chemical properties of the Japan Sea. 51pp.

MORIYASU, S. (1972): The Tsushima current. *In*: Kuroshio – Its physical aspects. (eds., H. STOMMEL and K. YOSHIDA), Univ. of Tokyo Press, 353–369.

NITANI, H. (1972): On the deep and the bottom waters in the Japan Sea. *In*: Researches in Hydrography and Oceanography (ed., D. SHOJI). Hydrographic Dept. Japan Maritime Safety Agency, Tokyo, 151–201.

PYTKOWICZ, R. M. (1971): On the apparent oxygen utilization and the preformed phosphate in the oceans. Limnol. Oceanogr., **16**, 39–42.

REDFIELD, A.C., B.H. KETCHUM and F.A. RICHARDS (1963): The influence of organisms on the composition of sea water. *In*: The Sea 2 (ed., M.N. Hill), 26–77.

ROEMMICH, D., T. McCALLISTER and J. SWIFT (1991): A transpacific hydrographic section along latitude 24°N: the distribution of properties in the subtropical gyre. Deep-Sea Res., **38**, Suppl., 1, s1–20.

SUDA, K. (1932): On the bottom water of the Japan Sea (Preliminary report). J. Oceanogr. Imp. Mar. Observatory, Kobe, Japan, **4**, 221-240 (in Japanese with English abstract) .

SUDO, H. (1986): A note on the Japan Sea Proper Water. Prog. Oceanog., **17**, 313–336.

SVERDRUP, H.U., M.W. JOHNSON and R.H. FLEMING (1942): The Oceans: their physics, chemistry and general biology. Prentice Hall, Inc.

YASUI, M., T. YASUOKA, K. TANIOKA and O. SHIOTA (1967): Oceanographic studies of the Japan Sea (1) – Water characteristics. Oceanogr. Mag., **19**, 177–192.

La mer 30: 157–167, 1992
Société franco-japonaise d'océanographie, Tokyo

Submarine cable voltage measurements between Pusan and Hamada

Byung-Ho CHOI[*1], Kuh KIM[*2], Young-Gyu KIM[*2], Kyung Soo BAHK[*3], Jeong Ok CHOI[*4] and Kazuo KAWATATE[*5]

Abstract: The voltage difference between the ends of telephone cable across the Korea Strait is measured for one year beginning March 1990. Spectral analysis and tidal analysis show that the voltage variations have most energies in low frequencies and some peaks at the tidal frequencies, which are highly correlated to the variation of tidal stream in the Korea Strait. Using the M_2 amplitude the transport per one volt is simply estimated as 35.95 Sv/volt.

1. Introduction

By the Faraday's law, an electromagnetic force induces electric potential difference in water flowing in a channel as it works as a moving conductor in the earth's magnetic field. If the potential difference is measured at the both ends of a submarine telephone cable laid at the bottom of a channel, the total volume transport of water flowing through the channel at any instant can be estimated.

LONGUET-HIGGINS (1949) first introduced the theoretical application of the Faraday's law for the purpose of estimating the transport for a shallow channel whose depth is small compared with its width. Since then this technique has been applied very successfully in the Dover Strait. BOWDEN (1956) indentified the main tidal constituents of the cable voltage and showed that they vary seasonally with sea conductivity. He also estimated residual flows using a calibration factor derived from the tidal signal and correlated them with local winds and sea-level gradients. Since BOWDEN's experiment CARTWRIGHT and CREASE (1963), PRANDLE and HARRISON (1975) also used this method to study water movements in the Dover Strait while HUGHES (1969) and PRANDLE (1980) applied this method in the Irish Sea and Pentland Firth respectively. ALOCK and CARTWRIGHT (1977) analyzed 10-year's voltage records in Dover Strait for tidal and non-tidal effects.

The theoretical work of LONGUET-HIGGINS (1949) had been advanced by SANFORD and FLICK (1975) and ROBINSON (1976). ROBINSON (1977) described a theoretical model which was capable of predicting the potential difference across the Dover-Sangatte cable.

LARSEN and SANFORD (1985) described the Florida Current volume transport from voltage measurements and recently LARSEN (1991) used in-service undersea telephone cable with repeaters to estimate the Florida Current transport.

In the Korea Strait KAWATATE *et al.* (1991) obtained a time series of the electric voltage records at the Japanese side of the submarine cable buried between Pusan and Hamada for the period of July 1987 to February 1988 together with a set of the current records measured southeast of the Tsushima Island. A cross-spectral analysis showed a strong correlation between the voltage and current variations.

There have been earlier efforts to estimate the transport passing through the Korea Strait and flowing into the East Sea (HIDAKA and SUZUKI, 1950; YI, 1966). However, because of shal-

*1 Department of Civil Engineering, Sung Kyun Kwan University, Korea
*2 Department of Oceanography, Seoul National University, Korea
*3 Korea Ocean Research and Development Institute, Korea
*4 Korea Telecommunication Authority, Korea
*5 Research Institute for Applied Mechanics, Kyushu University, Japan

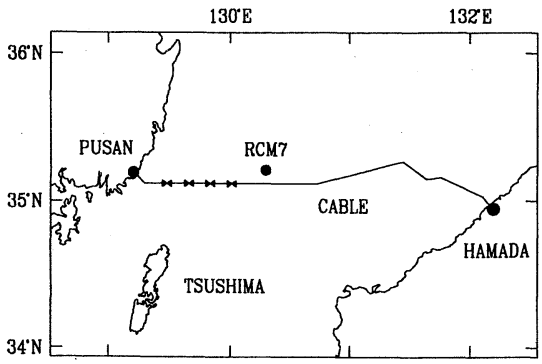

Fig. 1. Location map of submarine telephone cable and RCM current meters.

lowness of this region, dynamic calculation of geostrophic flow has a limitation of determining the reference level. One of our objectives is to apply the voltage measurement technique in the Korea Strait for a long-term monitoring of the transport variation of the Tsushima Current. As a follow-up of the measurements at Hamada Station, we took data of voltage variation at Pusan Station of the underwater cable across the Korea Strait beginning March 1990. This paper describes the preliminary results of data analysis to investigate the usefulness of the voltage records. We analyze one year data focusing at fluctuations at tidal frequencies mainly.

2. Data

The submarine cable between Pusan and Hamada is 281 km long, oriented mainly in the east-west direction and contains 50 repeaters (Fig. 1). The essential elements are shown in Fig. 2. We installed the data logger at the Pusan Submarine Cable Relay Station and have recorded the voltage fluctuations since March 29, 1990. The power supply voltage (Vs) is about −550 at Pusan and about +550 at Hamada, which compensate each other maintaining 1100 volts between two stations. This power voltage is measured from a pair of test points divided

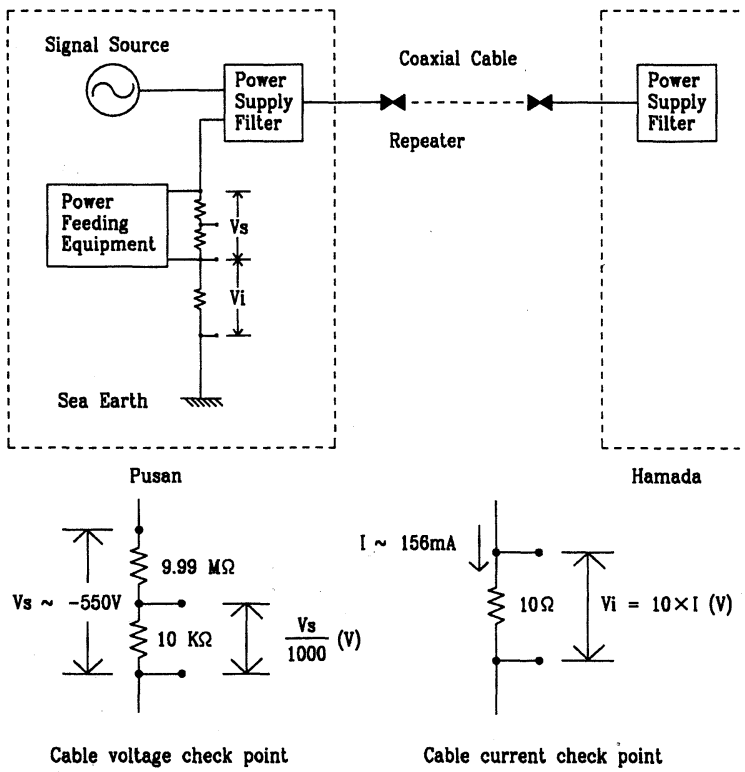

Fig. 2. Essential elements of submarine telephone cable for monitoring motion-induced voltages.

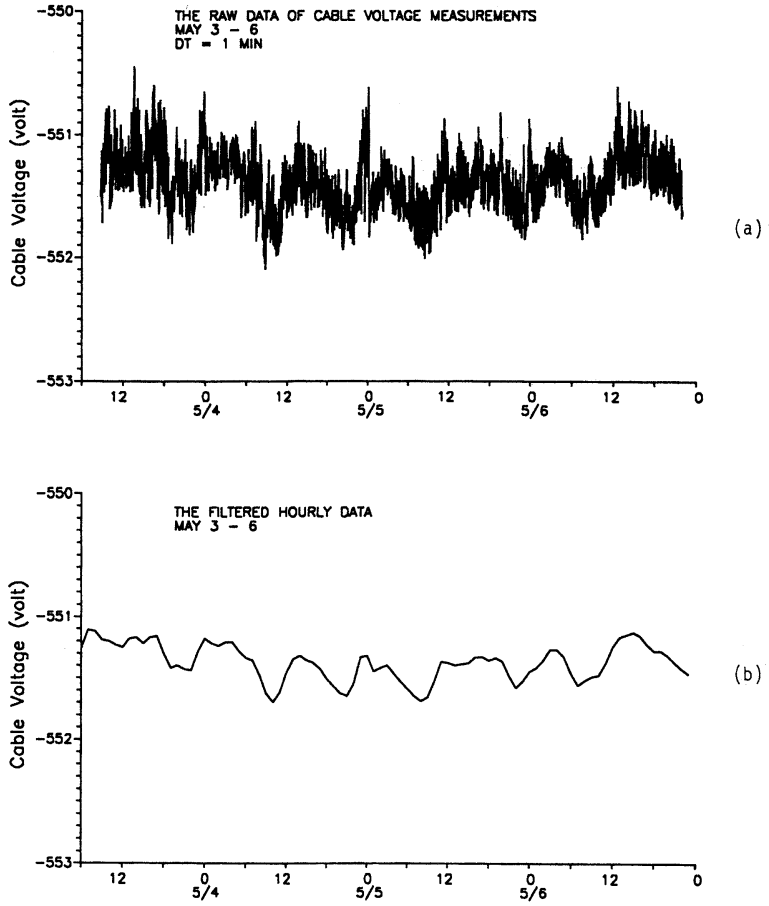

Fig. 3. Examples of (a) raw data and (b) filtered hourly data of voltage variations from May 3 to 6.

by 1000 at Pusan. The power supply current (I) is about 156 mA and determined from the voltage Vi measured from a pair of test points connected across a 10 ohm resistor. This power current flows through the power supply filter, the submarine cable and the repeaters and returns to the sea-earth ground through the ocean. Data acquisition system is further described by BAHK (1991) separately.

The logger samples the voltage every minute, which is an average over 8 seconds. About every 10 days, the data are retrieved through a dial up modem system. The retrieved raw data are filtered and subsampled to obtain hourly data for final analysis.

These cable voltages previously have been measured at Hamada Station from 1987 to 1988 (KAWATATE, 1991), and have continued to record at the same time as our recording. In this study we used one year data to March 20, 1991 at the Pusan and analyzed these data with RCM7 current meter data moored from May 11 to June 29, 1990 approximately at the mid-point of cable (Fig. 1).

3. High frequency response

An example of the raw data from May 3 through 6 is shown in Fig. 3(a). The voltage fluctuates between about −552 and −551 volts with a conspicuous semidiurnal periods.

In order to check the quality of our data and the significance of high frequency response, we selected sample data during 3 days in May, August, November and February, and calculated

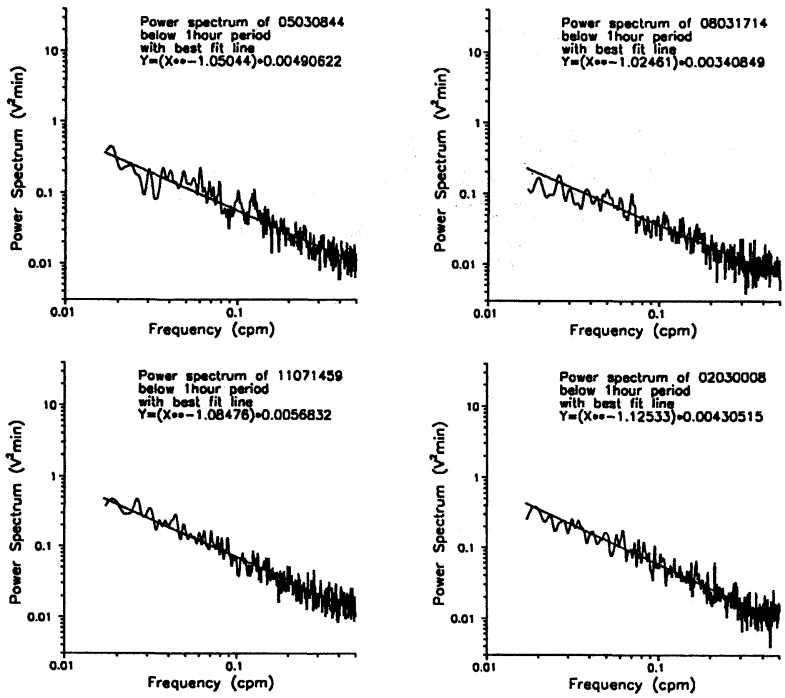

Fig. 4. Power spectra of about 3 days in each month.

the spectrum for each data (Fig. 4). These spectra are very similar to each other, linearly decreasing with frequency in logarithmic scale for frequencies corresponding to the period shorter than one hour. The decreasing slopes are −1.05, −1.03, −1.08 and −1.12 respectively, same in each month with the mean of −1.08. WUNSCH (1972) showed that the logarithmic slope was −3.5 above 2 cph in the ocean. The nearly constant slopes suggest that voltage response is systematic but may not be oceanic for high frequencies. BAHK (1991) suggested that the fast random change of less than 60 minutes was most likely caused by noises occurred from the cable system.

4. Voltage variation of hourly data

Because of our interest in the long-term variation, we applied a lowpass filter as follows.

$$x_0(t) = (1.5/N)x(t) + \sum_{r=1}^{N} Fr[x(t+r) + x(t-r)]$$

$$Fr = \cos^2 \tfrac{1}{2}\Omega r \sin(1+\tfrac{1}{2})\Omega r / 2N \sin \tfrac{1}{2}\Omega r, \quad (\Omega = \pi/N)$$

where N=18. The cut-off period of this filter is 2 hours with a half-power point at 4 hours. Fig. 5 shows the amplitude response and cut-off

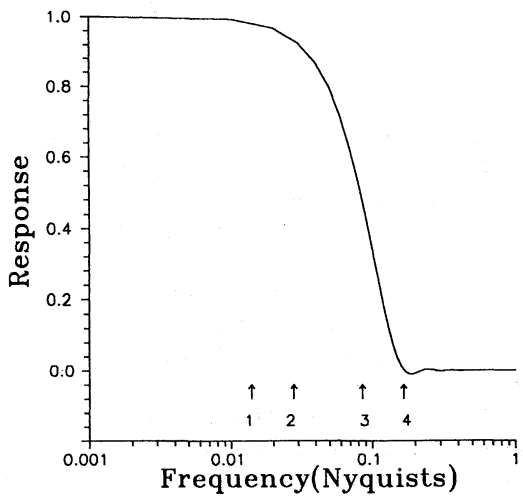

Fig. 5. Frequency response of filter used in analysis : 1. 0.00069 cpm (24 hours), 2. 0.00139 cpm (12hours), 3. half-power point 0.00417cm (4hours), 4. cut-off point 0.00833 cpm (2hours).

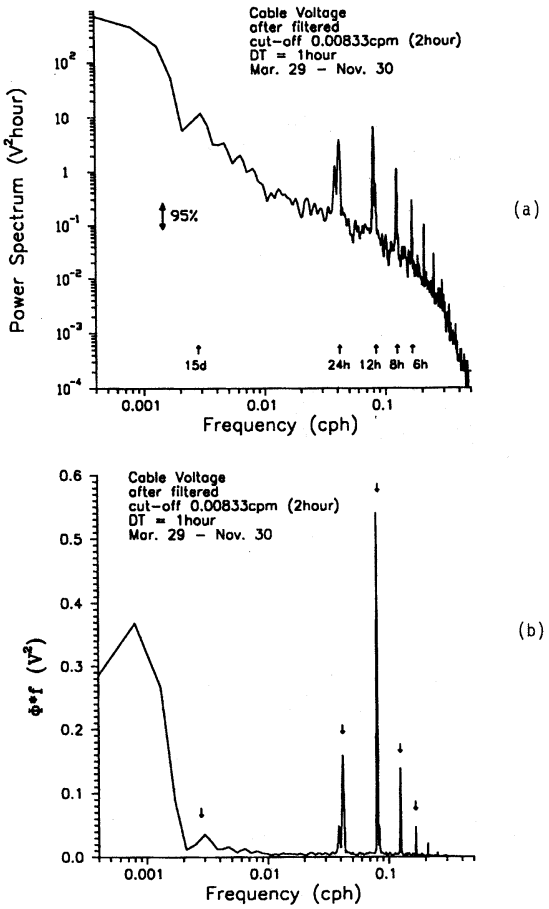

Fig. 6. (a) Spectrum of the hourly low pass cable voltage data, (b) energy conserving spectrum of same data.

frequency. The filtered series are subsampled every hour for final analysis. The example of the subsampled data is shown in Fig. 3 (b).

Fig. 6 (a) is the spectrum of the low pass data and Fig. 6 (b) is energy conserving spectrum of the same data. Most energies are contained in the low frequency with the period longer than about 20 days, with peaks at periods of half a month (0.003 cph), diurnal (0.0416 cph), semi-diurnal (0.0806 cph) and 8 hours (0.1248 cph). All these peaks correspond to tidal frequencies and semi-diurnal component has the highest peak among them. We compare the cable voltage with the north-south component of current measured by RCM7 and sea level changes at Pusan during the same period (May 11 to June 26). Fig. 7 indicates higher frequency voltage fluctuations superposed on a steadily increasing mean value. The fluctuating ranges of the speed and sea level change have a periodicity of about half a month. The spectra (Fig. 8) show that the north-south speed and sea level change also have large energies in the low frequencies and peaks at the same periods as the cable data. It should be noticed that the diurnal peak is higher than semi-diurnal one in the spectrum of the north-south speed unlike those of cable voltage and sea level change. It is speculated that low energy of the current is related to the closeness of the amphidromic point of the semi-diurnal tide to the location of the current meter mooring (Fig. 9; ODAMAKI, 1989).

5. Tidally induced voltage variations

As shown by spectral analysis the tidal components are dominant in the cable voltages as well as the current speed and the sea level changes. Thus we further analyzed the relationship by the harmonic analysis. The hourly values of cable voltage were analyzed in 9 discrete blocks of 29 day duration. The blocks started on the first day of each month from April 1990 to January 1991. The hourly values of the current speed and the sea level change were analyzed in block of 29 days from beginning of the current meter mooring. The analysis was performed using "TIRA" program from Bidston Observatory, IOS (Korea Ocean Research and Development Institute, 1979) which is based on a least squares harmonic method. The close frequency constituents were separated by reference to the values of the constituents of the vertical tides in Pusan.

(a) *Harmonic analysis of cable voltages*

The variation in each month's analysis of cable voltages is shown in Table 1. Table 1(a) represents the amplitude and (b) the phase.

For diurnal constituents while O_1 is consistent from month to month, but the other constituents Q_1, M_1, P_1, K_1 vary markedly. Following PRANDLE and HARRISON (1975), we think that this variation can be attributed to both the difficulty in separating these constituents from 29 day data set and to the electromagnetic tide of solar diurnal periodicity. Amplitudes show that K_1 is the largest and O_1 is the second. Among

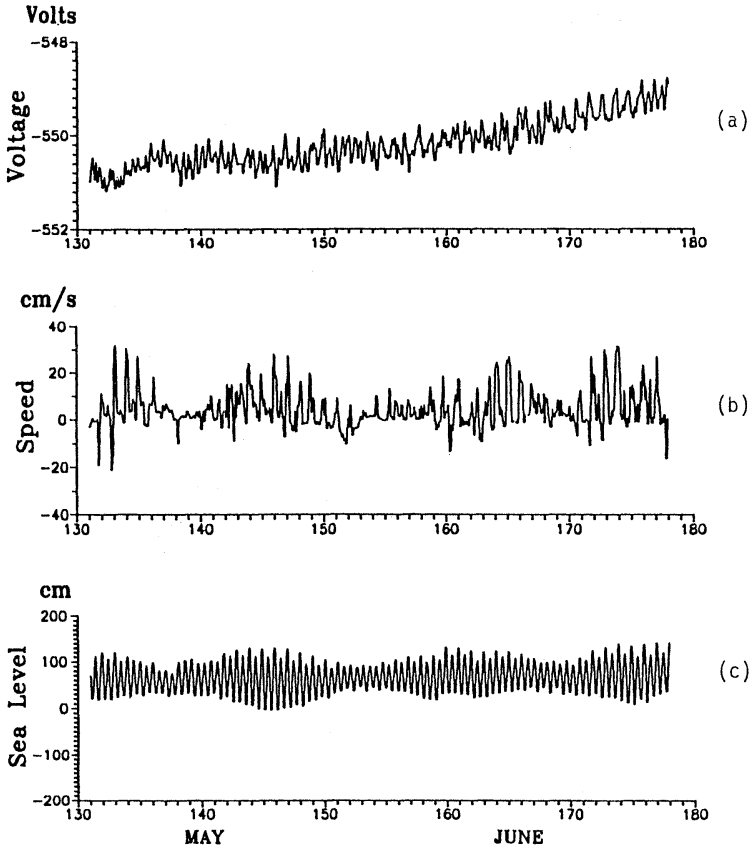

Fig. 7. Time series of (a) the filtered voltage, (b) north-south speed measured by RCM7 and (c) sea level change at Pusan during May 11 to June 26

the semi-diurnal constituents M_2 is the most dominant and consistent in amplitude and phase. The semi-annual fluctuation of the amplitudes of S_2 and K_2 constituents can be interpreted as interference between the two constituents which appears when the analyzed time series is not enough (RIKIISHI, 1982). The ter-diurnal constituents are smaller than semi-diurnal ones and MK_3 is the largest. The quarter-diurnal constituents are relatively small.

A spectral analysis of both hourly voltages and residual voltages was made. Desipite removal of tidal constituents considerable variations remain in the residual. The variations have the energies of about 45 percent of hourly data.

(*b*) *Harmonic analysis of the current speed and sea level change*

Table 2 shows the results of the analysis of current speed, sea level change and cable voltages during the same period.

While the semi-diurnal constituents are larger than diurnal ones in the cable voltages and sea level changes, the semi-diurnal constituents are not larger in the current speed. For diurnal constituents K_1 is the largest, O_1 is the second and P_1 is the third in three records However, for the semi-diurnal constituents S_2 is larger than M_2 in the current speed, while M_2 is larger in cable voltages and sea level changes.

The results of the phase show that in the speed and sea level S_2 tides are about one hour later than M_2, which corresponds to ODAMAKI (1989), but S_2 tide in cable voltage is about 7 hour later. The phase differences between the voltage measurements and speed may occur because the cable

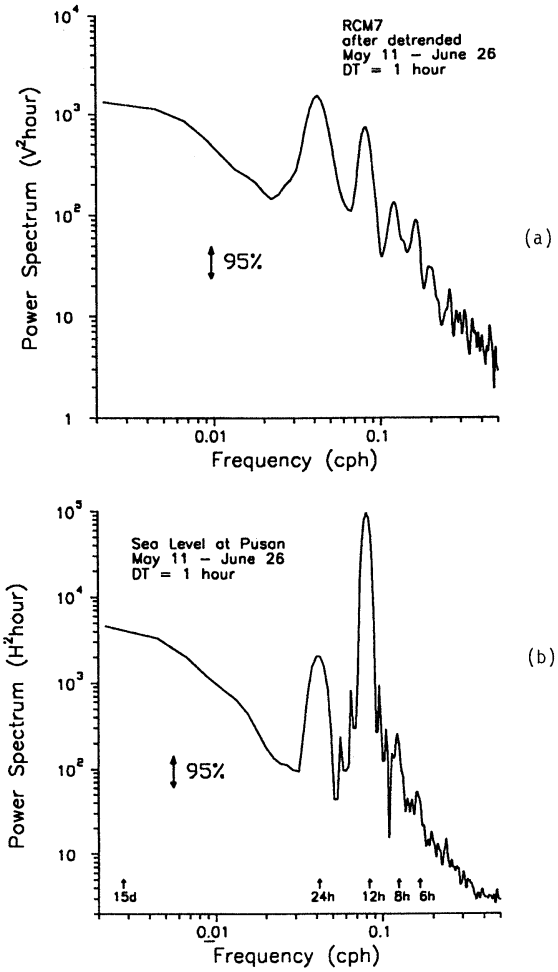

Fig. 8. Spectra of (a) north-south speed and (b) sea level change

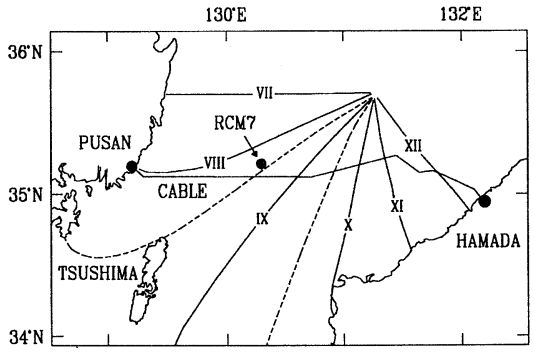

Fig. 9. M_2 tidal chart by ODAMAKI (1989)

voltage represents the integrated transport through the channel while the speed was measured at one point.

(c) *Estimation of the tidal transport*

The amplitude of M_2 transport is about 5.5 Sv according to ODAMAKI (1989) and KANG *et al.* (1991) and the harmonic constant of the cable voltage is 0.154 volts. Therefore the estimation of transport per one volt is 35.95 Sv/volt, which is equal to 105 cm/sec/volt.

According to LONGUET-HIGGINS (1949)

$$e = \delta VZL \times 10^{-8},$$

where $\delta = (1+(\kappa_0/\kappa_1)(L/2D))^{-1}$, κ_0 and κ_1 are the specific conductivities of the channel bed and water and V is depth mean velocity of water along the channel, which is assumed uniform across section. In the Korea Strait region, κ_0

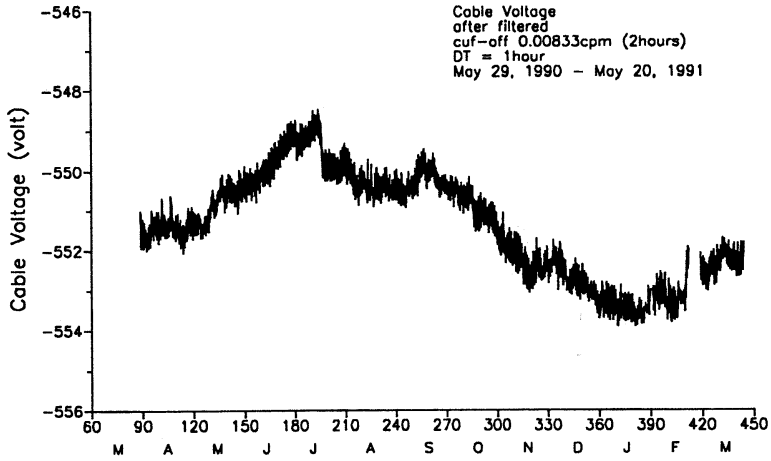

Fig. 10. A time series of the low pass data from Mar. 29, 1990 to Mar. 20, 1991.

Table 1.(a) Harmonic constants of the cable voltages in each month (amplitude).

Constituents		Apr	May	Jun	Jul	Aug	Sep	Oct	Nov	Dec	Jan	Mean	SD
Z_0	0.00	551.445	550.809	549.789	549.516	550.382	550.229	550.998	552.321	552.860	553.410	551.176	1.248
M_M	0.54	0.106	0.482	0.539	0.617	0.066	0.315	0.383	0.284	0.321	0.209	0.332	0.170
M_{SF}	1.02	0.030	0.211	0.291	0.051	0.085	0.031	0.257	0.125	0.236	0.145	0.146	0.092
Q_1	13.40	0.031	0.003	0.038	0.005	0.020	0.013	0.022	0.019	0.023	0.009	0.018	0.011
O_1	13.94	0.045	0.050	0.057	0.058	0.050	0.059	0.064	0.070	0.060	0.046	0.056	0.008
M_1	14.49	0.008	0.012	0.020	0.011	0.002	0.021	0.040	0.020	0.012	0.042	0.019	0.012
P_1	14.96	0.011	0.017	0.033	0.040	0.043	0.040	0.030	0.029	0.015	0.015	0.027	0.011
PI_1	14.92	0.001	0.001	0.003	0.003	0.003	0.003	0.002	0.002	0.001	0.001	0.002	0.001
K_1	15.04	0.033	0.053	0.101	0.121	0.131	0.123	0.093	0.090	0.046	0.045	0.084	0.035
PSI_1	15.08	0.001	0.002	0.004	0.004	0.005	0.005	0.003	0.003	0.002	0.002	0.003	0.001
PHI_1	15.12	0.002	0.003	0.005	0.006	0.007	0.006	0.005	0.005	0.002	0.002	0.002	0.002
J_1	15.59	0.003	0.022	0.029	0.026	0.020	0.035	0.023	0.018	0.016	0.032	0.022	0.009
OO_1	16.14	0.018	0.017	0.007	0.007	0.007	0.009	0.010	0.023	0.011	0.011	0.012	0.005
MU_2	27.97	0.014	0.008	0.000	0.011	0.012	0.020	0.013	0.006	0.027	0.036	0.015	0.010
N_2	28.44	0.037	0.039	0.026	0.038	0.022	0.028	0.035	0.012	0.048	0.038	0.032	0.010
NU_2	28.51	0.006	0.006	0.004	0.006	0.004	0.005	0.006	0.002	0.008	0.006	0.005	0.002
M_2	28.98	0.168	0.140	0.148	0.163	0.140	0.145	0.182	0.175	0.184	0.138	0.158	0.017
L_2	29.53	0.013	0.016	0.007	0.007	0.011	0.022	0.013	0.024	0.014	0.026	0.015	0.006
T_2	29.96	0.004	0.001	0.011	0.006	0.002	0.001	0.002	0.004	0.008	0.001	0.004	0.003
S_2	30.00	0.044	0.011	0.128	0.073	0.019	0.010	0.028	0.049	0.094	0.016	0.047	0.038
K_2	30.08	0.012	0.003	0.035	0.020	0.005	0.003	0.008	0.013	0.026	0.004	0.013	0.010
$2SM_2$	31.02	0.013	0.008	0.013	0.024	0.018	0.015	0.005	0.002	0.008	0.015	0.012	0.006
MO_3	42.93	0.015	0.007	0.011	0.006	0.018	0.001	0.014	0.007	0.004	0.010	0.009	0.005
M_3	43.48	0.009	0.002	0.017	0.007	0.004	0.007	0.004	0.026	0.015	0.006	0.010	0.007
MK_3	44.03	0.017	0.019	0.015	0.012	0.020	0.014	0.014	0.011	0.029	0.010	0.016	0.005
MN_4	57.42	0.004	0.008	0.008	0.004	0.013	0.008	0.014	0.007	0.003	0.003	0.007	0.004
M_4	57.97	0.006	0.008	0.015	0.011	0.013	0.002	0.009	0.009	0.005	0.006	0.008	0.004
SN_4	58.44	0.000	0.012	0.010	0.012	0.003	0.011	0.002	0.009	0.015	0.015	0.009	0.005
MS_4	58.98	0.009	0.008	0.008	0.007	0.010	0.014	0.006	0.014	0.010	0.005	0.009	0.003
$2MN_6$	86.41	0.006	0.001	0.005	0.001	0.007	0.000	0.002	0.005	0.003	0.005	0.004	0.002
M_6	86.95	0.004	0.002	0.003	0.004	0.004	0.007	0.004	0.005	0.004	0.002	0.004	0.001
MSN_6	87.42	0.004	0.006	0.003	0.005	0.003	0.002	0.006	0.004	0.007	0.005	0.005	0.002
$2MS_6$	87.97	0.004	0.003	0.002	0.005	0.006	0.001	0.004	0.004	0.009	0.007	0.005	0.002
$2SM_6$	88.98	0.004	0.010	0.003	0.005	0.012	0.003	0.008	0.004	0.005	0.009	0.006	0.003

$=0.1$ ℧/m and $\kappa_1=5$ ℧/m(UTADA *et al.*, 1986), magnetic intensity $Z=0.485$ Gauss (Korea Institute of Energy and Resources, 1990), $L=281$ km and $D=130$ m. By the relationship from LONGUET-HIGGINS , mean speed per one volt is about 167 cm/sec/volt, which is equal to the transport 57.18 Sv/volt, while 141 cm/sec/volt in the Dover Strait. Thus above simple estimation is thought to be correct in the order of magnitude.

6. Seasonal variation

Fig. 10 is a time series of the low pass data from Mar. 29, 1990 to Mar. 20, 1991. From March the voltage increased and reached a maximum in July and then decreased to a minimum in January. A significant seasonal variation appears with a range of about 5 volts. Nevertheless the seasonal variation does not appear in the voltage records at Hamada during the same period (personal communication). LARSEN

Table 1.(b) Harmonic constants of the cable voltages in each month (phase).

Constituents / Frequency		Apr	May	Jun	Jul	Aug	Sep	Oct	Nov	Dec	Jan	Mean	SD
Z_0	0.00	0.000	0.000	0.000	0.000	0.000	0.000	0.000	0.000	0.000	0.000		
M_M	0.54	7.328	141.405	215.794	63.302	51.011	239.938	190.761	175.845	264.163	205.672	10.748	126.827
M_{SF}	1.02	251.805	251.259	265.395	238.586	146.935	69.183	202.547	233.828	214.321	99.762	35.686	136.665
Q_1	13.40	256.734	141.907	263.699	282.718	283.226	248.052	178.647	279.514	279.937	140.565	66.222	139.246
O_1	13.94	263.050	269.610	256.234	272.107	249.132	300.869	285.522	297.978	293.598	245.767	273.364	19.193
M_1	14.49	171.114	249.354	144.817	12.767	334.968	262.555	17.760	196.436	340.891	76.373	316.426	97.280
P_1	14.96	293.481	266.674	251.797	258.463	239.712	300.691	339.655	349.791	260.475	320.487	287.019	36.704
PI_1	14.92	9.872	343.065	328.188	334.854	316.103	17.082	56.046	66.182	336.866	306.878	353.320	38.694
K_1	15.04	286.891	260.084	245.207	251.873	233.122	294.101	333.065	343.201	253.885	313.897	280.429	36.704
PSI_1	15.08	199.354	172.547	157.670	164.336	145.585	206.564	245.528	255.664	166.348	226.360	12.892	148.242
PHI_1	15.12	308.941	281.134	267.257	273.923	255.172	316.151	355.115	5.251	275.935	335.947	302.363	36.765
J_1	15.59	0.434	317.875	14.555	351.044	6.063	240.921	234.042	36.162	37.650	80.438	0.444	64.384
OO_1	16.14	24.545	240.302	340.888	207.183	225.154	333.156	85.410	80.388	233.239	327.258	303.114	85.290
MU_2	27.97	291.342	101.276	127.601	272.403	54.847	285.035	55.910	91.573	50.211	301.676	34.007	79.689
N_2	28.44	336.729	1.398	301.795	335.032	77.894	331.962	323.545	312.443	347.572	294.578	333.850	38.626
NU_2	28.51	332.053	356.722	297.119	330.356	73.218	327.286	318.869	307.767	342.896	289.902	329.174	38.626
M_2	28.98	2.046	348.851	355.929	359.475	359.640	6.034	10.450	355.720	353.190	4.136	359.546	6.090
L_2	29.53	32.112	117.830	157.555	255.064	84.207	180.607	339.321	274.750	324.020	340.555	336.989	100.893
T_2	29.96	310.931	250.655	147.609	120.896	252.382	15.709	311.439	329.271	284.486	255.562	285.323	77.836
S_2	30.00	314.006	253.730	150.684	123.971	255.382	18.784	314.514	332.346	287.561	258.637	282.417	77.860
K_2	30.08	306.353	246.077	143.031	116.318	255.457	11.131	306.861	324.693	279.908	250.984	284.370	78.258
$2SM_2$	31.02	353.084	175.820	242.359	46.776	247.804	194.174	227.628	98.036	211.729	345.330	13.867	123.839
MO_3	42.93	96.221	5.420	297.738	29.857	156.905	20.354	133.243	270.596	199.227	187.764	353.828	108.930
M_3	43.48	55.469	47.128	26.894	121.125	195.563	34.357	206.059	19.435	328.299	262.296	35.265	77.506
MK_3	44.03	211.279	94.676	137.251	196.655	57.469	232.130	298.747	122.867	315.338	271.474	33.456	129.811
MN_4	57.42	22.248	337.623	158.578	241.196	215.224	40.149	177.907	267.014	35.315	75.328	348.161	97.443
M_4	57.97	234.708	142.418	43.917	309.981	267.669	241.539	41.816	217.588	161.197	285.908	65.585	125.120
SN_4	58.44	100.234	214.400	158.086	343.095	267.698	173.803	304.420	78.307	173.696	150.726	352.464	129.828
MS_4	58.98	289.650	260.802	242.043	330.661	244.035	143.580	353.950	161.155	272.771	1.104	300.275	81.283
$2MN_6$	86.41	342.282	328.921	126.981	278.796	34.290	283.625	49.712	90.814	151.471	235.251	7.498	89.415
M_6	86.95	241.678	92.599	171.084	163.014	48.806	282.664	165.720	120.088	11.456	1.510	301.868	113.216
MSN_6	87.42	283.221	19.178	8.292	154.901	21.769	131.404	147.699	307.323	194.793	326.270	307.768	101.282
$2MS_6$	87.97	207.389	99.470	75.458	167.293	311.697	228.575	14.208	2.596	251.145	29.916	295.124	114.605
$2SM_6$	88.98	273.198	215.270	173.451	312.445	121.962	26.746	7.159	73.250	171.637	114.905	46.590	97.491

(1991) pointed out that the voltage variations observed at a telephone cable station are affected by temperature variations that cause variations in the resistance of the various components of the cable system. Actually, BAHK (1991) found that our voltage output was temperature-dependent. So we improved the recording system to also meaure ambient temperature to calibrate temperature drift.

7. Concluding remarks

An initial attempt to estimate the transport of the Tsushima Current through the Korea Strait using the cable voltage measurements have been performed.

Comparing the cable voltage with current meter observation and coastal sea level suggested that the voltage variation at the Pusan Station is closely related with the movements of the sea water in the Korea Strait, especially

Table 2. Harmonnic constants of the cable voltage, current speeds and sea levels at Pusan during 29 days from May 11, 1990.

Constituents	Frequency	Amplitude			Phase			Amplitude Ratio		Phase Diff.	
		Voltage (*e*)	Current (*V*)	Sea Lev (*H*)	Voltage (*e*)	Current (*V*)	Sea lev (*H*)	*V/e*	*H/e*	*V-e*	*H-e*
Z_0	0.00	550.480	3.630	64.020	0.000	0.000	0.000				
M_M	0.54	0.115	2.396	3.539	290.745	309.906	185.458	15.458	22.832	19.161	−105.287
M_{SF}	1.02	0.141	2.300	2.942	81.600	33.324	291.343	16.312	20.865	−48.276	−150.257
Q_1	13.40	0.008	0.955	0.275	320.497	265.673	79.136	119.375	34.375	−54.824	118.639
O_1	13.94	0.053	2.025	1.853	285.378	128.075	106.563	38.208	34.962	−157.303	−178.815
M_1	14.49	0.006	0.515	0.181	48.093	112.137	172.890	85.833	30.167	64.044	124.797
P_1	14.96	0.025	0.772	1.412	269.074	198.334	145.364	30.880	56.480	−70.740	−123.710
PI_1	14.92	0.002	0.062	0.114	345.465	274.725	221.755	31.000	57.000	−70.739	−123.710
K_1	15.04	0.076	2.370	4.334	262.484	191.744	138.774	31.184	57.026	−70.740	−123.710
PSI_1	15.08	0.003	0.086	0.157	174.947	104.207	51.237	28.667	52.333	−70.740	−123.710
PHI_1	15.12	0.004	0.122	0.222	284.534	213.794	160.824	30.550	55.500	−70.740	−123.710
J_1	15.59	0.032	0.375	0.812	14.728	210.228	219.519	11.719	25.375	195.500	−155.209
OO_1	16.14	0.021	1.356	0.248	265.947	29.292	223.595	64.571	11.810	−236.655	−42.352
MU_2	27.97	0.026	0.476	2.749	102.168	263.142	242.759	18.308	105.731	160.974	140.591
N_2	28.44	0.030	0.376	7.180	335.521	1.766	224.066	12.533	239.333	26.245	−111.455
NU_2	28.51	0.005	0.062	1.178	330.845	357.090	219.390	12.400	235.600	26.245	−111.455
M_2	28.98	0.154	2.095	40.559	348.690	332.211	234.549	13.604	263.370	−16.479	−114.141
L_2	29.53	0.020	0.086	1.175	171.254	347.269	287.264	4.300	58.750	170.015	116.010
T_2	29.96	0.003	0.206	1.508	181.928	3.760	270.078	68.667	502.667	−178.168	88.150
S_2	30.00	0.041	2.480	18.185	185.003	6.835	273.153	60.488	443.537	−178.168	88.150
K_2	30.08	0.011	0.672	4.930	177.350	359.182	265.500	61.091	448.182	−178.168	88.150
$2SM_2$	31.02	0.008	0.979	0.376	74.988	134.603	277.829	122.375	47.000	59.615	202.841
MO_3	42.93	0.003	0.788	0.856	241.969	115.938	54.463	262.667	285.333	−126.031	172.494
M_3	43.48	0.007	0.323	1.060	102.886	127.871	0.411	46.143	151.429	24.985	−102.475
MK_3	44.03	0.013	0.317	1.015	134.132	312.314	51.813	24.385	78.077	178.182	−82.319
MN_4	57.42	0.009	0.285	0.539	176.340	217.066	160.584	31.667	59.889	40.726	−15.756
M_4	57.97	0.009	0.213	0.505	317.104	336.201	171.478	23.667	56.111	19.097	−145.626
SN_4	58.44	0.009	0.479	0.180	179.810	107.670	56.028	53.222	20.000	−72.140	−123.782
MS_4	58.98	0.008	0.435	0.449	300.021	147.591	204.826	54.375	56.125	−152.430	−95.195
$2MN_6$	86.41	0.002	0.209	0.138	104.943	0.541	15.239	104.500	69.000	−104.402	−89.704
M_6	86.95	0.003	0.090	0.079	35.731	27.785	50.015	30.000	26.333	−7.946	14.284
MSN_6	87.42	0.005	0.031	0.227	86.441	21.389	189.139	60.200	45.400	−65.052	102.698
$2MS_6$	87.97	0.003	0.214	0.084	281.934	82.720	35.307	71.333	28.000	160.786	113.373
$2SM_6$	88.98	0.004	0.154	0.013	173.823	323.554	70.204	38.500	3.250	149.731	−103.619

tidal motions. However long-term variations shown in first year observation notably the seasonal variation are not yet to be concluded as oceanic. Therefore responses of data logger to the measuring environment including room temperature are presently being monitored carefully to have better quality of voltage signal for further analysis. The long-term signal also includes seasonal variation of the sea conductivity and geomagnetic flux (BOWDEN, 1956) and corresponding measurements are being planned.

Acknowledgements

Thanks are due to Dr. David PRANDLE and Mr. A. J. HARRISON of Proudman Oceanographic Laboratory, U.K. for valuable advices

during inception of voltage measurement program. We also thank the technical staff of the Pusan Submarine Cable Relay Station for assisting the measurements.

References

ALOCK, G.A. and D.E. CARTWRIGHT (1977): An analysis of 10 year's voltage records from the Dover-Sangatte cable. *In*: Voyage of Discovery (ed. M.V. ANGEL), Deep-Sea Research Supplement to Vol. **24**, 341-366.

BAHK, K. S. (1991): Development of a voltage measuring system for the PusanHamada submarine cable. Journal of Korean Society of Coastal and Ocean Engineers, **3**, 255-260.

BOWDEN, K.F. (1956): The flow of water through the Strait of Dover related to wind and differences in sea level. Phil. Trans. Roy. Soc. London, A, **248**, 517-551.

CARTWRIGHT, D.E. and J. CREASE (1963): A comparison of the geodetic reference levels of England and France by means of the sea surface, Proc. Roy. Soc., **A, 273**, 558-580.

HIDAKA, K. and T. SUZUKI (1950): Secular variation of the Tsushima Current. J. Oceanogr Soc. Japan, **16**, 28-31.

HUGHES, P. (1969): Submarine cable measurements of tidal currents in the Irish Sea. Limnol. Oceanogr., **14**, 269-278.

KANG, S.K., S.-R. LEE and K.-D.YUM (1991): Tidal computation of the East China Sea, the Yellow Sea and the East Sea. *In*: Oceanography of Asian Maginal Seas (ed. K. TAKANO), Elsevier Oceanography Series, **54**, 25-48.

KAWATATE, K., A. TASHIRO, M. ISHIBASHI, T. SHINOZAKI, T. NAGAHAMA, A. KANEKO, S. M IZUNO, J. KOJIMA, T. AOKI, T. ISHIMOTO, B.H. CHOI, K. KIM, T. MIITA and Y. OUCHI (1991): A cross-spectral analysis of small voltage variation in a submarine cable between Hamada and Pusan with speed variation of the Tsushima Warm Current. *In*: Oceanography of Asian Maginal Seas, (ed. K. TAKANO), Elsevier Oceanography Series, **54** 207-222.

Korea Ocean Research and Development Institute (1979): Time series (tidal) data processing system-preliminary report, 59-127.

Korea Institute of Energy and Resources (1990): Total magnetic intensity map. *In*: Submarine geological map of Korean continental shelf (series VII, the Korea Strait) .

LARSEN, J.C. and T.B. SANFORD (1985): Florida Current volume transport from voltage measurements. Science, **227**, 302-304.

LARSEN, J. C. (1991): Transport measurements from in-service underwater telephone cables. IEEE J. Oceanic Engineering, **16**, 313-318.

LONGUET-HIGGINS, M.S. (1949): The electrical and magnetic effect of tidal streams. Monthly Notices of the Royal Astromical Society, Geophysical Supplement. **5**, 285-307.

ODAMAKI, M (1989): Tides and tidal currents in the Tsushima Strait. J. Oceanogr. Soc. Japan, **45**, 65-82.

PRANDLE, D. (1980): Recordings of flow through the Pentland Firth using submarine telephone cables. "Meteo" Forsch-Ergebnisse, Reihe A, No. **22**, 33-42.

PRANDLE, D. and A.J. HARRISON (1975): Relating the potential difference measured on a submarine cable to the flow of water through the Strait of Dover. Sonderdruck aus der Deutschen Hydrographischen Zeit., **28**, 208-226.

RIKIISHI, K. (1982): Tidal analsis of an eqally or randomly spaced record with small number of data samples. J. Oceanogr. Soc. Japan, **38**, 373-384.

ROBINSON, I.S. (1976): A theoretical analysis of the use of submarine cables as electromagnetic oceanographic flow meters. Phil. Trans. Roy. Soc. London, A, **280**, 355-396.

ROBINSON, I.S. (1977): A theoretical model for predicting the voltage response of the Dover Sangatte cable to typical tidal flows. *In*: Voyage of Discovery (ed. M.V. ANGEL), Deep-Sea Research Supplement to Vol. **24**, 367-391.

SANFORD, T.B. and R.E. FLICK (1975): On the relationship between transport and motional electric potentials in broad, shallow currents. J. Mar. Res., **33**, 123-139.

UTADA, H., Y. HAMANO and T. YUKUTAKE (1986): A two-dimensional conductivity model across Central Japan. J. Geomagnetism and Geoelectricity, **38**, 447-473.

WUNSCH, C. (1972): The spectrum from two years to two minutes of temperature fluctuations in the main thermocline at Bermuda. Deep-Sea Res., **19**, 577-593.

YI, S. (1966): Seasonal and secular variations of the water volume transport across the Korea Strait. J. Oceanolog. Soc. Korea, **1**, 7-13.

La mer 30: 169–177, 1992
Société franco-japonaise d'océanographie, Tokyo

Ventilation of the Japan Sea waters in winter

A. S. VASILEV* and V. P. MAKASHIN*

Abstract: The Japan Sea is characterized by the unique vertical homogeneity of waters. A numerical model of the transport stream function was developed. The model was based on a quasi-stationary vorticity equation integrated with depth. The equation includes effects of eddy viscosity and parametrizes mixing processes that are most intensive in the "cold" area. In integrating the equation, the relaxation and run techniques are used. The analysis of mixing processes has been done in the "cold" area of the sea. This area is not directly influenced by warm Tsushima and East Korea Currents. The model results and hydrological data show that wind mixing, winter vertical circulation, large-scale three-dimensional dynamics of waters, and deep convection of the open sea are responsible for ventilation in the upper kilometer of the Japan Sea waters. The minimum concentration of dissolved oxygen in a layer of 1000 to 2000 m is evidently a result of relatively weak ventilation in deep waters. Bottom waters (deeper than 2000 m) are periodically replenished by shelf waters (saturated with the oxygen), sinking down along the continental slope of Primorye. According to estimations of shelf water density, the depth of sinking along the continental slope is controlled by a narrow range of density in the place of formation. This provides an important criterion for ecological monitoring of the bottom layer.

1. Introduction

The Japan Sea is a deep marginal basin, characterized by the limited water exchange with the Pacific Ocean, the East China and the Okhotsk Seas. Numerous results of hydrological measurements during more than half a century invariably confirm the anomalously high concentration of dissolved oxygen throughout all the depths, and vertical homogeneity of waters, most prominent in winter to the north of 41° to 42° N. Suffice it to say, that 84% of sea-water volume is characterized by temperature of 0° to 1° C, salinity of 33.96 to 34.14 ‰, and the concentration of dissolved oxygen of 5 to 7 μlpl (FUKUOKA, 1965; POKUDOV *et al.*, 1976; Sudo, 1986; Stepanov, 1961). These data characterize the mixing intensity of the Japan Sea waters. For all this, by estimations, only an insignificant part of the Pacific Ocean water (inflowing through the Korea Strait) is involved in the exchanging processes (HARADA and TSUNOGAI, 1986).

The downwelling on the periphery of cyclonic gyre and winter vertical circulation (STEPANOV, 1961) have been considered as the main processes of mixing. This can give a complete explanation, in particular, of the Japan Sea homogenization, because these processes take place in the other Far-Eastern seas (FUKUOKA, 1965) as well.

Many scientists have come to a conclusion that water filling the Japan Sea basin is formed in its northwestern part on Primorye shelf, and then sinks along the continental slope (GAMO and HORIBE, 1983; GAMO *et al.*, 1986; NITANI, 1972; SUDO, 1986; ZUENKO, 1989). This process gives a deep convection near the margins (KILLWORTH, 1983).

FUKUOKA and MISUMI (1977) in winter cruises of 1966–1967 found areas of surface waters that sink in the northwestern part of the sea beyond the shelf. These processes apparently look like the results of deep convection in the open sea (KILLWORTH, 1983).

YARICHIN and POKUDOV (1982) proposed a hypothesis that the vertical circulation cells

* Pacific Oceanological Institute, Far-Eastern Branch, Russian Academy of Sciences, Vladivoskok, Russia

exist in the northern part of the sea and are separated by the divergence zones. Main divergence zone lies in the center of the northern deep water basin and is marked by temperature and salinity distribution. But the reason of the vertical circulation remains obscure.

Thus, there are direct and indirect indications of a number of mixing processes. They are developed in the Japan Sea and are different in nature, intensity and scales.

Development of techniques of measuring the oceanological characteristics gives the opportunity to determine fine structure of water in the northern part of the sea that was previously considered almost homogeneous. Under the surface layer which directly interacts with the atmosphere, bounded by the lower boundary, and extremely poorly exposed in winter, the intermediate water mass occurs, bounded at a depth of about 1000 m by a layer of the minimum oxygen content (GAMO *et al.*, 1986). Deep water (1000 to 2000 m) characterized by the exponential decrease of temperature is separated from the well-mixed bottom water by a transitional layer (GAMO and HORIBE, 1983; GAMO *et al.*, 1986). Vertical structure gives the reason why each layer has the individual peculiarities of ventilation.

The authors make primary synthesization of hypotheses on mixing and ventilation of the Japan Sea water, on the basis of analysing its large-scale dynamic structure reproduced (concerning the lack of hydrological data in winter) with the help of the hydrodynamic model. Diagnostic calculations of the Japan Sea water circulation which are known from papers describe, as a rule, its separate elements (KOZLOV, 1971; SEKINE, 1986; YURASOV, 1979). In this study main attention is paid to the processes of mixing in the "cold " sea area which does not undergo the direct influence of warm Tsushima and East Korea Currents. According to the hypotheses, this is just the place where the most intensive mixing processes are developed in winter months.

2. Model and description of data

For calculating spatial evolution of current fields and of density, the authors use quasi-stationary friction model considering surface and bottom boundary layers, known spatial distribution of water density, β-effect, bottom relief, shore outlines and water exchange through the straits.

In developing the theory of diagnostic models the principles of the second generation self-similarity have been used; they give the opportunity to solve the spatial problem as a system of two-dimensional equations relative to some functions of self-similarity.

In this problem the natural self-similarity is used for distribution of sea-water density, which can be expressed as:

$$\begin{aligned}\rho(x,y,z,t) &= \xi(x,y,t)[\sigma(z,t)+d_1 a(x,y,t)(z-h)] \\ &\quad +d_2(z-h)c(t)+\rho^0(x,y,t) \qquad (1)\end{aligned}$$

where $\xi(x,y,t)$ is self-similarity function, $\sigma(z,t)$ stratification function determining the vertical structure of waters and calculated by the observed data, $\rho^0(x,y,t)$ density of sea-water on the surface, $a(x,y,t)$ some adjusting function providing zero mass flux through the bottom at the variable depth of the basin.

$\rho^0(x,y,t)$ is given. $\sigma(z,t)$ and $a(x,y,t)$ are determined before solving the boundary problem. And $\xi(x,y,t)$ should be estimated. $c(t)$ is a regulator of the "frozen" abyssal zone. h_K^D *and* $h_K^{\not d}$ are depths of abyssal zone and of bottom layer of Ekman friction. d_i is Kronecher's symbols with $d_i=0$ for $z<h_K^i$ and $d_i=1$ for $z\geqq h_K^i$.

Using the model (1) and linear form of the horizontal exchange due to water movement, the vector of horizontal velocity (U) is found as a linear combination:

$$\vec{U}=\sum_{i=1}^{i=k}\tilde{B}_i\vec{F}_i, \qquad (2)$$

where $\tilde{B}_i$ are square matrices determined as a result of integrating the equations of motion on the vertical coordinate. The non-linear inertial terms, horizontal and vertical turbulent exchange, variable Coriolis parameter (β-effect) and variable topography of sea bottom are concerned in these matrices. $\vec{F}_i$ is the external parameter of the problem which are related to the dynamics and thermohaline conditions of the

sea-surface and to the self-similarity function. The self-similarity function $\xi(x,y,t)$ is necessary for calculating the spatial distribution of density with the help of Eq. (1). It is determined after solving the equation of stream function (3) given as a result of integrating Eq. (2) on the vertical coordinate.

$$-\frac{\partial \Psi}{\partial \nu}+\Delta \Psi+\delta^{x}_{N1}\frac{\partial^2 \Psi}{\partial x^2}+\delta^{y}_{N1}\frac{\partial^2 \Psi}{\partial y^2}+\mu\frac{\partial \Psi}{\partial x}+\theta\frac{\partial \Psi}{\partial y}=F(\vec{T},\rho^0) \qquad (3)$$

where ν is the relaxation parameter, δ^{x}_{N1}, δ^{y}_{N1}, μ and θ the known integral coefficients, $\vec{T}$ the tangential stress of the wind, ρ the density of water at the surface.

The scheme of solving the problem is as follows. After solving Eq. (3) by a method of relaxation, splitting and run, and after determining the stream function of transport Ψ and the self-similarity function of density $\xi(x,y,t)$, the spatial distribution of currents velocities is determined by using (2), and the spatial distribution of sea water density is determined by (1). For calculations, a uniform grid with spacing of 30' in latitude and longitude and standard vertical coordinate have been used. Estimation of the dynamic influence of the atmosphere upon the sea surface has been performed on the basis of the semi-empirical relationships. Flow rates in the straits and through the sea margins ("liquid" margins) of the region have been determined as a result of calculating the currents with the help of a special model similar to the one considered above. For numerical calculation the "Relaxation Method of Minimum Errors" (MARCHUK, 1974) has been used. Mathematical statement of the problem and description of the model are given in VASILIEV (1988).

The initial fields of temperature and salinity of the sea surface and vertical profiles of hydrophysical characteristics for determination of stratification function are taken from the published oceanographical data on the Japan Sea by the R/V "Priliv" (DVNIGMI) from March 14 till April 4 in 1974 (POKUDOV *et al.*, 1976). During the survey, weak variable winds predominated. This allows us to use mean field of the surface atmospheric pressure for March (Altas of the Oceans, 1974), and to assume stationary regime of real geostrophic currents.

3. Results

The results of modelling the circulation integrated over depth (transport) are given in Fig. 1a. In the northwestern part of the sea, an elongated gyre is distinguished, the northern periphery of which forms the the Primorskoye Current beginning from 44° N. The southern periphery of the gyre is bounded by the East Korea Current. To the northeast of the Yamato Seamount, there is a vast anticyclonic pattern with two gyre centers. In the southern part of the sea, a zone of the divergence is observed from 40° N, 132° E southward. The Tsushima Current proper streaming along the Japan seashore and becoming weak in winter appears in a narrow coastal area. Resulting diagnostic description of the circulation essentially agrees with the general scheme of the Japan Sea circulation (YARICHIN, 1980) deduced by using the "dynamic heights method" (POKUDOV and TUNEGOLOVETS, 1975) and from the satellite data in winter (HUH and SHIM, 1987). The cyclonic gyre of the northwestern part of the sea is absent in some studies on circulation models (KOZLOV, 1971; SEKINE, 1986; YURASOV, 1979). In the present model, the inflow of the Pacific Ocean water through the Korea Strait amounts to 0.63 Sv. This value exceeds the estimate of water transport through the strait in March of 1974 (0.26 Sv) (POKUDOV and TUNOGOLOVETS, 1975). Still, it is close to the mean value for March (0.58 Sv) (LEONOV, 1960). According to this calculation, outflowing transport through the Straits of Tsugaru, La Perouse, and Tatarskiy are: 89%, 8% and 3%, respectively.

An additional numerical experiment aiming at determination of circulation pattern induced by the wind stress and surface heating and cooling has been performed. In this experiment, the gradients of atmospheric pressure three times as large as those of the previous experiment have been considered. This corresponds to the pressure gradients when deep cyclones pass in the northern part of the sea area. The temperature of water surface in the northwestern barotropic part of the sea has been decreased by 0.1 to 1.4 ℃ to such an extent that the density of surface

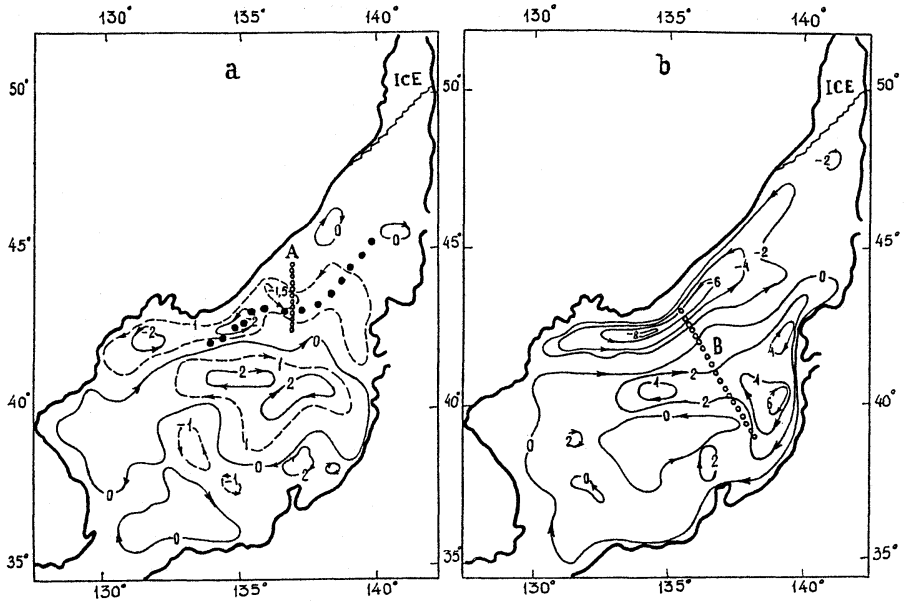

Fig. 1. Stream lines of integral circulation of the Japan Sea water (Sv).
a-average March field of atmospheric pressure is used;
b-atmospheric pressure gradients are increased by a factor of 3.
solid circles - divergence zones
open circles - oceanological sections

water becomes the same as that at 400 m depth. This shows the result of the convective mixing in the whole active layer.

The change in atmospheric pressure field has led to the increase of the maximum velocity of the wind from 6 mps in the initial field to 17 mps (affer data of Vladivostok weather station in March). At the coast the wind of more than 15 mps speed has been observed during 5 to 6 days. So, general intensification of the circulation has taken place. The quasi-stationary cyclonic gyre centered within 42° to 43° N and 134° to 135° E has been formed (Fig. 1b). In the infrared image of the sea surface obtained from the satellite on March 29 in 1979, a vast area of upwelling water characterized by low temperature has been observed exactly at this place (HUH and SHIM, 1987).

4. Discussion

The data on ventilation processes of the Japan Sea waters is presented (Table 1). The results of model calculations are used to explain these processes.

The thickness of surface homogeneous layer mixed by the wind (without considering the convection) was calculated by a previous model (VASILIEV, 1988). With the climatological atmospheric pressure data, thickness of the homogeneous layer is varied from 3 m in the southwestern part of the sea to 33 m near the seashore of Primorye. Increased gradients of the atmospheric pressure simulating storm in the numerical experiment lead to lowering the lower boundary of the mixed layer in the northwestern and northern parts of the sea down to 50 to 100 m. It may be concluded that even during strong winds, direct atmospheric influence does not penetrate deeper than 100 m, thus it restricts the role of wind mixing in ventilation of the lower layers (Table 1, Item 1).

The calculation of scales of the vertical circulation conditioned by winter cooling of the surface and salinity increase during the ice formation was carried out by IZUMI and ISHINO (1985) in the Okhotsk Sea. At the latitude of the La Perouse Strait, vertical scale of the thermohaline convection does not exceed 80 m.

Table 1. Main processes of ventilation of the Japan Sea in winter

Item number	Process	Area of predominant development	Vertical scale (m)	Layer	Source of information	Notes
1.	Wind mixing	in all places	100	surface layer	Vasiliev, Makashin (1990)	authors' calculations of thickness for the mixed layer
2.	Vertical circulation conditioned by winter cooling of the surface layer and salinity increase during ice formation	ice formation in the northern and northwestern parts of the sea	40-80	surface layer	Izumi, Ishino (1985)	estimations for the Okhotsk Sea at the latitude of the La Perouse Strait
3.	Vertical circulation conditioned by the large-scale dynamic structure	divergence zone in the northern part of the sea	1000	surface layer, intermediate layer	Yarichin, Pokudov (1982); Yurasov, Yarichin (1990)	hydrological data
4.	Deep convection of the open sea, intensively influenced by the atmosphere	to the north of latitude 41 °N	200-300	intermediate layer	Fukuoka, Misumi (1977)	hydrological data
5.	Shelf water, sinking along the continental slope (deep convection near the margins)	shelf and slope of the northwestern coast	depends on density of shelf water	bottom layer	Nitani (1972), Gamo et al. (1986)	hypothesis based on analysis of oxygen dynamics of the bottom water

However, this order of magnitude can not be considered as definitive for the Japan Sea. Along with the wind mixing, winter vertical circulation takes part in forming the surface mixed layer (Table 1, Item 2). The vertical circulation modified by large-scale processes (upwelling in the central part of the cyclonic gyre and downwelling in the anticyclone) involves an essentially thick layer of water. Fig. 2 presents dome-like isolines of salinity and dissolved oxygen concentration at a section carried out in March of 1982 (YURASOV and YARICHIN, in press). Disturbance of salinity field (and correspondingly, density field under a condition of more or less uniform temperature) is traced only down to 1000 m. The section intersects the quasi-stationary divergence zone described by YARICHIN and POKUDOV (1982). Coincidence of divergence zone and the quasi-stationary cyclonic gyre presents interesting features of embedded mesoscale eddies (Fig. 1a). It is supposed that the origin of convergence zone and related pattern are associated with the areas of upwelling in the center of cyclonic gyre. By the large-scale vertical circulation, the intermediate layer (up to 1000 m) is also ventilated. Below that layer the dissolved oxygen content reaches the minimum (Table 1, Item 3).

It is known that increased wind stress may lead to mixing of the upper layer with decrease of the buoyancy of that layer and eventually affects convection of the deep layer. Besides, intensified wind stress may cause weakening of stratification in the density field. The process of deep convection in the open sea passes through several phases of its development and is characterized by the hierarchy of scale ranging from the elementary cells to the inner areas of meso-scale cyclonic vortices, of which the scale is determined by the Rossby deformation radius (GASCARD and CLARKE, 1983; KILLWORTH, 1983). Along the section carried out in February

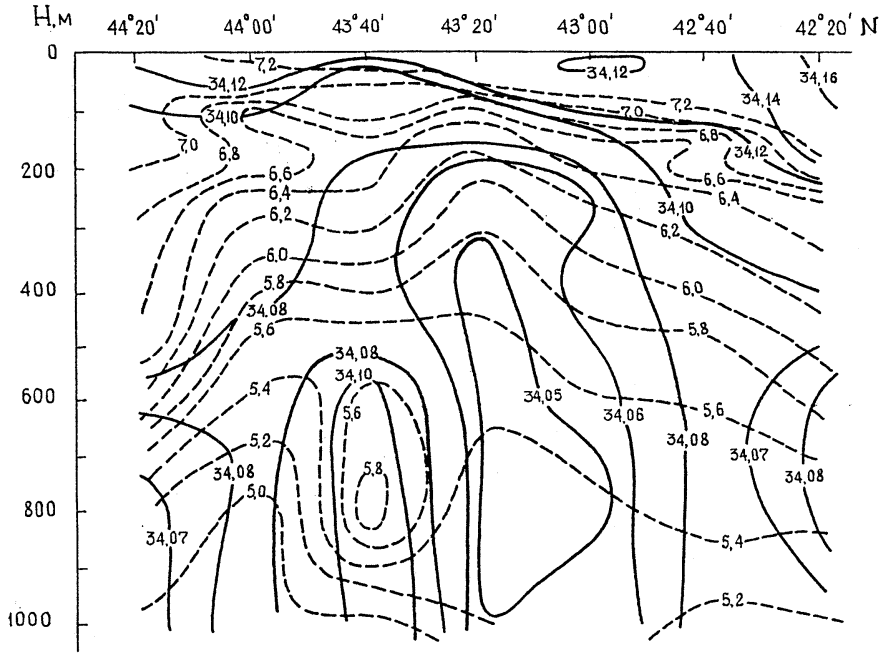

Fig. 2. Vertical section of salinity and concentration of dissolved oxygen in a divergence zone (Fig. 1a-A) in March of 1982 (YURASOV and YARICHIN, in press).
solid line - salinity, ‰; dashed line - dissolved oxygen, μlpl

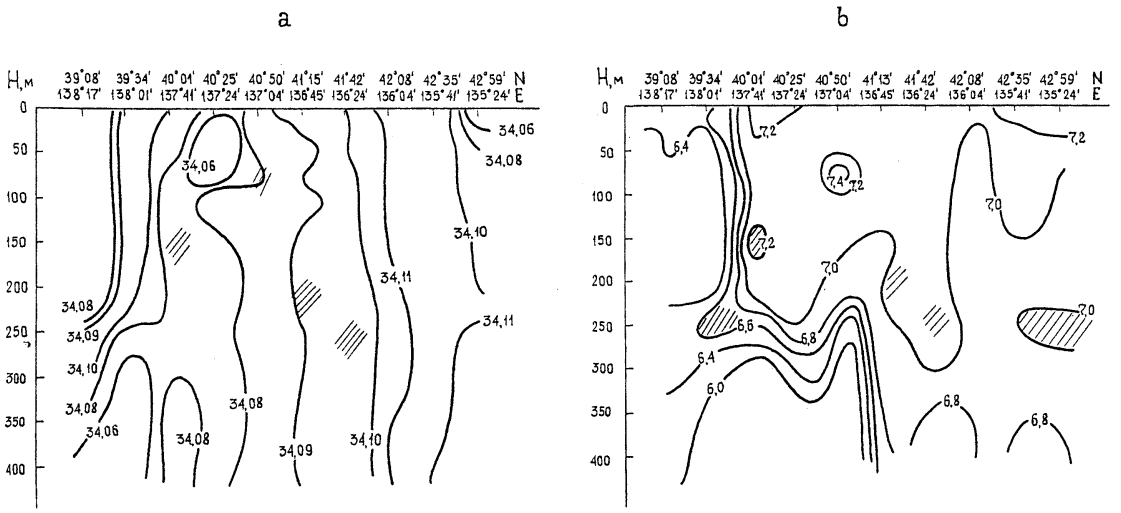

Fig. 3. Vertical section of: a) salinity (‰), b) concentration of dissolved oxygen (lpl) (Fig. 1b-B) in February of 1966. Dashed lines show secondary salinity minimum and oxygen maximum. The depth of extreme occurrences varies from 75 to 250 m (FUKUOKA and MISUMI, 1977).

of 1966 (FUKUOKA and MISUMI, 1977) the near-surface salinity minimum and maximum of dissolved oxygen concentration are lowered at some locations from 50 m to 250 m (Fig. 3b). The data of coastal weather stations indicate that the period of survey of the section was

Table 2. In situ density of the northern basin water of the Japan Sea, and of adiabatically sinking shelf water with different initial characteristics; T and S values of the under-surface layers are taken from Gamo and Horibe (1983) and Ohwada and Tanioka (1972)

Layer	H (m)	Background values			$\sigma_{s,t,p}$ of shelf water	
		in situ T (℃)	S (‰)	$\sigma_{s,t,p}$	T=0.00℃ S=34.00‰	T=−1.86℃ S=34.10‰
Surface layer	0	>0.00	<34.100	<27.380	27.299	27.450
Intermediate layer	500	0.42	34.068	29.686	29.658	29.836
	1000	0.15	34.070	32.036	31.993	32.197
Deep layer	1585	0.15	34.074	34.800	34.760	34.994
	2084	0.17	34.076	37.072	37.022	37.222
Bottom layer	2583	0.20	34.076	39.317	39.272	39.483
	3145	0.26	34.068	41.530	41.498	41.721

preceded by short periods (3 to 5 days) of strong wind with speeds of 20 to 25 mps accompanied by the air temperature drop of 22 to 25℃. Position of the area of surface water sinking coincides with the periphery of the quasi-stationary cyclonic gyre (Fig. 1b-B). These data indicate the presence of the neutral stratification extending to the north of 41° N as a result of accumulated effect of deep convection during previous weeks (Fig. 3b). The temperature range is small and density of the Japan Sea water depends on the salinity. The subsequent development of the vertical process is probably due to the absence of intermediate water mass with anomalous thermohaline characteristics relative to the upper and lower layers. Heavier upper layer density caused by interaction with the surface layer leads to the release of additional potential energy, leading to the convection down to the bottom, as it takes place, for example, in the Mediterranean (Killworth, 1983). In the Japan Sea, deep convection causing sinking and isentropic spreading provides ventilation of the intermediate layer (Table 1, Item 4).

Dissolved oxygen in the well-mixed Japan Sea bottom water (deeper than 2000 m) is mixed into the bottom layer of the oxygen saturated shelf water that sinks along the continental slope of Primorye to the south of 45° N (Table 1, Item 5; Gamo and Horibe, 1983; Gamo *et al.*, 1986; Nitani, 1972; Zuenko, 1989). Therefore, this process may be classified as deep convection near the margins (Killworth, 1983). Indeed, the shelf area including the shelf of the Peter the Great Gulf is a natural source of the cold dense water. Extremely intense ice cover of the gulf leading to salinity increase during a formation period of the permanent ice is an additional source of negative buoyancy. Winter monsoon provides removal of the dense water towards the continental slope. Table 2 gives the background values of in situ density of the northern basin water and corresponding density of the shelf water that sinks adiabatically. Comparison between these values shows that the depth of shelf water penetration is controlled by the small range of temperature and salinity. Their characteristics are determined within this range in winter. At T= 0.00℃ and S = 34.00 ‰, shelf water spreads only in the surface layer. By lowering the temperature to −1.86℃ (freezing point at S = 34.10 ‰), the shelf water may reach to the bottom, when taking account of the density distribution.

The observed exponential temperature change in a deep layer of the Japan Sea (1000 to 2000 m) indirectly confirms that it is formed by sinking of the intermediate layer to the homogeneous bottom layer. Deep layer is the most probable place where the small-scale heat and mass transfer processes develop. Mixing of the bottom layer may be partially initiated by the shelf water injections. Nitani (1972) considered the entering of shelf water into the bottom layer to occur only in severe winters. Studies of the long-period series of freezing dates for Suva Lake

(GORDON *et al.*, 1985; TANAKA and YOSHINO, 1982) lead us to the conclusion that the occurrences of the extremely severe winters in the Japan Sea are at about ten years intervals. Such periodicity is also confirmed by spectral analysis of the time series of the surface water temperature near the western coast of Japan (WATANABE *et al.*, 1986). There is yet no answer to the question of how often shelf water reaches to the bottom. For correctly estimating the volume of bottom water produced above the shelf of Primorye and renewal time of the deep sea layer, special investigations are needed. Only the first steps have been taken to resolve this problem (GAMO and HORIBE, 1983; HAMADA and TSUNOGAI, 1986). At the same time, determination of place of the bottom water formation and of conditions necessary for development of deep convection is the key to the ecological monitoring of the Japan Sea bottom layer.

5. Summary

1. Unique combination of the bottom topography, coastline shape outlines, climatic conditions and large-scale dynamic structure of the northwestern Japan Sea leads to intensive development of the mixing processes (different in nature and scales) responsible for the vertical homogeneity of the sea-water in the Japan Sea.

2. Wind mixing, winter cooling, large-scale vertical circulation and deep convection of the open sea drive the processes of ventilation in the upper kilometer of the Japan Sea waters. Bottom layer is injected by shelf waters sinking mainly along the continental slope of Primorye. Minimum concentration of the dissolved oxygen in a layer of 1000 to 2000 m is probably the result of the relatively weak ventilation of the deep water.

3. The depth of shelf water penetration is controlled by a small range of temperature and salinity at the location of deep water formation, which is important for ecological monitoring of the bottom layer.

References

Atlas of the Oceans (1974): The Pacific Ocean. Moscow, Glavnoye Upravleniye Navigatsii i Okeanografii.

FUKUOKA, J. (1965): Hydrography of the Adjacent Sea. (1) The Circulation in the Japan Sea. J. Oceanogr. Soc. Japan, **21**, 95–102.

FUKUOKA, J. and A. MISUMI (1977): Sinking in the Japan Sea (Preliminary Report). Bull. Fac. Fish. Hokkaido Univ., **28**, 143-153 (in Japanese).

GAMO, T. and Y.HORIBE (1983): Abyssal Circulation in the Japan Sea. J. Oceanogr. Soc. Japan, **39**, 220–230.

GAMO, T., Y. NOZAKI, H. SAKAI, T. NAKAI and H. TSUBOTA (1986): Spatial and Temporal Variations of Water Characteristics in the Japan Sea Bottom Layer. J. Mar. Res., **44**, 781–793.

GASACARD, J. C. and R. A. CLARKE (1983): The Formation of Labrador Sea Water. Part 2: Mesoscale and Smaller-Scale Processes. J. Phys. Oceanogr., **13**, 1779–1797.

GORDON, G. A., J. M. LOUGH, H. C. FRITTS and P. M. KELLY (1985): Comparison of Sea Level Pressure Reconstructions from Western North American Tree Rings with a Proxy Record of Winter Severity in Japan. J. Clim. Appl. Meteorol., **24**, 1219–1224.

HARADA, K. and S. TSUNOGAI (1986): ^{226}Ra in the Japan Sea and the Residence Time of the Japan Sea Water. Earth and Planetary Science Let., **77**, 236–244.

HUH, O. K. and T. SHIM (1987): Satellite Observations of Surface Temperatures and Flow Patterns in Sea of Japan and East China Sea, late March 1979. Remote Sens. Environ., **22**, 379–393.

IZUMI, M. and M. ISHINO (1985): Estimation for the Bottom Depth of the Vertical Convection Layer in the Southern Okhotsk Sea during Cooling Seasons. J. Tokyo Univ. Fish., **72**, 1–11.

KILLWORTH, P. D. (1983): Deep Convection in the World Ocean. Rev. Geophy. and Space Phys., **21**, 1–26.

KOZLOV, V. F. (1971): Approximate Calculation Results of the Integral Circulation in the Japan Sea. Meteorologiya i Gidrologiya, **4**, 57–63. (in Russian).

LEONOV, A. K. (1960): Regional Oceanography. Part I. Leningrad, Gidrometeoizdat, 766 pp. (in Russian).

MARCHUK, G. I. (1974): Numerical solving the problems of the ocean and atmosphere dynamics on the base of splitting methods. Leningrad, Gidrometeoizdat, 303 pp.

NITANI, H. (1972): On the Deep and Bottom Waters in the Japan Sea. *In*: Research in Hydrography and Oceanography. ed. D. SHOJI,

Hydrographic Department of Japan, 151–201.

OHWADA, M. and K. TANIOKA (1972): Cruise Report on the Simultaneous Observation of the Japan Sea in October 1969. Oceanogr. Mag., **23**, 47–58.

POKUDOV, V. V. and V. P. TUNEGOLOVETS (1975): New Scheme of the Japan Sea Winter Currents. Trudy DVNIGMI, **50**, 24–32 (in Russian).

POKUDOV, V. V., A. N. MAN'KO and A. N. KHLUSOV (1976): Peculiarities of the Hydrological Regime of the Japan Sea in Winter. Trudy DVNIGMI, **60**, 74–115 (in Russian).

SEKINE, Y. (1986): Wind-Driven Circulation in the Japan Sea and Its Influence on the Branching of the Tsushima Current. Progr. Oceanogr., **17**, 297–312.

STEPANOV. V. N. (1961, ed.): Main Features of the Japan Sea Geology and Hydrology. Moscow, USSR Academy of Sciences, 224 pp. (in Russian).

SUDO, H. (1986): A Note on the Japan Sea Proper Water. Progr. Oceanogr., **17**, 313–336.

TANAKA, M. and M. YOSHINO (1982): Re-examination of the Climatic Change in Central Japan Based on Freezing Dates of Lake Suwa. Weather, **37**, 252–259.

VASILIEV, A. S. (1988): Monitoring of Main Physical Fields of the Atlantic Tropical Zone, Using the Satellite Data (Decade Discreteness). Deposited in VINITI, May, N 5754-B88, 24 pp. (in Russian).

WATANABE, T., K. HANAWA and Y. TOBA (1986): Analysis of Year-to-Year Variation of Water Temperature along the Coast of the Japan Sea. Progr. Oceanogr., **17**, 337–357.

YARICHIN, V. G. (1980): Standard of Studying Circulation of the Japan Sea Water. Trudy DVNIGMI, **80**, 46–61 (in Russian).

YARICHIN, V. G. and V. V. POKUDOV (1982): Formation of Structural Features of Hydrophysical Fields and Currents in the Northern Deep Water Area of the Japan Sea. Trudy DVNII, **96**, 86–95 (in Russian).

YURASON, G. I. (1979): Investigation of the Threedimentional Circulation in the Japan Sea Water by Numerical Methods. *In*: Gidrofizicheskiye Issledovaniya v Severnoi Chasti Tikhogo Okeana i Dal'nevostochnykh Moryakh. Vladivostok, 83–97 (in Russian).

YURASOV, G. I. and V. G. YARICHIN. Currents of the Japan Sea. Vladivostok, Pacific Oceanological Institute, in press (in Russian).

ZUENKO, Yu. I. (1989): Formation of the Japan Sea Bottom Water on the Shelf of Primorye. Intern. Symp. on the Japan and Okhotsk Seas. USSR, Nakhodka, Sept. 14 to 20, 1989. Theses of the Soviet Participants Repts. Vladivostok, Pacific Oceanolog. Inst., 14 (in Russian).

La mer 30: 179–190, 1992
Société franco-japonaise d'océanographie, Tokyo

An estimation of extreme sea levels in the northern part of the Sea of Japan

Alexander B. RABINOVICH*, Georgy V. SHEVCHENKO*
and Svetlana E. SOKOLOVA*

Abstract: Extreme sea levels arising from combination of tides, storm surges, seasonal sea level variations, and tunamis were estimated for the Russian coasts of the Sea of Japan by the joint probability method. The individual sea level components were studied separately and subsequently their combined effects were considered. The highest extreme elevations were found at the stations De Kastri and Rudnaya Pristan, the lowest ones at the stations Nakhodka and Kholmsk. Several components play the essential role in the different sea areas: tides in the northernmost part of the Tartar Strait, tunamis in the region of Rudnaya Pristan, surges all over the coast. The tunami influence is negligible for short return period but may be important for long return periods.

1. Introduction

The intensive development of coastal areas, the construction of complex and expensive structures (such as nuclear power stations) increase the risk of flooding (or draining) and require the precise estimation of extreme high (or low) sea levels. The variability of sea level near the coast is related to various factors: tides, storm surges, seasonal fluctuations, tsunamis etc. The coincidence of these factors causes abrupt growths of the sea level, as it was observed, for example, on 5 November, 1952 in Severo-Kurilsk, Paramushir Is., where the catastrophic tsunami occurred at the high water of the spring tide (RABINOVICH and SKRIPNIK, 1984). With the enlargement of the time period, the probability of the coincidence of different unfavorable factors increases. It is natural that the relative importance of these factors (sea level components) depends sufficiently on the physical and geographical peculiarities of the specific regions.

The Sea of Japan is a proper object in this respect. Strong tides are observed in the northern part (in the region of the Tartar Strait) and in the south (in the Korean Strait). Devastating storm surges are common for the coastal regions finally. The tragic events due to the tsunami on 26 May, 1983, when more than 100 persons were killed (ABE and ISHII, 1987), have demonstrated a serious danger of this phenomenon for human lives and industrial activities on the coasts of the Sea of Japan. The reliable estimates of extremely high sea levels in this region as result of superposition of different sea level components, and the investigation of their relative role are an interesting scientific theme and also an important applied science problem.

The Gumbel's method based on annual extreme analysis of long observational series is commonly used for estimating maximum and minimum sea level elevations caused by storm surges and tides (for example, LENNON, 1963; GRAFF, 1981; WALDEN *et al.*, 1981; GERMAN and LEVIKOV, 1988). However, this method has limitation to evaluate extreme height which is related to superposition of tides or surges with rare events such as tsunami.

There are other methods devised specially to estimate tsunami risk and to construct tsunami zoning schemes without taking into account other dangerous factors (RASCON and VILLAREAL, 1975; GO *et al.*, 1985). These methods are quite suitable for the regions where tsunami

* Institute of marine Geology and Geophysics, Far East Branch, Russian Academy of Sciences, Yuzhno-Sakhalinsk - 2, 693002, Russian Federation

waves are manifested, being the most important cause of marine flooding (or draining), e. g. for the Pacific coasts of Russia or Japan, but are of little importance for the coastal areas exposed to various disasters of equal worth.

There are only a few attempts to deliberate tsunamis together with other sea level components. GARCIA and HOUSTON (1974) considered statistical effects of the astronomical tide in the prediction of tsunami runup for southern California coast. RABINOVICH and SKRIPNIK (1984) used joint probability method (PUGH and VASSIE, 1978, 1980) to estimate contribution of tsunamis, tides and storm surges to extreme levels for the region of Severo-Kurilsk. The appropriate method based on separate analysis of different sea level components and subsequent combination of their probability functions have been later improved by RABINOVICH and SHEVCHENKO (1990) to analyse the possible flooding on the northeastern coast of Sakhalin Island. The same method is chosen in this paper to evaluate extreme sea levels for the Russian coast of the Sea of Japan and to estimate the relative importance of various factors.

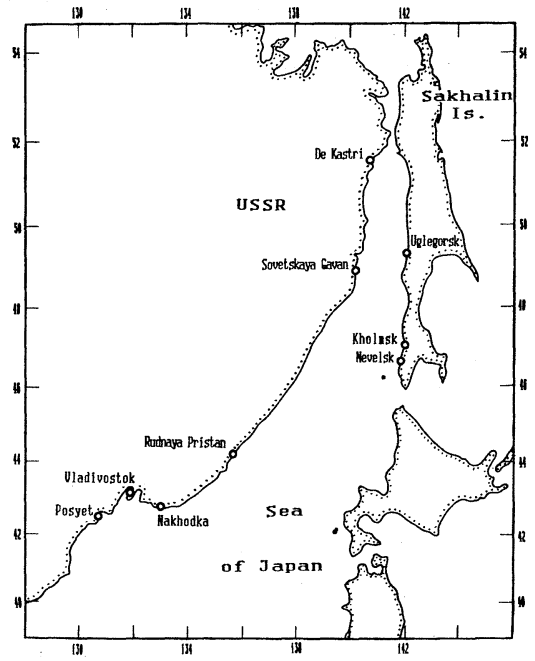

Fig. 1. Location of coastal tidal gauge stations.

2. The analysed data

Hourly tidal gauge values obtained in the World Data Center-B1 Obninsk at 9 coastal stations (Fig. 1) were used for analysis. The lengths of the records varied from 3.8 years for Sovetskaya Gavan to 12 years for Posyet, Nakhodka and Uglegorsk (Table 1). Most of the records were quite complete except for a few gaps when tidal gauges were out of work or had data of low quality. Two and half years were absent in the records of Vladivostok (1 July 1980–31 December, 1982), eight and half months in Rudnaya Pristan (19 December 1985 – 31 August 1986), two months (November–December, 1980) in Sovetskaya Gavan, one month (January, 1983) in Kholmsk, and two weeks in Posyet (1–14 February 1980). All available data carefully edited and corrected were used to estimate probability distributions of tidal and storm surge (non-tidal residual) components. Non-systematic gaps in the data are of no consequence to this kind of analysis (PUGH and VASSIE, 1978).

Time series of monthly mean and maximal sea levels for these stations (Table 1), and data on

Table 1. The list of sea level data.

Stations	Hourly data		Monthly data	
	Duration, years	Period	Duration, years	Period
Posyet	12	1977-88	36	1950–85
Vladivostok	9.5	1977–80, 1983–88	59	1926–45, 1947–85
Nakhodka	12	1977–88	38	1948–85
Rudnaya Pristan	11.4	1977–88	46	1948–79
Sovetskaya Gavan	3.8	1977–80	32	1974–86
De Kastri	11.4	1977–88	13	1974–86
Uglegorsk	12	1977–88	24	1963–86
Kholmsk	11.9	1977–88	40	1974–86
Nevelsk	11	1978–88	37	1974–50, 1954–86

individual storm surges for Vladivostok (1926–1953) and Posyet (1951–1985) completed by FIRSOV (1989) were used to obtain more accurate estimates of extreme sea levels.

3. Methods

The joint probabilty method (JPM) at first was proposed by PUGH and VASSIE (1978, 1980) to investigate combining probability functions of surge and tide, and to estimate extreme sea levels based on relatively short observational series. Similar methods for the same purposes were used also by WALDEN (1982), and RABINOVICH and SKRIPNIK (1986, 1984). RABINOVICH and SHEVCHENKO (1990) improved the method by taking into account tsunamis and other sea level components. Following their work, we describe briefly the philosophy of the method.

Sea level elevation (ζ) at any time (t) may be described as the sum of a few individual components

$$\zeta(t) = Z_0 + \zeta_T(t) + \zeta_S(t) + \zeta_W(t) + \zeta_t(t) \tag{1}$$

where Z_0 is mean level, ζ_T tides, ζ_S seasonal component, ζ_t tsunami, ζ_W meteorologically-induced (storm surge) component, which remains after mean level, tides and seasonal oscillations have been removed from the original records.

An analysis of sea level oscillations in the Sea of Japan made by SOKOLOVA *et al.* (1992) proved that the residual (non-tidal) variations and tides are practically independent, i.e. that the interaction of tides and meteorologically-induced oscillations in this region is weak.

In such a case, probability density P_Σ of oscilations caused by various uncorrelated factors may be represented by

$$P_\Sigma(y) = \int_{-\infty}^{\infty} P_1(x_1) \int_{-\infty}^{\infty} P_2(x_2) \ldots \int_{-\infty}^{\infty} P_{N-1}(x_{N-1}) P_N(y - x_1 - x_2 - \ldots - x_{N-1}) dx_1 dx_2 \ldots dx_{N-1}, \tag{2}$$

where, P_j are the probability density of each type variations, y and x_j are their levels, N is number of components.

Based on Eq. (2) with accounting (1), the probability of the total sea level height h can be expressed as the sum of probabilities of all possible combinations of individual components.

The probability of the sea level exceeding height h is

$$F(h) = \int_h^{\infty} P_\Sigma(\zeta) d\zeta . \tag{3}$$

The corresponding return period may be calculated as

$$T(h) = (nF)^{-1}, \tag{4}$$

where n is a coefficient related to the sampling intervals and duration of corresponding processes approximately equal to a number of independent samples in a year (PUGH and VASSIE, 1980).

Therefore, the problem of estimation of probability function and return period for extreme sea levels can be expressed by the probability densities of individual components.

For evaluating sea level components, it is important to consider their physical process. Tide is a determnistic part; based on 1 year observational series, it is possible to predict hourly tidal levels and extreme high tides for any reasonable periods (ZETLER and FLICK, 1985; WOOD, 1986). Seasonal oscillations are quasideterministic. Their phases and amplitudes may be changed from one year to another but, in general, they are relatively stable. Tidal and seasonal components may be combined. Tsunamis and storm surges are stochastic processes. To estimate their extreme heights it is possible to use double exponential distribution (GUMBEL, 1958; PUGH, 1987) as

$$F(h) = 1 - \exp(-\exp(-Y)), \tag{5}$$

where $Y = a(h - B)$ is the "reduced variate", a and B are the distribution parameters, which may be determined from observations.

An analysis of individual components and their extreme values is a subject of independent interest. That is why we present here only concise description of this analysis as well as estimation of their combination.

4. Tidal analysis and calculation of extreme tidal levels

High quality 1-year time series of hourly data

Table 2. Characteristics of tidal oscillations.

Stations	Form factor	Mean amplitude, cm	h max, cm
Posyet	0.95	11.9	20.4
Vladivostok	0.97	11.8	20.5
Nakhodka	1.08	10.7	18.9
Rudnaya Pristan	1.22	10.2	16.9
Sovetskaya Gavan	0.41	22.9	47.5
De Kastri	0.13	79.2	143.6
Uglegorsk	0.31	30.0	57.3
Kholmsk	1.39	8.8	18.1
Nevelsk	1.91	10.9	22.0

were used for harmonic tidal analysis by least square method. Harmonic constants of 67 constituents were computed for each station. In practice, however, for these sites it is not necessary to estimate all these harmonics for all the stations except De Kastri, because strong tides are observed only in the northern part of the sea. The average amplitude of tides $\bar{H}$ determined as

$$\bar{H} = \left(\sum_{j=1}^{8} H_j^2 \right)^{1/2}, \qquad (6)$$

where H_j are amplitudes of 8 main tidal constituents (Q_1, O_1, P_1, K_1, N_2, M_2, S_2 and K_2), for all southern stations (Posyet, Vladivostok, Nakhodka, Rudnaya Pristan, Nevelsk and Kholmsk (less than 12 cm), and De Kastri (about 80 cm), Table 2).

Using the harmonic constants hourly time series of predicted tides for period of 19 years (1980–1998) were simulated for all stations. Diurnal, semidiurnal and shallow-water tidal harmonics with amplitudes more than 0.5 cm were taken into account. Period of 19 years (more accurately 18.6 years) is a nodal period of tidal harmonics. This interval is necessary for estimation of high tides and correct generation of probability density functions (p. d. f.) (PUGH, 1987). Fig. 2 shows plots of annually extreme high tides and tidal variances for 4 stations: De Kastri, Uglegorsk, Sovetskaya Gavan and Posyet. Plots for all other stations are very similar to Posyet's ones.

Nodal cycle is well seen in variance changes. For northern stations the highest tides correspond to 1980 and 1997–98, the weakest tides to 1987-88; for Posyet and other southern stations

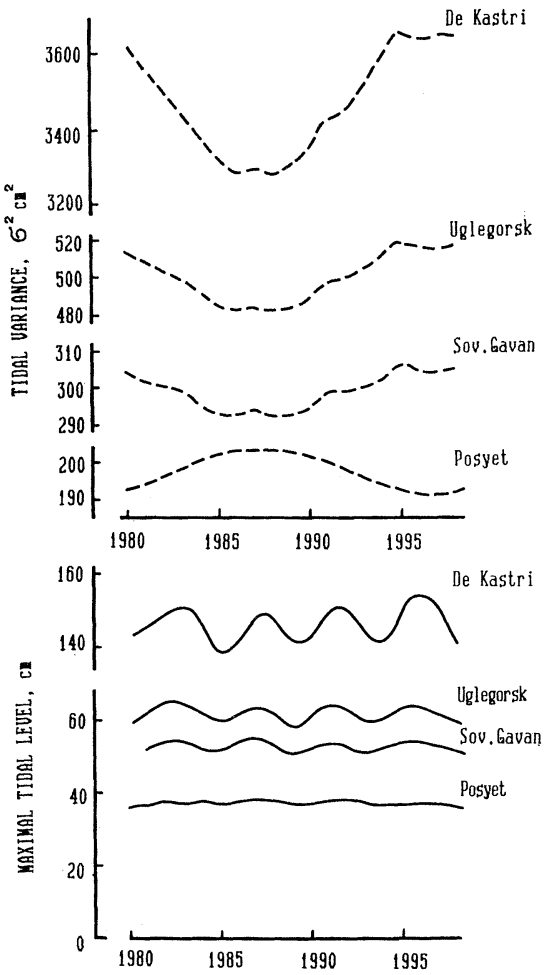

Fig. 2. Interannual variability of tidal variance and maximal tidal level at De Kastri, Uglegorsk, Sovetskaya Gavan and Posyet.

the tidal variance change is out of phase with northern stations. Such a tidal character is connected to a Form factor

$$F = \frac{(H_{K_1} + H_{O_1})}{(H_{M_2} + H_{S_2})}, \qquad (7)$$

indicating relative importance of the diurnal and semidiurnal constituents. Posyet and other southern stations have mixed tidal regime. For Nevelsk and Kholmsk diurnal tides are even prevailed. In contrast with that, in De Kastri, Uglegorsk and Sov. Gavan semidiurnal tides are dominant (Table 2).

The periodicity of annual tidal extreme is very different from the periodicity of variances. The 18.6-year cycle is practically not seen on the

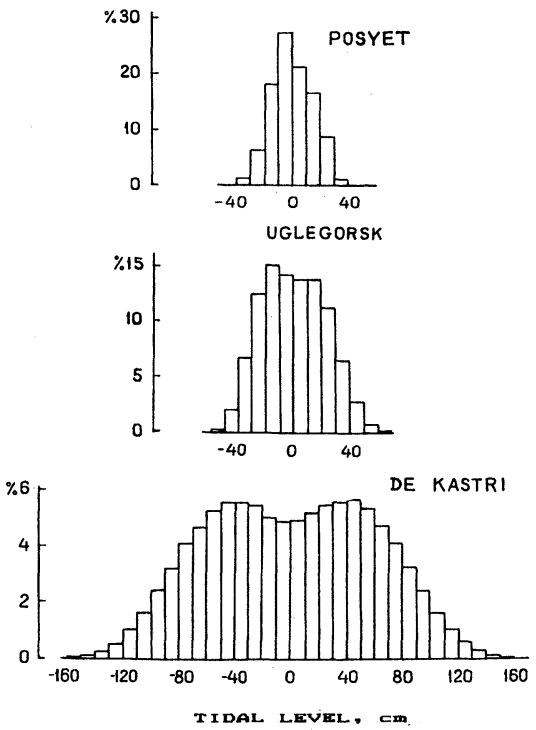

Fig. 3. Probability density distributions of tidal level based on 19-year hourly predictions.

plots but cyclic variability of about 4.4 years appears obviously for northern stations (Fig. 2). These results differ from the estimation of extreme high (and low) tides for Kuril and eastern Sakhalin stations (RABINOVICH and SKRIPNIK, 1986; RABINOVICH and SHEVCHENKO,1990) where only 8.6-year variabilities were strongly manifested. We have provided special tests for De Kastri. It showed that the 4.4-year cycle is caused by K_2 constituent, which has strong nodal anomaly (+0.315) and opposite in phase to that of M_2 and other semidiurnal harmonics.

The computed extreme high tides for all the stations during 1980–98 are presented in Table 2. Computations were done for 90 years (1901–1990) for three northern stations. The difference was less than 0.8 % (142.5 and 143.6 cm for De Kastri, 57.1 and 57.3 cm for Uglegorsk, 47.1 and 47.5 cm for Sov. Gavan). Thus it is not necessary to use so long tidal series in every station for estimation of high tides.

Tidal series for 19 years were used to make up p. d. f. with class interval of 5 cm (Fig. 3). Seasonal harmonics Sa and Ssa (see next section) also included in these calculations. The functions were relatively simple and unimodal for southern stations. They were more complicated and asymmetric for Uglegorsk, Sov. Gavan and intricate bimodal for De Kastri. These tidal p. d. f. were used for further computation of extreme sea level heights.

5. Seasonal variations

Seasonal changes of mean sea level in the Sea of Japan are related with many different factors: long period tides, atmospheric pressure, wind, solar heating, water density, circulation etc. (MIYAZAKI, 1955; GALERKIN, 1960; LISITZIN, 1967; SEKINE, 1991). Due to various reasons and their year-to-year changes, phases and amplitudes of the observed seasonal harmonics Sa and Ssa are more variable from year to year than those of the diurnal or semidiurnal tidal constituents (PUGH, 1987).

The whole series of mean monthly sea levels were used to compute amplitudes and phases of

Table 3. Characteristics of seasonal oscillations of sea level.

Stations	Duration, years	Sa		Ssa		*Fs*
		H, cm	ϕ°	H, cm	ϕ°	
Posyet	36	16.4 (21.1)	205.0	2.5 (7.9)	65.7	6.7
Vladivostok	58	15.1 (21.3)	207.0	1.8 (6.0)	57.9	8.6
Nakhodka	38	12.3 (18.6)	206.9	2.6 (6.6)	43.2	4.7
Rudnaya Pristan	46	9.0 (13.2)	206.2	2.2 (8.0)	57.8	4.2
Sovetskaya Gavan	32	6.7 (10.8)	212.9	0.6 (5.0)	69.7	12.0
De Kastri	13	12.4 (16.0)	205.1	0.4 (5.7)	227.9	30.2
Uglegorsk	24	8.0 (12.4)	218.0	1.1 (6.5)	322.0	7.3
Kholmsk	40	3.9 (7.4)	255.5	3.2 (7.0)	8.4	1.2
Nevelsk	55	3.0 (7.9)	279.4	3.2 (6.9)	8.1	0.9

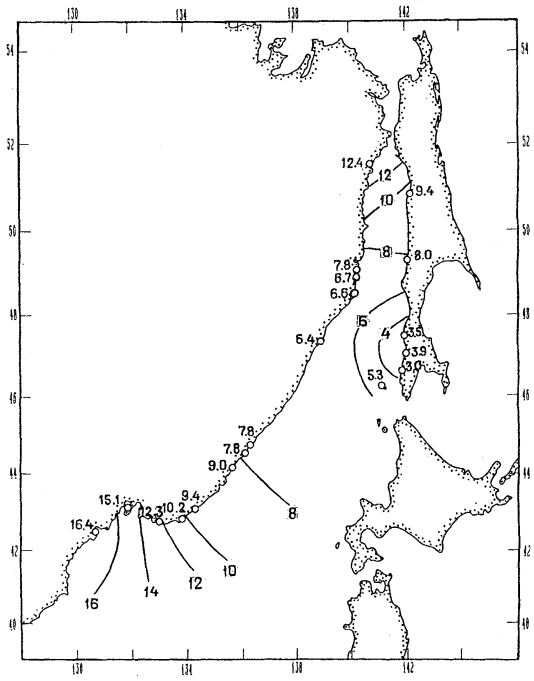

Fig. 4. Amplitudes (in cm) of annual constituent Sa in the northern part of the Sea of Japan.

annual (Sa) and semiannual (Ssa) constituents (Table 3). Individual yearly series were also processed to estimate maximal amplitudes which are presented in brackets. Computed values of seasonal constants are relatively stable and agree well with each other. Phase differences of the annual harmonic for all stations except Nevelsk and Kholmsk are less than 15°. Seasonal Form Factor, similar to those for usual tides

$$F_S = H_{Sa}/H_{Ssa} \qquad (8)$$

is from 4.2 (for Rudnaya Pristan) to 30.2 (for De Kastri), suggesting the seasonal variations have annual character for the greater part of the investigated region with maximum level in July-August and minimum level in January-February. Similar results were obtained also by MIYAZAKI (1955), GALERKIN (1960) and others.

There is an anomaly at the southwestern coasts of Sakhalin, where annual cyclicity is much weaker and semiannual one is stronger than at the other parts of the sea (F_S is 0.9 for Nevelsk and 1.2 for Kholmsk). There are two maxima (stronger one in December-January and weaker one in July-August) and two minima in this region.

A general picture of annual variation of sea level for the region under study is presented in Fig. 4 based on hand water level data. It is well seen that the seasonal oscillations are small in the southern part of the Tartar Strait and increase to the north (De Kastri) and to the south (Vladivostok, Posyet).

Average values of seasonal harmonics were used to calculate probability density functions together with tides. Usually maximal semidiurnal tides are observed during the time of the equinoxes in March and September when the constituents S_2 and K_2 are in the same phase; diurnal (or mixed) tides are enhanced in December–January and in June–July when K_1 and P_1 are in phase (ZETLER and FLICK, 1985). The summer maximum tides are summed up with seasonal maximum, providing total annual sea level maximum at this time.

Differences between average and extreme values of amplitudes are of about 4–6 cm (Table 3). This indicates that for some anomalous years seasonal oscillations may sufficiently exceed their average values. For example, the average value of mean monthly sea level in Vladivostok in August is 16.5 cm, and extreme mean monthly level is 25.3 cm; in Posyet they are 18.4 and 26.0 cm. The total range of extreme seasonal changes (from minimum to maximum) is 49 cm for Posyet and Vladivostok, 35 cm for Uglegorsk and 37 cm for De Kastri. An analysis of these extreme events and their influences on the entire extreme sea levels may be a subject of future study. In any case, results of seasonal variations analysis show that they play an important role in forming sea level elevations in the Sea of Japan and make significant contribution to their extreme heights.

6. Storm surges and meteorologically-induced oscillations.

Storm surges are one of the most widespread and ruinous marine hazards for coastal area of the Sea of Japan. A catalogue of storm surges for the Russian coasts for 1977–88 is elaborated now in IMGG (RABINOVICH and SOKOLOVA, 1991). All extreme sea level elevations related with atmospheric forcings were listed up and

Table 4. Characteristics of storm surges.

Stations	Observed maxima, cm	Frequency		h_{100}, cm
		≫30 cm	≫50 cm	
Posyet	73	1.75	0.17	89 (85)
Vladivostok	69	2.0	0.17	82(78)
Nakhodka	53	2.0	0.17	66
Rud. Pristan	68	3.7	0.75	84
Sov. Gavan	52	4.0	0.25	67
De Kastri	78	6.0	1.10	91
Uglegorsk	74	4.0	0.50	89
Kholmsk	71	3.0	0.10	74
Nevelsk	64	4.3	0.50	81

were used in this paper.

The residual series (after subtracting tides and seasonal variations) were used for analysis. These non-tidal residuals are related to meteorologically-induced sea levels. Storm surges are extreme manifestations of these oscillations; for correct estimates of the probability (or return periods) of high sea levels, it is necessary to take into account not only extreme but also usual meteorologically-induced background by similar way as it was made for tides.

The most important characteristics of natural marine disasters (average number per year) with heights $h \gg 30$ cm (surge phenomenon) and also with $h \gg 50$ cm (strong storm surge) are presented in Table 4.

For southern stations (Posyet, Vladivostok, Nakhodka) there are about 2 surges per year and a strong surge in 6 years. Strong surges occur 4 times more frequently for Rudnaya Pristan and 6 times more for De Kastri. Strong surges for the Sakhalin stations Nevelsk and Uglegorsk are occurred once in 2 years, but for the station Kholmsk located between Uglegorsk and Nevelsk only once in 10 years. This fact is apparently related to some topographical peculiarities of this region.

Gumbel's method was applied to estimate storm surge intensity. Computed values of surge heights (h_{100}) with probability 0.01 (i. e. with return period of 100 years) are given in Table 4.

The accuracy of these values depends on obsevational series length. To improve the estimates, additional information for the stations Vladivostok and Posyet was used. Weekly series of hourly sea level data with storm surges for some previous years (1926–53 for Vladivostok and 1951–1976 for Posyet) compiled by FIRSOV (1989) were cleared up from the tides and the obtained maxima were supplemented to the existing ones. New values of h_{100} for these relatively long series were calculated and given in brackets in Table 4. Small differences (about 4 cm) prove the reliability of the estimates. The decrease of values is apparently caused by possible exclusion of some strong surges which had occurred at low tides.

The residual hourly series for 1977–88 were used to generate p. d. f. as it was made for tides. Fig. 5 contains some typical examples of these distributions. About 100,000 individual sea level values were employed to obtain them. Probability density functions had appearance close to Gaussian function except on both sides of their tails. Results of extreme statistics based on Gumbel's distribution (5) were used to describe the maximal sea level elevations and to supplement actual p. d. f. Then, compound distributions applied in expression (1).

7. Tsunamis in the Sea of Japan

Tsunamis in the Sea of Japan are not so common as for the Pacific coasts. Nevertheless, a number of catastrophic tsunamis were observed in this area, e. g. on 12 May 1701; 2 August 1887; 29/30 August 1741, etc. (SOLOVIEV and GO, 1974). These tsunamis killed thousands of inhabitants and destroyed completely many villages and coastal structures. At least 4 tsunamis affected the Russian coasts of the Sea of Japan in this century: 2 August 1940; 16 June 1964; 1 September 1971 and 26 May 1983 (SOLOVIEV, 1978; SOLOVIEV *et al.*, 1986). All these tsunamis were generated by earthquakes

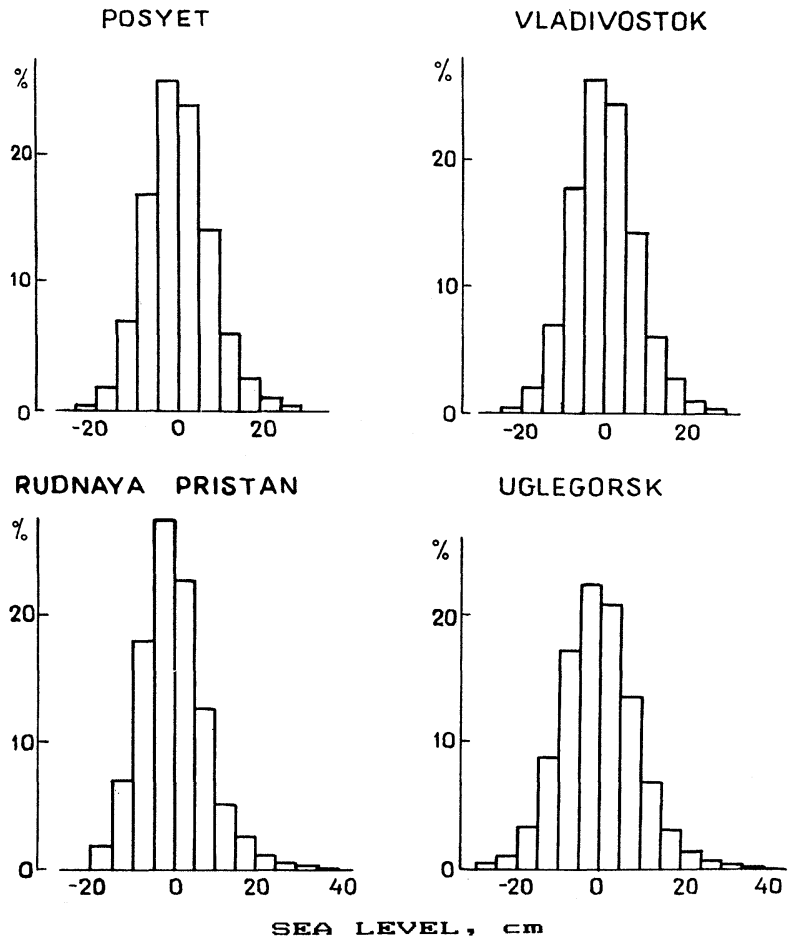

Fig. 5. Probability density distributions of residual (non-tidal) levels.

with epicenters near the coasts of Honshu, Hokkaido or South Sakhalin. In principle, Pacific tsunamis may also penetrate into this area through the Soya Strait as it was for the Chilean Tsunami on 22 May 1960 and for the Urup Tsunami on 13 October 1963 but usually these tsunamis are strongly faded out.

The tsunami on 26 May 1983. strongest tsunami in this century, was more than 10 m hight near the coast of Honshu Island (ABE and ISHII, 1987). Tidal gauge records of this tsunami at the Russian stations are presented in Fig. 6.

An estimation of tsunami risk for the Russian coast of the Sea of Japan was made by GO *et al.* (1984, 1985, 1988). In accordance to this method, the function describing the tsunami recurrence with wave height exceeding 0.1m may be represented as

$$N/T = A \exp(-h/h^*) \qquad (9)$$

for any coastal point. Here, N is the number of tsunamis with wave height $h \gg 0.1$ m recorded in the given point during T years, and A is a coefficient determined by observational data and physical cosiderations. Parameter A represents the frequency of large tsunamis and coefficient h^* characterizes relative amplification of tsunami waves near the coast. It is important that parameter A varies very insignificantly within one region.

The values of parameters A and h^* for the investigated points as well as maximal height of observed tsunamis are presented in Table 5. They are taken from works of GO *et al.* (1984, 1988) and corrected by the authors. Higher values of A for the Sakhalin stations in comparison

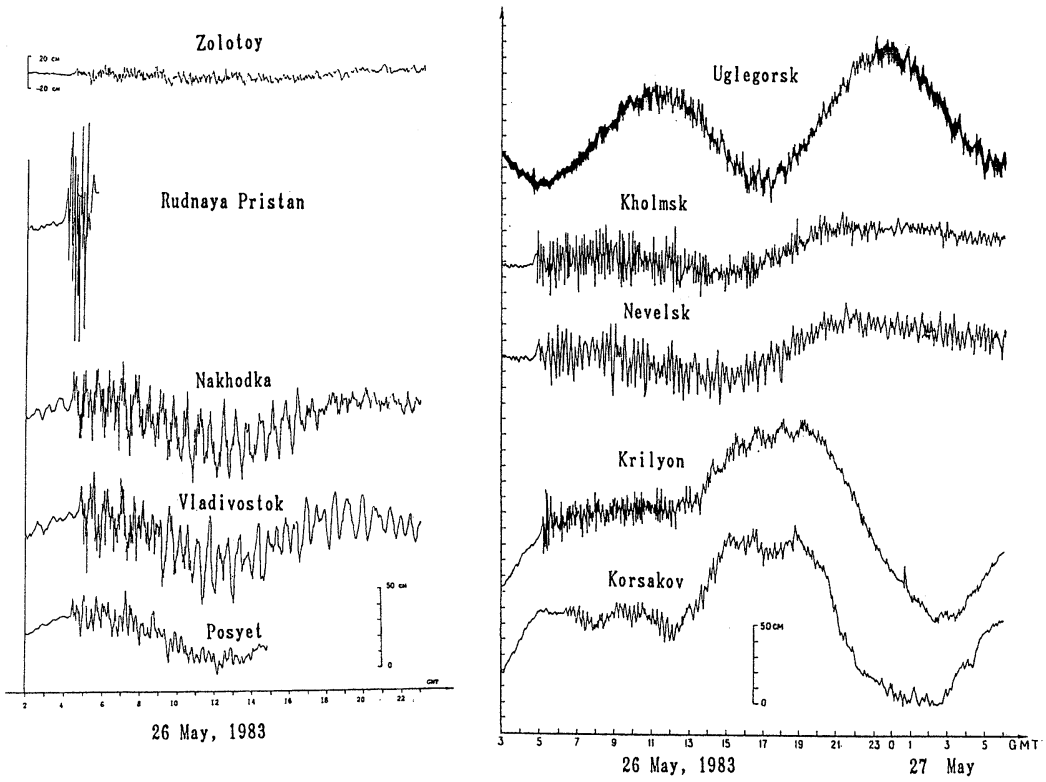

Fig. 6. Tidal gauge records of the tsunami on 26 May 1983 at USSR stations (from Go *et al.*, 1984).

Table 5. Parameters of tsunamis for the Russian coasts of the Sea of Japan.

Stations	Observed maxima, cm	A, year^{-1}	h^*, cm	h_{100}, cm
Posyet	15	0.10	17	40
Vladivostok	33	0.10	43	100
Nakhodka	30	0.10	35	80
Rud.Pristan	100	0.10	75	170
Sov. Gavan	4	?	?	?
Uglegorsk	15	0.18	17	50
Kholmsk	38	0.27	21	70
Nevelsk	50	0.23	25	80

with the continental ones are explained by influence of Pacific tsunamis reaching northeastern part of the sea but not the western coasts.

It follows from expression (9) that the maximum tsunami height for 100 years is proportional to the calibrated wave height h^*:

$$h_{100}=h^*\ln(100\,A) \qquad (10)$$

Calculated h_{100} are also given in Table 5.

To the authors' knowledge, there is only one record of tsunami in Sovetskaya Gavan. The small tsunami with wave height less than 4 cm was caused by the Moneron Earthquake on 1 September 1971 (SCHETNIKOV, 1978). It is not sufficient to estimate tsunami risk for this point.

Tsunami records in De Kastri are absent at all. Apparently tsunami waves have not reached this point.

Estimated values of h^* for most stations are less than 1 m. The exception is Rudnaya Pristan. Relatively strong tsunami waves for this

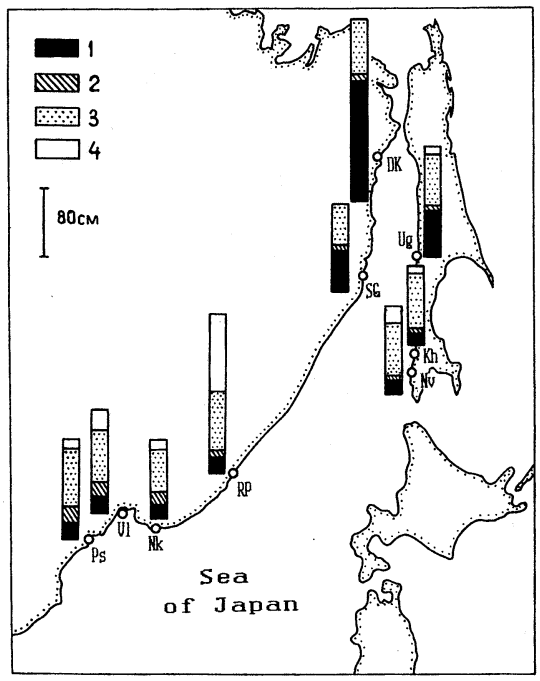

Fig. 7. Extreme sea level heights in the northern part of the Sea of Japan computed by superposition of tides (1), seasonal variations (2), storm surges (3) and tsunamis (4) for the stations Posyet (Ps), Vladivostok (Vl), Nakhodka (Nk), Rudnaya Pristan (RP), Sovetskaya Gavan (SG), De Kastri (DK), Uglegorsk (Ug), Kholmsk (Kh), and Nevelsk (Nv).

station are probably caused by resonance effects. This supposition is confirmed by significant seiche oscillations which are usually observed in the region of Rudnaya Pristan (FIRSOV, 1989).

Tsunami sequence in the area has approximately Poisson's character (GO *et al.*, 1985, 1988). The probability of tsunami height during T years will never exceed the value expressed by the formula

$$P(h,T)=\exp(A\exp(-h/h^*)). \qquad (11)$$

Expression (11) was used to calculate possible superposition of tsunamis with other sea level components and to estimate total extreme sea level elevations caused by various factors in accordance to (1). Results are presented in Fig.7 and Table 6.

8. Summary and discussion

Joint probability method allows us to produce realistic estimates of extreme sea levels based on relatively short observational series and to take into account several different factors.

Absolute estimates of total maximal levels for various stations at the Russian coast of the Sea of Japan with a return period of 100 years (Table 6) is one of the main results of this study. Specifically, it was found that the highest sea level elevations are related to De Kastri and Rudnaya Pristan, and the lowest ones to Nakhodka and Kholmsk.

Another interesting and new result is an estimation of extreme heights and relative importance of individual sea level components. Different components were shown to play essential role different parts of the sea: tides are especially strong in the northern part of the Tartar Strait, tsunami is the most dangerous factor in the region of Rudnaya Pristann, and surges have similar heights all over the Russian coasts of the Sea of Japan.

Table 6. Predicted maximal sea level heights by tides, seasonal oscillation, surge and tsunami (accumulated height).

Stations	Predicted level h_{100}, cm			
	Tides	+seasonal	+surge	+tsunami
Posyet	20	39	106(101)	116
Vladivostok	21	37	97(93)	119
Nakhodka	19	33	81	94
Rudnaya Pristan	17	28	93	185
Sovetskaya Gavan	48	54	102	?
De Kastri	144	151	216	216
Uglegorsk	57	63	123	133
Kholmsk	18	22	87	95
Nevelsk	22	26	85	97

Table 7. Extreme sea level estimated without (upper row) and with (lower row) consideration of tsunami waves

Stations	Return periods, years			
	10	25	50	100
Nevelsk	74	79	82	85
	80	85	90	97
Rudnaya Pristan	82	86	89	93
	94	104	135	185

Furthermore, subsequent contribution of various factors in total extreme sea level heights was also described (Fig.7). It is important to note that tsunamis have proved to be secondary factor for recurrency 1/100 years for all the stations except Rudnaya Pristan. It is clear that the probability of coincidence of two random dangerous factors, strong surge and tsunami, is small for short periods but may increase drastically with increase of return periods. An influence of tsunami waves on estimates of maximal sea level heights for different return periods is illustrated in Table 7. The additional increase of the total extreme sea level due to the tsunamis is only 6 cm for Nevelsk and 12 cm for Rudnaya Pristan for $T = 10$ years, but 12 and 92 cm for $T = 100$ years. Therefore, for short periods, the extreme heights are determined by tides, surges, and seasonal oscillations for all stations; for longer periods, tsunamis may play an essential role in forming extreme levels.

It would be interesting to verify the estimates with more complete observational data. Another question is inclusion of additional factors (e. g. seiches) and an estimation of extreme sea level oscillations together with wind waves.

Acknowlegments

The authors would like to thank Dr. Pavel B. FIRSOV for his generous contribution of monthly sea level data as well as storm surges data in Vladivostok and Posyet. We appreciate Roalt N. MANSUROV (IMGG)'s assistance in analysis of seasonal variations. We also express our sincere thanks to Prof. Kuh KIM of Seoul National University for his helpful remarks and valuable suggestions.

References

ABE, K. and H. ISHII (1987): Distribution of maximum water levels due to the Japan Sea Tsunami on 26 May 1983. J. Oceanogr. Soc. Japan, **43**, 169–182.

FIRSON, P. B. (1989): Mean, maximal and minimal monthly sea levels for the USSR stations in the Sea of Japan. Unpublished manuscript. Vladivostok: Far Eastern Hydrometeorological Research Institute (in Russian).

GALERKIN, L. I. (1960): On the physical grounds for the prediction of the seasonal sea level variations in the Japan Sea. *In*: Longterm Hydrometeorological Forecasts. Proc. Inst. Oceanol., USSR Acad. Sci., **37**, 73–91 (in Russian).

GARCIA, A. W. and J. R. HOUSTON (1974): Tsunami runup predictions for southern California coastal communities, USA. Proc. IUGG Conf. Tsunamis and Tsunami Research. Wellington, Roy. Soc. New Zealand, Bull. **15**, 5–17.

GERMAN, V.H. and S.P. LEVIKOV (1988): Probabilistic Analysis and Models of Sea Level Variations. Leningrad: Gidrometeoizdat, 231 pp. (in Russian).

GO, C. N., V. M. KAISTRENKO and K.V. SIMONOV (1984): Preliminary data on tsunami risk for the coast of the Sea of Japan. *In*: Nonstationary Longwave Processes on the Shelf of Kuril Islands. Vladivostok: FEB USSR Academy of Sciences, 138–141 (in Russian).

GO, C. N., V. M. KAISTRENKO and K.V. SIMOMOV (1985): A two-parameter scheme for tsunami hazard zoning. Mar. Geod., **9**, 469–476.

GO. C. N., V. M. KAISTRENKO, E.N. PELINOVSKY and K.V. SIMONOV (1988): A quantitative estimation of tsunami hazard and the tsunami zoning scheme of the Pacific coast of the USSR. Pacific Annual, Vladivostok: USSR Acad. Sci., Far Eastern Branch, 7–15.

GRAFF, J. (1981): An investigation of the frequency distributions of annual sea level maxima at ports around Great Britain. Estuarine, Coastal and Shelf Science, **12**, 389–449.

GUMBEL, E. J. (1958): Statistics of Extremes. New

York: Columbia University Press, 375 pp.

LENNON, G. W. (1963): A frequency investigation of abnormally high tidal levels at certain west coast ports. Proc. Inst. Civil Eng., **25**, 451–484.

LISITZIN, E. (1967): Sea level variations in the Sea of Japan. The International Hydrog. Rev., **44** (**2**), 11–22.

MIYAZAKI, M. (1955): Seasonal variations of the sea level along the Japanese coasts. Rec. Oceanogr. Works in Japan, **2** (3), 1–8.

PUGH, D. T. (1987): Tides, Surges and Mean Sea-Level. Chichester: J.Wiley, 472 pp.

PUGH, D. T. and J. M. VASSIE, (1978): Extreme sea levels from tide and surge probability. 16th Coastal Eng. Conf., Hamburg, 911–930.

PUGH, D. T. and J. M. VASSIE, (1980): Application of the joint probability method for extreme sea level computations. Proc. Inst. of Civil Eng., **69** (**2**), 959–975.

RABINOVICH, A. B. and G. V. SHEVCHNKO (1990): Estimation of extreme sea-level heights as the superposition of tides, storm surges and tsunamis. Summary. In: Tsunamis: Their Science and Hazard mitigation. Proceedings of the International Tsunami Symposium, July 31 - August 3, 1989. Novosibirsk, 201–205.

RABINOVICH, A. B. and A. V. SKRIPNIK (1984): Consideration of tidal and meteorological sea-level oscillations in estimates of tsunami-risk in the region of Severo-Kurilsk. *In*: Nonstationary Longwave Processes on the Shelf of Kuril Islands. Vladivostok: FEB USSR Academy of Sciences, 81–92 (in Russian).

RABINOVICH, A. B. and A. V. SKRIPNIK (1986): Probability estimates of extreme weather and tidal fluctuations of sea level in the Kuril region. Soviet Meteorol. and Hydrol., **4**, 63–68.

RABINOVICH, A. B. and S. E. SOKOLOVA (1992): On organizing a catalogue of storm surges for the Sea of Japan. Natural Hazards, **5** (**1**).

RASCON, O. A. and A. G. VILLAREAL (1975): On a stochastic model to estimate tsunami risk. J. Hydr. Res., **13**, 383-403.

SCHETNIKOV, N. A. (1978): The tsunami caused by the Moneron Earthquake, 1971. *In*: Tsunami Research in the Open Ocean, Moscow: Nauka Publ. House, 137–144 (in Russian).

SEKINE, Y. (1991): A numerical experiment on the seasonal variation of the oceanic circulation in the Japan Sea. *In*: Oceanography of Asian Marginal Seas, Elsevier Oceanography Series, **54**. Amsterdam, 113–128.

SOKOLOVA, S. E., A. B. RABINOVICH and K. S. CHU (1992): On the atmosphere-induced sea level variations along the western coast of the Sea of Japan. Lamer, **30**, 191–212.

SOLOVIEV, S. L. (1978): Principal data on tsunamis for the Pacific coast of the USSR, 1937-1976. *In*: Tsunami Research in the Open Ocean, Moscow: Nauka Publ.House, 61–136 (in Russian).

SOLOVIEV, S. L. and C.N. GO (1974): Catalogue of Tsunamis on the Western Shore of the Pacific Ocean. Moscow: Nauka Publ. House 310 pp. (in Russian; English translation in Fish. Aqua. Sci., 1984, Ottawa, Canada, No 5078).

SOLOVIEV, S. L., C. N. GO and KH. S. KIM (1986): Catalog of tsunamis in the Pacific, 1969-1982. USSR Acad. Sci., Soviet Geophy. Com., Moscow, 164 pp. (in Russian).

WALDEN, A. T., P. PRESCOTT and N. B. WEBBER (1981): Some important considerations in the analysis of annual maximum sea-levels. Coastal Eng., **4**, 335–342.

WALDEN, A. T., P. PRESCOTT and N. B. WEBBER (1982): An alternative approach to the joint probability method for extreme high sea level computations. Coastal Eng., **6**, 71-82.

WOOD F. J. (1986): Tidal Dynamics. Coastal Flooding and Cycles of Gravitational Force. Dordrecht: D. Reidel, 558 pp.

ZETLER, B. D. and R. E. FLICK (1985): Predicted extreme high tides for mixed-tide regimes. J. Phys. Oceanogr., **15** , 357–359.

La mer 30: 191–212, 1992
Société franco-japonaise d'océanographie, Tokyo

On the atmosphere-induced sea level variations along the western coast of the Sea of Japan

Svetlana E. SOKOLOVA*, Alexander B. RABINOVICH*
and Kyo Sung CHU**

Abstract: Simultaneous 3-month observational series (July - September, 1986) of sea level, atmospheric pressure and wind stress were used to investigate atmosphere-induced sea level variations along the Korean and USSR coasts of the Sea of Japan. Multi-input system spectral analysis and multiple regression analysis were applied to examine the data. An amount of 46 to 77 % of the total sea level energy was found to be coherent with atmospheric pressure and 5 to 37 % with additional influence of wind stress. The barometric factor for the period under study was changed gradually northward from −0.67 cm/mb for the southernmost station Sogwipo to −1.50 cm/mb for the northernmost station De Kastri. Influence of wind waves on mean sea level was studied for the stations Muko (Mugho) and Ulsan. It was found that wave set-up may sufficiently increase storm surge heights. The storm surge caused by the typhoon No 8613 "VERA" was examined in detail. Main parameters of this surge such as 'surge height', 'duration', 'steepness', 'variance', 'pressure factor' as well as meteorological characteristics in time of the storm surge were estimated for all 15 stations. Hindcasting of the surge by multiple regression equations gave quite satisfactory results. Non-linear interaction of storm surges and tides was also studied but found to have small effect.

1. Introduction

The Northwest Pacific is a region of high atmospheric activity. Annual number of typhoons is about one-third of the total world amount (AOKI, 1985). A great number of typhoons and severe extra-tropical cyclones pass over the Sea of Japan and have an influence on sea level variations. Deep atmospheric depressions accompanied by strong winds create extreme sea levels in this region. Storm surges cause heavy floods at the coastal areas with significant destructions and people sacrifices. To mitigate possible damages it is important to explore weather-induced sea level variations and their extreme manifestations.

Investigations of storm surges and sea level response to atmospheric disturbances for the northwestern part of the Pacific were carried out by many scientists. In particular, the region of Kuril Islands has been studied in detail at the Institute of Marine Geology and Geophysics (IMGG) (LAPPO *et al.*, 1978; LIKHAEVA and SKRIPNIK, 1981; LIKHACHVA, 1984; LIKHACHEVA and RABINOVICH, 1986b; SKRIPNIK and SOKOLOVA, 1990). This region as a boundary between the Pacific Ocean and the marginal Sea of Okhotsk is an area of great interest from scientific point of view, but Kuril Islands are populated sparsely. Therefore the practical importance of these works is limited.

On the contrary, the population density around the Sea of Japan is very high. Many complex and expensive constructions were made here in the recent years; that is why appropriate research of the region has the significant meaning. At the same time it would be interesting to compare forming mechanism of sea level variations at the Sea of Japan coasts and at the coasts of Kuril Islands, because the two regions have very different physical and geographycal conditions: the Sea of Japan is practically

* Institute of Marine Geology and Geophysics, Far East Branch, Russian Academy of Sciences, Yuzhno-Sakhalinsk-2, 693002 Russian Federation.
** Korea Ocean Science & Engineering Corp., 175-9, Huam-Dong, Yongsan-Gu, Seoul 140-190, Korea.

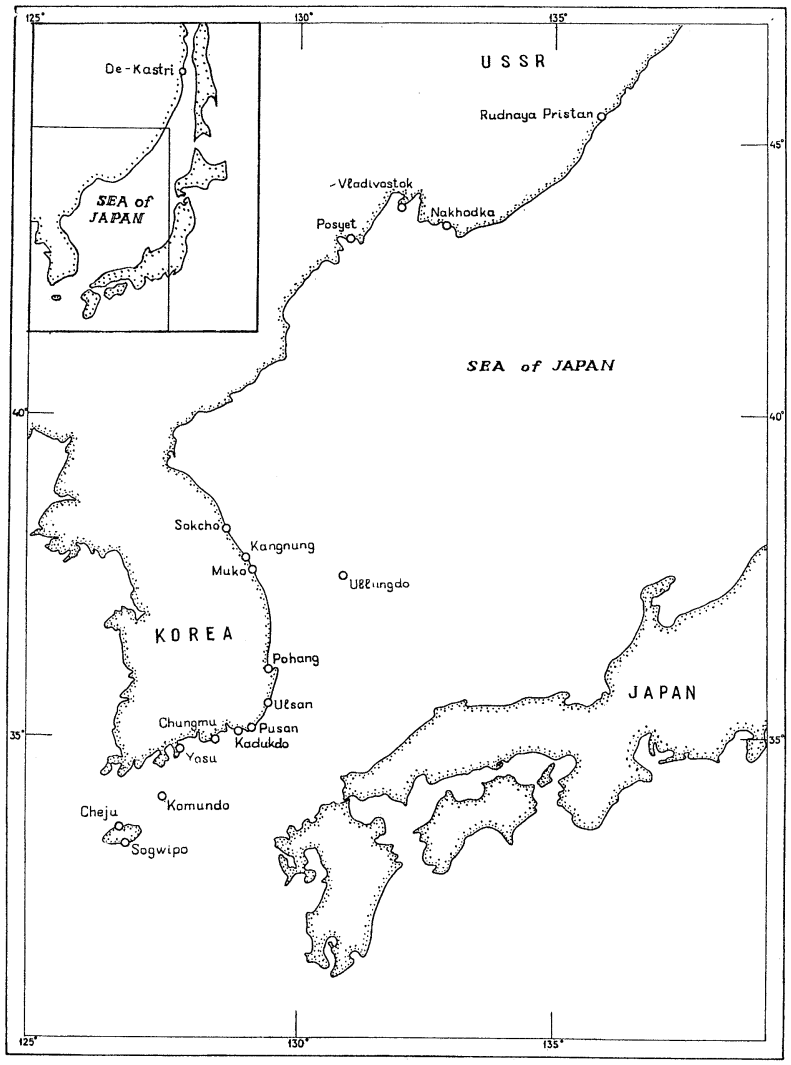

Fig. 1. Location of the coastal stations.

closed; the Pacific coast of the Kurils is open and has a narrow shelf with steep slope.

Sea level variability near the east (Japanese) coast of the Sea of Japan was investigated thoroughly by UNOKI (1959), ISOZAKI (1968, 1969) and other Japanese scientists. However, for the west (Russian and Korean) coasts this subject has been studied only fragmentarily. FIRSOV (1988) has analysed observed data to construct an empirical model of storm surges for the northwestern part of the Sea of Japan. The storm surges on the Korean coasts (first of all for the region of the Korea Strait) have been inspected by data analysis (HWANG, 1971; CHU, 1987; OH *et al.*, 1988) and by numerical modelling (KANG, 1988; OH and KIM, 1990).

The main purpose of this study was investigation of low-frequency (1–20 days) sea level variations on the Russian and Korean coasts of the Sea of Japan and estimation of their generating mechanism in different regions based on hydrometeorological data.

Typhoons are the main cause of strong storm surges at the coasts of the Sea of Japan. As it was shown by KANG *et al.* (1988), 240 out of 259 typhoons for the period 1904–1987 occurred

Table 1. The list of observational data.

Stations	Sea level			Atm. pressure			Wind			Wind waves		
	J	A	S	J	A	S	J	A	S	J	A	S
Sogwipo	1	1	1	3	3	3	1	1	1	*	*	*
Cheju	1	1	1	3	3	3	1	1	1	*	*	*
Komundo	1	1	1	—	—	—	—	—	—	—	—	—
Yosu	1	1	1	3	3	3	1	1	1	*	*	*
Chungmu	1	1	1	3	3	3	1	1	1	—	—	—
Kadukdo	1	1	1	—	—	—	—	—	—	—	—	—
Pusan	1	1	1	3	3	3	1	1	1	*	*	*
Pohang	1	1	1	3	3	3	1	1	1	—	—	—
Ullungdo	1	1	1	3	3	3	1	1	1	—	—	—
Ulsan	1	1	1	3	3	3	1	1	1	3	3	3
Muko	1	1	1	—	—	—	—	—	—	6	6	6
Kangnung	—	—	—	3	3	3	1	1	1	—	—	—
Sokcho	1	1	1	3	3	3	1	1	1	—	—	—
Posyet	1	1	1	3	3	3	3	3	3	—	—	—
Vladivostok	1	1	1	3	3	3	3	3	3	—	—	—
Nakhodka	1	1	1	3	3	3	3	3	3	—	—	—
Rud. Pristan	—	—	1	3	3	3	3	3	3	—	—	—
De Kastri	1	1	1	3	3	3	3	3	3	—	—	—

J is July, A is August, S is September; 1, 3, 6 are time intervals (in hours); * means fragmentary data

during three months: 74 in July, 103 in August and 63 in September. Therefore, just these months were chosen for the present analysis.

2. Data

Sea level data obtained at 18 stations on the coasts of Korea and Russia were used to investigate sea level response to meteorological forcing. These stations situated along the west coast of the Sea of Japan (Fig.1) are related to the regions with different topography and tidal regime. The shallowest water zones are located near the southern part of the Korean Peninsula and in the northern part of Tatar Strait (De Kastri station). The narrow shelf and steep shore are typical for the eastern Korean coast.

Observational data were supplied by the Hydrographic Office (Korea) and Hydrometeorological Administration (Russia). These data were represented by the time series of sea level and atmospheric forcing for July-September, 1986 (Table 1). The sea level data consisted of hourly tide gauge records. Atmospheric pressure and surface wind data were obtained mainly from the local observations at the same statinos. Complete 3-month simultaneous series were available for the majority of the stations, except Rudnaya Pristan where sea level data were absent and Komundo, Kadukdo where there were no meteorological data. For the Muko station atmospheric pressure and wind were taken at the neighbouring meteorological observatory of Kangnung. Series of atmospheric pressure had 3-hour time interval for all cases; wind data had time step of 1 hour for Korean and 3 hour for Russian stations. There were fragmentary wind waves data for some Korean stations, but only two of them (Muko and Ulsan) had complete 3-month series (of maximum wind wave heights) with 3-hour time step for Ulsan and 6-hour for Muko (Table 1). Series of significant wave heights had many gaps and their use was limited.

3. Methods

General analysis scheme is shown in Fig.2. Original data were carefully tested and corrected. Two different ways were used to represent surface wind data: by wind velocity components $W_x = |W| \sin \Psi$, $W_y = |W| \cos \Psi$ and wind stress components $T_x = k \rho |W| W_x$, $T_y = k \rho |W| W_y$, where W, Ψ are the wind speed and direction, ρ is the air density, k ($=0.0025$) is the wind drag coefficient. Two pairs of wind stress components were used: (1) onshore, longshore (T_x, T_y) and (2) zonal, meridional

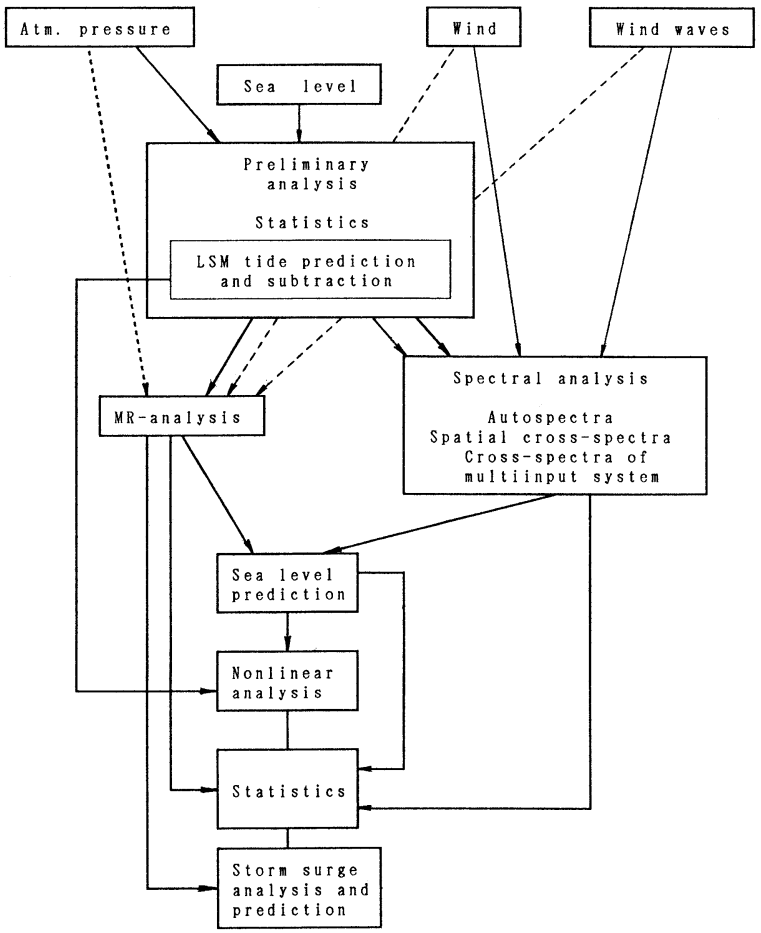

Fig. 2. Scheme of analysis.

(T_z, T_M). Meteorological and wind waves data were interpolated by spline function to obtain synchronous hourly series. Astronomical tides were removed from the initial sea level and then residual series were used for further analysis.

Two methods of data processing were applied: spectral analysis and multiple regression analysis (MRA). The first one included auto-and cross-spectral data examination and multi-input system analysis (MISA). The second method was realized in time domain which enabled to analyse not only full 3-month series, but also short segments connected with individual storm surges. It was possible to find response functions of the sea level to the atmospheric disturbances and to estimate contribution of different meteorological forces by both methods. Influence of additional factors on sea levels (wave set-up and non-linear tide-surge interaction) was also estimated.

The observational period was remarkable by propagation of typhoon No 8613, "VERA", one of the strongest and most distructive in the last 20 years (OH *et al.*, 1988; KANG *et al.*, 1988; KANG, 1988; OH and KIM, 1990). Significant storm surge was observed all over the Korean coasts and also in the Primorye Region of Russia. Statistical parameters of this storm surge were estimated for all stations except the northernmost station De Kastri where it was not revealed. MRA results were used for the storm surge hindcasting.

4. Tidal analysis

Tides are usually predominant in sea level oscillations. In particular, results of tidal analysis

Table 2. The amplitudes of major tidal constituents computed for the August, 1986.

Stations	Tidal variance, %	Tidal amplitudes, cm							
		Q_1	P_1	O_1	K_1	N_2	M_2	S_2	K_2
Sogwipo	96.7	4.3	8.4	18.1	25.2	16.4	73.4	32.5	8.8
Cheju	97.5	4.0	8.1	17.0	24.2	16.0	65.7	26.6	7.2
Komundo	98.4	3.3	8.3	17.0	24.2	18.8	85.6	38.5	10.1
Yosu	98.1	1.9	6.3	13.4	19.3	19.5	94.4	44.2	12.0
Chungmu	97.5	1.4	4.9	10.2	14.7	15.5	75.3	35.4	9.6
Kadukdo	96.4	0.5	2.0	4.3	7.2	10.3	54.0	27.3	7.6
Pusan	91.5	0.2	1.5	1.7	4.5	7.4	38.6	18.4	5.0
Ulsan	65.7	0.8	1.3	3.3	3.8	2.6	15.6	7.7	2.0
Pohang	22.9	1.2	1.3	4.3	3.9	0.8	3.0	0.7	0.2
Ullungdo	31.6	0.9	1.5	4.7	4.6	2.6	4.5	1.6	0.4
Muko	23.8	0.9	1.6	4.7	4.7	1.6	6.2	2.2	0.6
Sokcho	22.2	0.8	1.6	4.7	4.4	1.6	6.8	2.5	0.7
Posyet	28.0	0.7	1.8	4.7	5.2	1.7	7.5	3.2	0.9
Vladivostok	31.5	1.0	1.8	5.1	5.4	1.8	7.6	3.2	0.9
Nakhodka	32.1	0.9	1.9	5.1	5.5	1.5	6.6	2.7	0.7
Rud.Pristan*	39.5	1.3	1.8	5.0	5.4	1.2	6.0	2.7	0.7
De Kastri	94.7	1.6	2.3	6.4	6.9	19.0	68.7	25.4	6.6

* Tidal amplitudes in Rudnaya Pristan have been computed for September, 1986.

of the investigated region have demonstrated that for the stations located in the Korean Strait and De Kastri more than 94 % of total sea level variance is related to the tides (Table 2). For the stations situated at the east coast of Korea and for the southern Russian stations this percentage is less (22 to 40 %) but in any case it is significant. For correct examination of weather-induced elevations including storm surges, it is necessary to eliminate tidal oscillations.

It is possible to remove tides from the initial records by applying special low-pass or band-pass numerical filters (PUGH, 1987). The shortage of such method consists in distortion of the processes with near-tidal frequencies and reduction of extreme sea level deviation (i.e. actual storm surge heights).

Therefore it is better to predict tides based on results of harmonic analysis and to subtract them from the initial observational series. This method was used by OH *et al.* (1988) to analyse storm surges near the southern coast of Korea. They have calculated 64 tidal constants based on 1-year series of hourly data, then used these constants to predict tides during typhoon passages (including typhoon "VERA") and to remove them. The oscillations with period of about 12 hours which appeared distinctly in the residual records were, by the opinion of OH and KIM (1990), connected with influence of tidal currents.

In this paper we applied a similar method but with certain modification. Least square method was used to compute 37 tidal harmonics and to subtract tides from initial records for every monthly series separately. The use of additional harmonics in excess of 37 did not give further improvement of the residuals. This method gave good results: residual series were visually quite clean without tides except some small pieces of records of apparently poor quality (Fig.3); their spectra did not have any prominent maxima of tidal frequencies (Fig.4), either.

Amplitudes of major tidal constituents (Table 2) were in good agreement with those obtained by OH *et al.* (1988) from yearly series.

5. Spectral analysis of sea level and atmospheric pressure

We made spectral analysis of 3-month data series with FFT procedure. Kaiser-Bessel window (HARRIS, 1978) was used to improve spectral estimates. Power spectra of atmospheric pressure and sea level are shown in Fig.4. There is a good spectrum correspondence for different stations in the frequency band 0.07–1 cpd, i.e. in the 'synoptical frequency range' (LICHACHEVA,

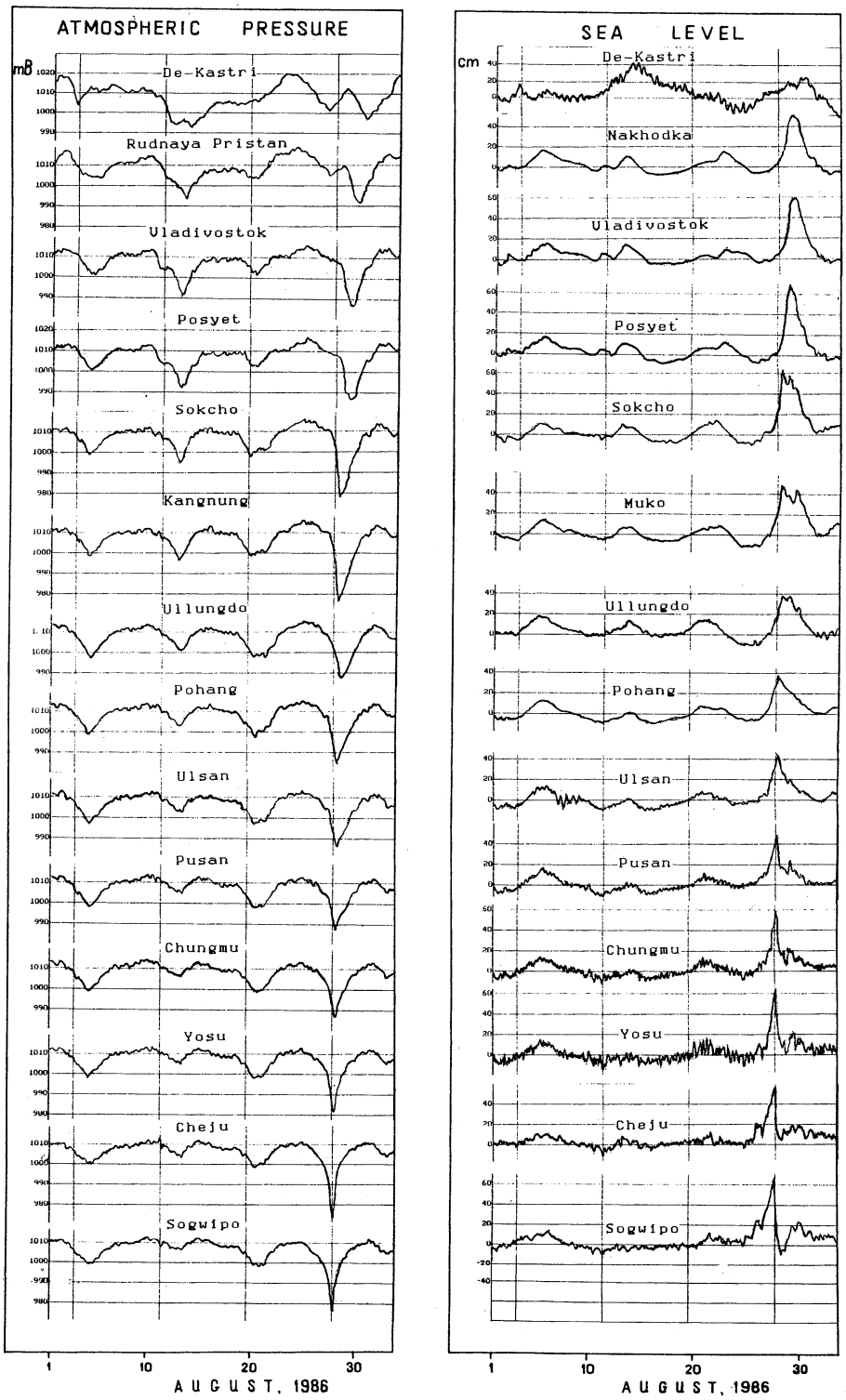

Fig. 3. Records of atmospheric pressure and non-tidal sea level variations in August, 1986.

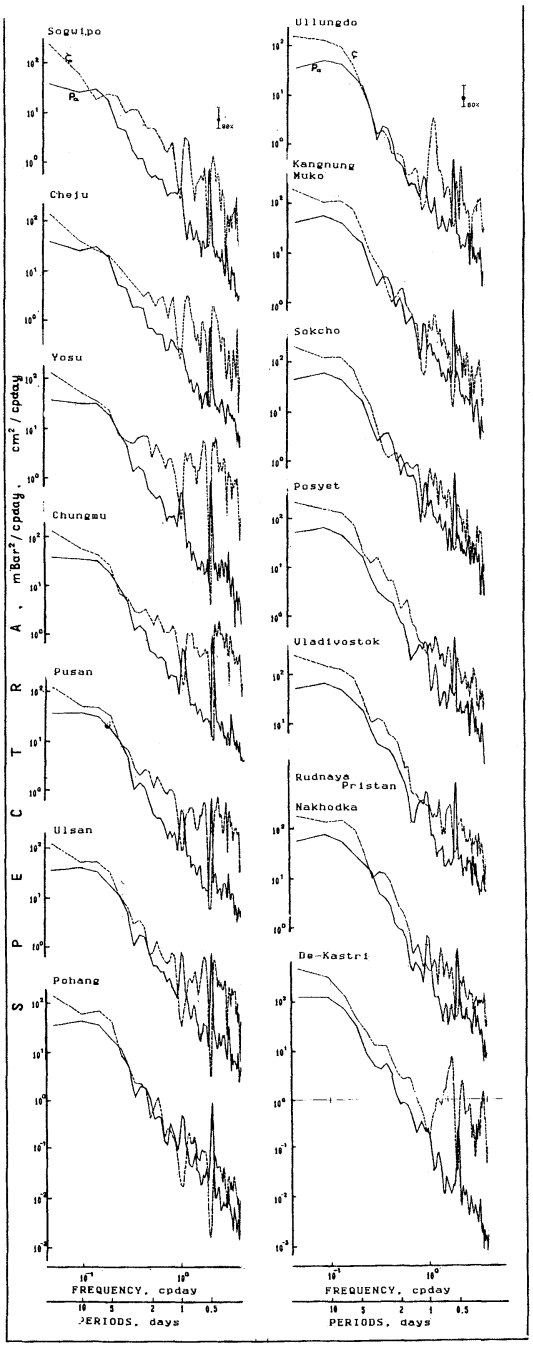

Fig. 4. Spectra of atmospheric pressure and sea level.

1984). The shape of low frequency sea level spectra resembles to that of atmospheric pressure, but their energy level is a little higher, which agrees well enough with results of ISOZAKI (1969) for the eastern coast of the Sea of Japan. Prevalence of sea level spectrum is manifested better for the northern stations. At higher frequencies there is increasing divergence in sea level and pressure spectra.

There is a prominent peak in the atmospheric pressure spectra at the frequency of 2 cpd caused by semidiurnal atmospheric tides. Diurnal maximum is not so notable; for some stations (Sogwipo, Cheju, De Kastri) it is practically absent (Fig. 4).

There is no obvious maximum in atmospheric spectra at the periods of about 5–6 days ('the synoptical maximum'), though usually well seen in the Northwestern Pacific (LIKHACHEVA and RABINOVICH, 1986a).

The sea level spectra are relatively smooth and have no evident peaks. However, there are a few exceptions. At the Ullungdo station an obvious maximum with period of 19.7 hours is well seen. This period is exactly equal to the inertial period for this station $T=\pi/\Omega\sin\Psi$, where Ω is the Earth's angular speed and Ψ is the geographical latitude. This coincidence is scarcely casual, especially taking into account that Ullungdo is a small isolated island in the open sea. Apparently corresponding sea level variations are caused by inertial currents or by internal waves of inertial period.

There is another interesting spectral feature. Results of the spectral analysis show that the least square procedure of tidal analysis has removed from the initial sea level series not only real tides but also some part of background noise, leaving deep troughs in appropriate parts of the spectra. Around these troughs there are peaks with periods: 29–30 and 21–22 hours for Sogwipo and Cheju, 13.5–14 and 11 hours for Cheju, Yosu and De Kastri (Fig. 4), i.e. these peaks are observed generally for the stations with strong tides. Although there are no tidal constituents with these periods, it is clear that these maxima are connected with tides and probably are the residuals of wide tidal extremes. MUNK *et al.* (1965) called this phenomenon 'tidal cusps' and explained the cause of this cusping as 'the non-linear interaction of the tidal spectral line with the low frequency continuum'. Apparently in our case these cusps are

related to the non-linear interaction of tides and mean flow.

Some spectral features of sea level may be related to eigen oscillations of the Sea of Japan. RIKIISHI (1986) computed these oscillations with periods of several hours and demonstrated that semidiurnal tidal structure corresponds very well with structure of appropriate proper oscillations. SATAKE and SHIMAZAKI (1988) made a similar investigation for tsunami frequency band and showed that spectral peaks in the period range of 50 to 210 min excited by the 1964 Niigata and 1983 Japan Sea tsunamis agreed quite well with the numerically computed periods of normal modes in the sea. Unfortunately there are no such investigations of subtidal modes of the Sea of Japan It may be interesting in future to compare meteorologically-induced sea level variations with normal mode structure.

We made a cross-spectral analysis of the data to examine spatial-temporal relations of the atmospheric and sea level variations. Coherence and phase functions were calculated between the southernmost station Sogwipo and all the others. Atmospheric pressure coherence is decreased gradually with increase of distance from Sogwipo. An exception is the frequency of semidiurnal atmospheric tides where coherence peaks exceeding 0.80 are practically independent of the distance (Figs. 5a, 6a). Sea level coherence along the coast at periods of 1–5 days is quite stable. Significant values persisted for a long distance (Figs. 5b, 6b).

We describe spatial-temporal changes of the atmospheric pressure coherence γ^2 (Fig.6) in the synoptical frequency range as

$$\gamma^2(L, T)=\exp(-aL^{\nu}/T^{\beta}), \qquad (1)$$

where a, ν, β are the empirical constants, T is period (in hours), L is length scale (in km). With this formula $\gamma^2 \to 1$ when $L \to 0$ or $T \to \infty$; on the contrary $\gamma^2 \to 0$ when $L \to \infty$ or $T \to 0$.

Based on Eq. (1) and coherence functions γ_{ij}^2 (L, T) between Sogwipo and all other stations, parameters a, ν and β were computed by least square method (LSM) from the expression

$$\sum_{i=1}^{N}\sum_{j=1}^{M-1}[\log(-\ln(\gamma_{ij}^2))-\log a-\nu\log L_j - \beta\log f_j]^2 \to min, \qquad (2)$$

where $f_i=1/T_i$, N is the number of frequencies in chosen band, M (=15) is the number of stations. Following values were obtained: $a=9.37\times10^{-3}$, $\nu=1.11$, $\beta=0.688$. Empirical formula (1) may be used for description of temporal and spatial coherent scales of atmospheric processes. For example, for T = 5 days: L=336 km for γ^2=0.8 and L=709 km for γ^2=0.6. Appropriate lengths estimated directly from Fig. 6a are approximately 340 and 705 km.

In this investigation only one-dimensional coherence scales were examined. Two-dimensional spatial and temporal scales of atmospheric processes had been inspected by LIKHACHVA and RABINIVICH (1986a) based on yearly series of atmospheric pressure for the whole Far East region. It was shown that coherence field is quasi-isotropic over the continental area and the Sea of Japan, and anisotropic only on the continent-ocean boundary. The typical scales were found to be 300–500 km for T=5 days and γ^2 = 0.8, which are in good agreement with those obtained in the present study.

Phase functions of both atmospheric pressure and sea level are close to be linear in the synoptical frequency band (Fig.5). LSM procedure was used to estimate the average speed and direction of atmospheric disturbances based on phase lags between the stations. It was found that the atmospheric processes were propagated to the northeast with mean speed of 40–50 km /h. Sea level variations moved longshore northward with almost the same velocity.

6. Spectral analysis of multi-input system

Sea-level continuum may be regarded as an output of multiple linear system with a number of input functions (weather variables) which are in general mutually coherent (GROVES and HANNAN, 1968; CARTWRIGHT, 1968; WUNSCH, 1972). To investigate such a system and to examine relations between meteorological forces and non-tidal residual sea level it is possible to apply multi-input system cross-spectral analysis (MISA) (BENDAT and PIERSOL, 1986). Three

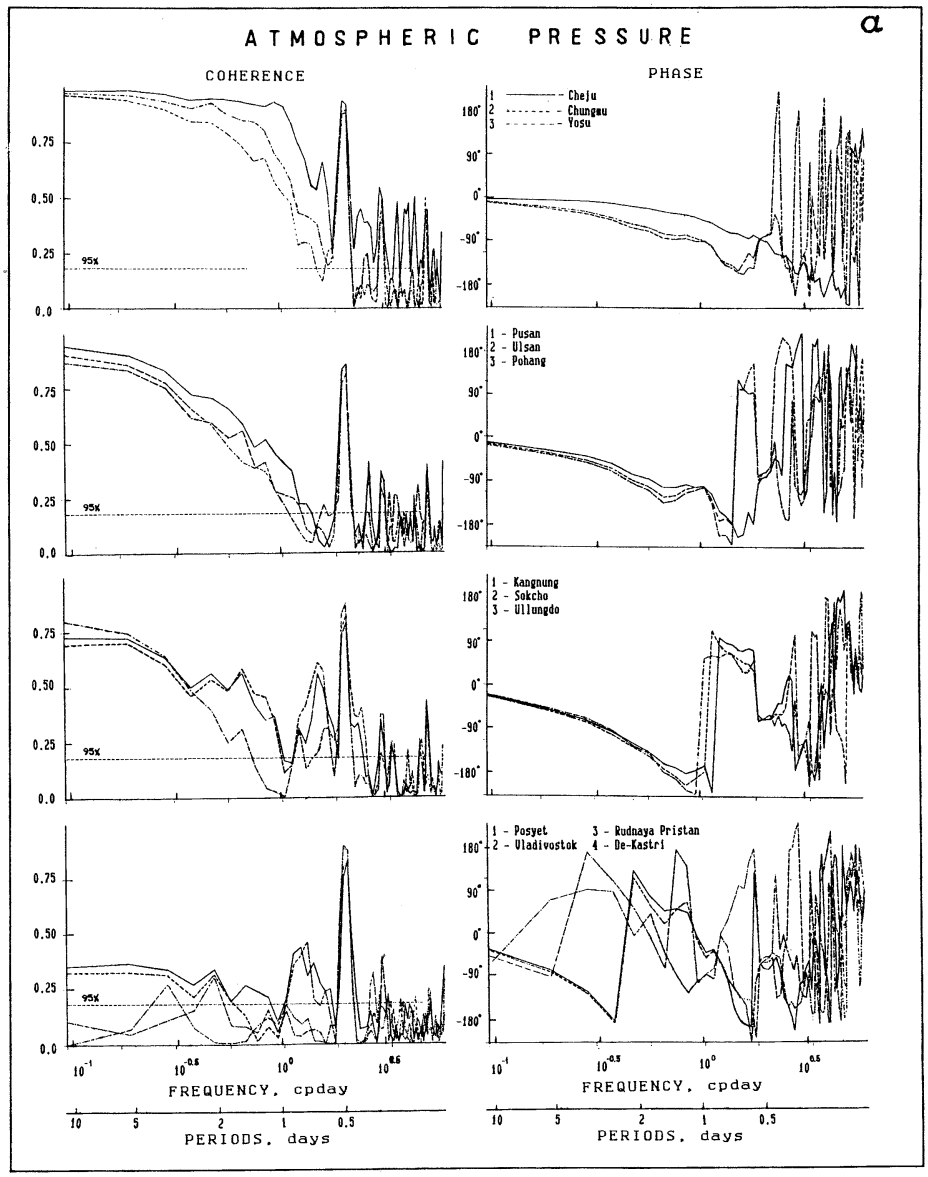

Fig. 5a. Coherence and phase functions of atmospheric pressure between Sogwipo and all the other stations.

input functions, atmospheric pressure, onshore and longshore wind stress components, were used for most stations. For two stations (Ulsan and Muko) the fourth input (wind wave height) was also used.

Multiple and partial coherence functions (BENDAT and PIERSOL, 1986) were calculated for all examined stations. Fig. 7 shows a high multiple coherence between external forces and sea level in the synoptical frequency band. Low-frequency coherency band has a certain tendency to narrow toward the north. The stations of the Korea Strait (Cheju, Sogwipo) have the zone of maximal coherence in the frequency range of 0.4 –0.7 cpd with values over 0.90. There is another coherence maximum at the frequency of about 1.5 cpd which is manifested better for Cheju and the eastern Korean and Russian stations and

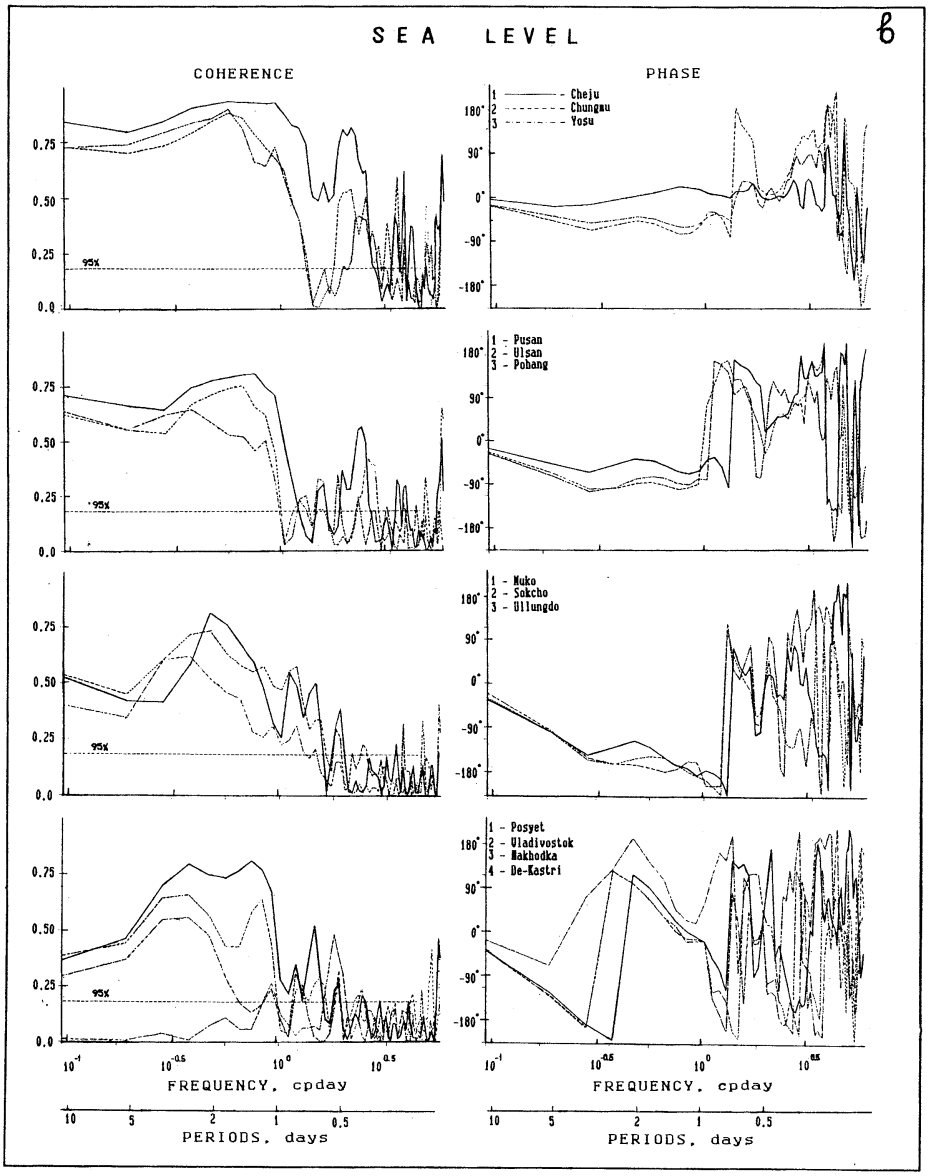

Fig. 5b. Coherence and phase functions of sea level between Sogwipo and all the other stations.

reaches highest values in excess of 0.8 at stations Muko, Sokcho and Posyet (Fig.7). These stations have also the third maximum at short periods.

Multiple coherent spectrum of output process is defined as (BENDAT and PIERSOL, 1986)

$$G_{vv}(f) = G_{yy}(f)\, \gamma^2_{y:x}(f), \qquad (3)$$

where G_{yy} is the spectrum of output, $\gamma^2_{y:x}$ is the multiple coherence of the system, f is the frequency. Coherent spectrum was integrated over the whole frequency band

$$R_{y:x} = \int_0^\infty G_{vv}(f)\, df \qquad (4)$$

to estimate total coherent part of the variance (Table 3). Similar expression but with re-

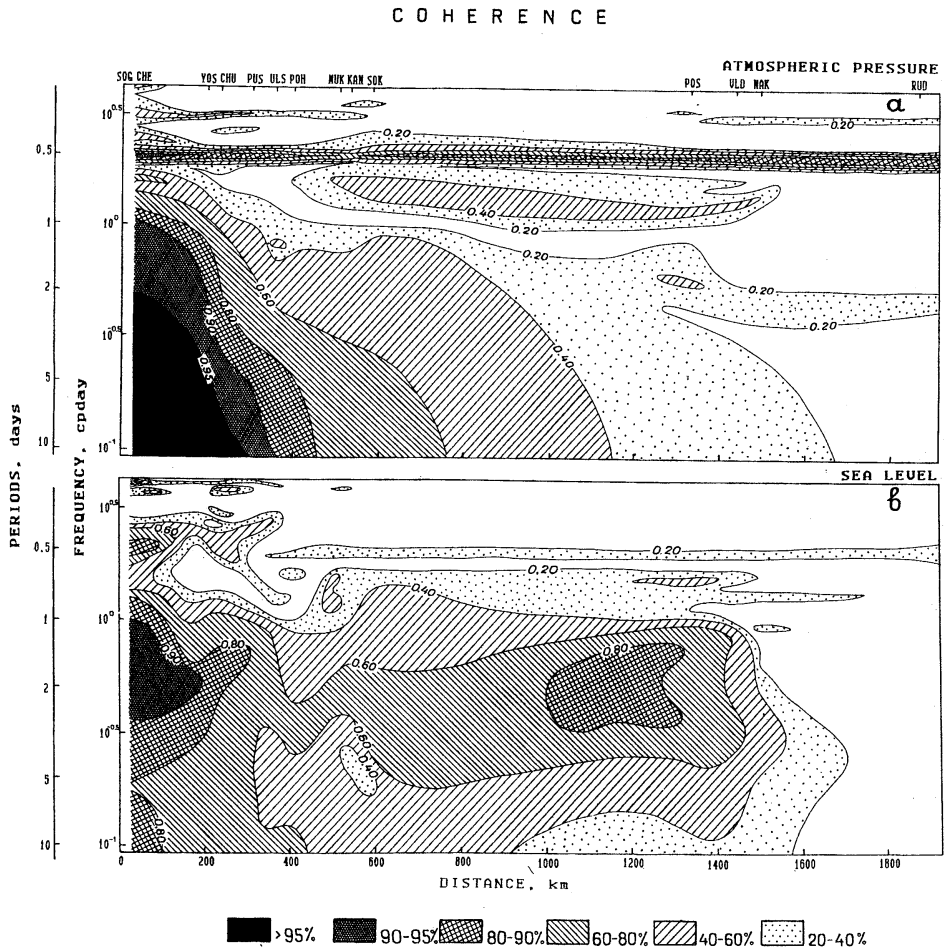

Fig. 6. Spatial coherence field of atmospheric pressure (a) and sea level (b) relative to the Sogwipo station.

placement of a multiple coherence by a partial one had been used for estimation of relative importance of individual inputs (WROBLEWSKI, 1978).

Energy of non-tidal sea level variations is reduced from Sogwipo (76 cm^2) to Pusan and Ulsan (49 cm^2) and then is increased northward reaching maximum in De Kastri (132 cm^2). These values are of the same order as for Japanese coasts (ISOZAKI, 1969) but less than in the region of Kuril Islands (80–175 cm^2) (LIKHACHEVE, 1984; RABINOVICH and SOKOLOVA, 1985).

Table 3 shows that atmospheric pressure is considered to be the main factor forming non-tidal sea level oscillations; 46 to 77 % of initial variance are coherent with pressure. The relative contribution of atmospheric pressure in the total sea level budget for the coasts of the Sea of Japan is about the same as that in the Kuril region (50–78 %), but additional deposit due to wind stress (9–33 %) is much higher here than there (0.3–9 %). Relatively higher role of wind stress in generation of weather-induced sea level oscillations, specifically storm surges, in the marginal seas with broad shallow water areas in comparison with zones of open ocean shelf with steep slope is well known (MURTY, 1984; PUGH, 1987). As a result amount of energy accounted by both wind stress components and atmospheric pressure is about 60–90 % of the total variance at the coasts of the Sea of Japan in

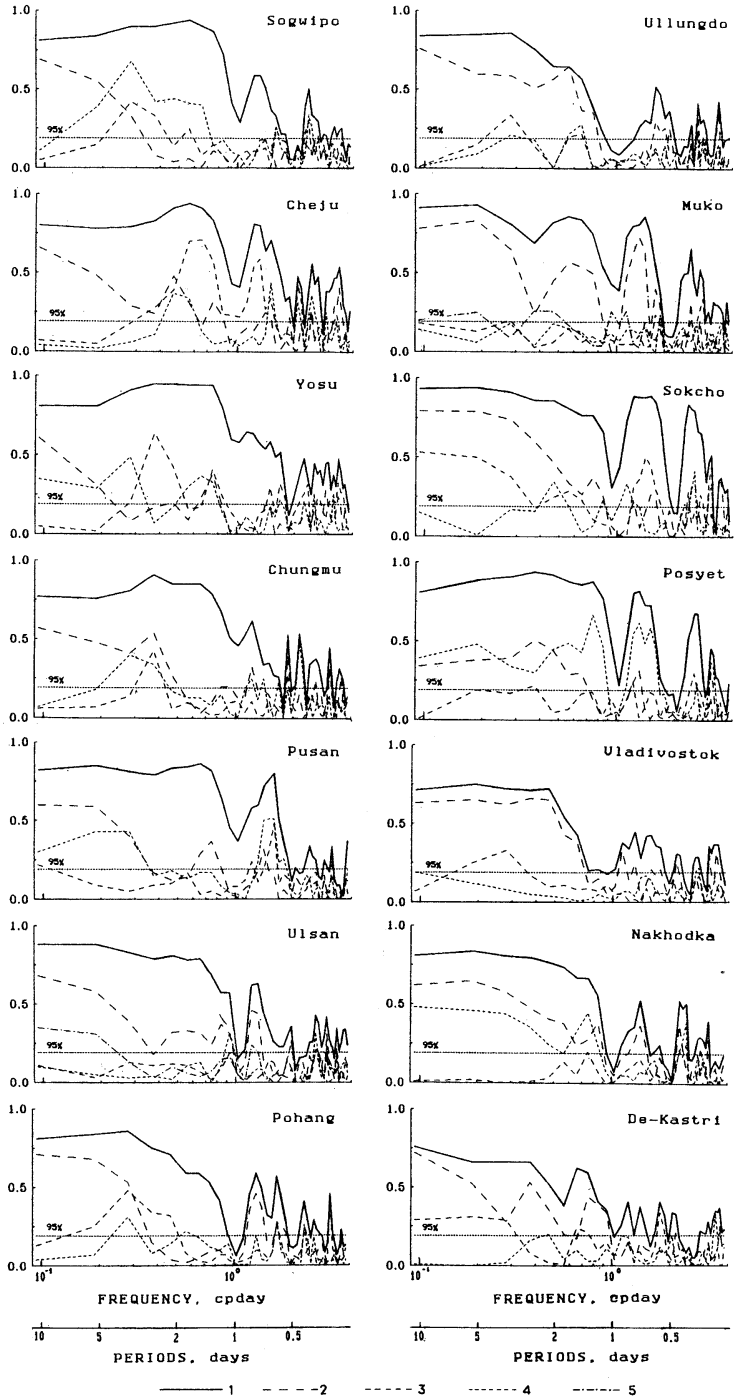

Fig. 7. Multiple and partial coherence functions for sea level oscillation.
1 - multiple coherence, 2 - partial coherence between sea level and atmospheric pressure, 3, 4 - partial coherence between onshore and longshore wind stress components, 5 - partial coherence between sea level and maximal wave height.

Table 3. Weather coherent and predicted (by MRA) non-tidal sea level variances.

Stations	Sea level variance, cm^2	Coherent variance, $cm^2/\%$			Predicted variance, $cm^2/\%$
		atm. pressure	wind	total	
Sogwipo	75.9	43.2/56.9	20.8/27.4	64.0/84.3	40.6/53.5
Cheju	57.6	36.9/64.1	5.1/8.9	42.0/72.9	27.0/46.9
Yosu	68.5	39.3/57.4	7.7/11.2	47.1/68.7	35.5/51.8
Chungmu	54.1	34.9/64.5	4.7/8.7	39.7/73.3	29.0/53.7
Pusan	48.6	28.9/59.5	9.5/19.5	38.4/79.1	29.0/59.7
Ulsan	48.9	30.5/62.4	7.7/15.7	38.2/78.1 (40.6/83.1)	27.2/55.6 (32.6/66.6)
Pohang	52.3	33.4/63.9	9.1/17.4	42.5/81.2	29.0/55.4
Ullungdo	74.4	49.3/66.3	11.1/14.9	60.3/81.1	44.8/60.2
Muko	84.7	63.0/74.4	10.2/12.0	73.3/86.5 (75.5/89.1)	54.1/63.9 (56.5/66.7)
Sokcho	99.4	76.7/77.2	14.6/14.7	91.3/91.9	68.0/68.4
Posyet	111.5	59.3/53.2	36.8/33.0	96.1/86.2	86.7/77.7
Vladivostok	103.5	53.2/51.4	20.7/20.0	73.3/73.9	62.6/60.5
Nakhodka	91.0	48.0/52.7	25.9/28.5	73.9/81.2	67.9/74.6
De Kastri	131.5	60.8/46.2	17.1/13.0	77.8/59.2	78.6/59.7

comparison with 55–70 % for the Pacific coast of the Kuril Islands (RABINOVICH and SOKOLOVA, 1985).

The largest wind contributions in sea level variance were found at the Sogwipo, Posyet and Nakhodka stations. Values in brackets in Table 3 are related to the 4-input system including wind wave heights.

Analysis of partial coherences for southern Korean stations showed that atmospheric pressure plays dominant role at the lowest frequencies to 0.2–0.3 cpd, but at the higher frequencies wind influence on sea level becomes comparable with or exceed that of atmospheric pressure (Fig. 7). For the eastern Korean and the Russian stations except Posyet sea level is more closely correlated with atmospheric pressure than with wind, practically for all examined frequencies.

7. Multi-regression analysis

We performed also the investigation of sea level response to weather forces in time domain, using multilple regression technique (GROVES and HANNAN, 1968; AMIN, 1978, 1982; RABINOVICH and SOKOLOVA, 1985; SKRIPNIK and SOKOLOVA, 1990). The appropriate regression equation may be represented as

$$\zeta(t) = \sum_{j=1}^{M} \sum_{i=1}^{L_j} w_j(\tau_{ij}) \cdot F_j(t - \tau_{ij}) + \varepsilon(t), \quad (5)$$

where ζ is the sea level (output), t is the time, F_j are the external forces (input), w_j is the set of regression coefficients (response weights) for each input, L_j is their number, M is the number of input processes, τ_{ij} are the time lag, ε is background noise uncorrelated with input functions.

Based on expression (5) it is possible to hindcast sea level variations by known input functions and response weights. Multiple regression analysis (MRA) is an efficient instrument to construct empirical forecasting formulae to predict storm surges.

An effective MRA computer program with arbitrary number of inputs and response coefficients was elaborated by RABINOVICH and SOKOLOVA (1985). This program was applied to analyse sea level variations with the same inputs as in cross-spectral analysis (MISA). The high-frequency oscillations uncorrelated with sea level were eliminated from the input functions by Kaiser-Bessel filter (HARRIS, 1978) with time window of 24 hours. The regression model was tested both with wind stress and wind velocity. Better results were achieved when wind stresses had been used.

The regression coefficients in expression (5) were determined by the least square method. Residual variances were minimized. Values of the coefficients M and time lags L_j were selected to optimize the computation.

Table 4. MRA results for 3-months serie and the individual storm surges.

Stations	3-month series				Storm surges			
	Regression coefficients on			Direction of eff.wind, (in degrees)	Regression coefficients on			Direction of eff.wind, (in degrees)
	P_a	T_z	T_M		P_a	T_z	T_M	
Sogwipo	−0.67	−87.2	18.5	102	−1.07	−78.8	4.2	93
Cheju	−0.79	−28.7	26.3	132	−1.62	−44.7	−27.1	58
Yosu	−0.98	−45.1	11.7	105	(−1.63)	(−55.5)	(52.6)	133
Chungmu	−1.06	−50.2	11.8	103	−2.25	−37.5	−27.1	54
Pusan	−0.99	−61.3	0.1	90	−1.07	− 8.8	18.7	111
Ulsan	−0.89	−50.4	83.6	150	−1.65	−50.3	19.3	111
Pohang	−1.04	−31.4	− 2.8	85	−1.53	−28.2	5.6	101
Ullungdo	−1.15	−35.4	48.1	143	−1.44	38.3	3.6	265
Muko	−1.22	58.4	− 2.9	273	−1.24	−65.7	426.1	171
Sokcho	−1.46	25.8	−12.9	296	−2.12	23.9	−70.7	341
Posyet	−1.36	−49.3	− 2.5	87	−2.20	−23.1	− 1.0	87
Vladivostok	−1.47	−29.9	− 1.5	87	−2.30	−35.7	−11.8	72
Nakhodka	−1.27	−49.2	−13.4	74	−2.06	−21.9	−8.5	69
De Kastri	−1.50	−75.9	−16.7	77	−	−	−	−

Three-month data series were processed with MRA. The weights were employed to restore non-tidal sea level (Table 3). For better comparison all input functions were taken with the same number of regression weight ($L_j = 4$) and with the same time lag (0, 6, 12 and 18 hours). Table 3 shows that generally it is possible to predict 47 to 77 % of sea level variance by this method. Use of four weights instead of one for every input (as it was made, for example, by AMIN, 1978) gave a slight improvement (from 3 to 11 %). The coherent energy estimated by MISA always exceeds that calculated by MRA technique because of limitations of regressional model. There is systematic reduction in the corresponding difference as additional weights are added to the analysis. But excessive increase of the number of weights causes instability of their values and worsens application of the regressional equations for forecast purposes. The special inspection is required to determine the optimum number of weights and appropriate time lags (ZETLER and MUNK, 1975).

Response weights for time lag $\tau_{ij}=0$ are presented in Table 4. The regression coefficient between atmospheric pressure and sea level ('barometric factor') is a problem of special interest. The corresponding values are relatively small in comparison with theoretical values −1.01 cm/mbar for the southernmost stations Sogwipo and Cheju (−0.67 and −0.79), and close to theoretical ones for the stations at the southeastern coast of Korea and Ullungdo Island (from −0.89 to −1.15) and large for the northern Korean and the Russian stations (from −1.22 to −1.50). A tendency of northward increasing barometric factor is well seen. The corresponding values estimated by ISOZAKI (1969) all over the coasts of Japanese Islands were more stable (from −0.69 to −1.13). It was shown by LIKHACHEVA and RABINOVICH (1986b) that reaction of sea level to variations of atmospheric pressure depends significanly on the direction of atmospheric disturbances in regard to continental shelf waves: when these systems are propagating in the same direction as free shelf waves as it takes place at the Okhotsk Sea coast of Kuril Islands, they produce considerably greater sea level response than when they are moving in opposite directions as at the Pacific coasts. The latter is the case of the Korean and Russian coasts where cyclones and typhoons are moving to the northeast and shelf waves to the southwest. This is the reason why it is necessary to look for another explanation of barometric factor increase. It is quite possible to explain that this peculiarity is connected with 'encloseness' of the Sea of Japan with only one wide entrance–the Korean Strait to its south. The stations Sogwipo and Cheju with minimal barometric factors are situated just in the Strait. De Kastri with maximum is the

remotest one.

It is neccesary to note that these estimates of barometric factors have been obtained from 3-month observational series (July-September, 1986). Seasonal and year-to-year variations of these factors are quite possible. From the other side the appropriate values are in good agreement with the results of ISOZAKI (1969) for the southern and western coasts of Japan.

Regression coefficients for wind stress components were used to calculate 'effective wind direction', i. e. the direction of the strongest wind influence upon sea level raising (PUGH, 1987) given by

$$\theta = \tan^{-1}(w_z/w_M), \qquad (6)$$

where w_z and w_M are regression coefficients for zonal and meridional components. Wind directions are measured clockwise from the north.

The southeast and east winds were obtained as effective for the majority of the Korean and Russian stations except Muko and Sokcho. There were no significant winds at the Muko (Kangnung) station during the examined period probably because of peculiarities of local observational conditions. This is the reason why determination of the effective wind direction is difficult to estimate for this station.

8. Storm surge caused by typhoon Vera, August 1986

The severe typhoon "VERA" was passing through the Korean Peninsula during 28－29 August, 1986 (Fig. 8). Atmospheric pressure in the center reached 950 mb. Maximal wind speed of 70 m/s was observed. This typhoon brought heavy damages on both human beings and properties at the Korean coasts.

Remarkable storm surges were caused by this typhoon at the all inspected stations except De Kastri (Fig. 3). According to RABINOVICH and SOKOLOVA (1992) main surge parameters were determined and presented in Table 5. The surge and total heights were accounted from mean monthly level; the total height is the sum of surge and tide. Time difference between them is shown in brackets. Duration of surge, its half-height, surge steepness (relation of surge height to half-height duration) and surge energy are shown. There were two surge maxima at the Ullungdo station, both of which are given in Table.

OH *et al.* (1988) had adduced similar height values of this storm surge for the southern Korean stations. The significant surge was observed at stations Sogwipo, Cheju, Komundo, Yosu and Chungmu as well as at stations Muko, Sokcho located at the eastern coast of Korea and in Primorye region of Russia (Posyet, Vladivostok and Nakhodka). Much less surge elevations took place at southeastern Korean stations Kadukdo, Pusan, Ulsan and Pohang (Table 5). These features of sea level reaction to atmospheric depression are closely related with the characteristics of typhoon, its track and transition speed. The typhoon "VERA" reached Korean Peninsula near its southwesternmost part (Cheomranam-do region) (Fig. 8); center pressure was about 960 mb, and the maximum wind speed was 70 m/s (OH and KIM, 1990). Wind set-up caused by strong on-shore winds and reinforced by the pressure fall generated destructive storm surge at the stations located in the Korean Strait. Numerical model of OH and KIM (1990) simulates this process quite convincingly. Propagating northeastward, the typhoon "VERA" crossed the eastern coast south of Muko station. On-shore winds forced wind set-up at the stations situated to the left of the typhoon track (Muko, Sokcho and others), while off-shore winds caused wind set-down at the southeastern stations. Apparently the strongest surges were observed at the eastern coasts of North Korea, where there were maximum on-shore winds (see Fig. 5, Kang *et al.*, 1988). The observed surge heights in North Korea were 105 cm in Wonsan, 106 cm in Chongjin, 68 cm in Sinpho and 55 cm in Senbong (KANG, 1988).

HWANG (1971) had collected data on the remarkable storm surges for southern and southeastern coasts of Korea for 1959–1970. The most powerful surge during this period was on 22–24 August, 1966 (102 cm in Cheju, 110 cm in Yosu). But for further northern stations no one had been as strong as the surge caused by typhoon "VERA".

It is well seen that height, character and duration of the storm surge varied significantly for

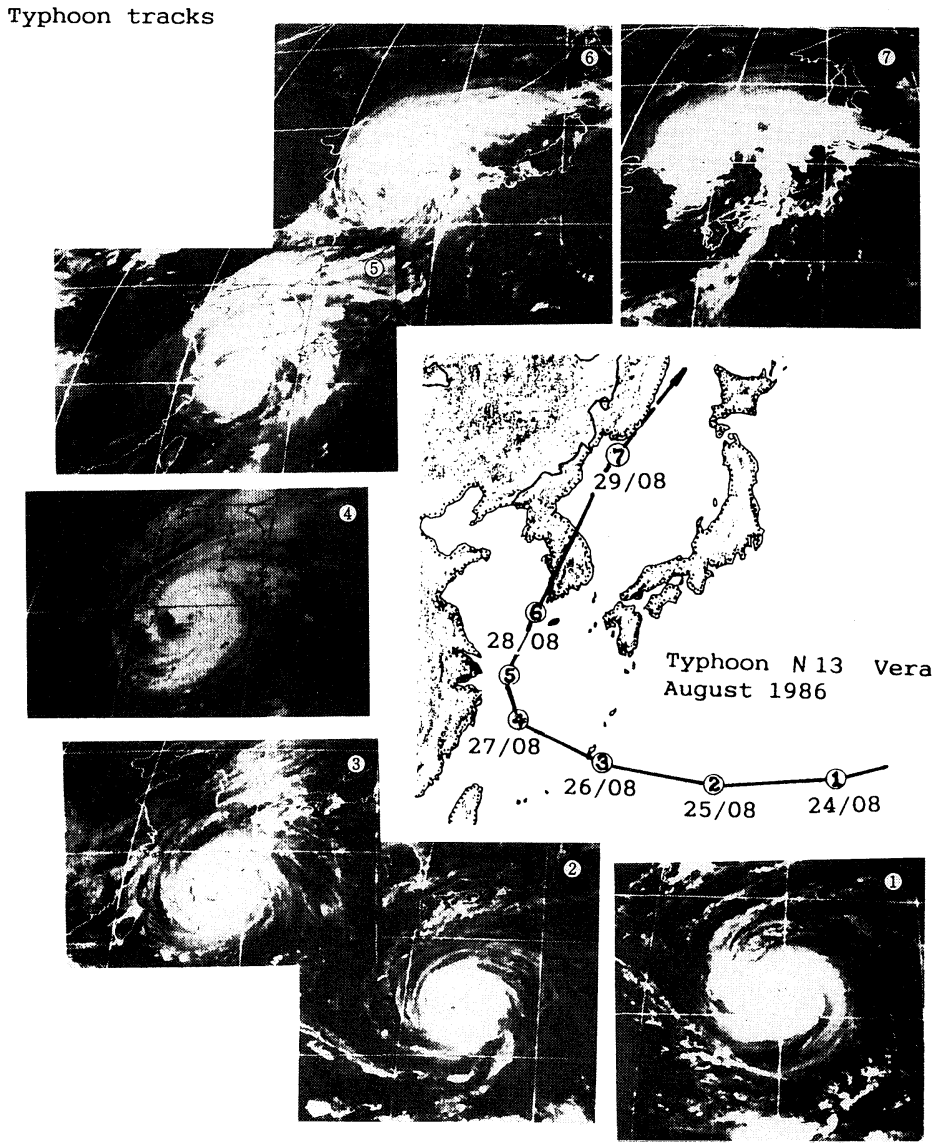

Fig. 8. Track of typhoon No 8613 "VERA" and its satellte images.

different regions. For the stations at the southern coast of Korea and in the Korea Strait it had character of relatively short (55–81 hours) and high (52–66 cm) sea level elevations with well manifested negative displacement behind the surge (Fig. 3, Table 5). The main features of the storm surge behaviour in this region were explained by numerical modelling (OH and KIM, 1990).

The surge height became smaller (37–49 cm) and more prolonged (118–138 hours) at the southeastern Korean coast. For the northern stations the situation changed to the opposite (Fig. 3, Table 5).

Table 6 shows the atmospheric parameters at the stations during this surge. 'Pressure fall' means the difference between the mean monthly value and observed minimal atmospheric pressure. Time difference between maximum of the surge and pressure minimum is given in brackets. It is interesting that for all stations this difference was positive, i. e. surge maxima

Table 5. Parameters of the storm surges caused by typhoon "VERA" (August, 1986) observed on the various coastal stations.

Stations	Time of surge Maximum, date, time	Surge height, cm	Total height(±t) cm (hours)	Surge duration, hours	Duration of half-height, hours	Steepness, cm/hour	Surge variance, cm^2
Sogwipo	Aug. 28, 06	66.3	67.6 (−3)	81	24	2.8	925.9
Cheju	Aug. 28, 05	54.5	70.0 (−1)	77	18	3.0	636.4
Komundo	Aug. 28, 07	52.4	66.8 (−5)	75	21	2.5	600.0
Yosu	Aug. 28, 11	65.0	92.9 (+3)	55	14	4.6	909.1
Chungmu	Aug. 28, 12	58.1	86.6 (+2)	73	15	3.9	575.3
Kadukdo	Aug. 28, 12	40.1	61.4 (+1)	55	20	2.0	418.2
Pusan	Aug. 28, 13	48.6	99.4 (0)	138	19	2.6	340.6
Ulsan	Aug. 28, 14	44.2	52.9 (0)	130	32	1.4	361.5
Pohang	Aug. 28, 14	37.7	38.1 (−1)	118	49	0.8	381.4
Ullungdo	Aug. 28, 19	37.1	39.1 (+10)	120	50	0.8	450.0
	Aug. 29, 15	37.4	39.1 (0)				
Muko	Aug. 28, 18	50.3	45.5 (0)	114	63	0.8	868.4
Sokcho	Aug. 28, 19	63.1	61.9 (+1)	122	48	1.3	1090.2
Posyet	Aug. 29, 13	69.6	77.8 (−2)	125	33	2.1	1040.0
Vladivostok	Aug. 29, 18	60.5	62.5 (−7)	114	40	1.5	1026.3
Nakhodka	Aug. 29, 18	52.5	54.3 (−7)	106	39	1.3	801.9

passed ahead of pressure minima.

Maximal and significant wind wave heights as well as wind speed and direction in the moment of the highest surges are also presented in Table 6. The wind direction corresponds quite well to the direction of effective wind (Table 4).

'Pressure factor' in the last column is defined as ratio of surge height to pressure fall. Actually the 'presure factor' is related not only to pressure fall but also to wind influence; this is why in most cases it is sufficiently bigger than 'barometric factor' obtained from the regression analysis as reaction to atmospheric pressure alone (Table 4).

Storm surge records were analysed separately by MRA method. The short observational series (4–7 days) were processed. For comparison in Table 4 the same parameters calculated for storm surges as for 3-months series are presented. The barometric response is higher for the storm surge than for the longer series but it has the same tendency to increase northward. It was revealed during the storm surge analysis in Yosu that atmospheric pressure and meridional wind stress are closely correlated. Therefore, the reaction to atmospheric pressure and wind stress was calculated independently. The corresponding values are given in brackets. There were relatively good agreements between two sets of computations except at Muko, Sokcho and Ullungdo. These stations were situated just on the track of the typhoon (Fig. 8).

Both sets of regression coefficients computed from 3-month series and from storm surge records were used for surge hindcasting. The results were in good agreement; improvement in storm surge restoring from applied response weights estimated from the same record was insufficient. Some examples of surge hindcasting based on average coefficients set are given in Fig. 9. It is interesting that wind stress insignificantly affected sea level variations in calm weather in comparison with atmospheric pressure, while it did significantly for the storm surge moment.

9. Wave set-up

Positive change of mean sea level in nearshore zone due to the presence of breaking incident waves ('wave set-up') is well-known phenomenon (BOWEN *et al.*, 1968; PUGH, 1987). The effect is physically distinct from 'wind set-up', because it can be present even without local wind, owing to swell from distant storms (THOMPSON and HAMON, 1980). The theoretical basis of wave set-up generation was elaborated by LONGUET-HIGGINS and STEWART (1964) who had shown

Table 6. Meteorological parameters of the storm surges caused by typhoon "VERA".

Stations	Minimal atm. pressure(±t) mb (hours)	Wind Speed, m/s	Wind direction	Wave height,m		Pressure fall, mb	Pressure factor, cm/mb
				H_{max}	$H_{1/3}$		
Sogwipo	976.2 (+ 3)	20.7	SSE	–	5.0	−32.9	−2.0
Cheju	973.3 (+ 4)	14.7	SE	–	1.0	−35.7	−1.5
Yosu	981.4 (+ 3)	16.7	S	7.0	4.5	−28.5	−2.3
Chungmu	986.6 (+ 3)	11.7	S	–	–	−23.9	−2.4
Pusan	987.4 (+ 3)	14.7	ESE	–	4.0	−22.3	−2.2
Ulsan	986.5 (+ 3)	9.0	SE	8.0	5.0	−22.7	−1.9
Pohang	985.8 (+ 4)	10.2	SSE	–	–	−24.9	−1.5
Ullungdo	988.1 (+ 3)	6.7	S	–	–	−21.8	−1.7
	988.1 (−16)	11.7	SSW				
Muko(Kangnung)	977.6 (+ 1)	6.0	ESE	4.5	3.0	−32.2	−1.6
Sokcho	977.7 (+ 1)	15.2	SE	6.0	3.5	−31.9	−2.0
Posyet	986.8 (+ 8)	18.0	NE	–	–	−22.8	−3.1
Vladivostok	986.6 (+ 4)	13.0	SE	–	–	−23.0	−2.6
Nakhodka	986.9 (+10)	12.0	ENE	–	–	−22.7	−2.3

that corresponding sea level changes inside the surf zone are related to the conservation of momentum flux of surface gravity waves entering shallow water.

Wave set-up may sufficiently increase storm surge heights. For example during the 1938 New England hurricane surge elevation was about 1 m greater at the relatively exposed areas where storm wave energy was dissipated as surf than at regions of calmer waters (GUZA and THORNTON, 1981). Unfortunately we could not investigate this factor in detail because of lack of data. Wave set-up was inspected very briefly only for the stations Ulsan and Muko. Maximal wind wave heights were regarded as additional inputs in MISA and MRA. It was found that wind waves are correlated with onshore wind, i. e. it is not easy to distinguish wave set-up from wind set-up. Nevertheless, supplement of the additional input increased coherent parts of the variances by 5 % for Ulsan and by 2.6 % for Muko. Appropriate values of predicted variance were increased by 9.7 and 4 % (Table 3).

Including wind wave input in the multiregressional analysis gave the appreciable improvement in hindcasting of the storm surge. Unpredicted variance reduced from 104.8 to 43.1 cm for Muko and from 40.3 to 13.0cm for Ulsan. Contribution of wind waves in addition to atmospheric pressure and wind stress to rise of the storm surge height for Ulsan is well seen in Fig. 9. Maximal wind wave heights (H_{max}) during the storm surge were 8 m at Ulsan and 4.5m at Muko. Significant heights ($H_{1/3}$) were 5 and 3 m respectively (Table 6).

There are some empirical relations between the height of wave set-up η_m and $H_{1/3}$. Specifically, GUZA and THORNTON (1981) found that change of mean sea level η_m owing to waves satisfies to the ratio

$$0.14<\frac{\eta_m}{H^{\infty}_{1/3}}<0.21 \qquad (7)$$

where $H^{\infty}_{1/3}$ is significant wind wave height in deep water.

We had only fragmentary data of significant wave heights, too scanty to apply MRA analysis. All these data were used to define empirical regression relations between $H_{1/3}$ and H_{max}. We found that

$$\begin{aligned} H_{1/3}&=5.5+0.66\,H_{max} \text{ for Ulsan} \\ H_{1/3}&=0.3+0.65\,H_{max} \text{ for Muko.} \end{aligned} \qquad (8)$$

Relations (8) were applied to get significant wave heights for 3-month series and to use them for further computations.

Residual sea level series were used after subtraction of the parts correlated with atmospheric pressure and wind stress. The following regression coefficients between $H_{1/3}$ and sea level were obtained:

Ulsan: $w_s=0.039$; Muko: $w_s=0.026$.

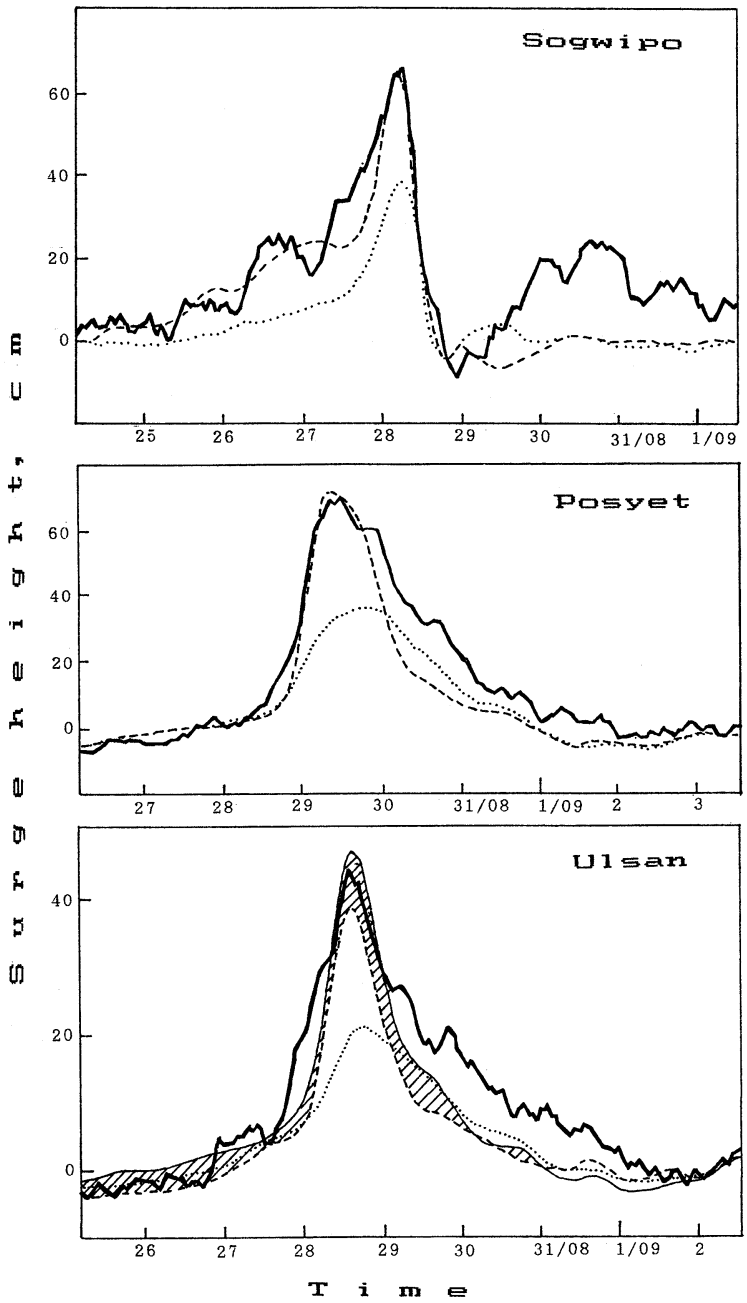

Fig. 9. Time series of recorded storm surges (solid line) and predicted by atmospheric pressure (dotted line) and by pressure and two wind stress components (dashed line). For the Ulsan station aditional part related to wave set-up is hatched.

Wind waves with significant wave height of 3 m cause sea level rise of 12 cm in Ulsan and 8 cm in Muko.

These values are less than those given in relation (7). One of the possible reasons of this difference is that part of wave set-up 'went away' from residual series together with wind coherent part. Another reason is that estimates

obtained by GUZA and THORNTON (1981) are related to smooth beach slope and may be inapplicable to measurements in bays and harbours. THOMPSON and HAMON (1980) found wave set-up in harbour may be represented as

$$\eta_m = \frac{3}{16}\frac{H_{1/3}^2}{h}, \qquad (9)$$

where h is the depth at the entrance of harbour.

To estimate suitableness of this formula to our situation we have made special computations of wave set-up with square of significant wave height as input function and obtained following regression coefficients:

Ulsan: $w_{ss}=0.80$; Muko: $w_{ss}=0.95$.

These values correspond to expression (9) if $h=23.5$ m for Ulsan and $h=20$ m for Muko; the depths are quite reasonable.

10. Influence of non-linear interaction of storm surges with tides.

Sea level variations described by expression (5) show linear response of the sea to external meteorological forces. It is possible to explain that residual background variations $\varepsilon(t)$ unpredicted by (5) are partly related to non-linear interaction of storm surges and tides. In this case non-tidal sea level may be represented as

$$\zeta(t) = \zeta_l(t) + \zeta_{nl}(t) + \varepsilon_r(t), \qquad (10)$$

where ζ_l is the linear sea level component obtained from (5) with regression coefficients, ζ_{nl} is the non-linear component and ε_r is background noise.

In accordance with AMIN (1982) special non-linear input functions were constructed for southern Korean stations which have relatively big amplitudes of tides (Table 2):

$$F_{nl}(t) = \zeta_l(t)\,\zeta_t(t), \qquad (11)$$

where ζ_t is pure predicted tidal series; non-linear sea component was estimated then from the equation

$$\zeta_{nl}(t) = \sum_{j=1}^{N} w_j(\tau_1) F_{nl}(t-\tau_j) + \varepsilon(t) \qquad (12)$$

by MRA technique. Only one regression coefficient was determined but with different time lags.

It was found that for long 3-month series influence of non-linear input is negligible but a certain non-linear influence is found out for storm surge records. Variances of background residuals have reduced: for Cheju from 48.1 to 35.4 cm (27 %), for Chungmu from 52.9 to 44.3 cm (16 %) and for Ulsan from 21.3 to 19.1 cm (10 %). For all other stations decreases of background variances during the storm surge were less than 4 %. Best results were achieved with time lags $\tau_j=3$–5 hours. The strongest influence of tide-surge interaction was observed just for the same stations (Cheju, Chungmu) with relatively strong shallow water tidal constituents M_4 and MS_4.

The non-linear effects during the storm surge caused by typhoon "VERA" are apparently the result of the interaction between tidal and storm surge currents. More detailed analysis of the phenomenon is a subject of the future study.

11. Summary and discussion.

We processed 3-month data series to study behaviour of non-tidal sea level variations along the Korean and Russian coasts of the Sea of Japan and reaction of sea level to meteorological forces. Two different approaches were used to examine the data: 1) investigation in frequency domain (spectral, cross-spectral analysis, multi-input system spectral analysis); 2) investigation in time domain (multiple regression analysis). Combination of these two approaches allowed us to make comprehensive examination of the subject.

It was found that in synoptical frequency band the atmospheric pressure plays principle role in forming non-tidal variations: 46 to 77 % of total sea level energy are coherent with pressure. These sea level variations move along the coast in the same direction as atmospheric disturbances. The barometric factor is increased northward; it is much less than theoretical value (-1.01 cm/mb) for southernmost stations Sogwipo and Cheju (-0.67 and -0.79) and

is much higher for the northernmost station De Kastri (−1.50). The same tendency is remained for individual storm surges but the corresponding values of barometric factor are bigger (from −1.07 to −2.30).

Energy of non-tidal sea level oscillations for the stations situated in the Korean Strait decreases from west to east with a minimal value at Pusan and then increases northward with maximum in De Kastri. Total amount of energy which is coherent with meteorological forces is changed from 59 % (for De Kastri) to 92 % (for Sokcho). Multiple regression analysis (MRA) allows to predict from 47 % (for Cheju) to 78 % (for Posyet) of sea level variance. Improvement of MRA prediction may be apparently achieved by use of additional response coefficients and better choice of corresponding time lags.

The relative importance of wind and wind waves in sea level generation is increased drastically during typhoon passages amplifying surge heights sufficiently.

The storm surge caused by the typhoon "VERA" was studied in detail. Some useful parameters were chosen to compare surge behavior with transformation along the coast. Regression weights computed from 3-month data series were used to hindcast this surge and results were quite satisfactory.

One of the most important questions is an applicability of regression models to disaster forecast. To solve this problem it is necessary to predict sea level changes. To estimate the principal possibility of such prediction a special test was made. The MRA calculations with subsequently increasing time lags were performed for both long series and storm surge segments. It turned out that quality of the forecast was fairly good for periods of 0–12 hours but rapidly became worse one day or more ahead.

An interesting but not well known problem is the influence of the secondary factors on sea level forming. We have studied briefly two of such factors: non-linear intraction of tides, weather-induced oscillations and wind set-up. It was found that in the investigated region the first factor plays a small role in the total budget of sea level energy; only during strong surges in shallow water areas with sufficient tidal variations it is possible to find weak display of such interaction; on the other hand spectral analysis shows certain evidence of nonlinear interaction of tides with mean flow.

Influence of wind set-up is appeared in the records at two stations Muko and Ulsan, especially in the periods of storms. It would be interesting to research this question for the other stations with more adequate data.

At last, it would be useful to investigate significance of free waves in sea level variations specifically continental shelf waves propagating along the Korean coast and shelf of the Primorye region of Russia. These waves usually are manifested in currents but may also affect sea level oscillations (Lappo *et al.*, 1978; LIKHACHEVA and SKRIPNIK, 1981). Preliminary investigation of sea level residuals has not revealed these waves in the processed data but it is desirable to explore this question more attentively.

References

AMIN, M. (1978): A statistical analysis of storm surges in Torres Strait. Aust. J. Mar. Freshwater Res., **29**, 479–496.

AMIN, M. (1982): On analysis and forecasting of surges on the west coast of Great Britain. Geophys. J. the Roy. Astr. Soc., **68**, 79–94.

AOKI, T. (1985): A climatological study of typhoon formation and typhoon visit to Japan. Pap. Meteorol. Geophys., **36**, 61-118.

BENDAT, J. S. and A.G. PIERSOL (1986): Random Data, Analysis and Measurement Procedures. New York, J. Wiley Inc.

BOWEN, A. J., D. L. INMAN and V. P. SIMMONS (1968): Wave 'set-down' and set-up. J. Geophy. Res., **73**, 2569–2577.

CARTWRIGHT, D.E. (1968): A unified analysis of tides and surges round North and East Britain. Phil. Trans. Roy. Soc. London, A **263**, 1–55.

CHU, K. S. (1987): On the Storm Surges and Tsunami Occurred in the Coast of Korea. Hydrogr. Office of Korea, 153 pp. (in Korean).

FIRSOV, P. B. (1988): On mechanism of storm surges forming in the northern part of the Sea of Japan. Proc. Far Eastern Hydrometeorol. Res. Ins., **132**, 3–21 (in Russian).

GROVES, G. W. and B.J. HANNAN (1968): Time series regression of sea level on weather. Rev. of Geophys., **6**, 129–134.

GUZA, R. T. and E.B. THORNTON (1981): Wave set-

up on a natural beach. J. Geophy. Res., **86**, 4133–4137.

HARRIS, F. J. (1978): On the use of windows for harmonic analysis with the discrete Fourier transform. Proc. Inst. Electrical and Electronics Eng., **66**, 51–83.

HWANG, J. P. (1971): On the variation of sea level due to meteorological disturbances on the coast of Korea. 1. Storm surges caused by typhoon Billie, 1970, on the west and south coasts of Korea. J. Oceanolog. Soc. Korea, **6**, 92–98 (in Korean).

ISOZAKI, I. (1968): An investigation on the variations of sea level due to meteorological disturbances on the coast of Japanese Islands (II): Storm surges on the coast of the Japan Sea. J. Oceanogr. Soc. Japan, **24**, 178–190.

ISOZAKI, I. (1969): An investigation on the variations of sea level due to meteorological disturbances on the coast of Japanese Islands (III): On the variation of daily mean sea level. J. Oceanogr. Soc. Japan, **25**, 91–102.

KANG, G. Y. (1988): Numerical computation of storm surges for the northern Korean coasts of the East Sea. Korean Meteorol. Hydrol., **4**, 27–29 (in Korean).

KANG, S. W., D. Y. LEE, K. S. PARK, J. S. SHIM, B. C. OH, K. C. JUN and S. I. KIM (1988): Hindcast of typhoon waves at the South and East Sea of Korea. Ocean Res., **10**, 57–67 (in Korean).

LAPPO, S. S., A. V. SKRIPNIK and A. B. RABINOVICH (1978): Relation between atmospheric pressure and sea level in the Northwestern Pacific Ocean. Soviet Meteorol. Hydrol., **12**, 50–55.

LIKHACHEVA, O. N. (1984): Induced sea-level variations off the coasts of the Kuril Island Chain in the synoptic range of frequencies. Oceanology, **24**, 190–194.

LIKHACHEVA, O.N. and A.B. RABINOVICH (1986a): Estimation of spatial and temporal scales of atmospheric processes in the energy-active zones of the world ocean. Integrated Global Ocean Monitoring. Proc. International Symposium, Tallinn, USSR, October 2–10, 1983, Vol.3. Leningrad: Gidrometeoizdat, 319–327.

LIKHACHEVA, O. N. and A. B. RABINOVICH (1986b): Reaction of sea level to variations in atmospheric pressure in the Kuril Ridge area. Oceanology, **26**, 704.

LIKHACHEVA, O. N. and A. V. SKRIPNIK (1981): Formation of weather fluctuations of sea level in the vicinity of the Kuril Chain. Izvestiya, Atmos. and Oceanic Phys., **17**, 372–377.

LONGUET-HIGGINS, M. S. and R.W. STEWART (1964): Radiation stresses in water waves: a physical discussion, with applications. Deep-Sea Res., **11**, 529–562.

MUNK, W. H., B. D. ZETLER and G. GROVES (1965): Tidal cusps. Geophy. J. Roy. Astron. Soc.,**10**, 211–219.

MURTY, T. S. (1984): Storm Surges - Meteorological Ocean Tides. Ottawa, Canada: Dept. Fisheries and Oceans, 897 pp.

OH, I. S., S. I. KIM and J. H. BONG (1988): Storm surges by the typhoons passing through the South Sea of Korea. J. Korean Meteorol. Soc., **24**, 72–84 (in Korean).

OH, I. S. and S. I. KIM (1990): Numerical simulations of the storm surges in the seas around Korea. J. Oceanolog. Soc. Korea, **25**, 161–181.

PUGH, D.T. (1987): Tides, Surges and Mean Sea-Level. Chichester: J.Wiley, 472 pp.

RABINOVICH, A. B. and S. E. SOKOLOVA (1985): Multiple regression for the analysis of sea level variations in the region of Kuril Islands. Theoretical and Experimental Investigations of Long Wave Processes. Vladivostok: FEB USSR Acad. Sci., 158–168 (in Russian).

RABINOVICH, A. B. and S. E. SOKOLOVA (1992): On organizing a catalogue of storm surges for the Sea of Japan. Natural Hazards, **5** (**1**).

RIKIISHI, K. (1986): The tidal and natural oscillations of the Japan Sea. Mar. Science, **18**, 448–455 (in Japanese).

SATAKE, K. and K. SHIMAZAKI (1988): Free oscillation of the Japan Sea excited by earthquakes –II. Model approach and synthetic tsunamis. Geophy. J., **93**, 457–463.

THOMPSON, R. O. R. Y. and B. V. HAMON (1980): Wave setup of harbor water levels. J. Geophys. Res., **85**, 1151–1152.

SKRIPNIK, A. V. and S. E. SOKOLOVA (1990): Peculiarities of storm surging in the region of South Kuril Islands. Natural Catastrophes and Disasters in the Far Eastern Region. Vladivostok: FEB USSR Acad. Sci., 294–311 (in Russian).

WROBLEWSKI, A. (1978): Determination of sea levels by the method of weightening functions in a linear system of three correlated inputs. Archiwum Hydrotechniki, **25**, 159–172.

WUNSCH, C. (1972): Bermuda sea level in relation to tides, weather, and baroclinic fluctuations. Rev. Geophys. Space Phys., **10**, 1–49.

ZETLER, B. D. and W.H. MUNK (1975): The optimum wiggliness of tidal admittances. J. Mar. Res., **33**, Supp., 1–15.

La mer 30: 213–221, 1992
Société franco-japonaise d'océanographie, Tokyo

On the distribution of bottom cold waters in Taiwan Strait during summertime

Joe WANG* and Ching-Sheng CHERN*

Abstract: The general behavior of a stratified current flowing into Taiwan Strait has been studied from CTD and ADCP surveys conducted in the summer. Spatial distributions of hydrographic parameters have provided significant clues for illuminating the effect of topography on flows in the strait. Cold and saline waters in the northern Taiwan Strait mainly appear in the west, for example, but not at the eastern portion of the strait. A northwestward protruded, underwater cold and saline water tongue at north of Peng-hu also always exists. The tongue, being likely a permanent feature appearing from the spring to the autumn, is caused by flow separation due to topographic effects of the Chang-Yuen sand ridge on the incoming stratified currents. Surface waters, being lighter than bottom waters, are able to flow over the ridge. Bottom waters, however, are forced to turn northwestward along the depth contour and enter into the western strait. Field ADCP measurements have suggested the total transport of the latter to be of the order of 0.2 to 0.3 Sv in the summer.

1. introduction

Upwelling phenomena observed in Taiwan Strait (TS) have recently drawn particular attention (e. g. CHEN *et al.*, 1982; CAI and LENNON, 1988; XIAO, 1988; LI and LI, 1989). Previous investigators have reported upwelling phenomena being frequently seen along the west bank of TS during summertime. One of the two major upwelling centers was found on the northwest side of Formosa Banks. The other was found near Hai-tang Island in northern Fuchien. These phenomena have been repeatable, seasonal processes. Wind stress, ocean circulation and bottom topography have all been relevant to the behavior of upwelling in TS.

Some topics appearing in the above-mentioned literatures, however, are incomplete. The blocking effect exerted by the shallow Formosa Banks to incoming stratified currents from the South China Sea (SCS), for example, was ignored by most of these authors (except LI and LI, 1989). The topography used by CAI and LENNON (1988) for their numerical examinations was oversimplified. Additionally, important features of both Peng-hu Channel and the submarine ridge north of Peng-hu were also absent in their modeling. The real situation has still remained obscure, even though LI and LI (1989) showed that the source of upwelled cold waters in TS comes from the northern SCS and they postulated three possible conduits for them.

Upwelling in TS is a significant process for the strait dynamics. The path as well as the flux of upwelled cold waters are also of central importance to local hydrography. General features of upwelling phenomena in TS were descriptively reported in previous literatures. The detailed mechanisms, e.g. the topographic adjustment of a stratified current after it entering TS and its responses to prevailing winds are, however, not clear. The adjustment process is emphasized here, and some of our surveys in TS during the past several summers are reported. The purpose of this paper is to explore the general behavior of a stratified current entering the rugged TS during a calm wind condition. Some of the above-mentioned ambiguities, e.g. the persistency, possible paths and volume transport of the cold inflow in TS are expected to be cleared up by the data acquired during field surveys. The methodology is briefly discussed in section 2.

* Institute of Oceanography, National Taiwan University Taipei, Taiwan, China

The characteristics of transect profiles and plane contours of hydrographic parameters are described in section 3. The ADCP measurements are reported in section 4. The topographic effect induced by a submarine ridge in TS on the incoming stratified current is addressed in section 5. Conclusions are presented, after the discussion of some relevant topics for future studies, in section 6.

2. Data and methodology

Field data of both CTD and ADCP, which were acquired from several summer cruises of the R/V Ocean Researcher I (ORI) during 1988 and 1989 (Table 1), were used for exploring the behavior of bottom waters in TS. An NBIS CTD with 32 Hz sampling rate was used on each station for monitoring the vertical profiles of temperature (T) and salinity (S) in real time. The CTD group was requested during each cast to descend the CTD underwater unit as close (within 2 m) to the seabed as possible. This was done since the property of the bottom water is of central importance to later analysis. In addition to the CTD casts, a shipborne RDI 150 kHz ADCP was used in each cruise (except ORI 161) for detecting the velocity of water flowing underneath the keel of the ship during the voyage. The ADCP was set in the bottom tracking mode with 4 m bin length and a 5 minutes sampling interval.

Table 1. Period and measurement items of ORI cruises used.

Cruise	Period	Items
161	1988/ 6/ 7—6/10	CTD only
169	1988/ 7/27—7/30	CTD and ADCP
177	1988/ 9/ 1—9/ 6	CTD and ADCP
214	1989/ 6/13—6/16	CTD and ADCP

The kinematic bottom boundary condition for inviscid flows over a solid bottom, i.e. the free-slip condition, implies that the bottom surface is a three dimensional stream surface (YIH, 1979). Any isothermal, isohaline or isopycnal surfaces may be inferred here also to similarly be three dimensional stream surfaces according

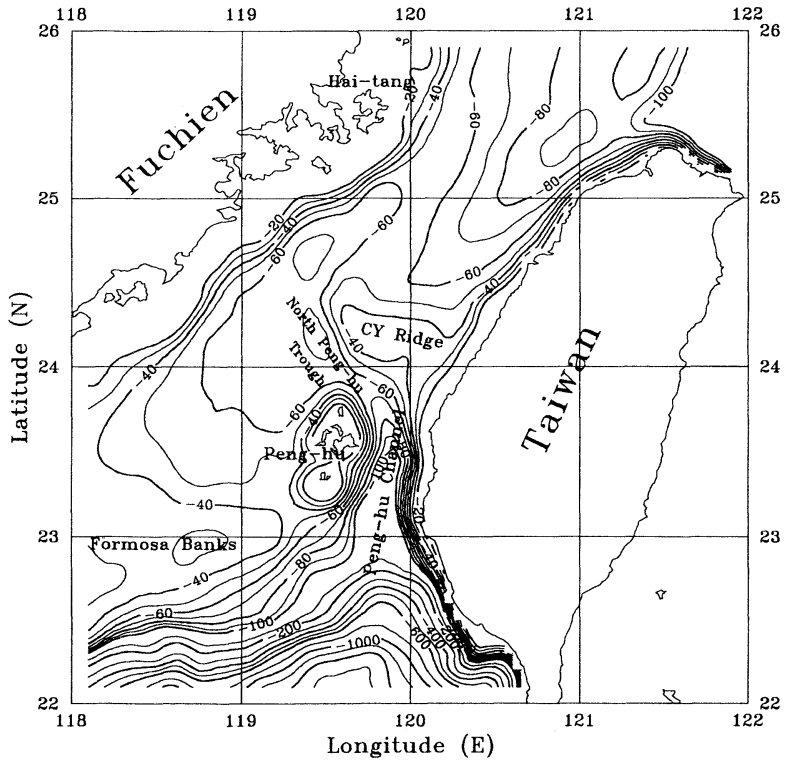

Fig. 1. The smoothed depth contour of Taiwan Strait (meters).

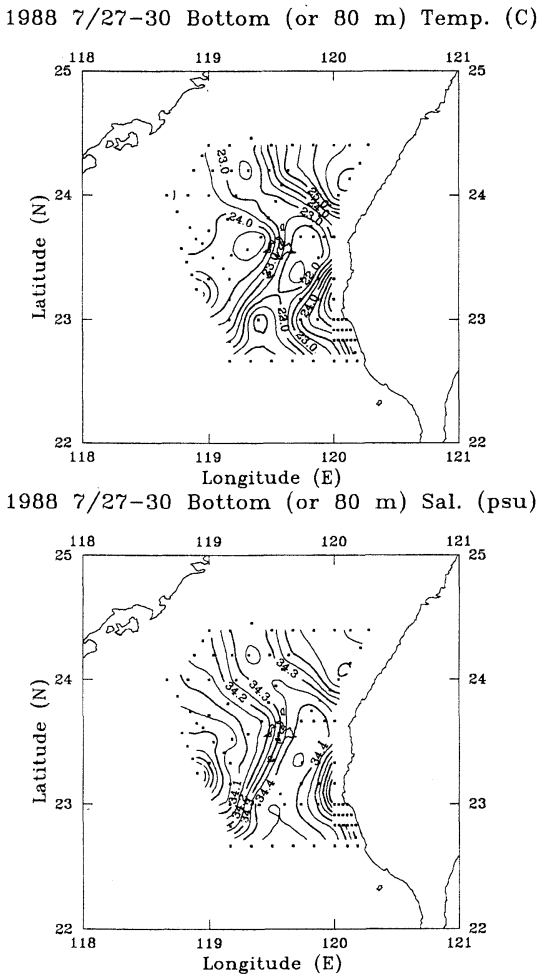

Fig. 2. Contours of T (℃, upper panel) and S (psu, lower panel) at 80 m depth or just above the bottom of TS during ORI 169, 1988 7/27-7/30.

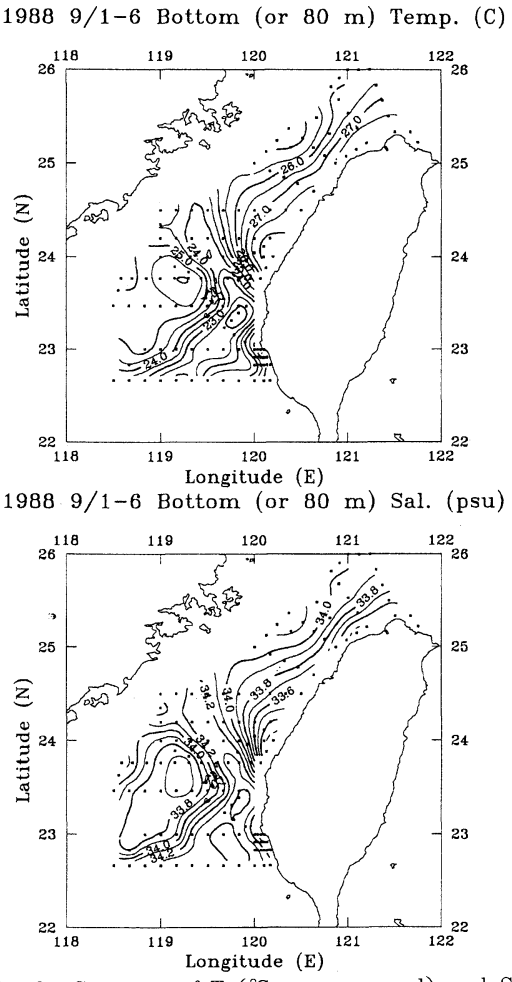

Fig. 3. Contours of T (℃, upper panel) and S (psu, lower panel) 80 m depth or just above the bottom of TS during ORI 177, 1988 9/1-9/6.

to the conservation of heat, salt and mass, if mixing is negligible and the flow is steady. The intersection of any two of these surfaces marks a streamline. This idea could be extended to a number of real situations. For example, isotherms (or isohalines and isopycnals) on the bottom surface may signify streamlines, if vertical profiles of either T or S are vertically uniform near the bottom and lateral mixing is negligible. The path and lateral boundary of cold flows on the bottom could be easily defined according to this argument. A core region composed by cold and saline waters could be determined here for each hydrographic section once the path and lateral boundary had been marked. Volume transport within the core would then be obtained from that determination and corresponding ADCP measurements.

3. Bottom topography and hydrographic patterns

An overview of the bottom topography of TS may be useful before addressing the hydrography. The submarine canyon (the Peng-hu Channel), that lays offshore of southwest Taiwan, is perhaps the most striking feature of the bottom topography of TS (Fig.1). The northwestward extension of the canyon is called the

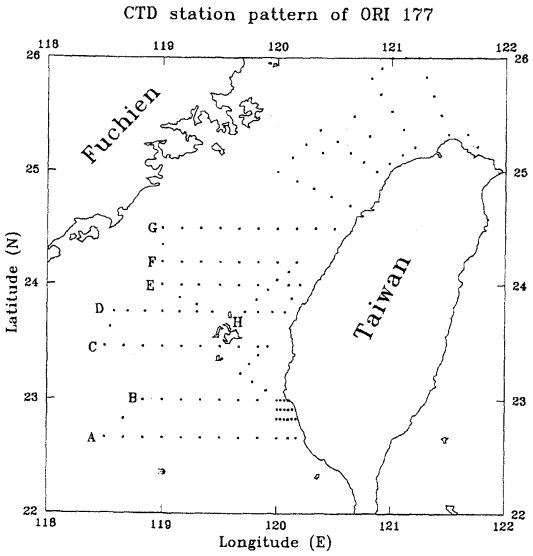

Fig. 4. The station pattern of CTD casts during ORI 177, 1988 9/1–9/6. Capital letters denote different sections. Sections A to G run from east to west. Only Section H runs from southwest to northeast.

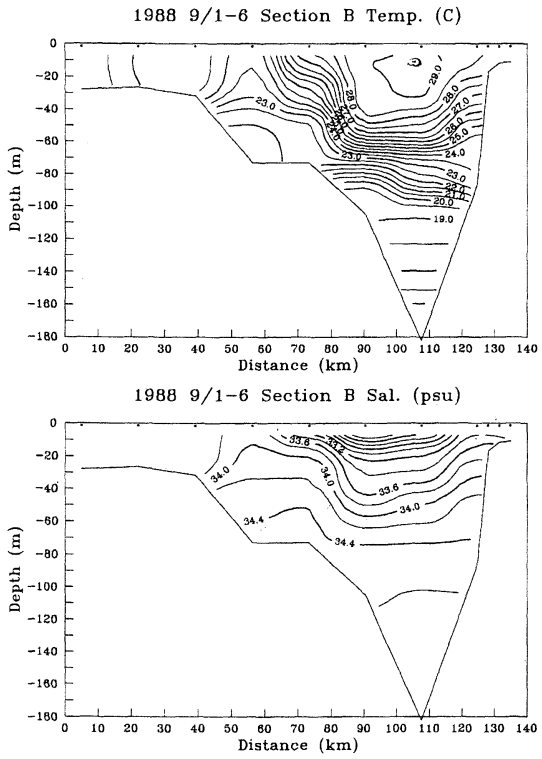

Fig. 5. Vertical transects of T (℃, upper panel) and S (psu, lower panel) along Section B of ORI 177.

North Peng-hu Trough hereafter. It joins the Peng-hu Channel northeast of Peng-hu Islands and is also a principal part of the submarine trough system in TS. Three highlands, in addition, exist in TS, i.e. Formosa Banks, Peng-hu Islands and a southeast-northwest oriented ridge at north of Peng-hu (the Chang-Yuen sand ridge or CY ridge; WANG and CHERN, 1989). The CY ridge and its extension divide the southwest and the northeast TS roughly into two basins (the south basin and the north basin for later reference). All of these features are likely to influence the flow pattern and the hydrography of TS as well.

The spatial distribution of passive parameters, e.g. T and S, could be used, under certain conditions, to signify the pattern of bottom flows (Section 2). Figs. 2 and 3 are two typical examples. The depth of 80 m is selected arbitrarily to be an upper limit since the majority portion of TS is shallower than 80 m (Fig. 1). Data used for the drawings of Figs. 2 and 3 are either at 80m depth or just above the bottom if the water depth is less than 80m.

A cold and saline water tongue appearing at north of Peng-hu is striking and common to all summer cruises of Table 1. Cold and saline waters that compose the tongue stem from the east of Formosa Banks and extend into the Peng-hu Channel. They turn northwestward after passing Peng-hu and form a protruded tongue-like pattern (Figs.2 and 3). Two relatively warmer but less saline regions exist on both sides of the tongue. One is located at the north basin. The other occupies a significant portion of the south basin and Formosa banks (Fig.3). Lateral rims of cold waters are, interestingly, almost parallel to local isobaths of 70 m on the left or 60 m on the right. Topographicall steering is the primary mechanism leading to the observed apparent trajectory of cold waters. Bottom streamlines on the south slope of the CY ridge are, moreover, directed to the northwest in a divergent manner. They, however, turn clockwise and converge to the northeast after passing the ridge (Figs. 2 and 3). The anticyclonic turning and convergence of streamlines can be qualitatively attributed to the cross-isobath movement due to

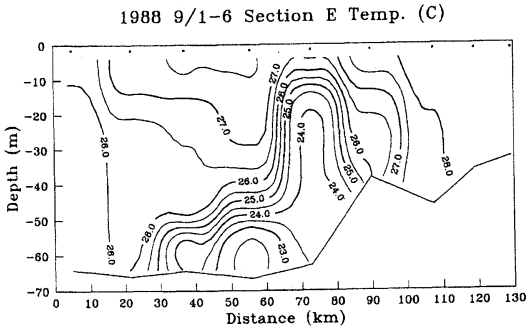

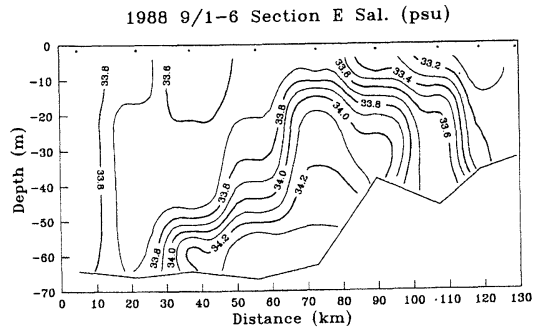

Fig. 6. Vertical transects of T (℃, upper panel) and S (psu, lower panel) along Section E of ORI 177.

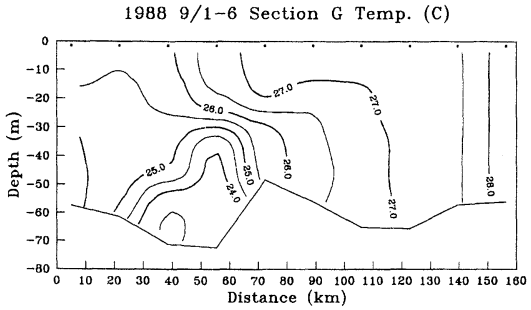

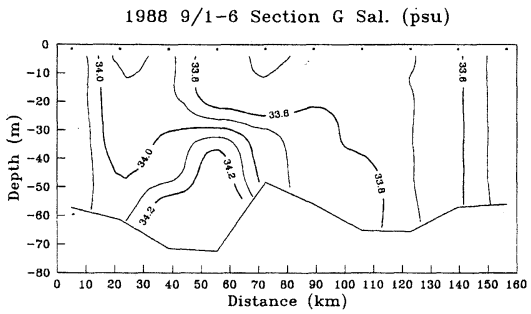

Fig. 7. Vertical transects of T (℃, upper panel) and S (psu, lower panel) along Section G of ORI 177.

waters flowing over the ridge. This flow pattern is dictated by the conservation of potential vorticity (NOF, 1979). The other warm region west of Peng-hu and north of Formosa Banks is also an interesting place. It unfortunately lies largely beyond the survey areas and must be the focus of future study.

The basic configuration of the tongue-like pattern is likely permanent from the spring through the summer to the autumn. This is reasonable since the basic aspects of the tongue-like pattern found in June, July and early September (as well as other two cruises in May of both 1988 and 1989 which are not included in Table 1) were approximately the same, but different from other winter cruises (WANG and CHERN, 1989). Therefore, a quasi-steady state assumption is acceptable. The cruise ORI 177 has been selected here for illustrating the details of the tongue. Several transects of T and S of ORI 177 shown in Fig. 4 are presented in Figs. 5–7. The water column is basically well-stratified in the Penghu Channel. It becomes, however, weakly stratified or uniform toward the west (Section B, Fig. 5). A different pattern is apparent at sections north of the CY ridge, where the water column is nearly uniform along the east bank, but more stratified toward the left bank of TS (Section G, Fig. 7). The action of near-bottom turbulence is not likely to be negligible there, considering the shallowness of the south basin and the vigorousness of tidal currents. An equilibrium between advective and detrainment processes is implied by the existence of a permanent tongue structure. The tongue-like pattern can not be maintained in the North Peng-hu Trough, unless a continuous supply of cold and saline waters exist in order to compensate the detrainment loss due to mixing. The existence of an undercurrent is implied by this.

4. ADCP measurements

Vertical sections of ADCP measurements during ORI 177 are presented in Figs. 8–10 for illustrating the spatial structure of the current field in TS. Corresponding hydrographic contours are

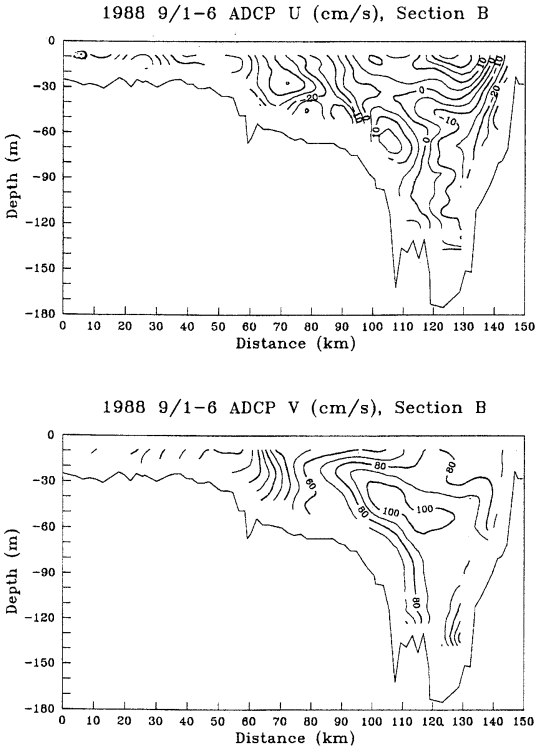

Fig. 8. Vertical transects of the eastward velocity component, U (cm s^{-1}, upper panel), and the northward velocity component, V (cm s^{-1}, lower panel), of ADCP measurements along Section B of ORI 177.

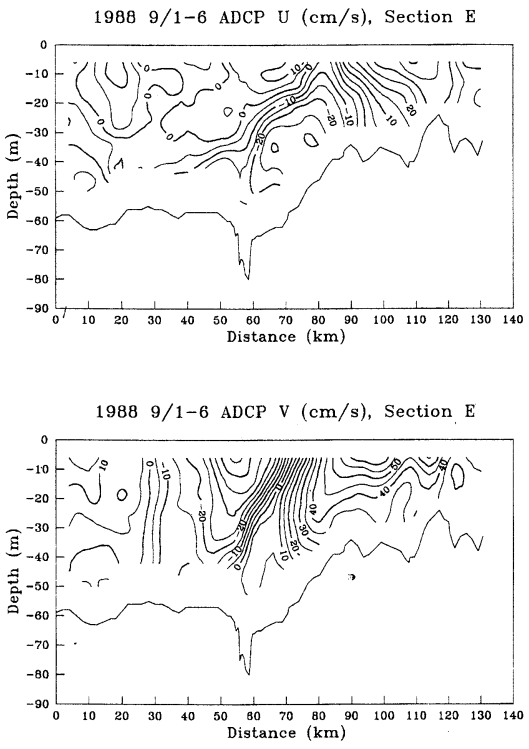

Fig. 9. Vertical transects of U (cm s^{-1}, upper panel) and V (cm s^{-1}, lower panel) of ADCP measurements along Section E of ORI 177.

shown in Figs. 5–7. Tidal currents are not feeble within the survey area. Aliasing induced by tidal variation is therefore embedded within these measurements. An apparent current, with a strength of the order of 80–120 cm s^{-1}, is shown by ADCP surveys (Figs. 5–7). It is along the eastern edge of the plateau which is composed by Formosa Banks and Peng-hu Islands. The current flows through Peng-hu Channel toward the CY ridge in the upper layer. The direction of the current changes from ENE (Section A) to NNE (Sections B and C), then to NNW (Section H) in front of the CY ridge. The current veers on and after passing the ridge from NE (Section E) to ENE (Section F). Its strength is significantly reduced. The axis of the stream, on the other hand, shifts more toward Peng-hu Island as it approaches the end of Peng-hu Channel. The uphill slope of the CY ridge is encountered by the flow there. A cyclonic turning with positive vorticity is then presented in Sections A to C. An anticyclonic veering associated with negative vorticity, however, successively occurs in Sections H, E and F. An undercurrent is, additionally, found in the lower layer to be flowing northwestward along the North Peng-hu Trough (Sections E and F; the former is shown in Fig. 9). The undercurrent veers to the northeast at a further downstream section to coincide with the orientation of local isobath (Section G, Fig. 10). In comparison with corresponding hydrographic patterns, a close correlation between the undercurrent and the cold water core is found; e.g. the zero contour of the eastward velocity component along Section E (Fig. 9, upper panel) roughly agrees with the isoline of either 26.5℃ or 33.7 psu (Fig. 6). Similar features are observed in other sections.

Tidal currents are significant in TS; the amplitude of the lunar principal, M_2 constituent, is approximately 70 cm s^{-1} in the Peng-hu Channel (CHUANG, 1985). Tidal currents cause aliasing

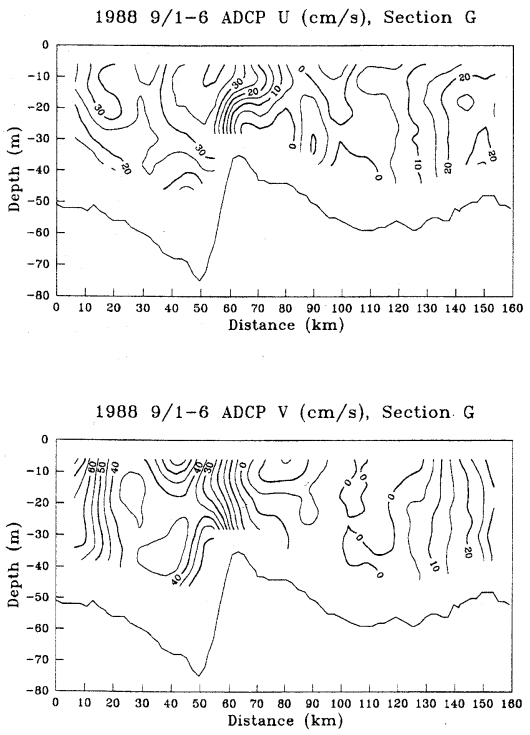

Fig. 10. Vertical transects of U (cms^{-1}, upper panel) and V ($cm\ s^{-1}$, lower panel) of ADCP measurements along Section G of ORI 177.

in ADCP measurements since they fluctuate periodically. Removing tidal influences from ADCP data is feasible if a precise tidal current prediction is provided. Another method is to take average over profiles from repeaed observations.

The procedure for the estimation of volume transport is straightforward. A common isoline of either T or S is first selected here from transect diagram of T or S as the bounding surface for defining the core of the cold water along the stream. The surface of 34.1 psu (and therefore 25.0℃) is chosen from hydrographic sections of ORI 177 to be the bounding surface. The velocity component normal to the section is next calculated from ADCP measurements. Extrapolation is carried out to fill in the blanked layers above the bottom. The volume transport is then estimated after integrating the normal velocity over the core area. The estimations are respectively 0.1, 0.4, 0.5 and 0.2 Sv for sections from E to H. A mean value of approximately 0.3 Sv is obtained for ORI 177. The validity of this procedure depends on the streamwise length scales for both the cold current and the tidal current, which must be much larger than the extent of the survey area. The values obtained remain tentative estimations because of poor knowledge of the length scales.

Table 2. The estimated volume transport of the cold current

Cruise No.	Transport (Sv)	Note
169	0.2	Average of 4 sections
177	0.3	Average of 4 sections
214	0.2	Average of 3 sections

Similar calculations for other cruises, but based on different criteria of T and S, have been made. Results are presented in Table 2.

Obtaining the exact quantity of volume transport is not an easy task. The validity of the foregoing estimations, however, could be judged indirectly by cross-checking with other observations such as measurements of moored current meters. The mean velocity of the near-bottom current at the north end of Peng-hu Channel was reported to be approximately 32 $cm\ s^{-1}$ during the 1984 summer (CHUANG, 1986). The value 30 m × 40 km is perhaps not an unreasonable estimation for the cross-sectional area of the undercurrent. By supposing the core pattern and the seasonal mean current remain roughly the same in different summers, a transport of 0.4 Sv is then obtained. This value is consistent with those shown in Table 2. The estimates obtained above seems to be robust, and the transport of the cold current in the summer is believed to be of the order of 0.2 to 0.3 Sv.

5. Topographic effect

The formation of a permanent undercurrent in TS could be interpreted in terms of flow–topography interactions. The phenomenon may be considered here from two points of view. For a rotational, steady and inviscid stratified flow under Boussinesq approximation, a quantity of

$$\frac{p}{\rho_0}+\frac{1}{2}u^2+g'z$$

is constant along a streamline, where p represents the departure from hydrostatic pressure; ρ_0 is the reference density at the free surface $z=0$; u is the water speed; and g' is the reduced

gravity (PHILLIPS, 1977). The width of the CY ridge is approximately 40 km (Fig.1), and we estimate $g' = 10^{-2}$ m s^{-2} and layer thickness of both surface and bottom waters to be 50 m from typical density profiles in Peng-hu Channel. These give the baroclinic Rossby deformation radius for the flow to be 10 km, much less than the scale of the CY ridge. The bottom flow in the vicinity of the CY ridge is then likely to be quasi-geostrophic.

Both isobars and isopycnals are equivalent to streamlines for a geostrophic flow. The latter then has to precisely follow the depth contour. The variation of pressure along a streamline is likely to be negligible if the flow is quasi-geostrophic, as compared to a variation of other terms in the Bernoulli invariant. Cross-isobath motions along a streamline basically involve the conversion of kinetic energy to potential energy. The criterion for quasi-geostrophic bottom currents which can not overpass the CY ridge is then likely to be

$$\frac{1}{2} V_0^2 < g' \Delta z,$$

where V_0 denotes the velocity of bottom flows at the entrance of the channel; Δz is the elevation difference between the top of the ridge and the base plane. Substituting g', $V_0 = 32$ cm s^{-1} (CHUANG, 1986) and Δz (about 40 m (Fig.1)) into the inequality, the bottom flow in Peng-hu Channel is considered not energetic enough to surmount the CY ridge; flow separation has to occur. The most suitable destination for the subsurface heavy water can be expected from the bottom topography (Fig. 1) to be the North Peng-hu Trough, which provides an optimum path to the cold inflow. The process of topographical steering dictates that separated subsurface waters flow northwestward along the trough and form a cold and saline tongue there. The deflection of bottom current exports cold and saline waters from the Peng-hu Channel toward Fuchien coast. This deflection initiates the laterally asymmetric density distribution found in downstream sections at the northern TS.

Light fluids aloft can easily overpass the CY ridge. This is in contrast to the underlying subsurface heavy waters in the Peng-hu Channel. When the surface layer water escapes from the channel and encounters the CY ridge, the water column expands laterally due to the widening of the water body and is compressed vertically due to the reduction of water depth. Both effects cause the current system to enter into a state of adjustment. Surface waters are assumed, for simplicity sake, to be homogeneous and the incoming current is assumed uniform, geostrophic and hydrostatic at the entrance of Peng-hu Channel. The situation is then geometrically and dynamically analogous to that studied by NOF (1978). A critical Rossby number Ro_C considered by NOF is of central importance to the adjusting flow pattern. A subcritical flow associated with an anticyclonic turning of streamlines appears on the ridge if the flow Rossby number $Ro > Ro_C$ (NOF, 1978, Fig. 3b). A supercritical flow emerges if $Ro < Ro_C$. Flow separation occurs, in this case, at the right wing of the current facing downstream (NOF, 1978, Fig. 4b).

The flow widens by a factor of about 2, from the CY ridge to Peng-hu Channel (Fig. 1). The initial thickness and the later reduction of thickness for the surface water are respectively 60 m and 20 m if the isothermal surface 26.0℃ is arbitrarily selected as the lower boundary of the upper layer. $Ro_C = O(0.4)$ is then achieved according to NOF's (1978) formula. A critical inflow velocity $Vo_C = 48$ cm s^{-1} is obtained with the width of Peng-hu Channel assumed to be 20 km. The velocity of upper layer currents during summertime in Peng-hu Channel usually exceeds this value (Fig. 8). No lateral separation then occurs on the CY ridge. The situation may signifieantly change in other seasons due to the weakening of northward flows. Flow separation is apparently unavoidable in winter. It may cause a southward flow region to the east of the CY ridge (WANG and CHERN, 1989).

6. Discussion and concluding remarks

A quasi-permanent, cold and saline undercurrent is found from previous CTD and ADCP measurements; it flows steadily along the North Peng-hu Trough then enters the western TS during summertime. The existence of this undercurrent appears to answer a number of questions on the source and path of cold waters in TS. This, however, is still insufficient for

interpreting the appearance of cold waters at northwest of Formosa Banks (LI and LI, 1989). The problem could be solved in terms of a study of WHITEHEAD (1985).

The coast of Fuchien is assumed, for simplicity sake, to be vertical and the bottom of the south basin is flat. The situation is dynamically similar to that analyzed by WHITEHEAD (1985), if the undercurrent is uniform both horizontally and vertically at the entrance of North Peng-hu Trough and the upper layer is motionless under a rigid-lid approximation. More than 85 % of the total volume transport will turn to the right, and the remainder 15 % to the left. This occurs due to the angle between the axis of the cold stream and the coastline of Fuchien being approximately 30°. The remaining 15 % may be theoretically expected to export cold and saline waters to the offshore of south Fuchien. What has actually occurred has yet to be determined and perhaps be the focus of future study.

The general behavior of currents in TS has been studied, based on CTD and ADCP surveys in TS during previous summers. The stratified incoming current in the Peng-hu Channel is found separating vertically in front of the CY ridge. Waters in the upper layer overrun the ridge. Subsurface heavy waters, however, turn to the northwest and form a permanent cold and saline water tongue protruding toward Fuchien coast during summertime. The volume transport of the cold current is estimated to be 0.2–0.3 Sv from ADCP measurements.

Acknowledgments

This work was sponsored by the National Science Council, the Republic of China, Grant No. NSC90-0209-M002A-19.

References

CAI, W. and G.W. LENNON (1988): Upwelling in the Taiwan Strait in response to wind stress, ocean circulation and topography. Estuarine, Coastal and shelf Science, **26**, 15–31.

CHEN, J., Z. FU and F. LI (1982): A study of upwelling over Minnan-Taiwan Shoal fishing ground. Taiwan Strait, **1**, 5–13 (in Chinese).

CHUANG, W.-S. (1985): Dynamics of subtidal flow in the Taiwan Strait. J. Oceanogr. Soc. Japan, **41**, 65–72.

CHUANG, W.-S. (1986): A note on the driving mechanisms of current in the Taiwan Strait. J. Oceanogr. Soc. Japan, **42**, 355–361.

LI, L. and D. LI (1989): Summer hydrographic features of channel west of Taiwan Shoal and the coastal upwelling. Taiwan Strait, **8**, 353–359 (in Chinese).

NOF, D. (1978): On geostrophic adjustment in sea straits and wide estuaries: Theory and laboratory experiments. Part 1: One-layer system. J. Phys. Oceanogr., **8**, 690–702.

PHILLIPS, O.M. (1977): The dynamics of the upper ocean. Second ed., Cambridge Univ. Press., New York.

WANG, J. and C.-S. CHERN (1989): On cold water intrusions in the eastern Taiwan Strait during the cold season. Acta Oceanogr. Taiwanica, **22**, 43–67 (in Chinese).

WHITEHEAD, J. A. (1985): The deflection of a baroclinic jet by a wall in a rotating fluid. J. Fluid Mech., **157**, 79-93.

XIAO, H. (1988): Studies of coastal upwelling in weatern Taiwan Strait. Taiwan Strait, **7**, 2, 135–142 (in Chinese).

YIH, C.-S. (1979): Fluid Mechanics, a concise introduction to the theory. Corrected edition, West River Press, Michigan.

La mer 30: 223–228, 1992
Société franco-japonaise d'océanographie, Tokyo

The influence of Taiwan Strait waters on the circulation of the Southern East China Sea

Ching-sheng CHERN* and Joe WANG*

Abstract: The circulation on the shelf north of Taiwan is determined by the dynamic balance between outflow from Taiwan strait and intruding Kuroshio subsurface water. When the strait flow is strong, the Kuroshio intrusion is confined to the outer shelf and the salinity of the surface layer waters on the shelf has a typical value below 34 psu. With decreasing strait outflow, the cool and saline Kuroshio subsurface water penetrates further into the midshelf of the southern East China Sea. As this current provides a major source of salt, the salinity becomes greater than 34.1 psu for waters around northern Taiwan offshore area under these conditions.

1. Introduction

Taiwan strait is a channel of shallow water connecting the East China Sea (ECS) and the South China Sea. Previous studies showed that there is a persistent northward flow through the strait. This current reaches a maximum, about 50 cm/s, in summer and decreases to about 10 cm/s during the northeast monsoon season in winter (CHUANG 1986, CHERN and WANG, 1989).

Along the east coast of Taiwan, the Kuroshio current flows steadily northward. After leaving the coast of Taiwan, the main stream turns northeast along the continental slope in the ECS. At the turning point, some cold and saline Kuroshio subsurface waters branch onto the continental shelf as indicated by the pattern of averaged surface velocity (QIU *et al.*, 1990) and hydrographic surveys (CHERN and WANG, 1990a) in this area.

By using a primitive equation general circulation model, CHAO (1990) considered the influence of the northward intruding Kuroshio water and Taiwan Strait water on the circulation pattern over the broad shelf of the ECS. When the outflow from the strait is strong, the advance of the northward intruding water manifests itself as a tongue-like feature over the midshelf. When the strait flow is weak, the intruding Kuroshio water penetrates close to the China coastal area and its front outlines a lopsided shape. This change of the front shape is attributed to seasonal variations of the monsoon winds. Direct hydrographic surveys over the ECS are consistent with this description (WANG, 1987; SONG, 1987).

Because the Taiwan Strait is shallow, its transport is strongly affected by variations in the wind field (WANG, 1990). In addition to the seasonal variation, the flow pattern north of Taiwan responds to alterations of surface winds with a period of several days. We present here two typical CTD surveys of the shelf area north of Taiwan in summer to illustrate this point. These data show that the outflow from the strait is blocked by the westward intruding Kuroshio water when the southwesterly winds are weak. When the southwesterly winds become strong, the strait water flows directly into the ECS and the cold Kuroshio water is displaced farther offshore.

2. Hydrographic observation

The hydrographic surveys were conducted on board the R/V Ocean Research I, during the periods July 1–5 and August 16–19, 1988 over the shelf/slope area near northern Taiwan (Fig. 1). The winds were mainly southwesterlies in the survey area, but varied in strength, during these

* Institute Of Oceanography National Taiwan University, Taipei, China

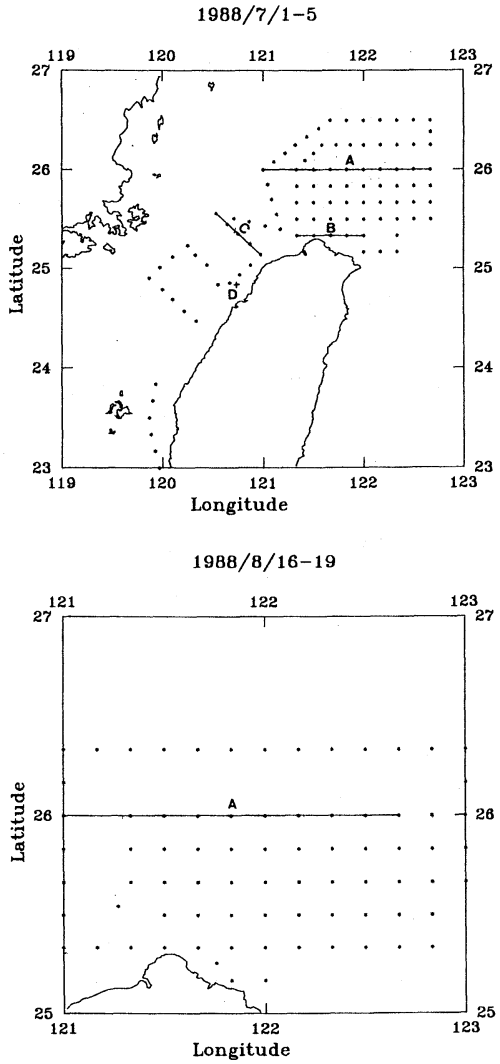

Fig. 1. Hydrographic station locations of the two cruises in July and August 1988. (A, B, C are positions of the three transect lines shown in Figs. 6, 8 and 3 respectively.)

two cruise periods. Fig. 2 is a stick diagram of winds measured, over these two periods, on a platform (station D in Fig. 1); about 25 km off the west coast of Taiwan winds were mild, with average speed of about 5 m/s, during the first cruise and increased to above 10 m/s in the period of the second cruise.

Temperature and salinity data were obtained at each station with a Neil Brown Instrument Systems conductivity-temperature-depth (CTD) meter. Fig. 3 shows temperature and salinity

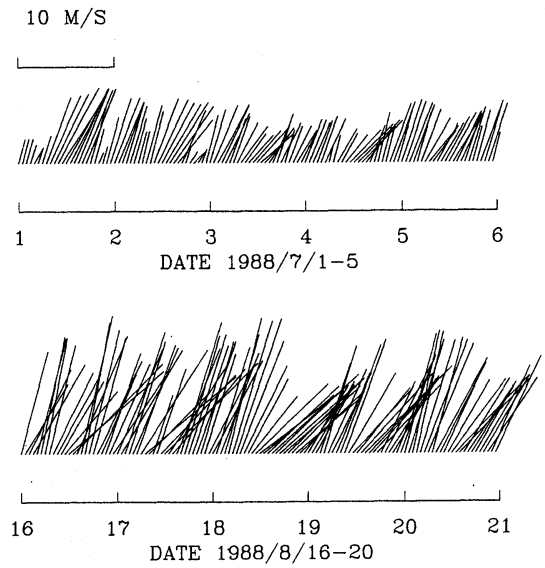

Fig. 2. Stick diagram of wind data measured on an offshore platform, station D in Fig. 1, during the two cruise periods.

transects across the strait (line C in Fig. 1) for the first cruise. The origin of line C is located at 25° 33.5' N, 120° 32' E. The water was weakly stratified with temperature > 27 °C and salinity < 34.1 psu in the eastern portion of the strait, whereas there emerged a distinct two-layer structure in the midstrait. This structure is typical of water in the Taiwan Strait during summer (WANG and CHERN, 1991).

Fig. 4 shows the distribution of temperature and salinity at 50 m depth for the first cruise. The Kuroshio, originating in cool and saline water with temperature < 26 °C and salinity > 34.2 psu, extended westward and tended to block the northeastward warm and less saline water from the eastern strait. Fig. 5 shows the distribution of temperature and salinity at 50 m depth for the second cruise. With increasingly strong southwesterly winds, the eastern strait water flowed northeastward directly into the southern ECS. The upwelled Kuroshio subsurface water is confined to the seaward portion of the shelf/slope area northeast of Taiwan.

Fig. 6 shows temperature and salinity transects at 26° N between 121° E and 122° 40' E (line A in Fig. 1) for the first cruise, and Fig. 7 shows transects along this same line for the second cruise. For mild wind conditions (Fig. 6)

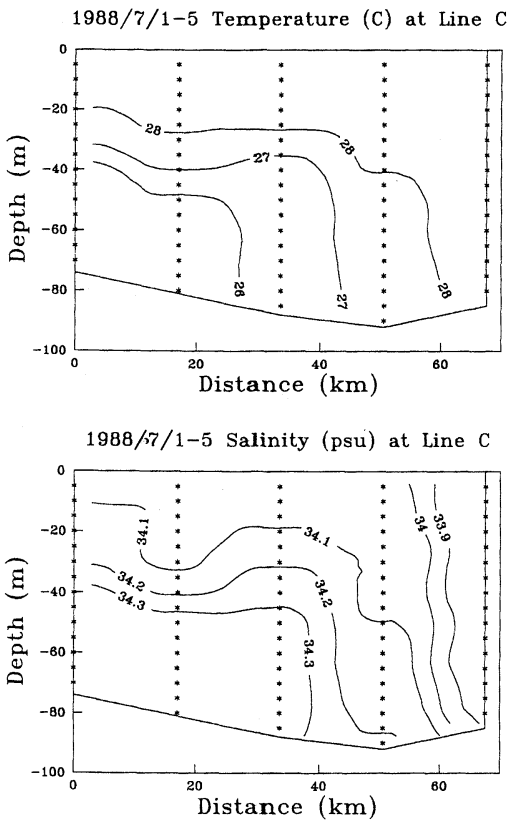

Fig. 3. Cross-strait transect of temperature (upper) and salinity (lower), along line C in Fig. 1, of the cruise during 1988/7/1-5.

over the whole observed shelf region a well stratified structure emerged, with the presence of cool and saline bottom water just below 50 m depth. The warm, little saline and weakly stratified eastern strait water was absent at this line.

For strong southwesterly wind conditions (Fig. 7), the upwelled Kuroshio water occurred at the outer part of the shelf and intruded into the midshelf only near the bottom. The warm and little saline strait water occupied the upper 60 m over the midshelf area.

3. Discussions

Previous observations showed that there is a permanent upwelling center of Kuroshio subsurface water above the shelf break northeast of Taiwan (UDA and KISHI, 1974; FAN 1980; CHERN *et al.*, 1990). The thermal wind effect associated with this upwelling pattern maintains

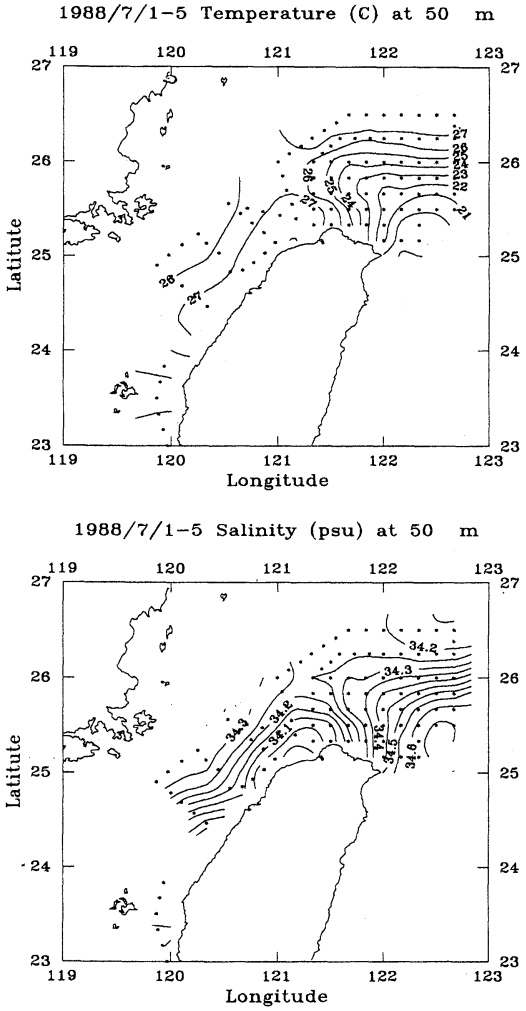

Fig. 4. Horizontal distribution of temperature (upper) and salinity (lower) at 50 m of the cruise during 1988/7/1-5.

a vertical velocity shear in the direction across the stream for incoming flow south of the upwelling front. Cross-stream baroclinic circulation of this kind favors the shoreward intrusion of upwelled Kuroshio water near the bottom of the shelf north of Taiwan. Our previous current measurements at north of Taiwan have shown the existence of a northwestward mean flow of about of 10-20 cm/s near the bottom with water temperature about of 17° C all the year round (CHERN and WANG, 1989).

The shoreward intrusion of upwelled Kuroshio water is a result of adjustment of Kuroshio as it

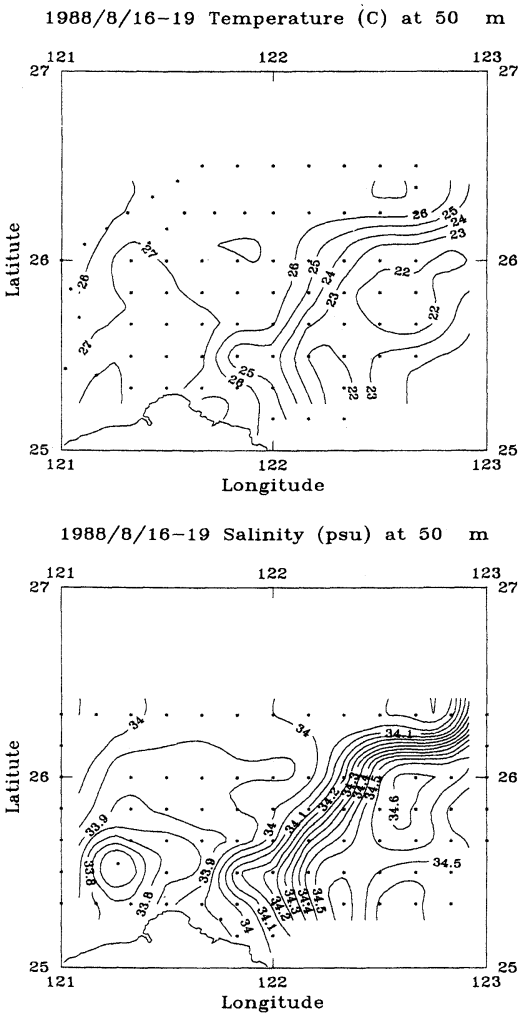

Fig. 5. Horizontal distribution of temperature (upper) and salinity (lower) at 50 m of the cruise during 1988/8/16-19.

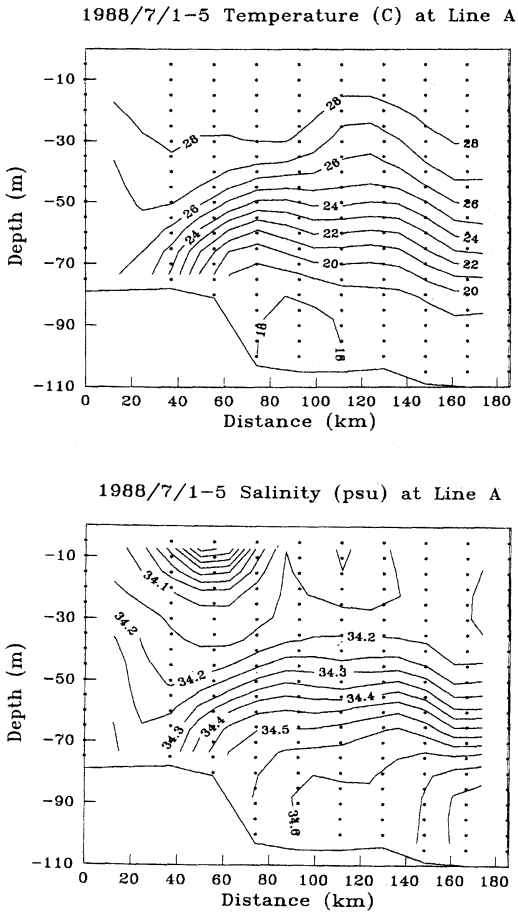

Fig. 6. East-west transect of temperature (upper) and salinity (lower), along line A in Fig. 1, of the cruise during 1988/7/1-5.

flows toward the steep shelf break of ECS; then local winds modulate its strength. In contrast, the flow in the Taiwan Strait shows strong wind-dependent variations. Because the circulation on the shelf north of Taiwan is determined mainly by the dynamic balance between the two jets from both sides of the island, its pattern is sensitive to changes in the wind field. The hydrographic data described above show this feature.

The shelf-edge upwelling of Kuroshio subsurface water provides a major source of salt for waters of the ECS. Our present surveys show that the outflow from the strait has a strong influence on the spreading of the upwelled water. As the strait flow weakens during periods of calm wind, the cool and highly saline upwelled water penetrate deeply into the midshelf region. Under these conditions and with strong vertical mixing maintained by the shear of internal tidal motions in this area (CHERN and WANG, 1990b), the salinity in the surface layer (>34.1 psu) becomes larger than the typical value (<34 psu) for surface water in the southern part of Taiwan Strait. When the strait flow intensifies during a period of strong southwesterlies, surface waters on the shelf near northern Taiwan retain little saline values.

As warm and little saline water leaves the

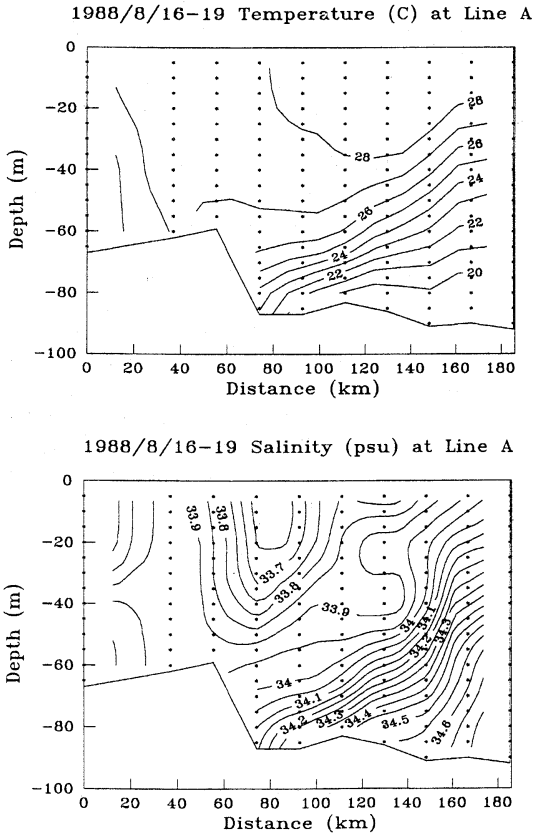

Fig. 7. East-west transect of temperarure (upper) and salinity (lower), along line A in Fig. 1, of the cruise during 1988/8/16–19.

northern end of Taiwan Strait, part of it tends to turn toward the open sea along the northern coast of Taiwan. The temperature and salinity transects (Fig. 8) at 25° 20′ N (line B in Fig. 1), of the first cruise show that waters of the eastern strait, having temperature $>$ 27 °C and salinity $<$ 34.1 psu, occur in the upper 60 to 40 m over the slope region. The data of the second cruise show similar distribution of temperature and salinity along this line. We have also observed a similar offshore transport of shelf waters, but with a larger volume transport under northeasterly wind conditions (CHERN *et al.*, 1990).

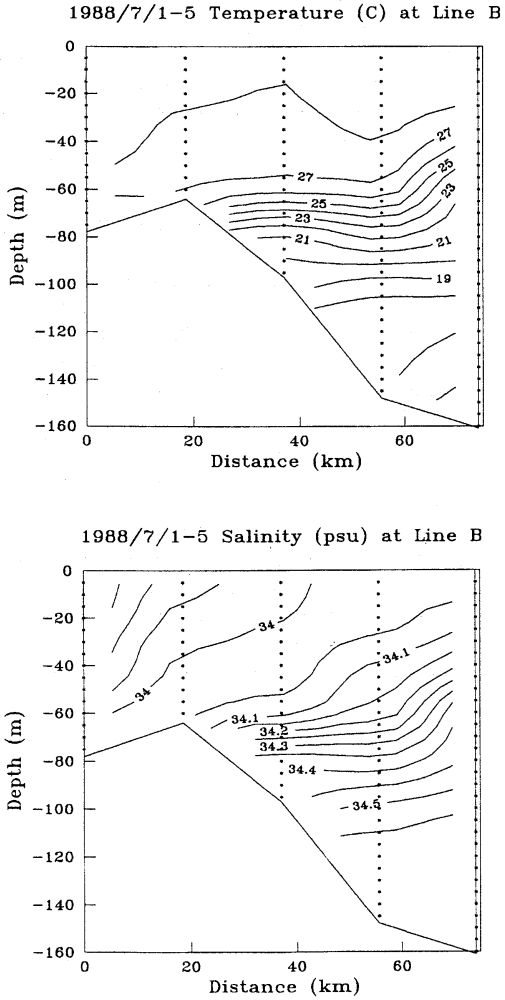

Fig. 8. East-west transect of temperature (upper) and salinity (lower), along line B in Fig. 1, of the cruise during 1988/7/1–5.

Acknowledgment

This study was supported by the National Science Council of the Repubilc of China, under the contract No. NSC80-0209-M002a-7.

References

CHAO, S.Y. (1990): Circulation of the East China Sea, I: The Kuroshio Influence. J. Oceanogr. Soc. Japan., **46**, 273–295.

CHERN, C.S. and J. WANG (1989): On the water masses at northern offshore area of Taiwan. Acta Oceanogr. Taiwan, **22**, 14–32.

CHERN, C.S. and J. WANG (1990a): On the Kuroshio

branch current north of Taiwan. Acta Oceanogr. Taiwan, **25**, 55–64.

CHERN, C.S. and J. WANG (1990b): On the mixing of waters at a northern offshore area of Taiwan. Terrestrial Atmospheric and Oceanic Sciences, **1**, 297–306.

CHERN, C.S. , J. WANG and D.P. WANG (1990): The exchange of Kuroshio and East China Sea shelf water. J. Geophys. Res., **95**, C9, 16017–16023.

CHUANG, W.S. (1986): A note on the driving mechanisms of current in the Taiwan Strait. J. Oceanogr. Soc. Japan., **42**, 355–361.

FAN, K.L. (1980): On upwelling off northeastern shore of Taiwan. Acta Oceanogr. Taiwan, **11**, 105–117.

QIU, B., T. TODA and N. IMASATO (1990): On Kuroshio front fluctuations in the East China Sea using satellite and in situ observational data. J. Geophy. Res., **95**, C10, 18191–18204.

SONG, W. (1987): Physical oceanographic features in the Kuroshio mainstream and its adjacent area in the East China Sea during June to July 1984 (in Chinese with English abstract), Essays on the Investigation of Kuroshio, X. Sun ed., Ocean Press, Beijing, 99–117.

UDA, M. and A. KISHI (1974): Cyclonic cold eddies along the edge of the Kuroshio current in the relation to the genesis and passage of cyclones, I, waters north of Taiwan. *In* Kuroshio III, Proc. 3rd Symp., Bangkok, Thailand, 1972, 199–218.

WANG, J. (1990): Oceanographic observations at CBK-11 platform and CFC drilling area. Special publication No. 61, Inst. Oceanogr., National Taiwan University.

WANG, J. and C. S. CHERN (1992): On the distribution of bottom cold waters in Taiwan Strait during summertime. La mer, **30** 213–221.

WANG, Y. (1987): Physical oceanographic features in the Kuroshio mainstream and its adjacent area in the East China Sea during December 1984 to January 1985 (in Chinese with English abstract), Essays on the Investigation of Kuroshio, X. Sun ed., Ocean Press, Beijing, 133–148.

La mer 30: 229–238, 1992
Société franco-japonaise d'océanographie, Tokyo

Numerical simulation for a northeastward flowing current from area off the Eastern Hainan Island to Tsugaru/Soya Strait

R. LI*, Q. ZENG*, Z. JI* and D. GUN*

Abstract: The upper-layer monthly-mean circulations in the Pacific Ocean are calculated by using a barotropic ocean model with a fine-horizontal resolution. We focus our attention on a northeastward flowing current which is closely related to the currents in the China Sea and Japan Sea. Simulated results show that, both in winter (January) and summer (July), the northeastward current starts from the region off the eastern Hainan Island, passing through the Taiwan Strait, East China Sea, the Korea Strait and Japan Sea, eventually entering the Pacific Ocean through the Tsugaru Strait in winter, but through the Soya Strait in summer. The distribution of the simulated sea surface elevation reveals that the combined effect of the sea surface slope in the direction of the current and that across the current from southeast to northwest is probably one of the major forces driving the current.

1. Introduction

The China Sea is an ideal monsoon region. A strong north or northeast monsoon blows in winter, while a weak south or southwest monsoon prevails in summer. Therefore, many oceanographers have taken it for granted that under the intense influence of the northerly monsoon in winter, the coastal current off the southeast coast of China flows leeward from northeast to southwest. In the late fifties and early sixties, the results obtained from the Chinese National Comprehensive Oceanographic Survey (1958–1960) denounced the traditional concept above about the coastal current off the southeast coast of China. GUAN *et al.* (1964) pointed out the following:

1. In the offshore region of eastern Zhejiang, besides the East China Sea Coastal Current flowing leeward close to the coast, there exists a current flowing northeastward against the wind in the area a little further away from the coast. They named the current "Taiwan Warm Current" at that time.

2. In the nearshore region of Shantou (east of 116° E), there also exists a current flowing northeastward against the wind. In addition, in the coastal area northeast of the Hainan Island, a windward current is also observed. The northeastward flowing currents observed in two regions mentioned above are considered to be connected with each other and are called the "South China Sea Warm Current."

In the early sixties, GUAN *et al.* (1964) conjectured that there might also exist a northeastward windward current in the deep and near-bottom layers of the western part of the Taiwan Strait, and further suggested that this conjecture should be confirmed by future observations. They also conjectured that besides the leeward cold current in winter there exists a windward current flowing northeastward off the southeast coast of China.

Based on the analysis of the observational data, GUAN (1984, 1986) showed that in winter there exists a windward current from the coastal area east of the Hainan Island, passing through the shore region of eastern Guangdong and the western part of the Taiwan Strait, and reaching the shore region of Fujian and Zhejiang.

GUAN (1986) also pointed out that there exists a water passage through the northeast of the South China Sea, Taiwan Strait, northwest of the East China Sea, the Korea Strait, and thought that this water passage has reference to

* LASG, Institute of Atmospheric Physics, Chinese Academy of Sciences

expounding the source of the Tsushima Warm Current.

FANG *et al.* (1988) indicated that the sea surface elevation difference between the Luzon Strait and the area east of Tsugaru and Soya Strait may induce a current starting from northeast of the South China Sea to Tsugaru/Soya Strait. FANG *et al.* (1989) named it "Taiwan-Tsushima-Tsugaru Warm Current System (TTTWCS)."

During investigating this current, GUAN and FANG could only rely on observations at some limited areas because the current measurements are still very scanty (Fig. 2). It is rather difficult to understand the complete picture of such a long current based only on the insufficient observations. Does this current really exist? If it does, what is the driving mechanism of it? Could it be confirmed by numerical simulations?

In order to answer these questions, numerical calculations have been done by using an ocean model which is the simplest form of the ocean-atmosphere coupling models presented by ZENG (1983). Some theories and methods applicable to numerical weather prediction (NWP) models and general circulation models (GCM) developed by Institute of Atmospheric Physics (IAP) have been incorporated into the model (e.g., ZENG *et al.*, 1987). In addition, techniques saving computational time have also been employed in the model (e.g., ZENG *et al.*, 1985, 1990).

2. Sketch of model

In a colatitude-longitude spherical surface coordinate system (θ, λ, z), the vertically-averaged equations of motion and continuity are adopted:

$$\frac{d\vec{v}}{dt} = -\nabla\phi - f^*\vec{k}^0\times\vec{v} - \kappa_2\vec{v} + \frac{\vec{\tau}}{\rho_0 h} + A_m\left[\Delta\vec{v} + \frac{1-\mathrm{ctg}^2\theta}{a^2}\vec{v} + \frac{2\mathrm{ctg}\,\theta}{a^2\sin\theta}\vec{k}^0\times\frac{\partial\vec{v}}{\partial\lambda}\right] \quad (1)$$

$$\frac{\partial\zeta}{\partial t} + \frac{1}{a\sin\theta}\left(\frac{\partial hv\sin\theta}{\partial\theta} + \frac{\partial hu}{\partial\lambda}\right) = 0, \quad (2)$$

Δ is the Laplacian operator on a sphere; $\vec{v}$ is the depth-averaged velocity vector; $h = h_0 + \zeta$ is the thickness of the water layer, h_0 is the undisturbed water depth, ζ is the sea surface elevation; ϕ $(=g\zeta)$ is the geopotential departure of the free surface; g is the acceleration of gravity: a is the Earth's radius: ρ_0 is the density of the seawater, taking $\rho_0 = 1.024\mathrm{g/cm^3}$; A_m is the lateral eddy viscosity coefficient; κ_2 is the bottom friction coefficient: $f^* = (2\omega\cos\theta + u\mathrm{ctg}\,\theta/a)$ is the apparent Coriolis parameter, ω is the angular speed of the Earth's rotation; $\vec{\tau}$ is the wind strees vector.

In order to design energy conserving time-space finite difference schemes conveniently, we introduce a variable substitution. If we substitute

$$\vec{V} \equiv \phi\vec{v}, \quad \phi \equiv \sqrt{gh_0 + \phi},$$

for $\vec{v} = \vec{\theta}^0 v + \vec{\lambda}^0 u$, Eqs. (1) and (2) can be rewritten as,

$$\frac{\partial\vec{V}}{\partial t} = -L_1(\vec{V}) - L_2(\vec{V}) - \phi\nabla\phi - f^*\vec{k}^0\times\vec{V} - \kappa_2\vec{V} + g\frac{\vec{\tau}}{\rho_0\phi} + A_m\phi\left[\Delta\vec{v} + \frac{1-\mathrm{ctg}^2\theta}{a^2}\vec{v} + \frac{2\mathrm{ctg}\,\theta}{a^2\sin\theta}\vec{k}^0\times\frac{\partial\vec{v}}{\partial\lambda}\right], \quad (3)$$

$$\frac{\partial\phi}{\partial t} = -\frac{1}{a\sin\theta}\left(\frac{\partial\phi V\sin\theta}{\partial\theta} + \frac{\partial\phi U}{\partial\lambda}\right), \quad (4)$$

where

$$L_1(F) \equiv \frac{1}{2a\sin\theta}\left(\frac{\partial Fv\sin\theta}{\partial\theta} + v\sin\theta\frac{\partial F}{\partial\theta}\right),$$

$$L_2(F) \equiv \frac{1}{2a\sin\theta}\left(\frac{\partial Fu}{\partial\lambda} + u\frac{\partial F}{\partial\lambda}\right), \quad (F = V \text{ or } U),$$

The lateral boundary condition is

$$\vec{V}_n \mid_\Gamma = 0, \quad (5)$$

wher Γ is the horizontal boundary. The subscript n represents exterior normal to the boundary Γ.

Under the lateral boundary condition (5), Eqs. (3) and (4) have some integral properties such as: (1) gross mass is conserved; (2) energy is conserved if the forcing and dissipation are omitted; (3) the nonlinear advection operators

are skew-symmetric; and (4) Coriolis force and curvature terms do not change the kinetic energy density.

In terms of those elementary discrete operators used by ZENG *et al.* (1987, 1990), we can get the difference equations on a C-grid which have the same integral properties as those of the continuum differential equations.

The model domain extends from 98.75° E to 69.75° W and from 60.25° N to 60.25° S as shown in Fig. 9b. We adopt idealized topography where the maximum water depth is taken to be 200 m, that is, we study a flat bottom barotropic ocean of 200 m depth which has realistic topography only for the shallow water regions such as the Bohai Sea, Yellow Sea and most of the East China Sea. Therefore, for the Pacific Ocean the model results mainly reveal the features of the upper layer circulation.

Most of the lateral boundaries are just the coastlines of Asia, North and South America. Those open boundaries to the north in the Bering Sea, to the southwest and to the south are replaced by closed boundaries. Along the northern and southern lateral boundaries we take $V=0$, while $U=0$ along the eastern and western boundaries.

The model horizontal grid size is chosen to be $\Delta\theta=0.5°$ and $\Delta\lambda=0.5°$, so that the total grid points are 384×242. The initial conditions are set as,

$$U=0,\ V=0,\ \phi=0 \text{ (i.e., } \zeta=0) \qquad (6)$$

The lateral eddy viscosity coefficient A_m is 10^7 cm^2/s and the bottom friction coefficient κ_2 is $3.3\times10^{-3}\times(u^2+v^2)^{1/2}/h$. Because our model is a free surface model, the timestep is greatly restrained by the surface gravity waves. In order to save computing time, we also adopt the splitting method used by ZENG *et al.* (1985) when integrating by taking $\Delta t_1=6$ min as a time step for the adjustment process and $\Delta t_2=60$ min for the processes of advection and dissipation.

Defining a generalized kinetic energy density $e_k=(U^2+V^2)/2$ and an available potential energy density $e_{ap}=\phi^2/2$, then the total kinetic energy is $KE=\int_s\int e_k ds$ and the total available potential energy is $PE=\int_s\int e_{ap} ds$, where s is the model domain and $ds\equiv a^2\sin\theta\, d\theta\, d\lambda$.

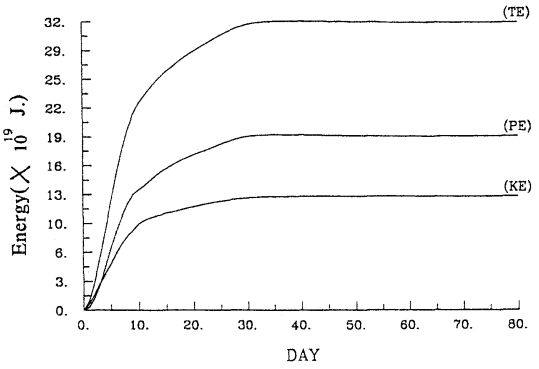

Fig. 1. Temporal variation of energy for January. PE: total available potential energy; KE: total kinetic energy; TE = PE + KE.

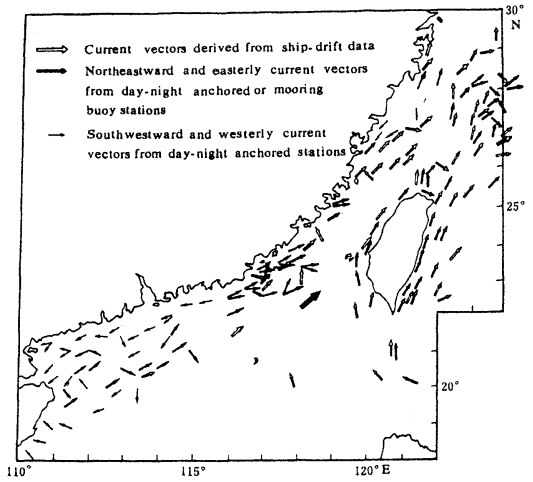

Fig. 2. Observed current vectors in winter off the southeast coast of China (from Guan, 1986).

Starting from the resting state represented by Eq. (6), the model forced by the monthly mean climatological wind stress (HELLERMAN and ROSENSTEIN, 1983) is integrated for 80 simulation days for each month. In order to examine the time dependent behavior of solutions, we also calculate the total kinetic energy and total available potential energy for each month. The temporal change of energy for January is shown in Fig. 1. Situations for other months are similar to Fig. 1. It can be shown from Fig. 1 that the total kinetic energy and the total available potential energy do not change appreciably after about 40 days. This indicates that the current speed and sea surface elevation at every point

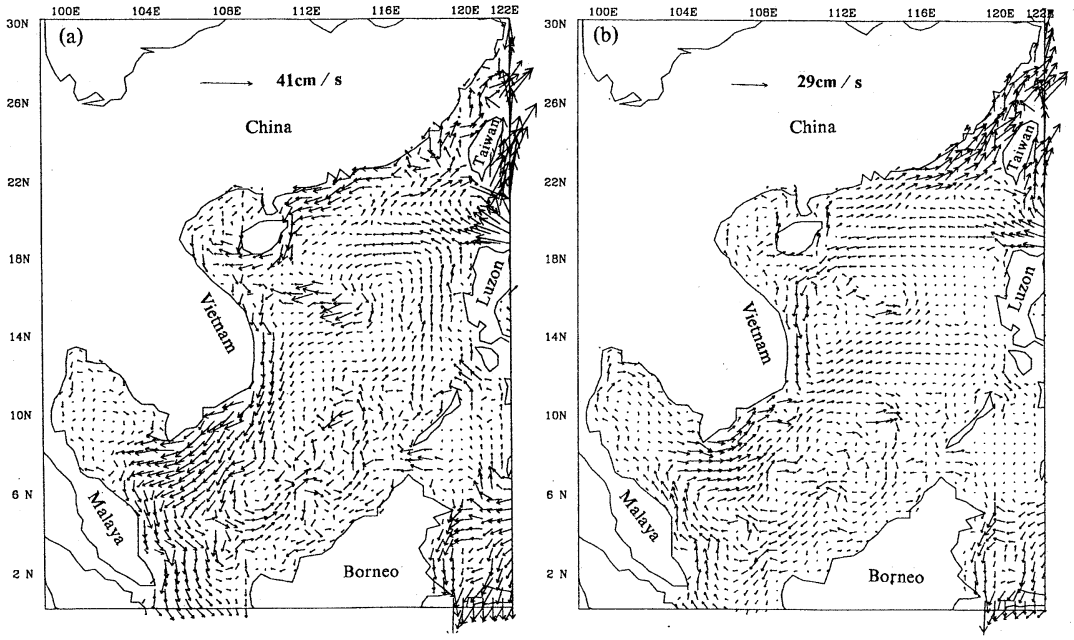

Fig. 3. Simulated depth mean velocity in South China Sea. (a) January, (b) July.

stay roughly the teady. Therefore, the results after 80 days of integration may represent the steady state upper layer circultation in the Pacific Ocean (i.e., the monthly mean current). From Fig. 1, we also observe that the total available potential energy corresponding to the sea surface elevations is greater than the total kinetic energy, which seems to indicate that the free surface model is more reasonable physically because it takes into account the transformation of the form of kinetic and available potential energy.

3. Results

Fig. 3 shows the computed monthly mean currents in the South China Sea (SCS). From Fig. 3a, it can be shown that under the intense influence of the northeasterly wind in winter, in the northern area of SCS, besides a leeward coastal current flowing southwestward, a windward current similar to the observed South China Sea Warm Current is very clearly visible. This current starts from the coastal region off the eastern Hainan Island flowing northeastward through Taiwan Strait and joining the Taiwan Warm Current. This strongly confirms the supposition raised by GUAN *et al.* (1964). In summer, a wide current also starts from the area off the eastern Hainan Island flowing northeastward through the Taiwan Strait and then entering the East China Sea as shown in Fig. 3b.

Fig. 5 shows the currents in the Bohai Sea, Yellow Sea and East China Seas as well as in the adjacent areas. It is evident from Fig. 5a that a branch of the Kuroshio north of Taiwan merges into the Taiwan Warm Current, and part of the water flow continuously along a cyclonic path and joins the left flank of the Kuroshio. Part of the Taiwan Warm Current flow northward reaching the southern edge of the Qiantangjiang Estuary, where it meets the extension of the Yellow Sea Coastal Current. They together turn to the east and flow northeastward. In the area northwest of Amami Oshima, the path of the Kuroshio exhibits an anticyclonic curvature, part of the Kuroshio water joining the northeast current mentioned above along the way to form a mixed water flowing east. In the area southwest of Kyushu, this current of the mixed water splits; the major branch turning to the southeast to merge the Kuroshio, and the other weaker branch being the Tsuhima Warm Current as described traditionally. The latter flows

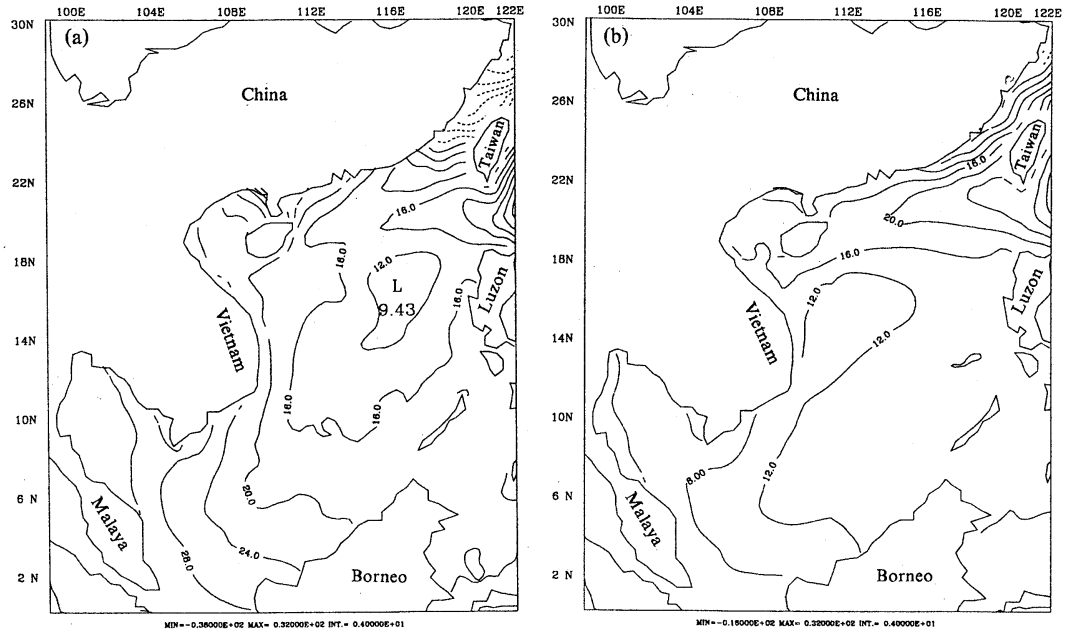

Fig. 4. Simulated sea surface elevation in the South China Sea. The contour interval is 4 cm. (a) January, (b) July.

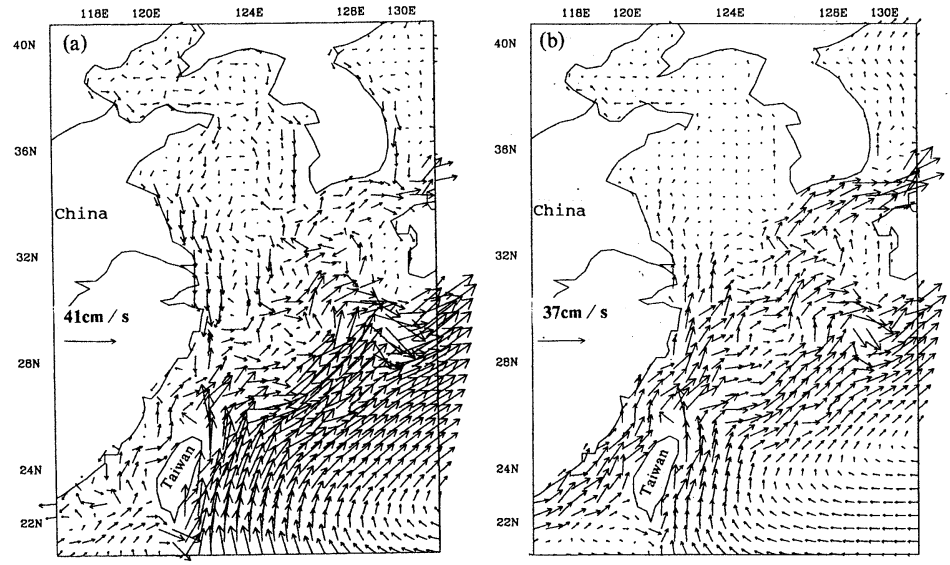

Fig. 5. Same as Fig. 3 but for the East China Sea and its adjacent area. (a) January, (b) July.

northward, passes through the Korea Strait and enters the Japan sea. Finally this current enters the Pacific Ocean through the Tsugaru Strait as shown in Fig. 7a.

It is obvious from Figs. 3a and 5a that the computed current patterns in the northern SCS and offshore region of eastern Zhejiang agree well with observations in Fig. 2.

In summer it can be clearly seen from Fig. 5b that from the Taiwan Strait to the Korea Strait the pattern of the northeastward flowing current is similar to that in winter except for a greater width. It moves into the Pacific Ocean mainly through the Soya Strait as shown in Fig.

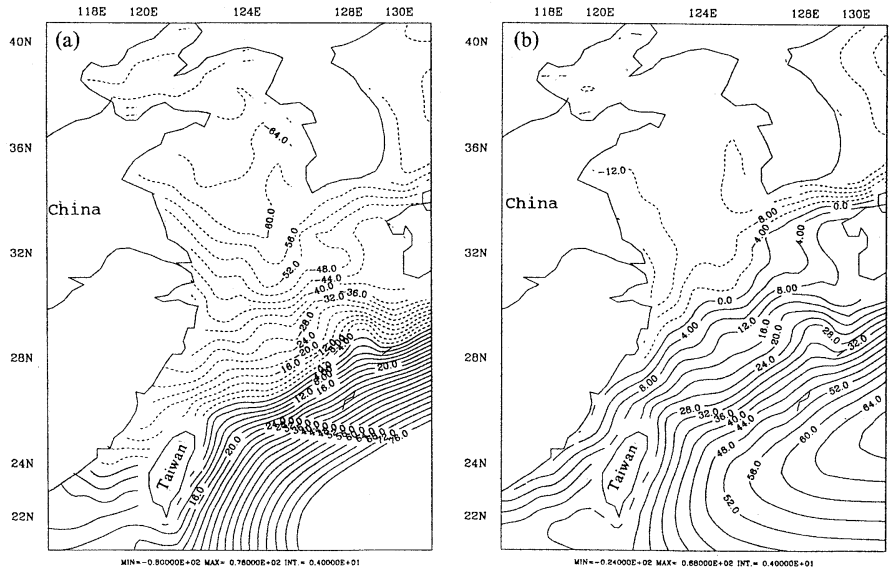

Fig. 6. Same as Fig. 4 but for the East China Sea and its adjacent area. (a) January, (b) July.

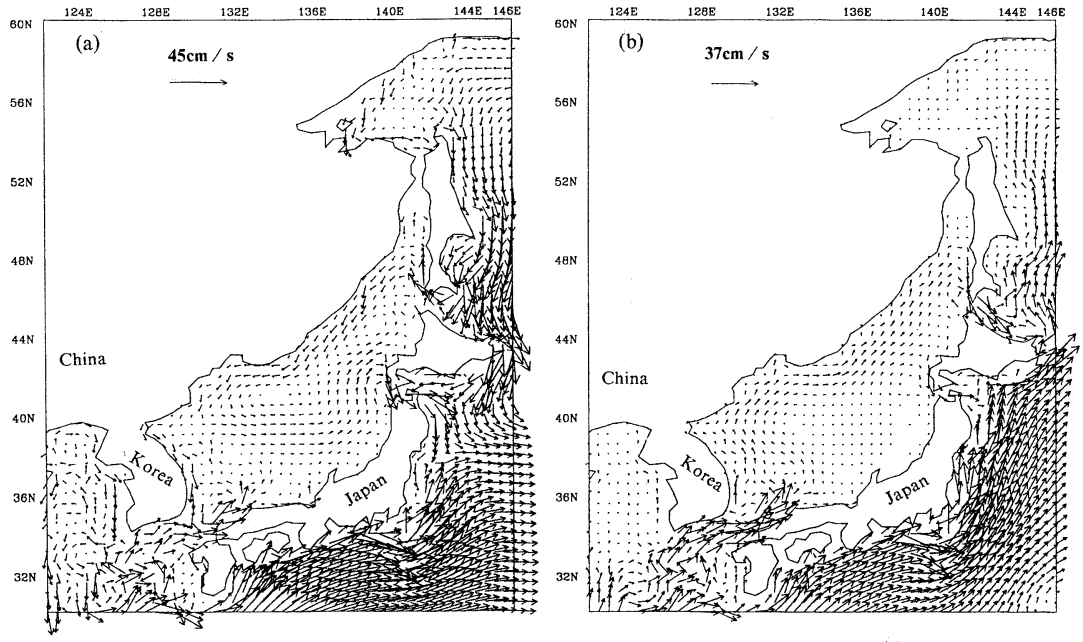

Fig. 7. Same as Fig. 3 but for the Japan Sea. (a) January, (b) July.

7b. We do not know whether it in reality passes, through the Soya Strait or not because we have no available observational data to confirm it. We were informed (TAKANO, private communication) that the Marine Environment Atlas–Currents in Adjacent Seas of Japan (compiled by Japan Oceanographic Data Center, published by Japan Hydrographic Association, 1973) shows that the flow is westward (from the Okhotsk Sea to the Japan Sea) in winter, and is eastward in spring, summer and fall, which is consistent with the model results in this paper.

From Fig. 5 we also see at about 30° N, 126° E that the winding current flows northward,

Table 1. Maximum and mean velocities as well as transports through the Taiwan and Korea Straits according to the model results.

month	Taiwan Strait			Korea Strait		
	$\|\vec{V}\|$ max(cm/s)	$\|\vec{V}\|$ mean(cm/s)	Q ($10^6 m^3/s$)	$\|\vec{V}\|$ max(cm/s)	$\|\vec{V}\|$ mean(cm/s)	Q ($10^6 m^3/s$)
Jan.	16.0	11.4	1.05	19.0	11.0	0.9
Jul.	23.0	15.8	2.07	32.0	19.3	2.2

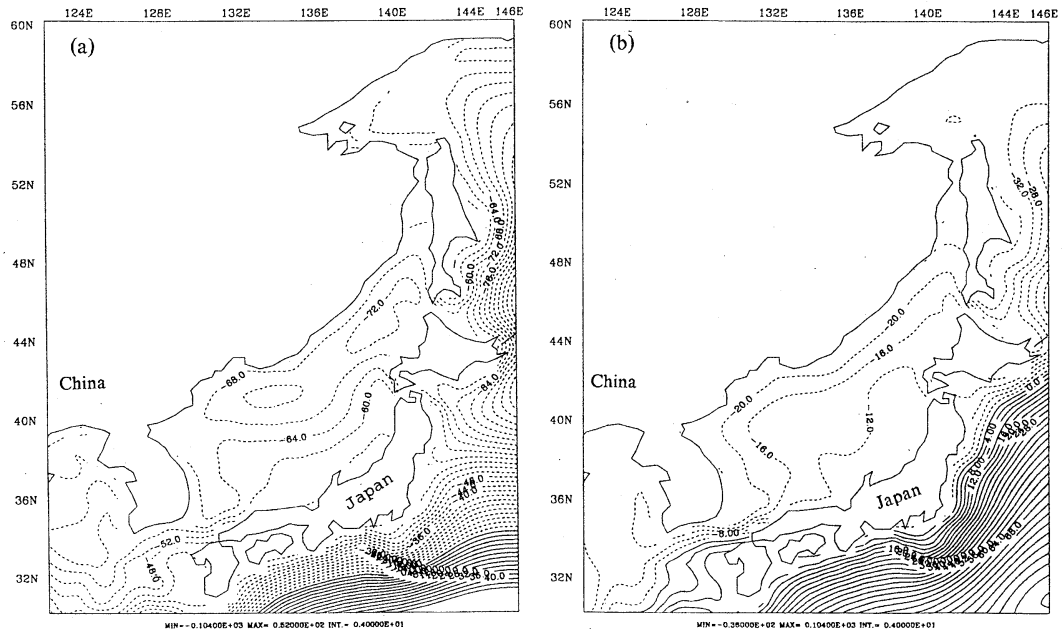

Fig. 8. Same as Fig. 4 but for the Japan Sea. (a) January, (b) July.

northeastward and then northwestward both in winter and summer. At about 32° 30′ N, 125° 30′ E, it turns to the northeast and fully enters the Korea Strait in summer, but it splits in winter into a small branch feeding the Yellow Sea to form the Yellow Sea Warm Current and another bigger one moving northeastward then entering the Korea Strait. In addition, there exists a cyclonic eddy in the northern East China Sea in winter. This windward current constitutes the western and northern flank of the cyclonic eddy.

On the basis of the above analysis it is evident that there indeed exists a long and narrow northeastward flowing current which starts from the region off the eastern Hainan Island, passing through the Taiwan Strait, East China Sea, the Korea Strait and Japan Sea finally entering the Pacific Ocean through the Tsugaru Strait in winter while through the Soya Strait in summer. Its proper name would be the "Hainan-Taiwan-Tsushima-Tsugaru/Soya Warm Current (HTTT/SWC)."

The maximum and mean values of the northeastward depth-averaged current velocity in the Taiwan Strait and Korea Strait as well as the volume transport through these two straits are given in Table 1. It is clear from Table 1 that the transport through the Taiwan Strait or Korea Strait is strong in summer but weak in winter, which is in good agreement with observations.

In order to facilitate the dynamical analysis, the computed sea surface elevations are given in Figs. 4, 6, 8 and 9. From these figures, it can be shown that the sea surface elevations are lower everywhere on the left of the "Hainan-Taiwan-Tsushima-Tsugaru/Soya Warm Current" but higher on the right of the current. Therefore, the sea surface slope is formed along the cross

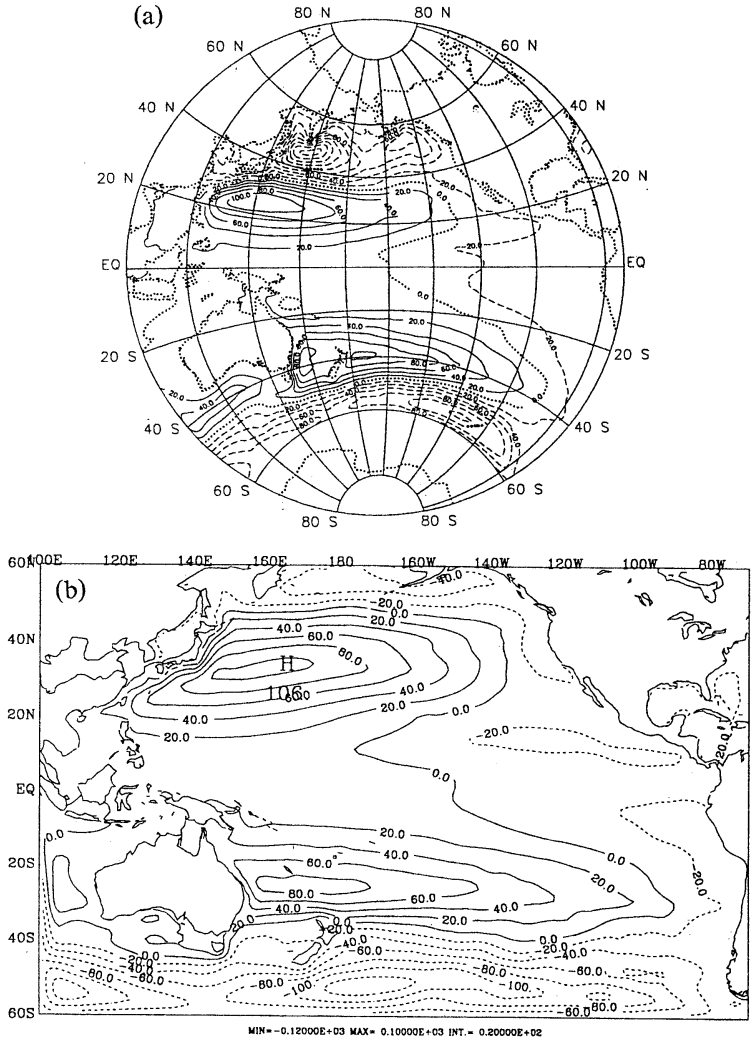

Fig. 9. Same as Fig. 4 but for the whole Pacific. (a) January, (b) July.

Table 2. Sea surface slope in the direction of the current, $\partial\zeta/\partial y$, and sea surface difference, $\Delta\zeta$, according to the computed results.

month	$\Delta\zeta$ (cm)			$\partial\zeta/\partial y$
	Hainan-Tsugaru	Hainan-Soya	Kitakyushu-Pusan	Shanwei-Tsushima
Jan.	90	84	13	-3.15×10^{-7}
Jul.	32	50	25	-1.4×10^{-7}

section of the current. The sea surface elevation differences, $\Delta\zeta$, between Kitakyushu and Pusan, between the area off the eastern Hainan Island and the area east of the Tsugaru/Soya Strait as well as the sea surface slope in the direction of the current, $\partial\zeta/\partial y$, from southeast of Shanwei to the central part of the Korea Strait along the axis of the current are given in Table 2.

Figs. 4, 6, 8 and 9 and Table 2, show that there exists not only the sea surface slope across the current, but also the sea surface slope in the direction of the current, the combined effect of

which may be one of the major forces driving the current. The friction at the bottom can counteract the pressure gradient force caused by the sea surface slope in the current direction, while the cross sectional slope from southeast to northwest can balance the Coriolis force and drives the northeastward current. From Fig. 9, it is obvious that these slopes of the sea surface are produced by the system of the wind-driven circulations in the Pacific Ocean.

4. Remarks

Based on the simulation results we make following remarks:

1. From the area off the eastern Hainan Island to the Tsugaru/Soya Strait, there exists a northeastward current both in winter and summer which may be driven by the sea surface slope both in the direction of the current and across the current from southeast to northwest.

2. The Tsushima Warm Current may be considered to originate mainly from the South China Sea Warm Current. In the area northwest of Amami Oshima, when flowing along an anticyclonic path, outer fringe water of the Kuroshio joins the northeastward current to form a mixed water flowing eastward. This current splits at about 30° N, 128° E and the major branch turns to the southeast and joins the Kuroshio again, while the minor branch flows northward which has been considered traditionally to be the origin of the Tsushima Warm Current. We believe that this weak northward branch is just a small part of the Tsushima Warm Current. It does not seem to be a direct branch of the Kuroshio. In fact, the water source of the Tsushima Warm Current mainly comes from the winding current which is further away from Kyushu.

3. The total available potential energy due to the fluctuation of the free sea surface is greater than the total kinetic energy (Fig. 1). Therefore, the effect of the pressure gradient caused by the fluctuation of the sea surface on the upper layer currents is also very important, which could not be examined rigorously not only because of the lack of observational data of the sea surface elevation, but also because of the omission of the sea surface fluctuation by the bottom topography.

4. Due to ignoring the effects of temperature, salinity and the variation of density in the model, simulated currents are mainly governed by such factors as wind stress, topography of the continental shelf, β-effect, nonlinear effect and coastal configuration. In order to reveal completely the formation mechanism of the currents, simulations should be carried out for a baroclinic ocean model based on the full primitive equations in the future.

Acknowledgments

The authors wish to thank Prof. B.X. GUAN and X.H. ZHANG for helpful discussions and valuable comments, Dr. Z.J. ZANG, N. BAO and Z.X. LONG for providing the plotting routines, Miss X. WANG and Y.B. SUN for typing the manuscript.

References

FANG, G. and B. ZHAO (1988): A note on the main forcing of the northeastward flowing current off the southeast China coast. Prog. Oceanogr., **21**, 363–372.

FANG, G., B. ZHAO and Y. ZHU (1989): Water transports through the Taiwan Strait and East China Sea measured with current meters. *In* Programme and Abstracts. Fifth JECSS, Workshop, Kangnung, Korea, p30.

GUAN, B.X. (1984): An evidence for the current flowing northward against wind in winter in the East China Sea and South China Sea. Report of the study and investigation for the Bohai, Yellow and East China Seas, 142–150 (in Chinese).

GUAN, B.X. (1986a): A sketch of the current structures and eddy characteristics in the East China Sea. Studia Marina Sinica, **27**, 1–21 (in Chinese with English abstract).

GUAN, B.X. (1986b): Evidence for a counter-wind current in winter off the southeast coast of China. Chin. J. Oceanol. Limnol., **4**, 319–332.

GUAN, B.X. and S.J. CHEN (1964): The current systems in the near-sea area of China Seas. Report of the Chinese National Comprehensive Oceanographic Survey, 1–85 (in Chinese).

GUAN, B.X., D. WENLAN and H. MAO (1964): The winter surface current systems of the southern Huanghai Sea and the northern East China Sea and discussions of some related problems. (In Chinese)

HELLERMAN, S. and M. ROSENSTEIN (1983): Normal monthly windstress over the world ocean with error estimates. J. Phys. Oceanogr., **13**, 1093–

1104.

ZENG, Q.C. (1983): Some numerical ocean-atmosphere coupling models. Proceedings of the First International Symposium on Integrated Global Ocean Modelling, Tullin, USSR.

ZENG, Q. C. and X. H. ZHANG (1987): Available energy conservative finite-difference schemes for baroclinic primitive equations on sphere. Chinese Journal of Atmospheric Sciences, **11**, 121–142.

ZENG, Q.C., Z.Z. JI and R.F. LI (1985): A numerical model of offshore currents and some tests. Proceedings of the International Symposium on Oil Development Enviroment of the South China Sea, 15–21.

ZENG, Q.C., X.H.ZHANG, C.G.YUAN, R.H.ZHANG, N. BAO and X.Z. LIANG (1990): IAP ocean general circulation models. Proceedings of the Third International Summer Colloquium on Climate Change Dynamics and Modelling, 331–350.

La mer 30: 239–250, 1992
Société franco-japonaise d'océanographie, Tokyo

Numerical simulation of seasonal cycle of world ocean general circulations

X. -H. ZHANG*, N. BAO* and W. -Q. WANG*

Abstract: A revised version of the IAP four-layer world ocean general circulation model is presented. The new version has been integrated for 180 years for an annual mean simulation and for subsequent 40 years for a seasonal cycle simulation. Analysis of the annual mean and monthly mean results including temperature, salinity, sea surface elevation, currents and energy indicates that the upper two layers of the model have already reached an equilibrium, while the lower two layers have not. The simulated sea surface temperature has been remarkably improved compared with the previous results due to the use of Haney-type heat flux formulation at the sea surface. The annual mean and seasonal salinity have also been simulated with reasonable accuracy by using a buoyancy equation and a simple sea surface buoyancy flux condition. One of the important characteristics of the model's available surface potential energy defined by ZENG (1983) is that its value over the southern ocean is greater than that over the northern ocean reflecting a strong gradient in the Antarctic Circumpolar Current. The strongest signal of seasonal variability for the surface current has been found in the Somali Current just as pointed out by HAN (1984). It has also been found that the seasonal forcing penetrates into the model's subsurface layer only in the Indian Ocean.

1. Introduction

The first multi-layer version of the IAP (Institute of Atmospheric Physics, Chinese Academy of Sciences) ocean general circulation model (OGCM) was presented in 1988 (ZHANG and ZENG, 1988; ZHANG and LIANG, 1989). The model was designed based on a set of full primitive equations without the "rigid-lid" approximation (ZENG, 1983). In the vertical, a set of "standard" stratification parameters were introduced into the governing equations of the model, and all the thermodynamic variables including temperature, salinity, density and pressure were replaced by their departures from the "standards" (ZENG, 1983; ZENG *et al.*, 1991). The model's geography was fairly realistic except that the Arctic Sea was not included in the model and that the northern boundary of the North Atlantic was closed. The so-called C-grid (ARAKAWA *et al.*, 1977) with the grid size of 4° in latitude and 5° in longitude was used in the model's horizontal discretization. The bottom topography of the model was highly smoothed with the maximum depth of 3200 m and the minimum depth of 1000 m to adapt to a terrain-following coordinate. In fact, the model used the "sigma"-coordinate in the vertical (ZENG, 1983) and had four layers with the variable thickness. The maximum depths of the four layers were 100 m, 500 m, 1,500 m and 3,200 m, respectively. The spatial finite-difference schemes of the model were designed to conserve the "available" energy (ZENG and ZHANG, 1987) defined as the sum of kinetic energy (KE), available potential energy (APE) and available surface potential energy (ASPE), which is related to the sea surface fluctuation in an OGCM providing that the source and sink terms of the model are in a perfect equilibrium.

The model was integrated by using an asynchronous technique based on the "flexible" coefficients (ZENG *et al.*, 1982) for more than 20

* Laboratory of Numerical Modelling for Atmospheric Sciences and Geophysical Fluid Dynamics, Institute of Atmospheric Physics, Chinese Academy of Sciences, Beijing, 100080 China

years for the advection terms and more than 60 yeard for the vertical thermal diffusion in response to the observed annual mean atmospheric forcing including wind stress, air pressure and air temperature at the sea level. The preliminary success of the model in reproducing qualitatively many aspects of large-scale features of the annual mean world ocean general circulation indicates that the fundamental design of the IAP OGCM is reasonable and its use is feasible in practice.

While the preliminary success is encouraging, there is still a lot to be done, e.g., the inclusion of the salinity variation in the model's integration. There are some problems to be solved, e.g., the simulated sea surface temperature in the tropical western Pacific is 2–3℃ lower than the observation. In addition, the integration is far from being long enough for the model to reach a quasi-steady state and to be validated confidently. Therefore, in the past two years, continuous efforts have been made on the model's improvement by IAP, and a revised version of the model is presented now. The new model has been integrated for 180 years with the observed annual mean atmospheric forcing and for subsequent 40 years with the seasonal atmospheric forcing. The results show that significant improvements have been achieved.

In this paper, the new version of the IAP world OGCM and its performance will be depicted. The new version itself will be briefly described in contrast with the old version in Section 2. Some results of the annual mean simulation especially those improved aspects compared with the previous results will be shown in Section 3. A somewhat detailed portrayal of the simulated seasonal cycle of ocean general circulation will be given in Section 4.

2. Model description

The new version of the IAP world OGCM is different from the original version (ZHANG and LIANG, 1989) mainly in the following aspects.

a) To include the variation of salinity in the model's integration, we introduce the Archimedean buoyancy into the model defined as $g' = -g\rho'/\rho_0$, where $\rho' = \rho - \bar{\rho}$ is the difference between the density of the sea water, ρ, and its "standard" vertical profile $\bar{\rho} = \bar{\rho}(z)$. The $\bar{\rho}(z)$ is obtained by using the "standard" vertical temperature profile, $\bar{T} = \bar{T}(z)$, and salinity profile, $\bar{S} = \bar{S}(z)$, in the state equation of the sea water (Eckart, 1958). Let $T' = T - \bar{T}$ and $S' = S - \bar{S}$, then a linearized version of the state equation of sea water, which represents the relationship among the perturbed density ρ', perturbed temperature, T' and perturbed salinity S', can be derived, and accordingly the Archimedean buoyancy is expressed as

$$g' = g(\alpha_T T' - \alpha_S S') \tag{1}$$

where α_T is the thermal expansion coefficient and α_S is the density-salinity coefficient, both of them being functions of the depth z.

Thus S', one of the prognostic variables of the original model, is replaced by g' in the new version, and correspondingly the perturbed salinity equation and the boundary condition at the surface are replaced by a buoyancy equation and a buoyancy condition which are directly derived by using the equations and boundary conditions for the perturbed temperature and salinity (ZHANG and BAO, 1990). The perturbed salinity, one of the diagnostic variables of the new model, is calulated by using Eq. (1) while g' and T' are predicted.

The APE is now defined as

$$APE = \frac{\rho_0}{2} \iiint \left(\frac{g'}{N}\right)^2 dz\, ds \tag{2}$$

where N is the Brunt-Väisälä frequency determined by using the "standard" stratifications of temperature and salinity, and $N^2 > 0$ is true everywhere for large-scale oceanic circulations. With S', one of the prognostic variables in the original model, however, we have to use an alternative expression for APE, i.e.,

$$APE = \frac{\rho_0 g}{2} \iiint \left(\frac{\alpha_T}{\Gamma_T}(T')^2 + \frac{\alpha_S}{\Gamma_S}(S')^2\right) dz\, ds \tag{3}$$

where $\Gamma_T = d\bar{T}/dz$ and $\Gamma_S = d\bar{S}/dz$. The problem is that Γ_S decreases with depth within the thermocline (e. g., LEVITUS, 1982), thereby making the APE not definable in terms of Eq. (3). That is why the Archimedean buoyancy, g', rather than the perturbed salinity, S', is used

as a prognostic variable in the new version.

The "standard" stratifications of temperature and salinity in the original model were taken from the work of BRYAN and COX (1972), which represents the observed medium values of temperature and salinity in the world ocean rather than the globally averaged ones. As a result, the "standard" sea surface temperature is only 15℃ which is 3℃ lower than the observed global annual-mean SST. In the new model, therefore, the observed global annual-mean temperature and salinity (LEVITUS, 1982) are taken as the "standard" ones instead of the original ones. Meanwhile, a linearized state equation of sea water relating the perturbed density, temperature and salinity is directly derived by using the Eckart formula rather than the Bryan-Cox formula.

b) The heat flux at the air-sea interface, as the upper boundary condition for the thermodynamic equation, is computed for 150 years by using the Newtonian cooling formulation which is the same as that used in the original version. The formulation can be written as

$$F=\rho_0 C_p \mu_T (T_a - T_1) \tag{4}$$

where T_a is the observed sea level air temperature, T_1 represents the simulated ocean surface layer temperature, and μ_T^{-1} represents the rate of thermal penetration through the surface with a value of 2 day m^{-1}.

After 150 years, a Haney-type formula such as

$$F=D(T_A - T_1) \tag{5}$$

is used to replace Eq. (4). Here, D is the heat transfer coefficient and $T_A = T_a + Q_l/D$ represents the "apparent" atmospheric equilibrium temperature, where Q_l depends on the net downward solar radiation flux, downward atmospheric long wave radiation flux, and latent heat flux. D and Q_l are computed as functions of climatological atmospheric parameters obtained from various sources (HAN, 1984).

In contrast to Eq. (4), Eq. (5) gives $\mu_T^{-1} = D/\rho_0 C_p$, which is a variable parameter ranging from 0.8 to 1.9 day m^{-1}. Further, Q_l/D representing the difference between the "apparent" air temperature, T_A, and the real air temperature, T_a, is significant in the tropical areas, which is a crucial factor for the improvement of the simulated tropical SST.

c) One of the most important parameters in the OGCMs is the vertical thermal diffusivity which the e-folding scale depth of the thermocline is almost proportional to (BRYAN, 1987). Unfortunately, the vertical diffusivity is one of the most uncertain parameters in the OGCMs due to the lack of the observational data necessary for its determination. The constant diffusivity ($10^{-4} m^2 s^{-1}$) used in the original model does not seem to be a reasonable choice because the solution to the corresponding vertical thermal diffusion equation will approach a vertically homogeneous state while the adiabatic bottom boundary condition is used.

In the new version, a depth-dependent vertical thermal diffusivity defined as (BRYAN and LEWIS, 1979)

$$k=k(z)=10^{-4}[0.8+(1.05/\pi)\tan^{-1}\{4.5\,(z-2500)/1000\}] \tag{6}$$

is used instead of a constant one. The value given by Eq. (6) is about $0.3\times10^{-4} m^2 s^{-1}$ within the surface layer and about $1.3\times10^{-4} m^2 s^{-1}$ near the bottom, which is compatible with observational evidences (ROOTH *et al.*, 1972; MUNK, 1966). Although the vertical diffusivity representation may not be suitable everywhere, we find that its smallness within the upper layer is favorable to the heat accumulation in the upper ocean (BAO and ZHANG, 1991).

d) The C-grid and the relevant finite-difference schemes used in the original version are substituted by the B-grid and the corresponding available energy-conserving finite-difference schemes (ZENG and ZHANG, 1987) in the new version in order to reduce the small scale noise excited more easily in full primitive equation model than in model with the "rigid-lid" approximation. Comparative experiments with the two kinds of grid show that the B-grid is more favorable to suppress the noise between the two adjacent grids than the C-grid especially around the Antarctica. The reason for this is that the B-grid and the conventional horizontal diffusion scheme are complementary to one another in respect to controlling computational noise as pointed out by BATTEEN and HAN

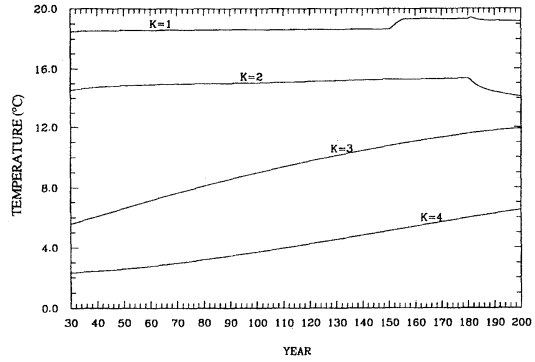

Fig. 1. Computed global annual-mean temperature during the years 30–200 of integration.

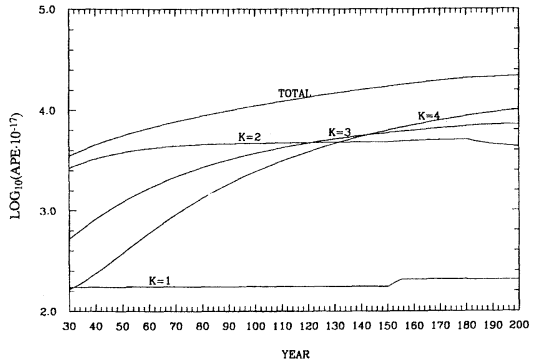

Fig. 2. The rate of the computed APE increase for the years 30–200 of integration.

(1981).

e) To decrease the horizontal variability of the layer thickness, the minimum depth near the coastal region is increased up to 1600 m which is half the maximum depth in the new version. Furthermore, the maximum thickness of the surface layer is now reduced to 50 m in order to lower its thermal inertia.

3. Improved annual mean simulation

First, the model was integrated for 180 years in response to the observed annual mean sea level wind stress (HAN *et al.*, 1981), sea level air temperature and pressure (ESBENSEN *et al.*, 1981) and sea surface salinity (LEVITUS, 1982). The integration started from a motionless initial state, of which the sea surface was flat and the departures of temperature and salinity were zero. To establish a benchmark solutions which may be used in evaluating various time integration techniques in the future, the "leap-frog" method with a time step of 10 minutes combined with an Euler-forward scheme employed once a month is used in the present model. In addition, a 9-point smoother is used once every 5 years for the current velocity components and every year for the temperature and salinity to suppress the computational noise of the prognostic variables. Also, the horizontal viscosity coefficient, A_m, is increased to $1.2\times10^6 m^2 s^{-1}$ from its original value of $0.8\times10^6 m^2 s^{-1}$.

As mentioned in Section 2, the sea surface heat flux was calculated by using Eq. (4) with $\mu_T=0.5$ m day^{-1} for 150 years and after that by using Eq. (5) with D and T_A being computed from the observed annual mean atmospheric data and some empirical parameters (HAN, 1984). Such a change has been proven very important for improving the simulated surface layer temperature as shown in Fig. 1, in which the maximum undergoes a rapid increase between the year 150 and 156. Comparing the horizontal distributions of the temperature for the year 150 (Fig. 3b) and the year 163 (Fig. 3c) we find that the latter is much closer to the observation (Fig. 3a) than the former, especially in the warm pool region of the western Pacific.

It can be shown from Fig. 1 that the global annual-mean temperatures of the first and second layers have already reached the equilibrium by the end of the integration. This can also be shown in the temporal evolution of the global annual-mean salinity for the upper two layers, the annual mean ASPE and of the annual mean KE (not shown here). On the other hand, the same is not true for the two lower-layer temperatures and salinities, which continuously increase in the course of the integration reflecting a rather significant trend of the annual mean APE (Fig. 2). We speculate that this phenomenon is due to the lack of the formation of the bottom water in this model.

Fig. 4b shows the simulated annual mean surface salinity, which is in good agreement with the observation (Fig. 4a). Such an agreement comes easily from the use of the observed salinity data rather than the evaporation, precipitation and runoff data in the computation of the fresh water flux at the sea surface (ZHANG and BAO, 1990).

One major feature of the IAP OGCM is the relaxation of the "rigid-lid" assumption. There-

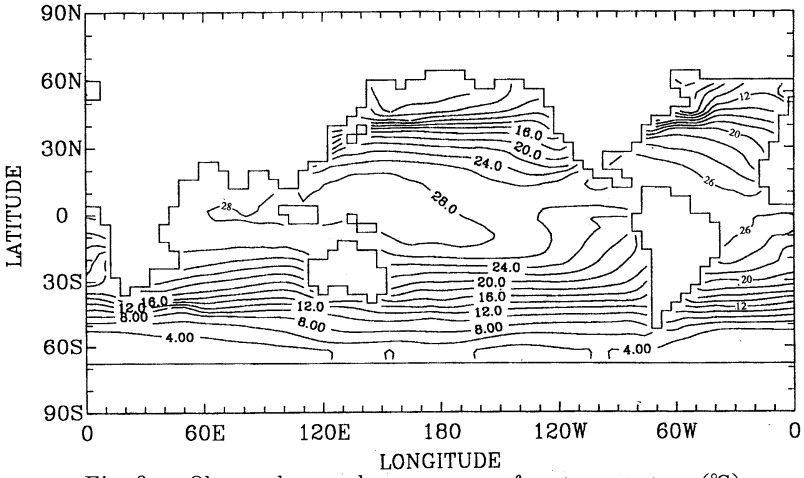

Fig. 3a. Observed annual mean sea surface temperature (℃).

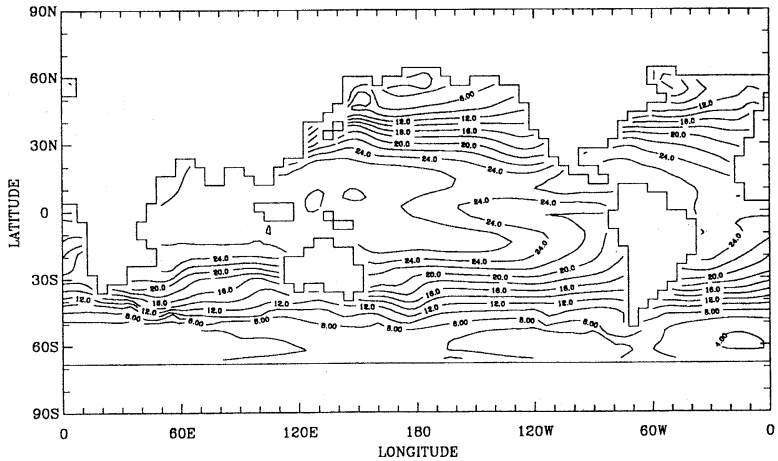

Fig. 3b. Simulated sea surface temperature (℃) in the year 150.

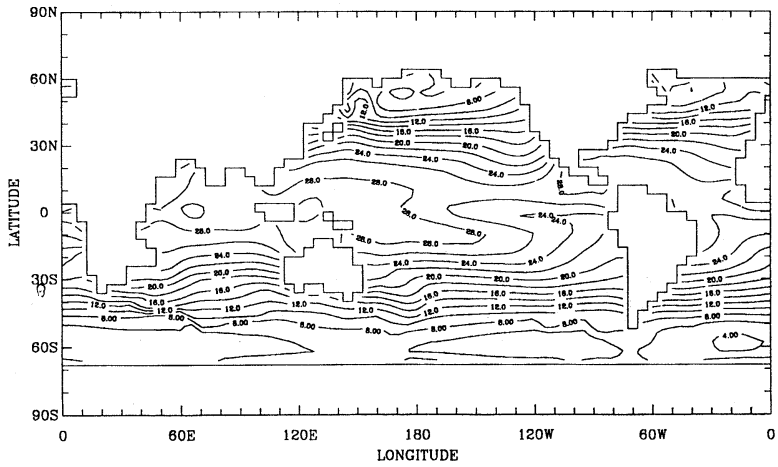

Fig. 3c. Simulated sea surface temperature (℃) in the year 163.

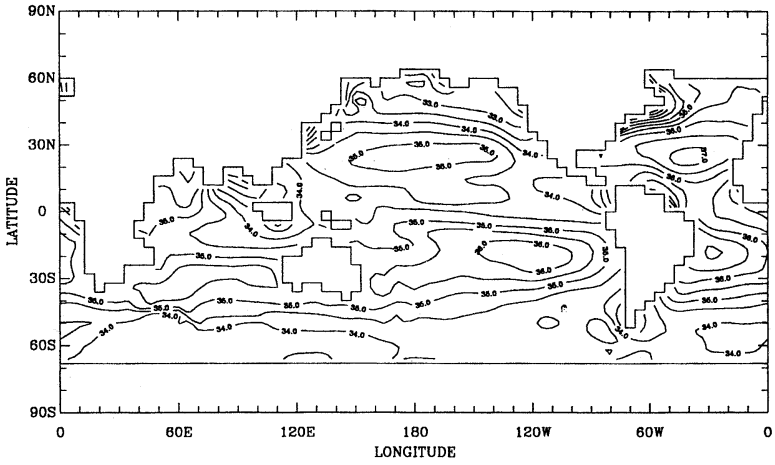

Fig. 4a. Observed annual mean surface layer salinity (g kg^{-1}) (from LEVITUS, 1982).

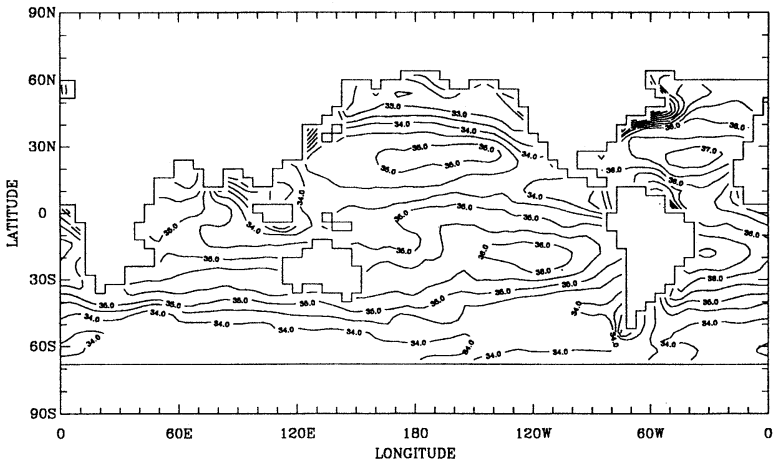

Fig. 4b. Simulated annual mean surface layer salinity (g kg^{-1}) in the year 180.

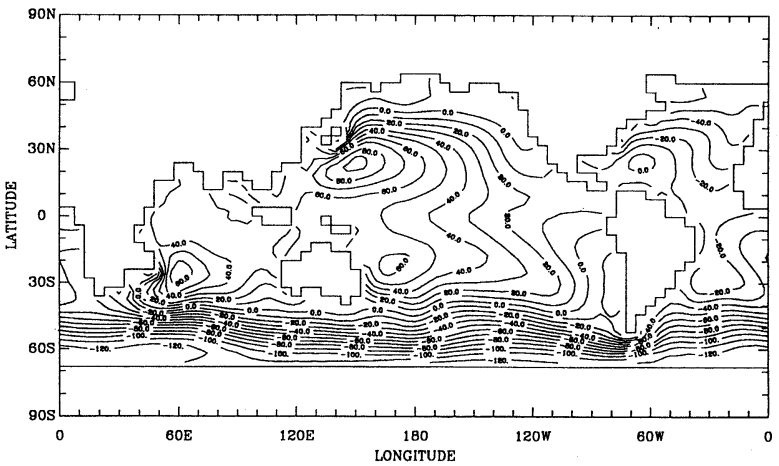

Fig. 5. Simulated sea surface elevation (cm) in the year 180.

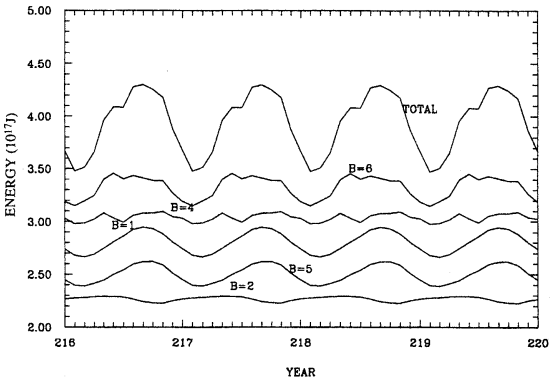

Fig. 6. Monthly mean available surface potential energy in five basins.
B=1 - North Pacific (+ 2.00); B=5 - South Atlantic (+ 1.75);
B=4 - South Pacific (+ 2.00); B=6 - Indian Ocean (+ 2.25).
B=2 - North Atlantic (+ 2.00);

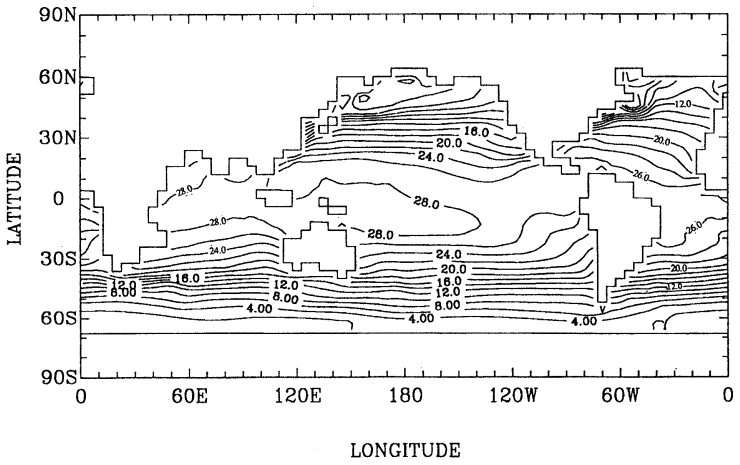

Fig. 7a. Observed monthly mean SST (℃) in March (from ESBENSEN *et al.*, 1981).

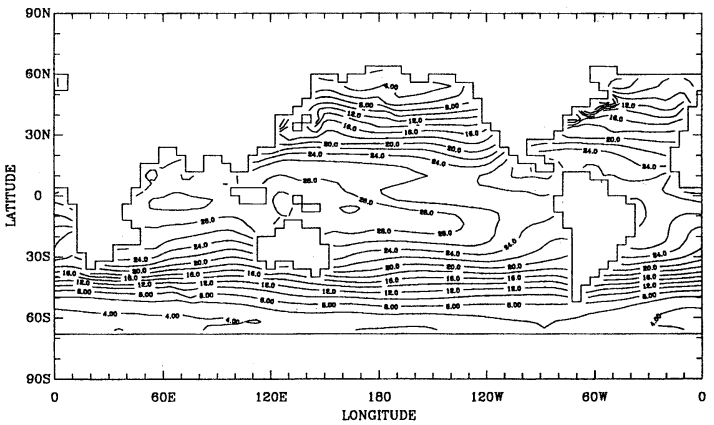

Fig. 7b. Simulated monthly mean surface layer temperature (℃) in March (year 200).

fore, the sea surface elevation is one of the model's prognostic variables. Fig. 5 shows the simulated annual mean sea surface elevation for the year 180, in which the highest region in the western Pacific with a central value greater than 90 cm is much closer to the observed result (WYRTKI, 1975) than that simulated by the original model (Fig. 12 of ZHANG and LIANG, 1989). Meanwhile, the simulated poleward gradient around the Antarctica is much stronger than in the original model. It implies that the Antarctic Circumpolar Current, which was poorly described in the old model, has been improved remarkably in the present simulation.

4. Some results of seasonal cycle simulation

After 180 years of simulation with the annual mean forcing the model has been integrated subsequently for another 40 years with the observed seasonal atmospheric forcing. The sea level wind stress, air pressure, T_A, D and sea surface salinity are updated at the end of each day by the linear interpolation of the consecutive monthly mean values (HAN *et al.*, 1981; ESBENSEN *et al.*, 1981; LEVITUS, 1982). The model's climate undergoes an adjustment during the first few years due to the change in forcing conditions from steady to periodic. However, a periodical solution is reached soon after except for some lower

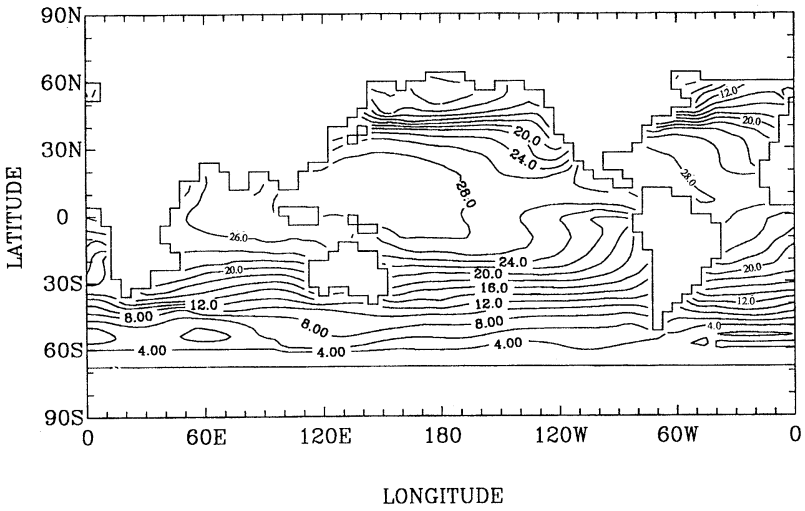

Fig. 8a. Observed monthly mean SST (℃) in September (from ESBENSEN *et al.*, 1981).

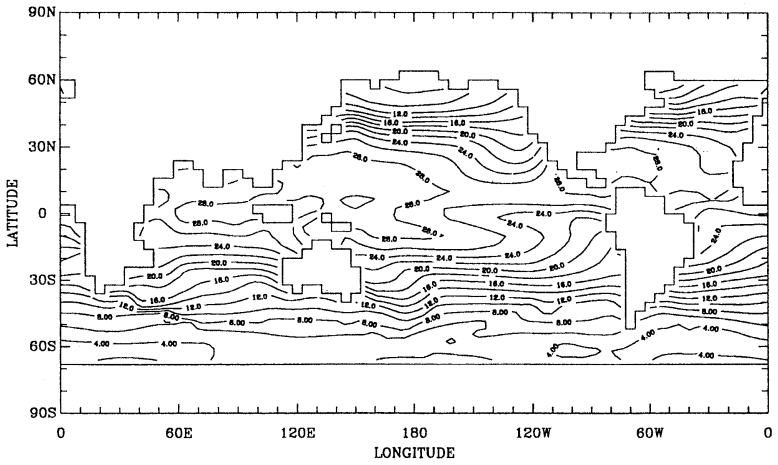

Fig. 8b. Simulated monthly mean surface layer temperature (℃) in September (year 200).

layer variables. In the following, the model's seasonal cycles will be depicted by using the consecutive monthly mean values of some variables during the last 20 years (years 200–220).

Fig. 6 shows the variation of monthly mean ASPE during the last 4 years (years 216–220) defined as

$$ASPE = \frac{\rho_0}{2g} \int (gz_0)^2 ds \qquad (7)$$

where z_0 is the sea surface elevation with its average value being zero. Some perfect periodical oscillations can be found from not only the global ASPE but also the basin-based ASPE. One of the important features for the basin-based ASPE is that its value in the South Pacific (B=4) is greater than in the North Pacific (B=1) and so is in the Atlantic (B=5 and B=2) reflecting the strong sea surface slope around the Antarctica (Fig. 5). However, the seasonal cycle of the ASPE in the South Pacific is weaker than that in the North Pacific, which is opposite to the contrast in the seasonal cycle of the ASPE between the South and North Atlantic.

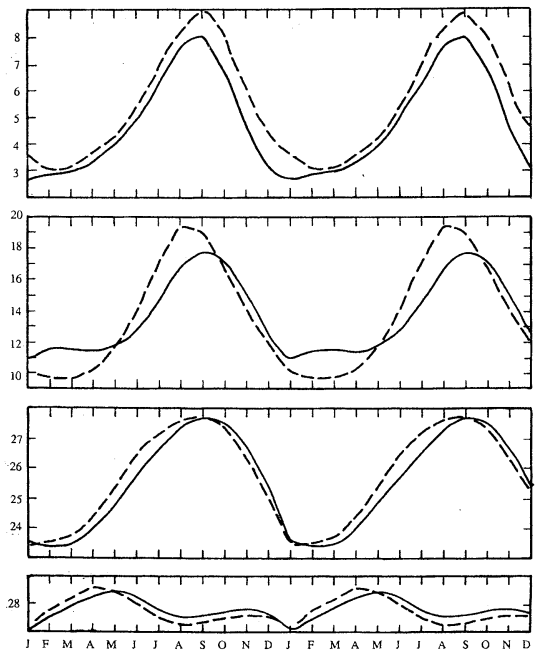

Fig. 9. Simulated (solid line) and observed (dashed line) zonal mean SSTs (℃) at 2°N, 22°N, 42°N and 62°N (from the bottom to the top).

Figs. 7a, b are the observed and simulated SSTs in March. A good agreement is in the warm pool region of the western Pacific. On the other hand, the simulated maximum SST in the equatorial Indian Ocean, which is over 30℃, does not seem to be realistic. Besides, the simulated SSTs over the equatorial central and eastern Pacific regions are more than 1℃ lower than the observation, which may be related to the overestimated cold water upwelling by the model. Similar features are also found in the simulated SST in September (Fig. 8) with the contrast between the warm water in the western Pacific and the cold water in the eastern Pacific being sharper than in March.

The zonal averages of both the simulated and observed temperatures are computed at each of the four latitudes 2° N, 22° N, 42° N and 62° N, and the results are shown as a function of time in Fig. 9. Some typical characteristics such as the large seasonal variability in the middle and high latitudes, and the semi-annual variation with relatively small amplitude near the equator (HAN, 1984) are reproduced. In general, the simulated results are in good agreement with the observations despite some small discrepancies in the amplitude and phase (e.g., the simulated annual amplitude at 42° N is 2℃ lower and lags the observation by 1 month).

The simulated surface currents for January and July are shown in Figs. 10a and 10b, respectively. Remarkable seasonal differences are found by comparing the simulated major current systems such as the Equatorial Current, Gulf Stream, Kuroshio, Somali Current, and the Australia Current for January and July. The sharpest seasonal contrast between January and July seems to be in the Indian Ocean. For instance, as shown in Fig. 11, the seasonal amplitudes of the maximum northward and eastward currents in the Indian Ocean are 13 cm s^{-1} and 18 cm s^{-1}, respectively, by the Somali Current just as pointed by HAN based on the results of OSU OGCM (HAN, 1984). The corresponding values in the North Pacific are only 5 cm s^{-1} and 4 cm s^{-1}, respectively (Fig. 12). Furthermore, the seasonal forcing over the Indian Ocean can penetrate into the second layer of the model, which is about 275 m deep, resulting in an annual amplitude of 5 cm s^{-1} for the maximum northward

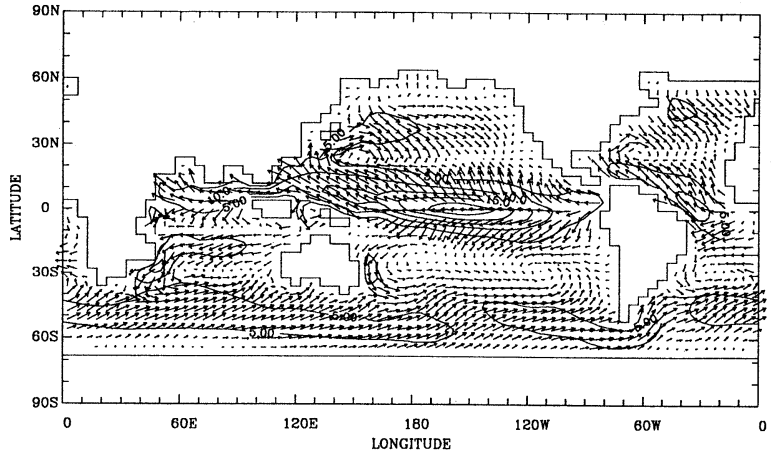

Fig. 10a. Simulated monthly mean surface layer current with isopleths of current speeds (cm s^{-1}) in January.

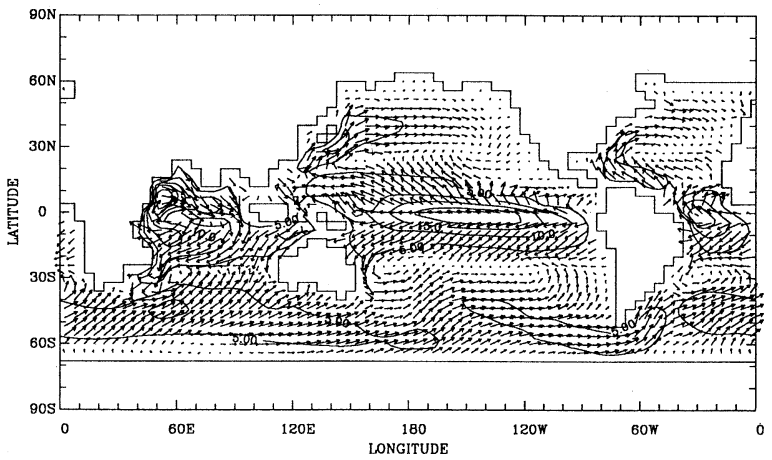

Fig. 10b. Simulated monthly mean surface layer current with isopleths of current speeds (cm s^{-1}) in July.

current in the subsurface layer (Fig. 11a). On the other hand, no significant signal of seasonal variability in the subsurface layer has been found in the other basins.

Acknowledgements

We thank Miss Xuan WANG for assistance in preparing the manuscript and figures and Dr. Zhuo LIU for proofreading the text. We also thank the reviewers for their helpful comments, many of which are incorporated in the final text.

This work was supported by the National Natural Science Foundation and the Academia Sinica of the People's Republic of China.

Reference

ARAKAWA, A. and V.R. LAMB (1977): Computational desigin of the basic dynamical processes of UCLA general circulation model. *In* Methods in Computational Physics, Vol. 17, General Circulation Models of the Atmosphere, J. CHANG (Ed.), Academic Press, New York, 173–265.

BAO, N. and X.H. ZHANG (1991): Effect of ocean thermal diffusivity on global warming induced by increasing atmospheric CO_2. Adv. Atmos. Sci., **8**, 421–430.

BATTEEN, M. and Y.-J. HAN (1981): On the computational noise of finite-difference schemes used in ocean models. Tellus, **33**, 387–396.

BRYAN, F. (1987): Parameter sensitivity of primitive equation ocean general circulation

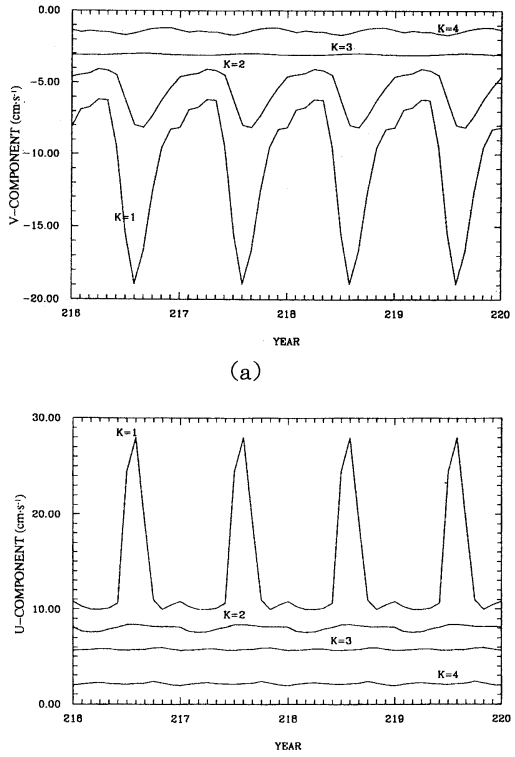

Fig. 11. Simulated seasonal variation of maximum northward currents (a) and maximum eastward currents (b) in the Indian Ocean (cm s^{-1}).
K=1 - surface layer (−2.0 for v and +1.0 for u);
K=2 - second layer (−3.0 for v and +2.0 for u);
K=3 - third layer (−2.0 for v and +3.0 for u);
K=4 - bottom layer (−0.5 for v and +1.0 for u).

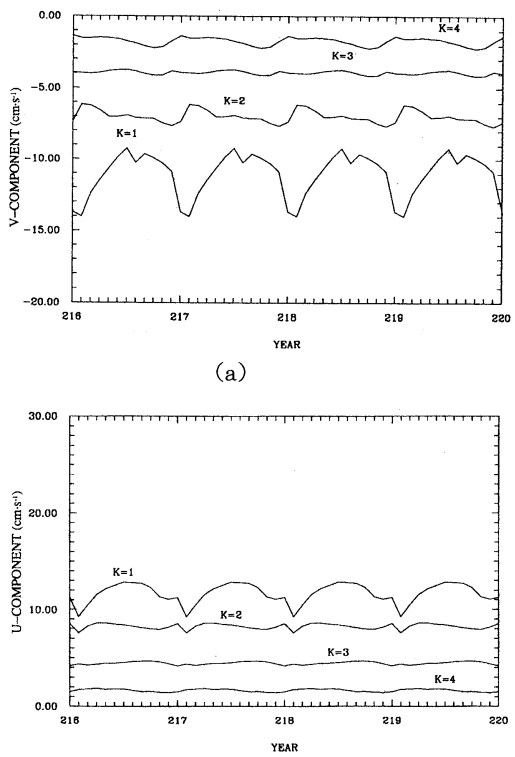

Fig. 12. Simulated seasonal variation of maximum northward currents (a) and maximum eastward current (b) in the North Pacific (cm s^{-1}).
K=1 - surface layer (−0.0 for v and +2.0 for u);
K=2 - second layer (−1.5 for v and +2.0 for u);
K=3 - third layer (−3.0 for v and +3.0 for u);
K=4 - bottom layer (−1.0 for v and +1.0 for u).

models. J. Phys. Oceanogr., **17**, 970–985.

Bryan, K. and M. Cox (1972): An approximate equation of state for numerical models of ocean circulation. J. Phys. Oceanogr., **2**, 510–514.

Bryan, K. and L.J. Lewis (1979): A water mass model of the world ocean. J. Geophys. Res., **84**, 2503–2517.

Eckart, C. (1958): Properties of water. Part II. Am. J. Sci., **256**, 225–240.

Esbensen, S.K. and Y. Kushnir (1981): Heat budget of the global ocean: Estimates from surface marine observations. Report 29, Climatic Resarch Institute, Oregon State University, Corvallis, Oregon, 271 pp.

Han, Y.-J. (1984): A numerical world ocean general circulation model. Part I : Basic design and barotropic experiment. Part II : A baroclinic experiment. Dyn. Atmos. and Oceans, **8**, 107–172.

Han, Y.-J. and S.-W. Lee (1981): A new analysis of monthly mean wind stress over the global ocean. Report 26, Climatic Research Institute, Oregon State University, Corvallis, Oregon, 148 pp.

Levitus, S. (1982): Climatological Atlas of the World Ocean. NOAA Professional Paper 13, U.S Government Printing Office, Washington, D. C., 173 pp.

Munk, W.H. (1966): Abyssal recipes. Deep-Sea Res., **13**, 707–730.

Rooth, C.G. and H.G. Ostlund (1972):Penetration of tritium into the Atlantic thermocline. Deep-Sea Res., **19**, 481–492.

Wyrtki, K. (1974): The dynamic topography of the Pacific Ocean and its fluctuations. Report

H-16-74-S. Hawaii Inst. Geophy., 19 pp.

ZENG, Q.C. (1983): Some numerical ocean-atmosphere coupling models. First International Symp. Integrated Global Ocean Monitoring. Tallinn, USSR.

ZENG, Q.C. and X.H. ZHANG (1987): Available energy conservation schemes for primitive equations of spherical baroclinic atmosphere. Chin. J. Atmos. Sci., **11**, 121–142.

ZENG, Q.C., X.H. ZHANG and R.H. ZHANG (1991): A design of an oceanic GCM without the rigid lid approximation and its application to the numerical simulation of the circulation of the Pacific Ocean. J. Mar. Systems, **1**, 271–292.

ZENG, Q.C., Z.Z. JI and C.G. YUAN (1982): Design of difference schemes for primitive equations. Scientia Sinica, Series B, XXV(2), 183–199.

ZHANG, X.H. and N. BAO (1990) : Buoyancy equation and salinity computation. Annual Report 1989, Laboratory of Atmospheric Sciences and Geophysical Fluid Dynamics, Institute of Atmospheric Physics, Academia Sinica, 193–203.

ZHANG, X.H. and Q.C. ZENG (1988): Computational desigin of world ocean general circulation model. Chin. J. Atmos. Sci., special issue, 149–165.

ZHANG, X.H. and X.Z. LIANG (1989): A numerical world ocean general circulation model. Adv. Atmos. Sci., **6**, 44–61.

La mer 30: 251–262, 1992
Société franco-japonaise d'océanographie, Tokyo

Volume and heat transports of the Kuroshio in the East China Sea in 1989

Yaochu YUAN*, Jilan SU* and Ziqin PAN*

Abstract: A modified inverse method is used to compute the Kuroshio in the East China Sea with hydrographic data and moored current meter records obtained during early summer and autumn in 1989. In this method the geostrophic assumption is not imposed. The vertical viscous term in the momentum equation as well as the vertical diffusion term in the conservative equation and the heat exchange at the surface are all considered. The computed volume transports at R_1 (PN) section are 35 and $31\times10^6 m^3/s$ during early summer and autumn, respectively, in 1989. The heat transports are 2.50 and $2.29\times10^{15}W$ there during early summer and autumn, respectively, in 1989. About $1.29\times10^{13}W$ of heat is transferred into the ocean from atmosphere over the region of computation during early summer of 1989 and about $2.80\times10^{13}W$ of heat from the ocean to the atmosphere during autumn of 1989. A countercurrent is present in the deep layer during both periods. The total volume transport of the Taiwan Warm Current is about $1.5\times10^6 m^3/s$.

1. Introduction

Most of the previous studies on the volume transport of the Kuroshio in the East China Sea were based on the dynamic method (e.g. GUAN, 1982 and 1988; NISHIZAWA *et al.*, 1982). The level of no motion is normally set at 7 MPa. The annual mean volume transport thus computed for the Kuroshio through the PN section in the East China Sea is usually around $20\times10^6 m^3/s$. (The position of the PN section is the same as section R_1 shown in Fig. 1(a)). Recently YUAN, ENDOH and ISHIZAKI (1991) and YUAN, SU and PAN (1991) applied the inverse method to compute the current structure and volume transport of the Kuroshio in the East China Sea. Their results showed that the conservation of mass is not satisfied by the dynamic method and approximately satisfied by the inverse method. In these studies the geostrophic relation was assumed, as is the normal practice for inverse method (WUNSCH, 1978). However, the geostrophic assumption is not always valid (YUAN *et al.*, 1986).

In this paper, a modified inverse method is proposed to compute the current structure of the Kuroshio in the East China Sea. The hydrographic data and moored current meter records used were obtained in early summer and autumn of 1989.

* Second Institute of Oceanography, SOA, P. O. Box 1207, Hangzhou 310012, China

2. Modified inverse method

Both the vertical friction term in the momentum equation and the vertical diffusion term in the density equation are kept in our modified inverse method. In addition, the heat flux through the sea surface is also considered. In the following we shall discuss the rationale and results.

1) The vertical friction term in momentum equation is kept because the East China Sea shelf is shallow. If we further take the rigid-lid assumption, the boundary conditions at the surface are then

$$\rho_0 A_z \frac{\partial u}{\partial z}=\tau_x,\ \rho_0 A_z \frac{\partial v}{\partial z}=\tau_y$$
$$w=0 \qquad (1)$$

where the x-axis is parallel to hydrographic section, the y-axis normal to the section, and the z-axis upward. $\tau\ (\tau_x, \tau_y)$ is the wind stress vector, u and v are the horizontal velocity components, and w the vertical velocity component.

No-slip boundary condition is specified at the

bottom, i.e., at $z=-H(x, y)$

$$u=v=w=0 \tag{2}$$

For constant A_z an approximate expression for the horizontal velocity can be found (see YUAN *et al.*, 1986). For example, the v component can be written approximately as

$$v=v_\tau+v_G+v_B \tag{3}$$

v_τ is the surface Ekman velocity component subject to the wind stress τ, v_G is the geostrophic velocity, i,e.,

$$v_G = b_0-\frac{g}{f\rho_0}\int_z^{z_0}\frac{\partial\rho}{\partial x}\,dz \tag{4}$$

where b_0 is the value of v_G at the reference level z_0 and is an unknown to be computed. v_B is the bottom Ekman velocity components. If the pressure gradient is mainly in the along-section direction, i.e., $|\partial p/\partial x| \gg |\partial p/\partial y|$, then v_B can be expressed simply as (YUAN at al., 1986):

$$\begin{aligned} v_B=&-2\,(\cos aH \operatorname{ch} aH \cos az \operatorname{ch} az \\ &+\sin aH\, sh\, aH \sin az \operatorname{sh} az)\; v_G \\ &/(\cos aH+\operatorname{ch} aH) \end{aligned} \tag{5}$$

in which

$$a=(f/2A_z)^{1/2}$$

2) SARKISYAN (1977) has shown that in either the density or salt equation, the convection terms are of dominant importance and the horizontal diffusion terms are smaller than the vertical diffusion term. If we keep all convection terms and the vertical diffusion term in the density and salt equation but drop the horizontal diffusion terms, then the following equations for the j th layer of box i can be obtained:

$$\begin{aligned} &\iint_{A_{i,j}} \rho\,(x,y,z)\,C(x,y,z)\,v\,(x,y,z)\,\delta_{i,j}\,dA_{i,j} \\ &=C_j\rho_j w_j\delta_j A_j-C_{j-1}\rho_{j-1}w_{j-1}\delta_{j-1}A_{j-1} \\ &\quad+K_v\Big[\iint_{A_j}\frac{\partial(\rho C)}{\partial z}\,dA_j-\iint_{A_{j-1}}\frac{\partial(\rho C)}{\partial z}\,dA_{j-1}\Big] \end{aligned} \tag{6}$$

K_v is the vertical diffusion coefficient, assumed to be constant, $\delta_{i,j}$ (δ_j, δ_{j-1}) takes the value of 1 for flow into the box and -1 for flow out of the box. When $C(x, y, z)=1$, Eqn. (6) represents the mass conservation, and when $C(x, y, z)=S(x, y, z)$. Eqn. (6) represents the salt conservation equation. $A_{i,j}$ is the lateral face for the j th layer of box i, A_{j-1} and A_j are the projection of the upper and bottom faces of the j th layer of box i on the horizontal plane, respectively. In the standard inverse method, all terms on the left hand side of Eqn. (6), i.e. the vertical fluxes in the conservation equation, are neglected (e.g. WUNSCH, 1978). However, as we shall see later, the vertical fluxes due to the surface and bottom Ekman layer effect can not be neglected in the deep layer.

From Eqns. (3)–(6), we can write the following matrix

$$Ab=\Gamma \tag{7}$$

where b is $N\times 1$ matrices, and unknowns (b_0, w_j), A and Γ can be computed from the hydrographic and wind data.

3) Considering that the heat flux q_e at the sea surface is unknown, the following constraints are imposed, i.e.,

$$q_{e,1}\leq q_e\leq q_{e,2} \tag{8}$$

where $q_{e,1}$ and $q_{e,2}$ are, respectively, minimum and maximum statistical monthly average values in the survey area. We take the values of $q_{e,1}$ and $q_{e,2}$ as given by the Institutes of Oceanography and Geography of the Academia Sinica in 1977. q_e is an unknown to be computed. Positive value of q_e indicates heat transfer from the ocean to the atmosphere, and negative value of q_e indicates the heat transfer from the atmosphere to the ocean.

Eqn. (7) is solved with the inequalities (8) imposed. This is a mathematical problem of quadratic programing. Details of the computation of the problem can be found in WUNSCH (1982). If Eqn. (7) is solved without the inequalities (8), it is a linear programing problem (e.g. FIADEIRO and VERONIS, 1982; YUAN *et al.*, 1990).

On the choice of an optimum reference level, we use the FIADEIRO and VERONIS's method

(1982). Each box is divided into K layers. The geostrophic velocity v relative to z_0 level is given by

$$v=-\frac{g}{f\rho_0}\int_{z_0}^{z}\frac{\partial\rho}{\partial x}\,dz \tag{9}$$

We difine

$$T_{j,e}=\oint\int_{z_{j+1}}^{z_j} v\,dz\,dx, \quad (e=1,2;\cdot;M) \tag{10}$$

and

$$T_0^2=\sum_{e=1}^{M}\sum_{j=1}^{K}T_{j,e}^2 \tag{11}$$

where M is the number of boxes. A good choice for a reference level z_0 is such that T_0^2 is the minimum. If $z_0>H$(the water depth) at some stations, the reference levels at these stations are reset to be H.

The volume transport (VT) Q_m is defined as

$$Q_m=\int_L dx\int_{-H}^{0} v\,dz \tag{12}$$

where L is the width of the section, Substituting Eqn. (3) into Eqn. (12), we obtain

$$Q_m=Q_{m,\tau},+Q_{m,G}+Q_{m,B} \tag{13}$$

where

$$\begin{aligned} Q_{m,\tau}&=\int_L dx\int_{-H}^{0} v_\tau\,dz\\ Q_{m,\tau}&=\int_L dx\int_{-H}^{0} v_G\,dz\\ Q_{m,\tau}&=\int_L dx\int_{-H}^{0} v_B\,dz \end{aligned} \tag{14}$$

$Q_{m,G}$ is the geostrophic transport, $Q_{m,\tau}$, is the surface Ekman transport due to the surface wind stress and $Q_{m,B}$ is the bottom Ekman transport due to the bottom friction.

The heat transport Q_t due to ocean currents across a section S is well approximated by

$$Q_t=\iint_s \rho\,C_p T\vec{v}\cdot\vec{n}ds \tag{15}$$

Let

$$\left.\begin{aligned} \vec{v}&=\bar{\vec{v}}+\vec{v}'\\ T&=\bar{T}+T' \end{aligned}\right\} \tag{16}$$

in which $\bar{\vec{v}}$ and $\bar{T}$ are the depth-averaged velocity and temperature, respectively, $\vec{v}'$ is the baroclinic velocity component and T' is the deviations from the average temperature. Then Eqn. (2) becomes

$$Q_t=\iint_s \rho\,C_p\bar{T}\bar{\vec{v}}\cdot\vec{n}dzdx+\iint_s \rho\,C_p T'\vec{v}'\cdot\vec{n}dzdx \tag{17}$$

The heat transport (HT) components can be now divided into two parts, namely, the barotropic and baroclinic components.

3. Data and parameters

In this study both the hydrographic data and moored current meter data are used. During the early summer cruise in 1989, a short-term (5 May–7 May) moored station M_2 was located on section S_5 (Fig. 1.(a)) at 241 m water depth. One current meter was set at 80 m depth and the observed average volocity is 8.2 cm/s and 24° clockwise from north. During the autumn cruise in 1989, a moored station M_1 was located on section S_2 (Fig. 1.(b)) at 100 m water depth. Two current meters were set at 40 and 80 m depths, and their observation period was from Oct. 11 to Oct, 22. The time-averages of the observed velocities at 40 m and 80 m depths were (14.6 cm/s, 31°) and (13.5 cm/s, 8°), respectively. For this computation, only the observed velocity at 80 m level is used as a known value of velocity at the 80 m reference level in Eqn. (7).

Both the vertical diffusion coefficient K_v and vertical eddy coefficient A_z are assumed to be constant. We have experimented with different values of these coefficients, namely, A_z=50 and 100 cm²/s and K_v=1 and 10 cm²/s.

The average wind direction and speed as observed on board R/V Shijian were 223° (SW) and 6.5 m/s during the early summer cruies of 1989 and 43.7° (NE) and 9.3 m/s during the autumn cruise of 1989, respectively. Because of the lack of accurate wind data, a steady uniform wind field for each cruise with the above respective average values is assumed.

To compare the effects of the vertical viscous terms and the vertical diffusion terms we try two values of vertical eddy coefficient A_z (50 and 100cm²/s) and two values of vertical

diffusion coefficient K_v (1 and 10cm^2/s). The values of q_{e1} and q_{e2} are taken to be, respectively, -1.7 and 0.8×10^3 J/cm^2 d for the early summer cruise and 1.3 and 2.1×10^3J/cm^2 d for the autumn cruise (see Institute of Oceanography and Geography, 1977). For comparison we have also carried out computations without imposing the inequality constraints.

4. Numerical experiments

Figures 1. (a), (b) show the bathymetry, hydrograhic sections and computation boxes for the early summer and autumn, respectively, in 1989. The computation points are at the midpoints between neighboring hydrographic stations. All boundary sections of the computation boxes are divided into layers according to isopyncal $\sigma_{t,p}$ values of 24, 27, 30 and 33. For example at the section S_5 during early summer cruise, the depths of $\sigma_{t,p}=24$, 27, 30 and 33 levels lie between 30 to 120 m, 250 to 350 m, 650 to 700 m and around 1250 m, respectively (Fig. 2)

To compare the computation results for different physical parameters we carried out a number of experiments. The symbol CA-i-j denotes a particular experiment. i=1,2 denote the early summer and autumn cruises, respectively, in 1989. j=1 indicates that the inequality constraints are not imposed and j=2 the inequality constraints are imposed.

From Eqns (9)–(11), the values of T_0^2 for different reference levels are computed. For the early summer data the minimum value of T_0^2 is found at H, the water depth, and thus the reference level is taken to be the water depth H. For the autumn data the minimum of T_0^2 is at z_0 =600 m level. However, since the value of T_0^2 at $z_0=H$ is close to the minimum value, in order to compare the results of the two data sets, the reference level for the autumn data is also taken at the water depth.

For the two values of vertical diffusion coefficient K_v(1 and 10 cm^2/s), the respective computed volume transports differ by less than 4%. The computed volume transport for different values of vertical eddy coefficient A_z(50 and 100 cm^2/s) changes less. In the following discussions the results are all based on $A_z=100$ cm^2/s and $K_v=10$ cm^2/s.

Because of the shallowness of the surface layer

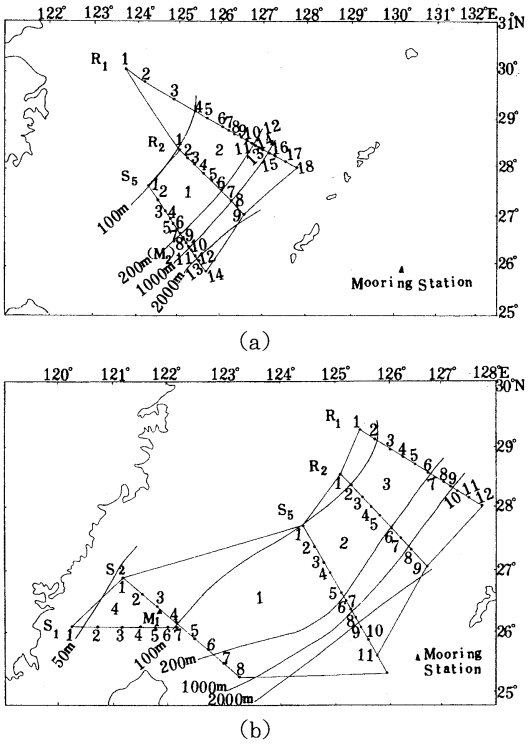

Fig. 1. Sketch of bottom topography (in meters), and locations of hydrographic and mooring stations and computation boxes (a) for early summer (May and June) of 1989 and (b) for autumn (October) of 1989.

and also the lack of surface boundary conditions for salt, consideration of the salt convection-diffusion equation for the surface layer or not usually has no significant effect on the computation results. Our experiments confirm it, too. It is found that the two cases where the salt equation for the surface layer is considered or not result in relative changes of volume transports by less than 0.1%. Hence all results presented in the following discussions are based on consideration of the salt convection-diffussion equations for all layers except the surface layer.

On the numerical computation of this method, we discuss the following questions.

Table 1 lists the balances of the volume, salt and heat transports by the modified inverse method and those by the dynamic method, respectively. For meaningful comparison, the level of no motion for the dynamic method is also taken to be the water depth H. Box-1 is bounded by sections S_5 and R_2 of the early

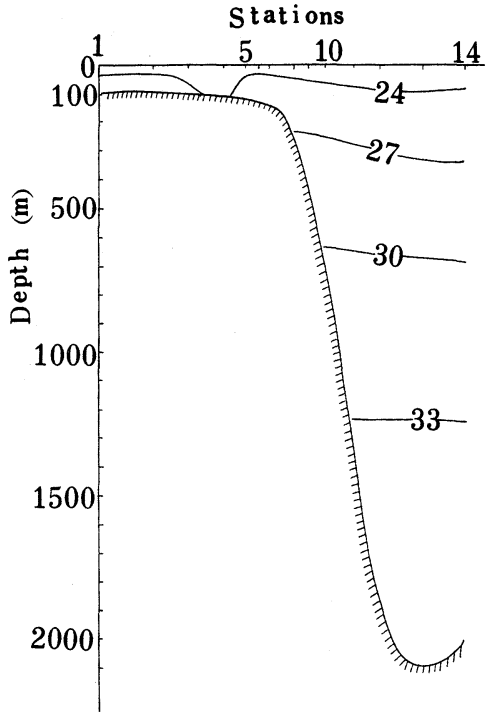

Fig. 2. Isopycnal levels along section S_5 for early summer (May and June) of 1989.

summer observation in 1989 (Fig. 1(a)) and box-2 is bounded by the same sections of the autumn observation in 1989 (Fig. 1(b)). Table 1 indicates that (1) for the dynamic method conservations of volume, salt and heat transport are all not satisfied; (2) conservations of both volume and salt are satisfied approximately for CA-i-1 and CA-i-2.

According to the data given by Institute of Oceanography and Geography of Academia Sinica (1977), the bounds of the magnitude of the heat flux at the sea surface for boxes 1 and 2 is 10^{12}~10^{13}W. For case CA-i-1 which dose not impose the inequalities (8), the unbalanced amount of the heat flux is of the order of 10^{13} ~10^{14}W (Table 1), much larger than the bounds of the heat flux at the sea surface given above. This means that the heat flux at the sea surface can not be obtained by case CA-i-1, and the inequality constraints. Egn. (8) are necessary for obtaining approximately the heat flux at the sea surface.

Table 1. The balance of the volume, salt and heat transports in box-1 during early summer of 1989 and box-2 during autumn of 1989.

Box	Method	$\triangle_m$	$\triangle_s/34.5‰$	$\triangle_t$
	Dynamic method*	−1.72	−1.69	−8.34
Box-1	CA-1-1	−0.02	0.00	−5.91
	CA-1-2	−0.02	−0.01	−0.72
	Dynamic method*	−3.78	−3.85	−29.51
Box-2	CA-2-1	0.04	−0.00	−12.85
	CA-2-2	0.04	−0.03	0.61

Note

*: The level of no motion is set at the water depth H.

$\triangle_m$: balance of volume transport into the box (positive into the box, units: $10^6m^3/s$).

$\triangle_s$: balance of salt transport into the box (positive into the box, units of $\triangle_s/34.5‰$: $10^6m^3/s$)

$\triangle_t$: balance of heat transport into the box (positive into the box, units: 10^{13}W).

In the following we compare the results obtained with the modified method (CA-i-1 and CA-i-2) and the dynamic method.

Table 2 shows that the difference in VT obtained by the modified method (CA-i-1 and CA-i-2) and dynamic method is not large. However, the differences in VT at the lateral sections west of either box-1 or box-2 is large. For example, the VT through the lateral section west of box-1 is $0.6\times10^6m^3/s$ for case CA-1-2 (Fig. 5), but $0.25\times10^6m^3/s$ with the dynamic method. It is worthy of note that the Ekman transport at the section is maximum when the wind direction is parallel to this section. During early summer of 1989, the angle between the orientation of section S_5 (R_2 and R_1) and the wind direction is large. Thus the wind stress has little effect on the VT of the Kuroshio. However it has important effects on the VT at the lateral sections of the boxes, especially the lateral section on the shallow shelf. Table 3 shows that there are some differences in VT obtained with the modified method (CA-i-1 and CA-i-2) and dynamic method for the autumn observation of 1989.

To see the effect of the imposed surface heat flux inequality we compare the results of CA-i-1 and CA-i-2 (Tables 2 and 3). The relative changes of volume transport (VT) and heat transport (HT) between CA-1-1 and CA-1-2 are both less than 2% for the data of early summer of 1989 (Table 2). For the data of autumn of

Table 2. Comparison of the VT ($10^6 m^3/s$) and HT($10^{15}W$) at sections obtained with the dynamic method and the modified inverse method (CA-1-1 and CA-1-2) during early summer of 1989.

Method	section S_5		section R_2		section R_1	
	VT	HT	VT	HT	VT	HT
Dynamic method*	29.2		28.8		36.1	
CA-1-1	30.3	2.28	29.1	2.09	35.0	2.52
CA-1-2	30.4	2.31	28.7	2.06	34.6	2.50

*: The level of on motion is set at the water depth H.

Table 3. Comparison of the VT($10^6 m^3/s$) and HT($10^{15}W$) at sections obtained with the dynamic method and the modified inverse method (CA-2-1 and CA-2-2) during autumn of 1989.

Method	section S_5		section S_5		section R_2		section R_1	
	VT	HT	VT	HT	HT	HT	HT	HT
Dynamic method*	11.4		33.0		21.2		30.6	
CA-2-1	15.3	1.43	22.1	2.30	18.3	1.72	30.5	2.24
CA-2-2	16.0	1.51	29.2	2.53	17.6	1.56	31.0	2.29

*: The level of on motion is set at the water depth H.

Table 4. The horizontal and vertical volume transports through the section or the face in each layer of box-1 for early summer in 1989

layer	section S_5	$(EL)_1$	section R_2	$(WL)_1$	$(VVT)_j$	$\triangle_j$
1st	6.94	−0.73	− 6.73	0.25	0 0.24	−0.03
2nd	15.40	−2.81	−11.86	0.39	−0.24 −0.87	0.01
3rd	7.59	−0.75	− 8.55	0	0.87 0.85	0.01
4th	0.42	1.28	− 1.30	0	−0.85 0.45	−0.00
5th	0.05	0.64	− 0.25	0	−0.45 0	−0.01
total	30.40	−2.37	−28.69	0.64	0	−0.02

Note
$(WL)_1$: the western lateral section of box-1
$(EL)_1$: the eastern lateral section of box-1
$(VVT)_j$: the upper and lower numbers denote the vertical volume transports at the upper and lower faces of the j-th layer, respectively.
$\triangle_j$: the balance of volume transport into the j-th of box-1.
(positive into the layer, units; $10^6 m^3/s$).

1989, however, although relative changes of both VT and HT between CA-2-1 and CA-2-2 are small for section R_1, large relative change of HT reaches 9% at both sections R_2 and S_5 (Table 3). At section S_5 the relative change of VT between CA-2-1 and CA-2-2 is as high as 24%. This indicates that the data of autumn of 1989 is probably noisier than the data of early summer of 1989. In the following, our discussions will concentrate mainly on results with inequality constraints, (8) imposed.

Now we discuss the horizontal and vertical

Table 5. The horizontal and vertical volume transports through the section or the face in each layer of box-2 for the early summer in 1989

layer	section PN	$(EL)_2$	section S_5	$(WL)_2$	$(VVT)_j$	$\triangle_j$
1st	− 7.68	1.22	6.73	0.12	0 −0.43	−0.04
2nd	−17.34	2.84	11.86	0.42	0.43 1.81	0.02
3rd	− 9.01	0.74	8.55	0	−1.81 1.53	0.00
4th	− 0.65	0.63	1.30	0	−1.53 0.25	0.00
5th	0	0	0.25	0	−0.25 0	0.00
total	−34.68	5.43	28.69	0.54	0	−0.02

Note
$(WL)_2$: the western lateral section of box-2
$(EL)_2$: the eastern lateral section of box-2
$(VVT)_j$: the upper and lower numbers denote the vertical volume transports at the upper and lower faces of the j-th layer, respectively.
$\triangle_j$: The balance of volume transport into the j-th of box-2. (positive into the layer, units; $10^6 m^3/s$).

volume transport in each layer using the early summer observation as the example. Tables 4 and 5 show that over 95% of the VT of the Kuroshio is in the 1st, 2nd and 3rd layers, i.e., above the 700 m level. Comparing the magnitude of the horizontal VT of the Kuroshio with the vertical volume transport (VVT), the magnitude of the VVT is much less then the Kuroshio VT in the 1st, 2nd and 3rd layers. However, they are same order in the 4th and 5th layers. Finally, the horizontal volume transport through the western lateral section of box, i.e. the section on the shallow shelf in the East China Sea, is of the same order at the vertical volume transport (Tables 4, 5 and Fig. 5).

During the autumn of 1989 the moored station M_1 has two observation depths, 40 and 80 m. The observed average velocity at 80 m is used for computation. The computed velocity at the 40 m level of the same station has a 16.1 cm/s component normal to section S_2, which agree well with the observed value of 14.5 cm/s.

5. Velocity and volume transport distribution during early summer (May-June) of 1989

5.1 Velocity distribution

Fig.3 shows the velocity distribution at section S_5 for case CA-1-2. The core of the Kuroshio is located over the slope. The maximum velocity is found at the 75 m level with a magnitude of 111 cm/s. As found in previous studies (e.g. YUAN and SU, 1988), in the deep layer, the axis of the Kuroshio seems to be further eastward as it flows northward. There are two countercurrents in the Kuroshio region. One is at the bottom layer near the shelf break and its maximum speed is greater than 30 cm/s. The other is below 800 m level over the lower part of the continental slope, but its speed is smaller than 2 cm/s.

At section R_2, the Kuroshio core is located also over the shelf break. The 100 cm/s isotach reaches as deep as 125 m and the maximum velocity is found at 50 m with a magnitude of 129 cm/s. There is no countercurrent below the Kuroshio. However, there is a countercurrent over the shelf at the bottom layer near the shelf break.

The Kuroshio speed at section R_1 is greater than at other sections, probably due to both the shallow water depth there and the merging of currents from the eastern lateral section of box-2 (Fig. 5). Its maximum velocity (about 149

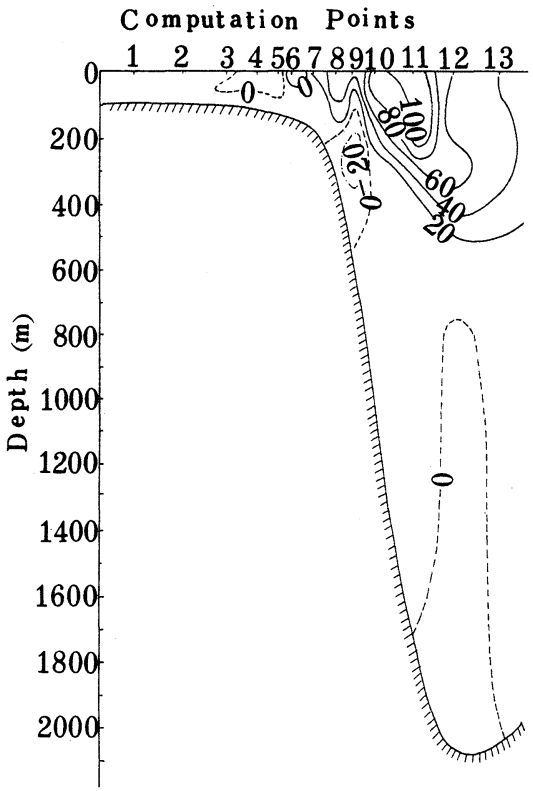

Fig. 3. The velocity distribution at section S_5 during early summer of 1989 for case CA-1-2. (units: cm/s)

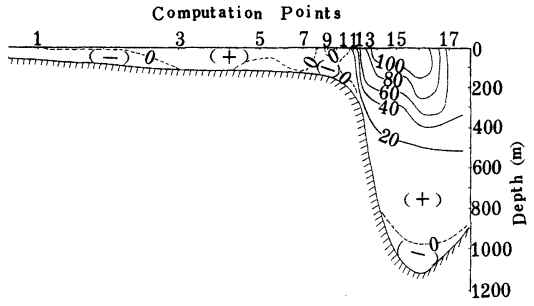

Fig. 4. The velocity distribution at section R_1 during early summer of 1989 for case CA-1-2. (units: cm/s)

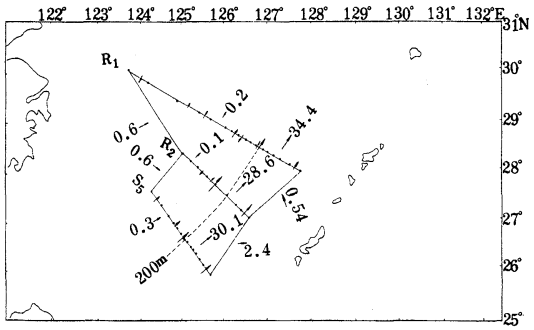

Fig. 5. Volume transport distribution in the computational region during early summer of 1989 for case CA-1-2. (units:$10^6 m^3/s$)

cm/s) is found at the surface (Fig. 4). At the 200 and 400 m levels the maximum velocities are 90 and 39 cm/s, respectively, and their positions are both located east of the surface maximum. Landward of the front there is a southward current on the shelf and its maximum velocity is about 20 cm/s. Under the Kuroshio there is a very weak southward current at the bottom of the trough.

5.2 Volume transport distribution

There is a cyclonic gyre or a southward current west of Kuroshio (Fig. 4). The Kuroshio width is more than 100 km. The volume transport (VT) of the Kuroshio at sections S_5 and R_1 is about 30 and $35 \times 10^6 m^3/s$, respectively, greater than the computed Kuroshio VT during early summer of 1988 (YUAN, SU and PAN., 1991). The intrusion of the Kuroshio water over the shelf at section R_5 is further to the west than that at sections S_5 and R_1 (Fig. 5). This is in agreement with the position of Kuroshio axis (Figs. 3 and 4).

Finally, as previous studies (SU and PAN, 1987; YUAN *et al*, 1987) pointed out, there is the northeastward current over the East China Sea shelf, which was called Taiwan Warm Current, and it may be considered as being a combination of two current systems, an inshore branch and an offshore branch. The VT of Taiwan Warm Current (TWC) which also flows through the computational region is about $1.5 \times 10^6 m^3/s$, i.e. $0.6+0.6+0.3=1.5(10^6 m^3/s)$(Fig. 5). When this shelf current flows northeastward through section R_1, most of it has a tendency to converge to the shelf break, similar to the findings of previous studies (e.g. YUAN and SU, 1988).

6. Velocity and volume transport distributions during autumn (October) of 1989

6.1 Velocity distribution

The velocities at section S_2 during the 1989 autumn cruise are not very large (Fig. 6). There

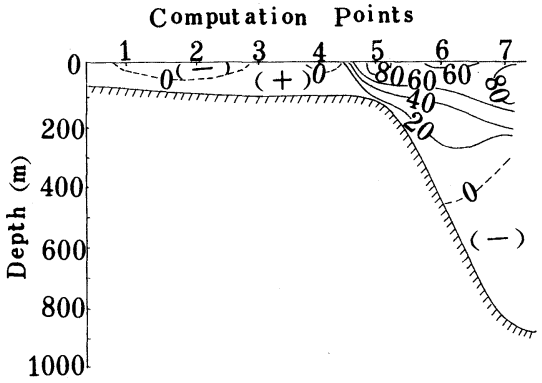

Fig. 6. The velocity distribution at section S_2 during autumn of 1989 for CA-2-2. (units:cm/s)

are two cores at section S_2. One is located at the shelf break. Its maximum velocity is about 86.4 cm/s at 25 m level. The other is located over the lower part of the slope and the velocities from 25 to 125 m levels are all greater than 80 cm/s. Below the latter core there is a countercurrent and its maximum speed is greater than 10 cm/s. At the shallow end of shelf there is a southward current in the surface layer, probably due to the strong northeast winds, but near the bottom the current is still northward (Fig. 6).

Fig. 7 shows that the core of Kuroshio at section S_5 is located close to the shelf break and the Kuroshio front is evident. Its maximum velocity is greater than 150 cm/s at the 25 m level. There is a countercurrent occupying most part of the Okinawa Trough below 600 m. This current is rather strong; for example, its velocities at the 1000 and 1500 m levels are greater than 9 and 4 cm/s, respectively. This countercurrent extends back to section R_2 (Fig. 8). Its strength at section R_2 is even strong. Its maximum speed is greater than 22 cm/s at 800 m level, and at 1000 m level its velocity is still greater than 15 cm /s. Furthermore, the core of this countercurrent is closer to the continental slope than it is at section S_5. Consistent with this, the core of the Kuroshio at section R_2 is now located over the shelf break (Fig. 8). The maximum velocity of the Kuroshio is about 90 cm/s at the 25 m level.

Like the early summer case, the Kuroshio Current speed at section R_1 is also greater than at other sections (Fig. 9), probably because of the shallow water depth at section R_1 and the merging of currents from the eastern lateral

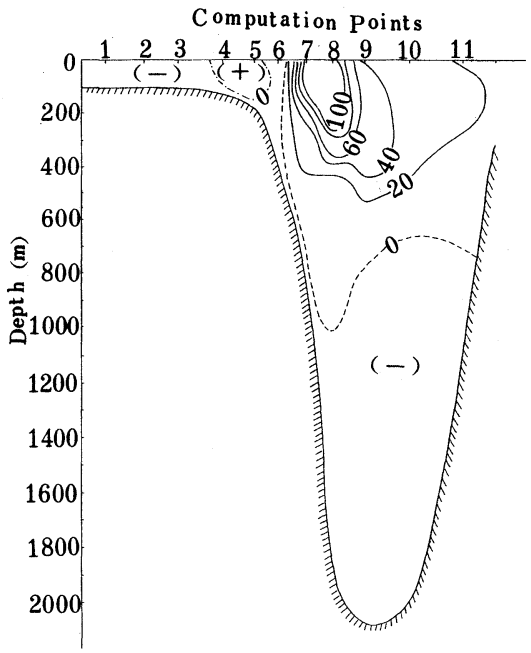

Fig. 7. The velocity distribution at section S_5 during autumn of 1989 for case CA-2-2. (units: cm/s).

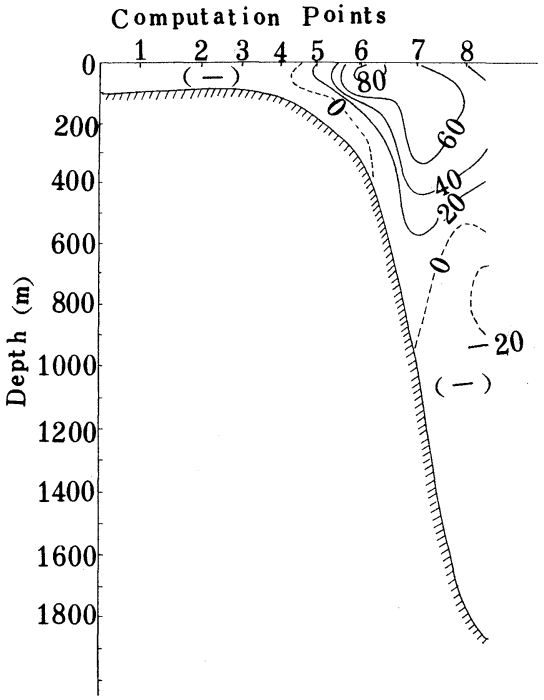

Fig. 8. The velocity distribution at section R_2 during autumn of 1989 for case CA-2-2. (units: cm/s)

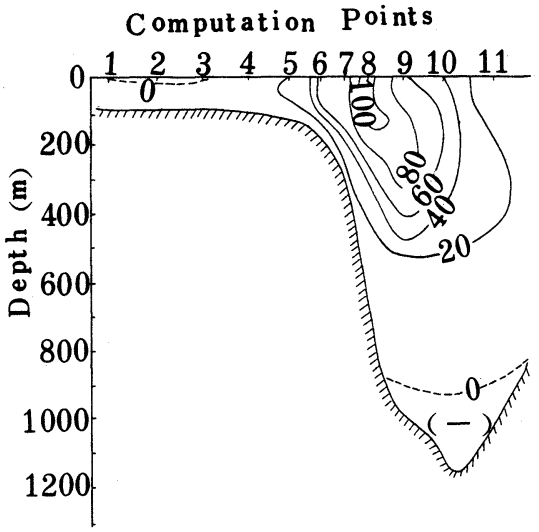

Fig. 9. The velocity distribution at section R_1 during autumn of 1989 for case CA-2-2. (units: cm/s)

section of box-3 (Fig. 10). Its maximum velocity is about 133 cm/s at 25 m level at point 8 of R_1. There is a countercurrent below 950 m level, but its velocity is smaller than at other sections.

6.2 Volume transport distribution

Fig. 10 shows the distribution of volume transport in the computational region during autumn of 1989 for case CA-2-2. The volume transport through section R_1 is about $30 \times 10^6 m^3/s$. Its VT is larger than during the same seasons of 1987 and 1988. However, it is less than during early summer of 1989 (Fig. 5). The countercurrent during autumn of 1989 is rather strong. Its VT is around $3 \times 10^6 m^3/s$ at section R_2 and $4 \times 10^6 m^3/s$ at section S_5. However, the volume transport of the countercurrent at sections R_2 and S_5 for CA-2-1 are 4 and $7.5 \times 10^6 m^3/s$, respectively. Thus, the difference of the computed countercurrent VT between CA-2-1 and CA-2-2 is large for section S_5. We shall comment on this matter later in this paper.

Fig. 10 also shows that there is a cyclonic gyre on the shelf north of Taiwan. The temperature distribution indicates that it is a cold gyre. Fig. 10 also shows that the total VT of TWC which flows into this computational region is about $1.5 \times 10^6 cm^3/s$.

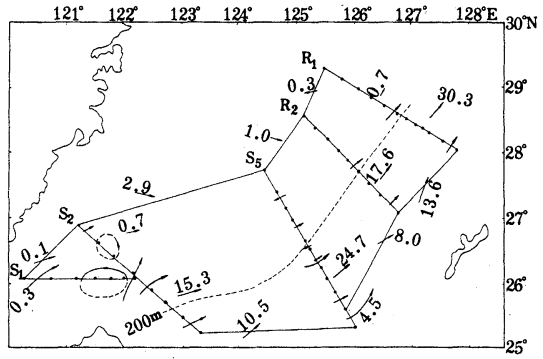

Fig. 10. Volume transport distribution in the computational region during autumn of 1989 for case CA-2-2. (units:$10^6 m^3/s$).

7. Heat transport

Table 6 lists the computed VT and HT of the Kuroshio through section R_1 for the early summer cruise and sections R_1 and S_5 for the autumn cruise. Other sections covered only parts of the Kuroshio and their results are not listed. For comparison the VT and HT of the Gulf Stream (Hall and Bryden, 1982) are also listed in Table 6. The symbols $Q_{t,1}$ and $Q_{t,2}$ denote the barotropic and baroclinic components of heat transport and the symbol $\tilde{T}$ is defined as the average temperature:

$$\tilde{T} = Q_t (\rho C_p Q_m)^{-1} \tag{18}$$

In general, the barotropic component of the heat transport seems to be larger than the baroclinic component for either the Kuroshio or the Gulf Stream, except for the Kuroshio at section S_5 during autumn of 1989 when the baroclinic component is higher than the barotropic component.

The computed results for case CA-i-2 show that during early summer of 1989 the heat transfer is from the atmosphere to the ocean for boxes 1 and 2 and their values are 7.2 and $5.7 \times 10^{12} W$, respectively, totaling $1.29 \times 10^{13} W$. During autumn of 1989 the total heat transfer is from the ocean to the atmosphere and it is about $2.80 \times 10^{13} W$. The values of these heat exchanges at the sea surface are less than 0.5% of the HT of the Kuroshio through each section. This means that high quality hydrographic data is necessary to obtain reliable heat flux values at the sea surface.

Table 6. The comparison of VT (units:10^6m^3/s) and HT(units:10^{15}W) between the Kuroshio (CA-i-2) and Gulf Stream

Current system	time	section	VT	HT	$\tilde{T}$(℃)	$Q_{t,1}$	$Q_{t,2}$
Kuroshio	early summer of 1989	R_1	34.6	2.50	17.64	1.60	0.90
Kuroshio	autumn of 1989	R_1	31.0	2.29	18.11	1.71	0.58
Kuroshio	autumn of 1989	S_5	29.2	2.53	21.20	1.17	1.36
Gulf Stream*	annual mean in 1973	Florida Straits	29.5	2.38	19.71	1.88	0.50

* From Hall and Bryden, (1982).

To see the effect of the inequality constraints (8) on the computed heat flux at the sea surface, we compare case CA-i-2 with case CA-i-1 again. The computed results of case CA-1-1 show that during early summer of 1989 there is 5.65×10^{13} W of heat transferred into the ocean from the atmosphere over the computational region, about 8 times larger than the computed value for case CA-1-2. The difference of the computed air-sea heat fluxes between CA-2-1 and CA-2-2 during autumn of 1989 is even larger. For example, the heat transfer from the ocean to the atmosphere through the sea surface of box-1 is 1.03×10^{13}W for case CA-2-2, but 38.02×10^{13}W for case CA-2-1 and in opposite direction from the atmosphere to the ocean. This seems to indicate that the quality of the 1989 autumn cruise data is not so good as the 1989 early summer cruise data and the inequality constraints, (8) is necessary for the inverse computation.

8. Summary

A modified inverse method is used to compute the Kuroshio in the East China Sea, based on the hydrographic data and moored current meter records obtained during both early summer and autumn of 1989. It is found that:

1) In general, on a broad shallow shelf the surface Ekman velocity component due to the wind stress can not be neglected; thus our modified inverse method is useful in shallow seas. When the quality of the hydrographic data is poor, to obtain the heat flux at the sea surface, the inequality constraints at the sea surface. (8) seems to be needed.

2) The vertical volume transport (VVT) has less effect on the total volume transport of the Kuroshio. However, the VVT can not be neglected in the deep layer. The VVT is of the same order of magnitude as the horizontal volume transport through the west lateral section of box, i.e. the section on the shallow shelf in the East China Sea.

3) The volume transports at section R_1(PN) are 35 and 31×10^6m^3/s during early summer and autumn, respectively, in 1989. The heat transports at R_1 (PN) section are 2.50 and 2.29×10^{15} W during early summer and autumn, respectively, in 1989.

4) The Kuroshio Current speed at section R_1 is greater than at other sections, probably due to both the shallow water depth at section R_1 and the merging of currents from the eastern lateral section of box-2 (Fig. 5) or box-3 (Fig. 10).

5) A countercurrent is present in the deep layer during both cruises of 1989. It is stronger during autumn of 1989.

6) The VT of TWC flowing into this computational region is about 1.5×10^6m^3/s during both cruises of 1989.

7) During both cruises of 1989 the barotropic components of HT is in general larger than the corresponding baroclinic components. About 1.29×10^{13}W of heat is transferred into the ocean from the atmosphere over the computational region during early summer of 1989 and about 2.80×10^{13}W of heat from the ocean to the atmosphere over the computational region during autumn of 1989.

References

FIADEIRO, M.E and G. VERONIS (1982): On the determination of absolute velocities in the ocean. J. Mar. Res., 40, Suppl., 159–182.

GUAN, BINGXIAN (1982): Analysis of the variations of volume transport of Kuroshio in the East China Sea. *In*: Proc. Japan–China Ocean Study Symp.,K. HISHIDA *et al.*, eds, Tokai Univ. Press, 118–137.

GUAN, BINGXIAN (1988): Major feature and variability of the Kuroshio in the East China Sea. Chinese. J. Oceanol. Limnol., **6**, 35–48.

HALL, M.M. and H.L. BRYDEN (1982): Direct

estimates and mechanisms of ocean heat transport. Deep-Sea Res., **29**, 339–359.

Institute of Oceanography and Geography, Academia Sinica (1977): The Atlas of heat balance at the sea surface in the Bohai Sea, Yellow Sea and East China Sea, Chinese Science Press, 160 pp.

NISHIZAWA , J., E. KAMIHIRA, K. KOMURA, R.KUMABE and M.MIYAZAKI (1982): Estimation of the Kuroshio mass transport flowing out of the East China Sea to the North Pacific. La mer, **20**, 37–40.

SARKISYAN, A.S. (1977): The diagnostic calculations of a large-scale oceanic circulation. *In*: The sea, vol.6, E.D.Goldberg *et al.*, eds, Wiley-Interscience Publication, 363–458.

SU, JILAN and PAN YUQIU (1987): On the shelf circulation north of Taiwan. Acta Oceanologica Sinica, **6** (Suppl. 1), 1–20.

WUNSCH, C. (1978): The general circulation of the North Atlantic west of 50° W determined from inverse methods. Rev. of Geophy. Space Phys., **16**, 583–620.

WUNSCH, C. and J.F. MINSTER (1982): Methods for Box Models and Ocean Circulation Tracers: Mathematical Programing and Nonlinear Inverse Theory. J. Geophy. Res., **87**C, 5647–5662.

YUAN, YAOCHU and SU JILAN (1988): The calculation of Kuroshio Current Structure in the East China Sea–Early Summer. Progress in Oceanography, **21**, 343–361.

YUAN, Y., M. ENDOH and H. ISHIZAKI (1991): The Study of the Kuroshio in the East China Sea and Currents East of the Ryukyu Islands. Acta Oceanologica Sinica, **10**, 373–391.

YUAN, YAOCHU, SU JILAN and PAN ZIQIN (1990) Calculation of the Kuroshio Current South of Japan During Dec., 1987–Jan., 1988. Proc. Investigation of Kuroshio (Ⅱ), 256–266.

YUAN, YAOCHU, SU JILAN and PAN ZIQIN (1991): A Study of the Kuroshio in the East China Sea and the Currents East of the Ryukyu Islands in 1988. *In*: Oceanography of Asian Marginal Seas. K. TAKANO, ed. Elsevier Science Publishers, 305–319.

YUAN, YAOCHU, SU JILAN and XIA SONGYUN (1986): A diagnostic model of summer circulation on the northwest shelf of the East China Sea. Progress in Oceanography, **17**, 163–176.

YUAN, YAOCHU, SU JILAN and XIA SONGYUN (1987): Three dimensional diagnostic calculation of circulation over the East China Sea Shelf. Acta Oceanologica Sinica, **6** (Suppl. 1), 36–50.

La mer 30: 263–274, 1992
Société franco-japonaise d'océanographie, Tokyo

Temporal and spatial variations in the Bottom Cold Water on the shelf off San'in coast, Japan

Yutaka ISODA* and Hisaaki OOMURA**

Abstract: The main thermocline off San'in coast in the Japan Sea intersects a gentle slope on the shelf. A large displacement of this thermocline from the shelf edge to the inshore region has been frequently observed from accumulated hydrographic observation data. Such a displacement means the evolution of a cold-water region over the shelf, which is called the Bottom Cold Water (BCW). In order to clarify the temporal and spatial variations in the BCW, we analyzed a time series of the bottom-water temperature data from December 1980 to December 1982, measured by a submarine telephone cable on the shelf between Japan and Korea.

We found that intense evolutions of the BCW over the shelf occur 6 to 9 times in a year, rather than seasonal variations of the BCW. Although such events sometimes are followed by a few cycles of oscillations, they show eastward phase propagations of 7 to 10 cm s^{-1} at a typical wavelength of a few hundreds of kilometers. These characteristics may identify such motions as bottom-trapped Rossby waves originating from disturbances around the wastern entrance of the Tsushima/Korea Strait.

1. Introduction

The Japan Sea is a marginal sea of the North Pacific Ocean and is a semi-enclosed basin with its depth reaching more than 3000m. The Tsushima Current flowing into the Japan Sea through the Tsushima/Korea Strait forms three branches off the San'in coast in the Japan Sea as shown in Fig.1(a). Fig.2 shows horizontal current profiles by ADCP at 10m, 50m, and 100m depth, vertical distributions of temperature along Section A off Hamada (for location see Fig. 1(b)), and wind vectors at Hamada in summer 1988 (a) (ISODA and MURAYAMA, 1990) and summer 1989 (b)(ISODA *et al.*, 1992). Both observations were carried out under a light wind with speed of less than 1 m s^{-1}. Nevertheless, observation (a) exhibits a large displacement of the main thermocline from the shelf edge to the inshore region, while observation (b) shows that the thermocline intersects the shelf edge. Thus, it seems that the large displacement of the thermocline shown in observation (a) cannot be explained by using the coastal upwelling theory in the wind-forced regions. In addition, it can be seen that the positions and shapes of the flow on the shelf may be also largely affected by the location of the main thermocline.

The large displacement of the main thermocline around the shelf edge means the evolution of a cold water region over the shelf, which is called the Bottom Cold Water (hereafter referred to as the BCW). For a long time, this BCW has been believed to exist over the shelf off San'in coast. This was based on the results of accumulated hydrograpghic observations (e.g. UDA, 1931; YAMASAKI, 1969; MORIWAKI and OGAWA, 1988, 1989; ISODA and MURAYAMA, 1990). However, the detailed horizontal structure of the BCW, its variation period, and the possible cause of such variations are not yet clarified, because such an irregular phenomenon as the BCW in time and space cannot be detected from the monthly or bi-monthly hydrographic observations.

A submarine telephone cable lies on the shelf between Japan and Korea as shown in Fig. 1(b), The bottom-water temperatures along the submarine cable were measured for the purpose of

* Department of Civil and Ocean Engineering, Ehime University, Matsuyama, 790 Japan
** Fuyo Ocean Development and Engineering Co., Ltd., Bakurou-chou 10-6, Tokyo, 103 Japan

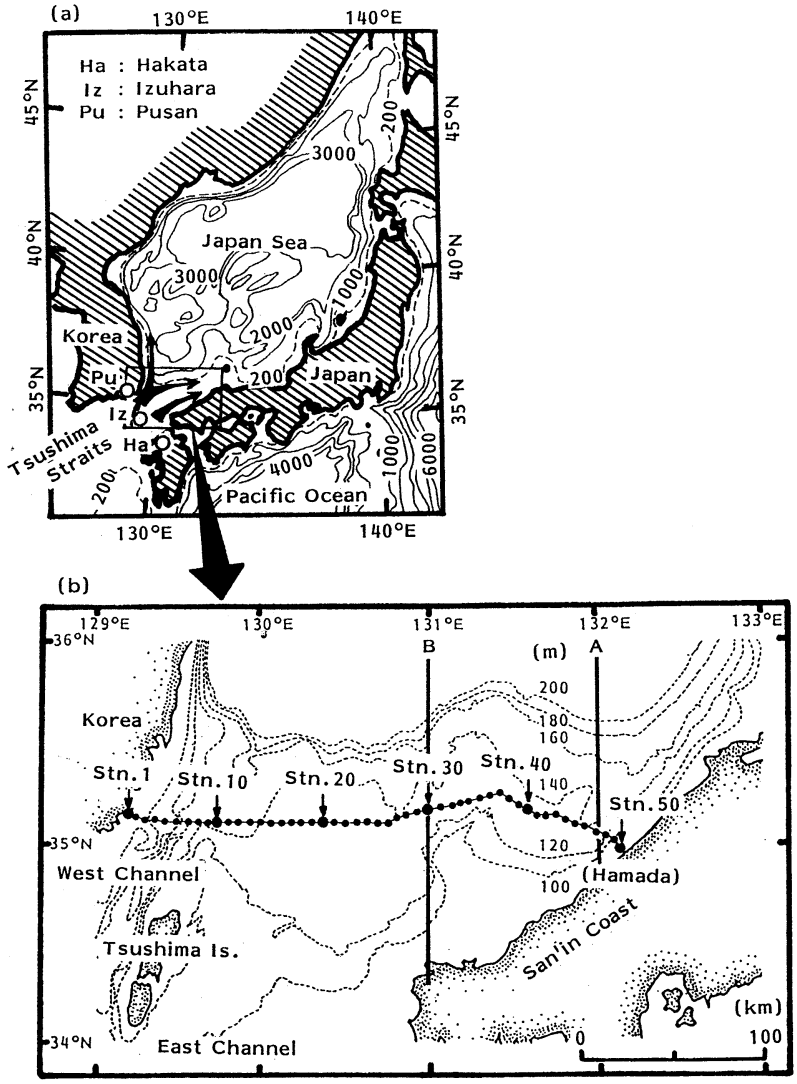

Fig. 1 (a) Map of the Japan Sea. The three branches around the Tsushima/Korea Strait are shown schematically by heavy arrows. Locations of the tide-gaugestations are shown by open circles. (b) Bathymetric chart from 100m to 200m depth on the shelf off San'in coast, showing locations of bottom-water temperature stations along the submarine cable. A and B indicate the observation lines.

maintenance and inspection. The cross-shelf (or nearly north-south) migration of the BCW front, which is the thermal front at the southern end of the BCW, can be inferred from these temperature data, because the BCW front moves just over the submarine cable as shown in Fig.2. Such continuous data in time and space on the shelf are scarce and are very valuable. We analyzed two-year temperature data along the submarine cable. The characteristics of the seasonal and the short-term variations in the BCW distribution over the shelf are described in this paper.

2. Data

The observation sites of bottom-water temperature on the shelf off San'in coast are shown in Fig. 1(b). The temperature sensor is installed in a repeater on the sea bottom for amplifying the signal. There are 50 repeaters arrayed on the submarine cable.

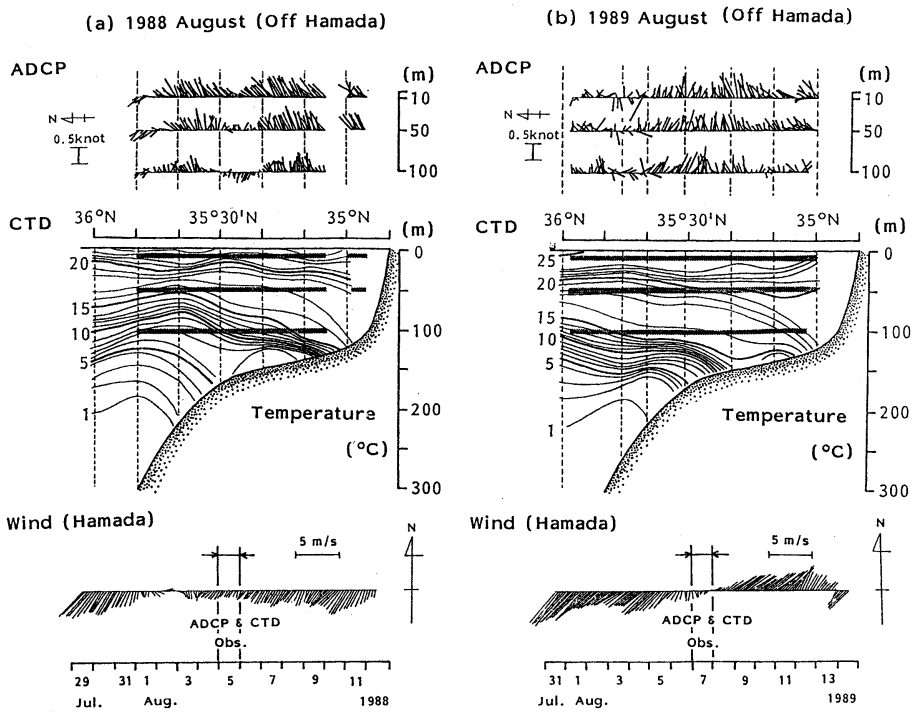

Fig. 2. Horizontal current profiles deduced from ADCP at 10m, 50m, and 100m depth (upper), vertical distribution of temperature (middle) across Section A in Fig.1(b), and time series of 24-hour running mean wind vectors during 2 weeks at Hamada (lower) on 5 August 1988 (a) from ISODA and MURAYAMA (1990) and 7 August 1989 (b) from ISODA *et al.* (1992). Three heavy horizontal lines in the middle panel indicate the observed depths and regions of ADCP.

Two-year temperature data at one week intervals from December 1980 to December 1982 were analyzed in this study. However, water temperatures at Stn.24 were not observed throughout the entire period due to some mechanical trouble. The missing time series data for Stn. 24 were constructed by linear interpolation of values at adjacent stations. Data were not taken at all stations from 23 December 1980 to 27 January 1981 and from 8 September to 15 September 1981. Hydrographic temperature data measured by the Fisheries Agency Japan (1985, 1986) at Shimane, Yamaguchi, and Fukuoka Prefectural Fisheries Experiment Stations in 1981 and 1982, are used to understand the spatial distributions of the BCW.

Since the shelf off San'in coast is directly connected to the Tsushima/Korea Strait, the flow variations on the shelf might be monitored by those in the Strait. Flow variations in the Tsushima/Korea Strait are investigated by examining sea-level differences across the Strait (e.g. KAWABE, 1982). Daily mean sea-level data from 1981 to 1982 are available at Pusan (Hydrographic Office of the Republic of Korea) and at Izuhara and Hakata (Japan Maritime Safety Agency). The positions of these tidal stations are also shown in Fig. 1(a). Since the momentum balance normal to the flow direction may be geostrophic, it can be expected that variations of sea-level difference between Hakata and Izuhara and those between Izuhara and Pusan reflect the variations of surface velocity in the East and West Channel of the Tsushima/Korea Strait, respectively. From the variations of sea level difference in both channels, the cross-shelf flow structure on the shelf will be roughly inferred.

3. Data analysis

Seasonal variations in the BCW

Fig. 3 shows the temporal variation in tem-

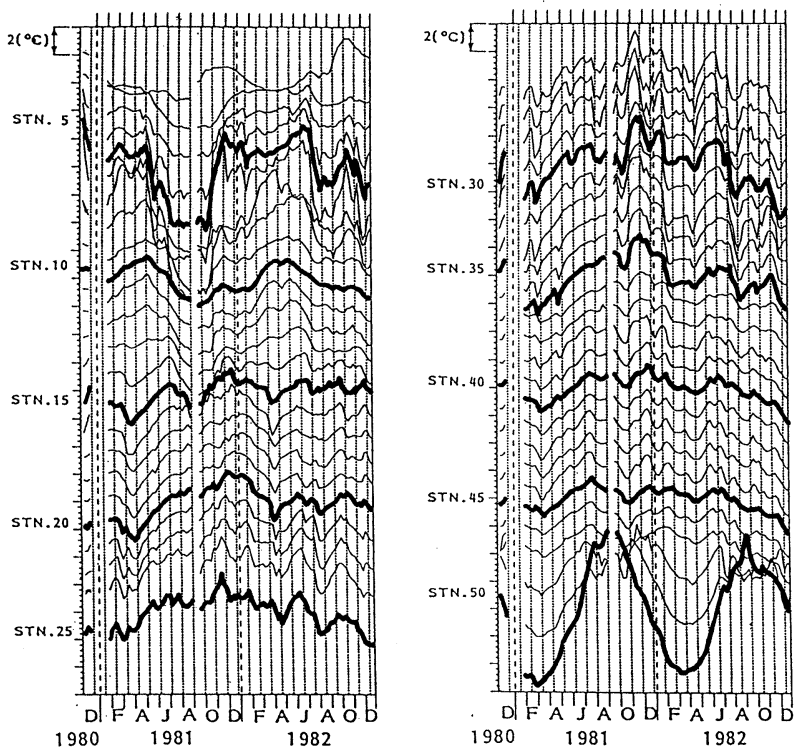

Fig. 3. Temporal variations in temperature from Stn.1 to Stn.50. Interval between dotted (broken) lines denotes a period of 4 weeks (1 year).

perature at each station. It is found that the shelf along the submarine cable can be divided into the following three regions based on the difference in the patterns of seasonal variation. Region (1) from Stn.1 to Stn.15, which corresponds to the entrance of the West Channel, has the maximum temperature in winter and the minimum in summer. Region (2) from Stn.16 to Stn.47 does not have a dominant seasonal variation, but has significant year-to-year variation with the maximum temperature in winter 1981. Region (3) from Stn.48 to Stn.50 may be considered as the region where the near-shore branch of the Tsushima Current exists and has a large seasonal variation with the maximum temperature in summer and the minimum in winter. Thus, the change of the seasonal cycle near the Japanese coast demonstrates completely opposite signs from that near the Korean coast.

The seasonal variation of sea-level difference between Izuhara and Pusan is very large while that between Hakata and Izuhara is small (KAWABE, 1982). It is considered that sea-level difference in the West Channel represents volume transport of the Tsushima Current rather than that in the East Channel. Then, temporal variations at Stn.5 in the region (1) and at Stn.50 in the region (3) are compared with the 21-day running mean of the difference in daily mean sea-level between Izuhara and Pusan, and each relationship is shown in Fig. 4. The variations of sea-level difference may indicate that the volume transport of the Tsushima Current is small from January to May and increases considerably from June to August. After reaching a maximum from August to October, the transport gradually decreases.

The seasonal changes of temperature at Stn. 5 occur rather rapidly. The large temporal gradients of temperature are seen in June and November, whereas the temperature in the other months tends to be relatively constant. It is suggested that the large spatial temperature gradient region, i.e. the BCW front, passes through the entrance of that West Channel in June and November. Therefore, we may conclude that

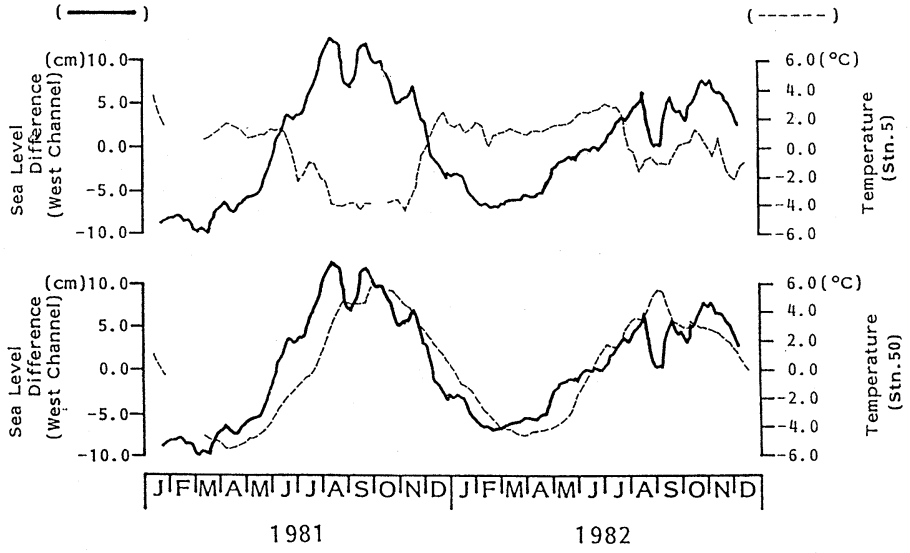

Fig. 4. The 21-day running mean of difference in daily mean sea-level between Izuhara and Pusan, i.e. at the West Channel, is indicated by heavy lines. Dashed lines show seasonal variations of bottom-water temperature at Stn.5 (upper) and Stn.50 (lower).

BCW front shifts southward (northward) along the Korean coast as corresponding to the increase (decrease) of volume transport in June (November). Such seasonal flow variation around the West Channel has also been indicated from the current measurements (BYUN and SEUNG, 1984) and the hydrographic data analysis (OGAWA, 1983; ISODA, 1989; ISODA and YAMAOKA, 1991).

It can be seen that the shape of the temperature variation at Stn.50 is roughly sinusoidal, and nearly the same as the variation patterns of sea-level difference. The correlation between the variation characteristics of the water temperature and those of sea-level difference suggests that the height of the water column along the Japanese coast increases when the water temperature near the Japanese coast increases. Such characteristics of the Tsushima Current may demonstrate the structure of the coastal boundary current, which may be strongly trapped along the Japanese coast (HANAWA, 1984; ISODA and YAMAOKA, 1991).

Short-term variations of the BCW

It is evident from Fig. 3 that the short-term variations are very pronounced only in the region (2). These variations look somewhat periodical in nature with a period of several tens of days. Their up/down-peak times are not the same among stations and tend to shift slightly from the Korean side's stations to the Japanese ones. To enhance such horizontal propagation characteristics of short-term variations, we calculated the temporal temperature gradient (TTG) within one week period at each station, i.e. temperature values of week $n+1$ minus those of week n at each station. The results together with bottom topography along the submarine cable line are shown in Fig. 5. The lateral axis in this figure is the distance from Pusan to Hamada the and time advances downward. Positive TTG values denote an increase of water temperature and negative values (blacked) denote a decrease. That is, the black color areas correspond to the BCW evolutions. Its propagation features are displayed by shaded arrows. From this figure, the following characteristics are evident: i) The BCW with the short-term variations may not be developed over the whole shelf all at once, but is often continuous and complex, presumably as a result of meander events closely spaced in space or time. There are, however, occasions starting with a relatively intense burst of motion, sometimes followed by a few cycles of oscillations as in

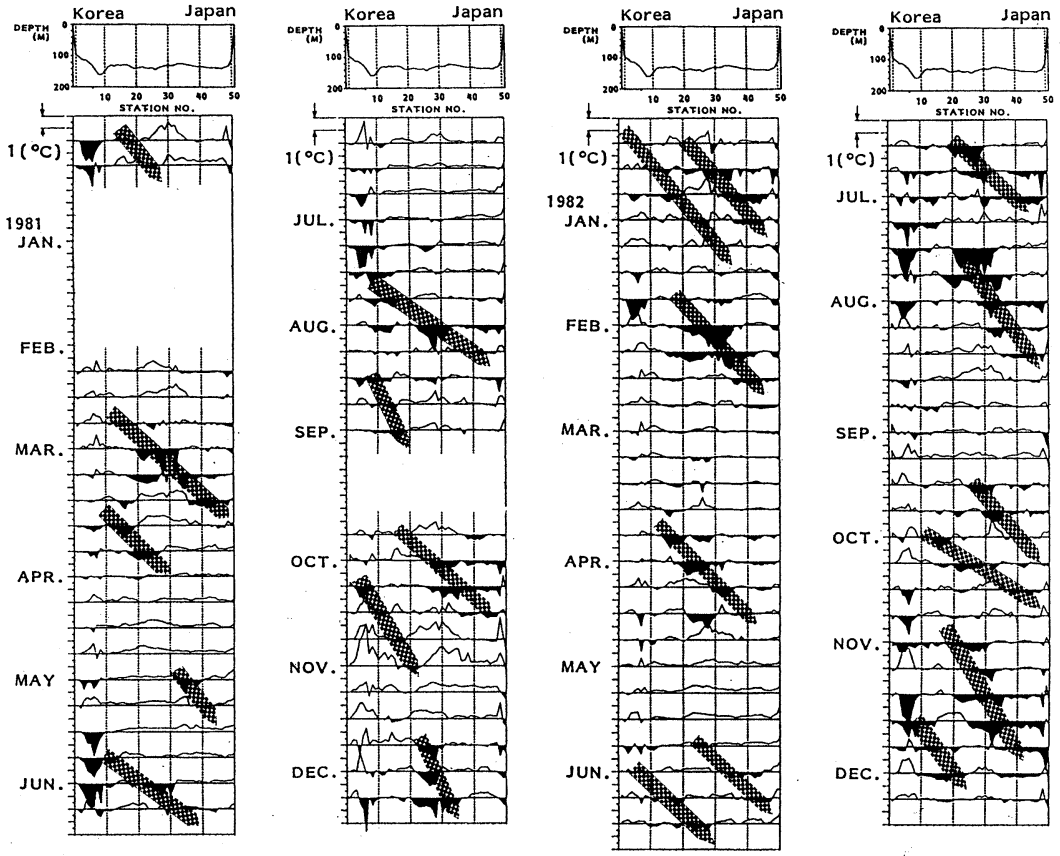

Fig. 5. Temporal temperature gradient (TTG) within one week at each station. Positive TTG values denote an increase of water temperature and negative values (blacked) a decrease. The shaded arrows display the propagation features of Bottom Cold Water evolution, which correspond to the blacked TTG areas. The bottom topography along the submarine cable line is shown in the upper part of each panel.

February to March in 1981, November to December in 1981, June in 1982, and November in 1982. Such events occurred 6 to 9 times in a year; the time scale of variations can be regarded as having periods of 40 to 60 days.

ii) It is inferred from reading the horizontal distribution of TTG variations that the horizontal scale of meandering along the shelf is approximately a few hundred kilometers.

iii) The phase of variations has moved gradually eastward. The area of phase propagation begins around the western entrance of the Tsushima / Korea Strait. The averaged eastward phase speed is estimated to be 7 to 10 cm s^{-1}; the phase propagates over about 170 km in 3 to 4 weeks in the region (2).

The synoptic pattern of the BCW can be drawn by using the convetional hydrographic observation data of the Fisheries Agency Japan, because these data were obtained during several days at the beginning of each month and, in addition, the BCW has very slow variations in time as mentioned above. Near-bottom (and 200m depth) horizontal temperature distributions on (and off) the shelf are shown in Fig. 6(a) for 1981 observations and in Fig. 6(b) for 1982 observations with the TTG distributions. That is, Fig.6 shows the horizontal distribution of the line where the main thermocline intersects the bottom slope, a feature of the BCW front. Three TTG distributions shown in each figure were also taken at nearly the same time as the corresponding hydrographic observations. At first sight, considerable spatial variations of the

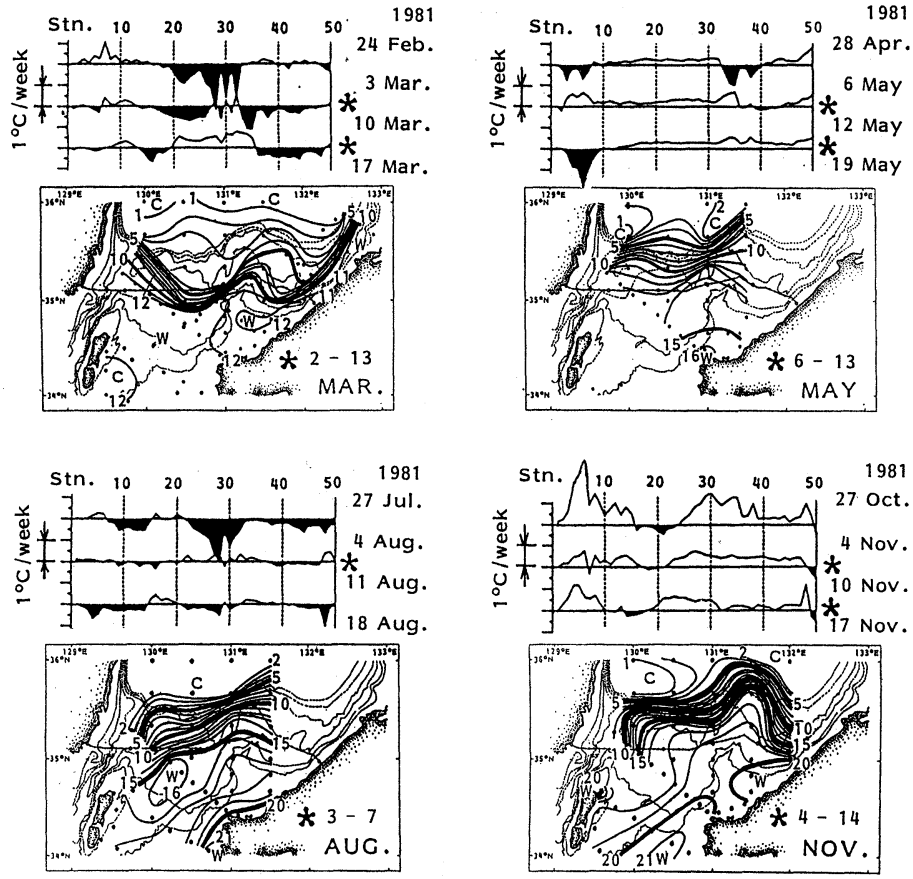

Fig. 6. Near-bottom (and 200m depth) horizontal temperature distributions, i.e. the feature of the BCW front, on (and off) the shelf for 1981 observations (a) and 1982 observations (b). The three TTG distributions shown in the upper part of each panel were taken at nearly the same time as the corresponding hydrographic observations.

BCW front are noted. From a comparison of horizontal temperature distributions at the same month in 1981 and in 1982, we cannot find the seasonal characteristics of the flow patterns. For example, there is a large meandering path in March 1981 and August 1982, but a flow along the shelf edge in March 1982 and August 1981. Although a meandering path can be seen in November in 1981 and 1982, the shapes of meandering differ from each other.

We can detect large meanders of these BCW fronts with the cross-shelf amplitude of 50 to 100 km in March and November 1981, and in August and November 1982. Such southward evolution of the BCW front corresponds to the boundary between positive and negative TTG value areas. This situation means that the southward depression will propagate eastward with time. On the other hand, a similar meander is not clear in May and August 1981, in March and May 1982, and then spatial TTG variations at those times are surely small. From these characteristics, it is clear that the short-term variations shown in Figs.3 and 5 are caused by the cross-shelf migrations of the wave-like BCW front on the shelf.

Next, to see the short-term variations of the geostrophic current in the Tsushima / Korea Strait, we calculate the cross-correlation analysis between sea-level differesnces in the West and East Channels. The statistical period is 512(=2^9) days (from 11 April 1981 to 4 septem-

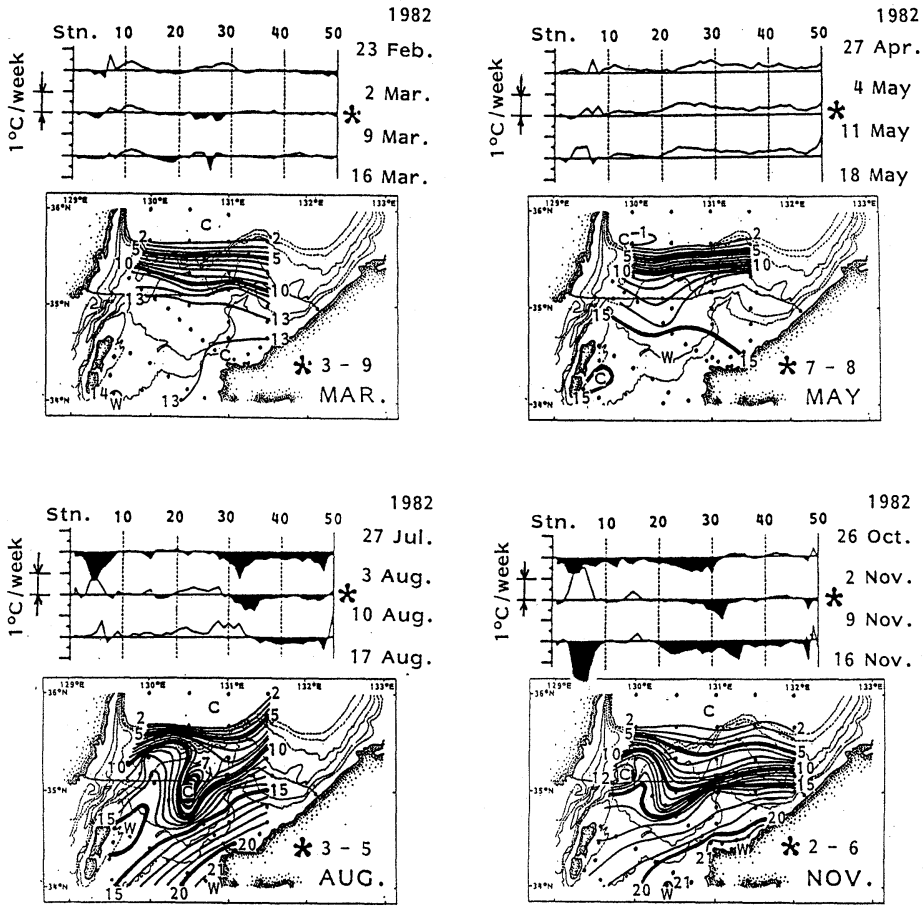

Fig. 6(b)

ber 1982) and the result is shown in Fig. 7. Hence, the Nyquist frequency is 0.5 cpd and the degree of freedom is 4. A common conspicuous spectral peak with a good correlation (95 % confidence limits of coherence-squared value is about 0.43) is seen at a period of a 50 days and its frequency band roughly coincides with that of the BCW variations. It is found that the phase difference of flow between both channels is surprisingly out of phase, although those channels are adjacent to each other (see in Fig. 1).

We will then investigate the relation between the variations of flow and water temperature by applying bandpass-filtering methods, although the statistical period is too short to analyze the data statistically. In Fig. 8, we superimposed the bandpass-filtered anomaly time series for the variations in both channels of sea level difference (thick lines) and temperature at Stn.35 (dashed lines) with a period of 42 to 63 days. Here, Stn.35 is situated on the central shelf off the San'in coast and its amplitude is relatively large. It is found that both variations of the flow and water temperature tend to be large for the same period from summer to winter 1981, although the phase of both variations cannot be discussed due to the slow variations of the BCW with relatively short wavelength. Besides, time series of sea-level show that the pattern of variations between the East and West Channels is surely opposite. Thus, it is inferred that flow structures with short-term variation have relatively small spatial scale in the cross-shelf direction and are out of phase between the coast and the shelf edge.

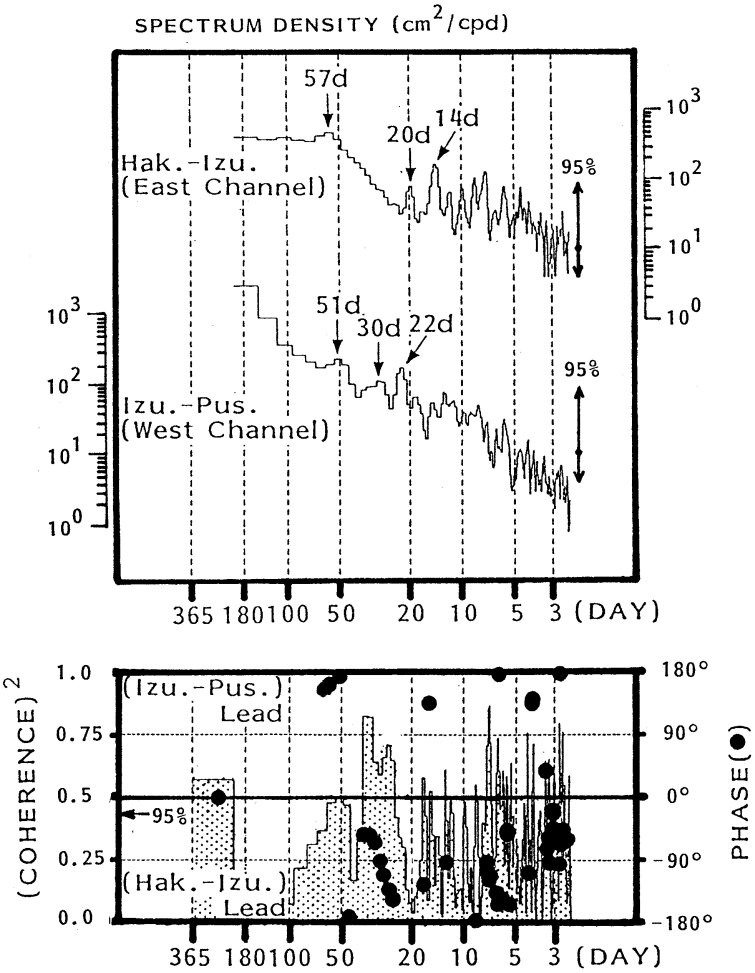

Fig. 7. Cross-spectrum between sea-legvel difference at the West and East Channel using 512-day data from 11 April 1981 to 4 September 1982. Phase values with more than 0.43 coherence squared are shown by solid circles.

4. Conclusion and discussion

By using the bottom-water temperature data observed along the submarine cable, we analyzed the characteristics of temperature variation in time and space on the shelf off San'in coast. Only the water temperature close to the Korean coast and the Japanese coast has the dominant seasonal variation. The BCW front shifts into the Tsushima/Korea Strait along the Korean coast corresponding to the increase of inflow volume transport of the Tsushima Current. This behavior may be due to the development of baroclinic structure in summer. Bottom-water temperature near the Japanese coast is strongly affected by seasonal water characteristics of the Tsushima Current. On the other hand, the water temperature on the shelf off San'in coast has no dominant seasonal variation, but has significant year-to-year variation. Besides, the following interesting behaviors of the BCW are superimposed on such year-to-year variations. Intense evolutions of the BCW over the shelf off San'in coast occur 6 to 9 times in a year, having periods of 40 to 60 days, sometimes followed by a few cycles of oscillations. Such events show eastward phase propagation with a phase speed of 7 to 10 cm s^{-1}, a typical wavelength of a few hundreds kilometers and cross-shelf amplitude

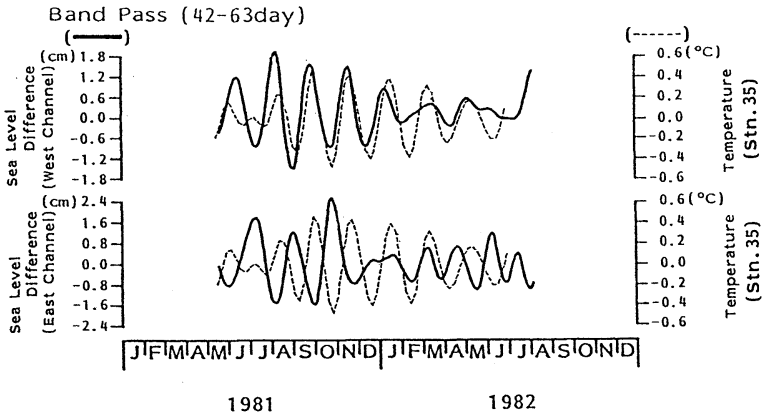

Fig. 8. The bandpass-filtered anomaly time series for the range of 42–63 day period. The heavy lines in the upper and lower panel are sea-level difference at the West and East Channel, respectively. The dashed lines in both panels show variations in water temperature at Stn.35 located at the center of the submarine cable.

of 50 to 100 km distance.

Finally, to investigate the type of such observed waves, the theoretical dispersion relations of free waves off San'in coast are compared with the observed data. ISODA *et al.* (1991) showed that the phase speed of external and internal Kelvin waves which could exist at the shelf off San'in coast were estimated as about 1400 m s^{-1} and 1.6 m s^{-1}, respectively. Besides, if the observed wave may be regarded as a barotropic shelf wave, it must be a higher-mode wave, 5th higher or 6th or mode wave, with many nodes in the cross-shelf direction (ISODA *et al.*, 1991). However, the observational data shown in Fig. 6 deny the possibility of such higher-mode waves. Therefore, it may be difficult to explain the observed wave by the gravity wave or shelf wave of barotropic mode.

Next, we shall consider the topographic Rossby wave affected by a stratification, because the main thermocline has existed around the shelf edge throughout the year as shown by the present study. The wave equation and wave dispersion relation of the topographic Rossby wave by Rhines' theory (RHINES, 1970) are as follows.

$$p=A\exp(i(kx+l_n y+\omega t))\cosh(\mu z) \quad (1)$$

$$\tanh(\mu H)=-\frac{N^2\alpha k}{f\omega\mu} \quad (2)$$

where $$\mu=N(k^2+l_n^2)^{1/2}/f \quad (3)$$

Here x and y are Cartesian coordinates directed along-shelf and across-shelf, respectively, z the vertical coordinate directed upward from the sea surface, p the pressure, α (=40m/100 km =0.0004) the bottom slope gradient, $f=8.5\times10^5$ s^{-1} the Coriolis parameter, H(=120m) the mean depth, ω the wave frequency, k the along-shelf wavenumber, $l_n=2n\pi/L$ (L is the shelf width and $n=1,2,3,..$) the cross-shelf wavenumber, and N^2 the Brunt-Väisälä frequency. From eqs. (1) and (3), it is found that such a wave tends to be a bottom-trapped mode (large μ at (1)) in the case of strong stratification (large N^2), short wavelength (large k) or higher-mode wave (large l_n).

The density data were collected from the observed data by Fisheries Agency Japan in March and September 1981 along Section B in Fig.1. March is the season of vertical mixing in winter, and September is the season with the development of the seasonal thermocline. Using these data we calculated the variation in Brunt-Väisälä frequencies and the corresponding theoretical dispersion curves for the first three modes. The profiles of density, the Brunt-Väisälä frequency, and dispersion curves are shown in Fig. 9 for each month. For the purpose of comparing the theoretical curves with the observations, we shall use the Brunt-Väisälä frequency value near the shelf edge, i. e. $N^2=3.0\times10^{-3}$ s^{-1} in March and $N^2=10.0\times10^{-3}$ s^{-1} in September, and the observed wave's ω-k region as

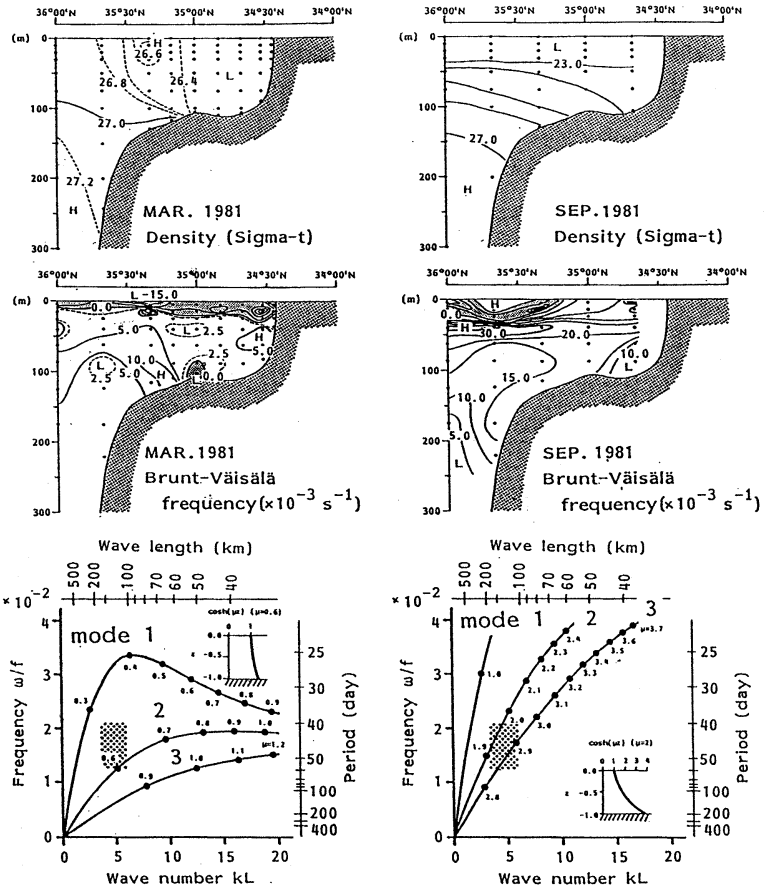

Fig. 9. Density (upper) and Brunt-Väisälä frequency (middle) profiles along Section B in Fig. 1(b). Lower panels denote dispersion curves of the first three modes for the profile given by eqs (2) and (3) (adapted from RHINES, 1970). The vertical profiles of cosh (μz) which is calculated using the value at each shaded area corresponds to that of the current. Shaded areas denote the observed ω-k relation.

denoted by the shadow area in the dispersion curves. It may be possible that the observed wave can be explained by the 2nd or 3rd mode bottom-trapped Rossby wave in both months. It is suggested that the alongshore flow component in the cross-shelf direction is out of phase between the coastal area and the shelf edge area, when the short-term variations of the BCW are passing off San'in coast. Such a result would also coincide with that inferred from the analysis of sea level differences in the Tsushima/Korea Strait.

As for the primary mechanisms responsible for the BCW evolution, we cannot believe that its evolution always occurs when upwelling-favorable winds prevail. This is because most of the wind energies in the southwestern area of the Japan Sea area are concentrated around several-day periods. The annual mean BCW front, i.e. the main thermocline, is situated along the shelf edge and hits the topographic protrusion of the Korean peninsula (MORIWAKI and OGAWA, 1989), and the water characteristics of the Tsushima Current on the shelf have large seasonal change in temperature and salinity (OGAWA, 1983; MORIWAKI and OGAWA, 1988). From the above characteristics, we speculate that the short-term variations of the BCW will be generated by a kind of geostrophic adjustment process between inner and outer shelf around the Korean coastal area or by the baroclinic instability process of the Tsushima

Current. In our forthcoming studies, we plan to investigate the low-frequency changes of sea conditions off the Korean coast and to physically explain the generation mechanism of the BCW variations.

Acknowledgments

The original bottom-water temperature data along the submarine cable were kindly provided by the Kokusai Denshin Denwa (KDD) Co., Ltd. We are grateful to Mr. S. TAKOTANI of the Hamada cable landing station of KDD Co., Ltd. for allowing us to have access to the temperature data. We also express thanks to Prof. T. YANAGI of Ehime University for his useful comments on the manuscript as well as Dr. H. TAKEOKA and Mr. H. AKIYAMA of our laboratory, and to Dr. J. ADACHI and Dr. T. MURAYAMA of Shimane Prefectural Experimental Fishery Station for their help in data collection. The data processing was carried out on a FACOM M-360 at the Computer Center of Ehime University.

References

BYUN, S.K. and Y.H. SEUNG (1984): Description of current structure and coastal upwelling in southwest Japan Sea - summer 1981 and spring 1982, *In*: Ocean Hydrodynamics of the Japan and East China Seas, ed. T. Ichiye, Elsevier, 83–93.

FISHERIES AGENCY JAPAN (1985, 1986): Hydrographic temperature data. The Results of Fisheries Oceanographical Observation January to December 1981, 1982.

HANAWA, K. (1984): Review: Coastal Boundary Current (in Japanese). Bulletin on Coastal Oceanography, **22**, 67–82.

ISODA, Y. (1989): Topographic effect of the Tsushima Islands on the Tsushima Warm Current (in Japanese). Bulletin on Coastal Oceanography, **27**, 76–84.

ISODA, Y. and T. MURAYAMA (1990): Bottom cold water and flow structure of the Tsushima Warm Current (in Japanese). Bulletin on Coastal Oceanography, **28**, 85–95.

ISODA, Y. and H. YAMAOKA (1991): Flow structure of the Tsushima Warm Current passing through the Tsushima / Korea Straits (in Japanese). Bulletin on Coastal Oceanography, **28**, 183–194.

ISODA, Y., T. YANAGI and H.J. LIE (1991): Sea-level variations with a several-day period along the southwestern Japan Sea coast. Continental Shelf Research, **11**, 167–182.

ISODA, Y., T. MURAYAMA and T. TAMAI (1992): Variabilities of current and water temperature due to meteorological disturbances on the shelf off San-in coast (in Japanese). Bulletin on Coastal Oceanography. **29**, 197–205.

KAWABE, M. (1982): Branching of the Tsushima current in the Japan Sea. Part 1. Data analysis. J. Oceanogr. Soc. Japan, **38**, 95–107.

MORIWAKI, S.and Y. OGAWA (1988): Hydrographic features of the "Bottom Cold Water" on the continental shelf (in Japanese). Bull. Tohoku Regional Fisheries Res. Lab., **50**, 25–47.

MORIWAKI, S. and Y. OGAWA (1989): Influences of the "Bottom Cold Water" on Demersal fishes in the southwestern Japan Sea (in Japanese). Bull. Tohoku Regional Fisheries Res. Lab., **51**, 167–181.

OGAWA, Y. (1983): Seasonal changes in temperature and salinity of water flowing into the Japan Sea through the Tsushima / Korea Straits (in Japanese). Bull. Jap. Soc. Fisheries Oceanogr., **43**, 1–8.

RHINES, P. (1970): Edge-, bottom- and Rossby waves in a rotating stratified fluid. Geophy. Fluid Dyn., **1**, 273-302.

UDA, M. (1931): Sea conditions in the Japan Sea and its around sea areas (in Japanese). Reports of Fisheries Exp. Stn., **5**, 57–190.

YAMASAKI, S. (1969): About the Bottom Cold Water (in Japanese). Bull. Jap. Soc. Fisheries Oceanogr., **14**, 93–101.

La mer 30: 275–285, 1992
Société franco-japonaise d'océanographie, Tokyo

Wave characteristics changes under a strong tidal current influence

Im Sang OH and Yoo Yin KIM*

Abstract: It is well known that a strong current influences a wave field in several ways, such as frequency shift, amplitude changes. In the present study, we reexamined the influences of current on a wave field in a theoretical point of view in the first half of this paper. In the next half, we compared the observed wave heights with the computed wave heights with tidal currents. We also compared the computed wave spectra with tidal currents and those wihout tidal currents. The wave measurements are conducted at the Maldo Island from Nov. 7 to Nov. 10, 1990, which is located in the west coastal area of Korea. For the computations, Shallow Water Wave model (SWW model : OH *et al.*, 1990) was used.

In the typical range of tidal currents and elevation of the Maldo area, the influence of tidal currents on waves is large than that of tidal elevations, i.e., water depth changes of the ranges. For the area, the observed wave heights show considerable differences from those with current. The difference may be larger in some areas with stronger tidal currents. The model calculations show 7–12% difference in the wave energy spectra with and without currents in the shallow water wave model.

1. Introduction

A wave field in some area can be strongly influenced by steady or variable currents if the currents of the area are strong. In those areas, the current should be considered in estimating the wave energy. The Yellow Sea is an area of this kind.

There are several ways that a horizontal current can modify surface gravity waves. One way of modifications is to wavelength. A current can locally stretch or shrink features in a wave train. This wave train distortion produces a "Doppler shift" in wave period. Another way is to wave orthogonals. Wave orthogonal is a line perpendicular to the local wave crest direction. In this study the wave refraction due to tidal currents is not considered since the wave refraction due to tidal currents is generally much smaller than that due to water depth variations.

Another type of modification occurs also in the pressure field accompanying waves. This change can be an appreciable source of error in measuring wave heights or periods if an existing current is not accounted for. In particular, a significant error can sometimes arise if bottom pressure measurements are used to determine surface wave heights and lengths.

The studies of wave-current interaction, in particular the influence of currents on waves, have been done extensively in the past decades (Interested readers refer to PHILLIPS (1969), PEREGRINE (1976) and THOMAS (1981) for their detailed and comprehensive reviews of waves on currents). The followings are the brief reviews of the studies.

A significant theoretical advance of wave-current interaction was achieved by LONGUET-HIGGINS and STEWART (1960, 1961), who introduced the concept of radiation stress. A year later, WHITHAM (1962) introduced so-called Whitham's method which uses the averaged Lagrangian and the concept of wave action. PHILLIPS (1969) formulated a wave spectral transformation on currents theoretically in water of finite depth, and showed that the spectral energy density in the wavenumber space is constant following a wave group.

HUANG *et al.* (1972) showed the relative changes of spectral energy ($\bar{\phi}$) under different

* Department of Oceanography, Seoul National University, Seoul 151–742, Korea

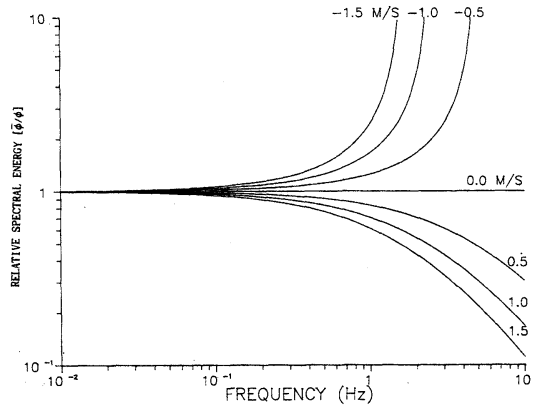

Fig. 1. Relative changes of frequency spectra under different current conditions (HUANG *et al.*, 1972).

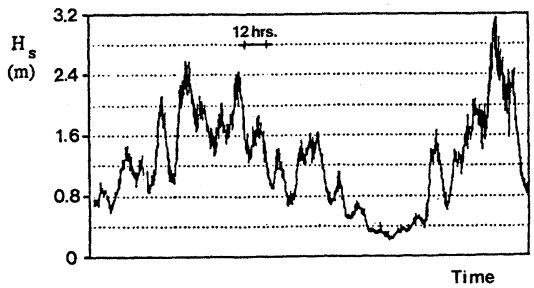

Fig. 2. Measured significant wave height H_s (TOLMAN, 1990).

current conditions to the Kitaigorodskii-Pierson-Moskowitz frequency spectrum (ϕ) as the basic spectral form for zero current condition (Fig. 1).

The interaction between wind-generated surface waves and tidal currents (VINCENT, 1979), the effect of tidal currents on the velocity spectrum (LAMBRAKOS, 1981), and the influences of unsteady currents on wind wave propagation on the scale of shelf scale (TOLMAN, 1990) are also studied. TOLMAN showed that a wave height modulation is up to 50 % with a period of approximately 12 hours in the Southern North Sea (Fig. 2). Numerical method (WANG and YANG, 1981) and laboratory experiments (LAI *et al.*, 1989) are also applied to the study of current effects.

In the present study, we reexamined the influence of strong currents on a wave field. At the same time, we measured the wave heights and tidal currents at the Maldo from Nov. 7 to Nov. 10, 1990 (See Fig. 3 for the location and bottom contours of the Maldo area). The wave fields for the period are simulated by using Shallow Water Wave model (SWW model: OH *et al.*, 1990). The computed wave heights with considering tidal currents are compared with the observed ones. The computed wave spectra with and without tidal currents are also compared in order to estimate the order of magnitudes of the influence of currents on wave field.

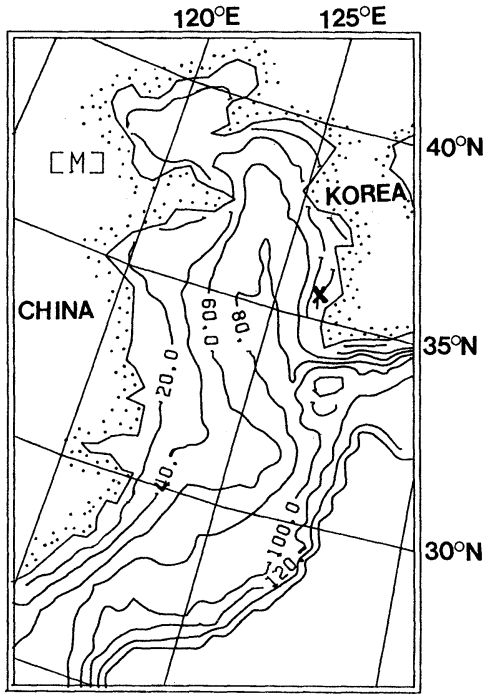

Fig. 3. Location of the experimental site (point x), Maldo area and the depth contours of the Yellow Sea.

2. Theoretical considerations

a. Steadiness of Tidal Current

It is necessary to have a clear appreciation of the relative magnitude of time and length scales for both the waves and the currents for a better understanding of their interactions. A large-scale current, such as a tidal current, might be an example which varies very little, say, no more than a few percent over a distance of one wavelength, L, or over a time of one wave period, T.

Waves, however, propagate over a tidal current for a considerably long time. Then the

variability of the current must be accounted. The critical period of a current, the semidirunal tide, for example, can be estimated as

$$T_c = |U_{\max}| / |\partial U / \partial t|_{\max} \quad (1)$$

when the tidal current $U(t) = U_{\max} \sin(\omega t)$ is assumed. Here, $U_{\max}$ and ω are the maximum speed and the tidal frequency, respectively. Considering the tidal component M_2 for the Maldo area, we get $T_c \simeq 2$ hour. Thus, if waves are propagating over the tidal currents for more than two hours, the unsteadiness of the current needs to be considered, and if a propagation time is less than T_c the tidal current can be considered as a steady current.

b. Effect of the Presence of Current on Wave Field

If a wave train is propagating in a medium moving with velocity $U(u, v; \vec{x}, t)$, the frequency of waves passing a fixed point, apparent frequency ω, is given by

$$\omega = \vec{k}\, U(\vec{x}, t) + \sigma(\vec{k}, h) \quad (2)$$

where σ is the intrinsic frequency whose functional dependence on wave number $\vec{k}$ and water depth h is known as the dispersion relation. If the nonlinear dynamic interaction is neglected, the dispersion relation is of the form:

$$\sigma^2 = gk \tanh(kh) \quad (3)$$

where g is the gravity, $k = |\vec{k}|$. From (3) we have the relative wave phase speed C_0 as

$$C_0 = [(g/k) \tanh(kh)]^{1/2} \quad (4)$$

and the absolute phase speed C_a is given by

$$C_a = C_0 + U \quad (5)$$

If the water depth h, intrinsic frequency σ, and the current speed and direction of U are known, we can calculate the wave number of no current by (3) and apparent frequency ω by (2), and then the wave number under current influence can be determined as follows.

$$\omega = [gk \tanh(kh)]^{1/2} + uk \cos\theta + vk \sin\theta \quad (6)$$

where u, v are component currents in x- and y-direction, respectively, and θ is the angle between the wave-ray and x-axis.

c. Combined Effects of Current and Water Depth on Wave Field

The changes of wave lengths, phase speeds and Doppler frequencies for variable water depths are shown in Fig. 4 for each effective tidal current speed giving influence to the wind waves. The positive tidal current speed means that the current flows in the same direction as the waves do, i.e., co-current. For this computation, we used the combined form of dispersion relations of (2) and (3). The figure shows that the wave length, phase velocity, and Doppler frequency with co-currents are larger than those with counter-currents. In general, the influence of counter-currents on waves is larger than that of co-currents as we expected.

It is worthwhile to note that if we consider the typical ranges of tidal currents and elevations for the study area are 1.5 m/s and 5 m, respectively, the influence of tidal currents on waves is larger than that of tidal elevations, i.e., water depth changes of the ranges.

Fig. 5 shows the relations between the apparent frequency ω and wave number k. When there is no current, k_{o1}, k_{o2}, and k_{o3} are the wave numbers for constant water depths, h_1, h_2, and h_3, respectively. ω_0 is the frequency of no current. If there exists a flow U which is against the wave propagation direction, U can be considered as a slope for the linear equation for k. Thus, the left hand side of the equation will be a line whose slope is U and its cross section is ω_0 in ω-k plane. The values k_1, k_2, and k_3 at which the line crosses the curves of constant depths h_1, h_2, and h_3, respectively, are the wave numbers, and ω is the frequency in common for the wave numbers.

If there exists an opposing current, two solutions for k can be found. These solutions converse to k_c as U increases. The wave number k_c is called as a critical wave number. The frequency ω_c is a critical frequency at the critical wave number k_c.

In the range of wave number bigger than the

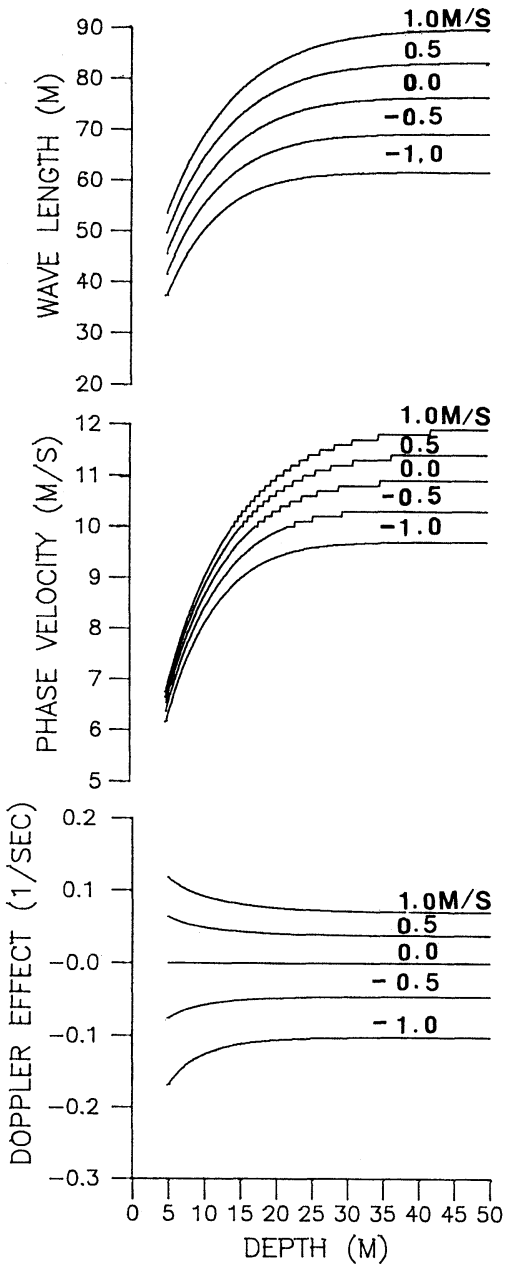

Fig. 4. Variations of wave length, phase velocity and Doppler effect depending upon water depth and effective current speed changes.

critical wave number k_c, when the flow U increases, the solutions for k and the corresponding frequency decrease to k_c and ω_c, thus, the wave lengths and period increase. In the wave number range smaller than k_c, the solution and corresponding frequency increases to converge

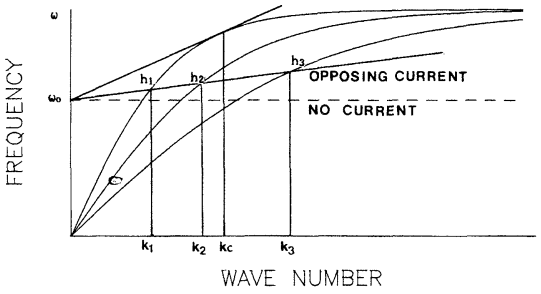

Fig. 5. Wave number and frequency relationship with opposing current.

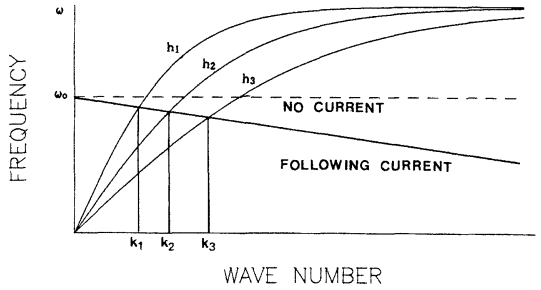

Fig. 6. Wave number and frequency relationship with following current.

to k_c and ω_c. The wave lengths and the period decrease. In this range, the changing rate of wave number increases as the current increases and as the water depth decreases.

Fig. 6 shows the ω-k solution for the case of co-current, in which the direction of wave propagation is identical to the current. In this case, since the solution for k and the corresponding frequency are always smaller than those of no-current, the wave lengths and period become longer. The changing rate of the wave numbers increases as the water depth decreases.

3. Comparisons of spectra with and without currents

In order to investigate the influences on wind waves due to tide, we measured wave heights and tidal currents at the Maldo area (See Fig.3) for the period of Nov. 7 to Nov. 10, 1991. The instrument used for the measurements is a multi-functional pressure type gauge which can measure wave heights, tides and their current directions and speeds. It was moored at the sea bottom of 20 m depth.

Wind speeds and tidal currents during the measurement period for the whole Yellow Sea

are simulated. Using these wind and tidal current data wave heights are calculated by the Shallow Water Wave model (SWW model: OH *et al.*, 1990). In the following two subsections, the models are briefly explained.

a. Shallow Water Wave model

In shallow water, the wave train will have new experiences such as strong tidal currents with rapid variations of water depth, bottom friction, refraction, shoaling, and wave breaking. The present SWW model includes those effects in calculations. We chose this model because it has been applied to the present study area successfully (OH *et al*, 1990). The model uses a prefixed grid system and a finite difference method with a jumped technique. It has 208 component waves : 13 classes of wave period and 16 classes of propagation direction. It utilizes HASSELMANN (1960)'s idea. According to him, the development of an angular spectral density $E(T, \theta, x, y, t)$ can be described by the following relation,

$$\frac{dE(T, \theta, x, y, t)}{dt} = S(T, \theta, x, y, t) \tag{7}$$

where S is a source function for the wave field, and T, t and θ are wave period, time and wave propagation direction, respectively. Since the group velocity and the propagation direction change as the energy of each component wave moves, the energy equation should be expressed as,

$$\frac{dE}{dt} = \frac{\partial E}{\partial t} + \frac{\partial E}{\partial x}\frac{dx}{dt} + \frac{\partial E}{\partial y}\frac{dy}{dt} + \frac{\partial E}{\partial T}\frac{dT}{dt} + \frac{\partial E}{\partial \theta}\frac{d\theta}{dt} = S \tag{8}$$

We converted this into an equation which can be used for the computations of wave energy along a wave ray. If we assume the wave period is conserved, the energy balance equation becomes

$$\frac{dE}{dt} = \frac{\partial E}{\partial t} + \frac{\partial E}{\partial s}\frac{dS}{dt} + \frac{\partial E}{\partial \theta}\frac{d\theta}{dt} = S_{in} + S_{ds} + S_{bf} \tag{9}$$

where the source function of the right hand side consists of S_{in}, energy input from wind field, S_{ds}, energy loss due to viscosity and breaking, and S_{bf}, energy dissipation due to bottom friction. For the energy input, the formula which is used by GELCI and DEVILLAZ (1975) in their DSA-5 wave model, is utilized in the present study. The energy loss due to viscosity is considered by assuming the eddy viscosity coefficient is proportional to the total wave energy. The total time derivative of the wave energy of a component wave, $E_{T,\theta}$, is

$$\frac{dE_{T,\theta}}{dt} = I - AE_{T,\theta} \tag{10}$$

where the energy input due to wind, I is

$$I = \int_{\text{component}} \int \frac{C_{in}T^2(W-2T)^3}{W^3}\frac{2}{\pi}\cos^2(\theta-\phi)\, dT\, d(\theta-\phi), \tag{11}$$

and

$$A = 18\times10^{-9}E_{tot} \tag{12}$$

Here, W is the wind speed in knot, ϕ the wind direction, and E_{tot} is the sum of all the componental waves.

Energy dissipation due to bottom friction is also considered by utilizing COLLINS (1972) model. The bottom frictional energy dissipation is assumed to be proportional to the mean water particle velocity and to the frequency-directional spectrum. S_{bf} is

$$S_{bf} = C_f \alpha(T,h) \langle V \rangle E(T,\theta) \tag{13}$$

where C_f is the bottom friction coefficient, $\alpha(T,h) = gkC_g/(2\pi\sigma^2\cosh^2 kh)$, C_g the group velocity, and $\langle V \rangle$ is the ensemble average of a water particle velocity of water depth h.

Wave breaking due to water depth is included by using a simple formula by YOUNG (1988) as

$$E_{\max} = 0.0355\, h^2 \tag{14}$$

The $E_{\max}$ is the maximum possible total energy at a computational grid point. If the total energy is greater than $E_{\max}$, then the excess energy is drained from the longer wavelength component first.

The computation is conducted in the following

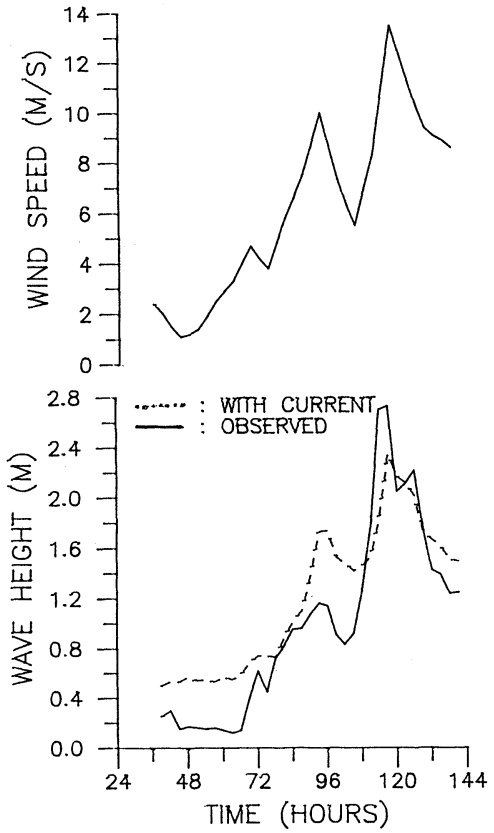

Fig. 7. Computed wind speed (upper), and the observed and the computed wave heights (lower) for the Maldo from Nov. 7 to Nov. 10, 1990.

order by using the former step's result as an input

$$\left[\left[\left[\frac{dE}{dt}=S_{in}+S_{ds}\right]_{i}+S_{bf}\right]_{ii}-\frac{\partial E}{\partial s}\frac{ds}{dt}\right]_{iii} - \frac{\partial E}{\partial \theta}\frac{d\theta}{dt}\Big]_{iv} \quad (15)$$

More detailed descriptions may be found in OH *et al.*(1990).

Precalculated tidal currents were used in the model by equation (6). New frequency was calculated for all the wave components at each grid point (i, j).

$$\omega_{ij}=[gk_{ij}\tanh(k_{ij}h_{ij})]^{1/2}+u_{ij}k_{ij}\cos\theta_{ij} + v_{ij}k_{ij}\sin\theta_{ij} \quad (16)$$

The SWW model runs on the assumption that wind velocities and tidal currents are consistent

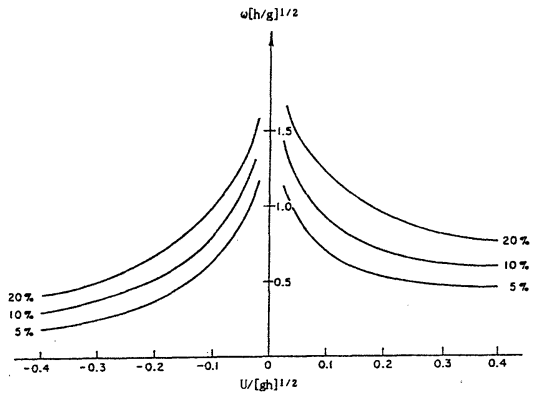

Fig. 8. Relative errors in surface wave amplitude calculated from bottom pressures due to neglect of a current component parallel with the wave direction (PERIGRINE, 1976).

for 3 hours. The tidal constituent M_2 which is dominant in the Yellow Sea is the only component considered for the tidal current computations.

b. Sea Surface Wind Model and Tidal Current Model

The sea surface wind model used in the present study is the one which was developed by BONG *et al.* (1987, 1988, 1989, 1990). The model is based on CARDONE (1969, 1978). According to him, at the upper limit of the Ekman layer the wind velocity becomes the geostrophic wind, and in surface layer the wind velocity has a logarithmic profile and it vanishes at the surface. The model is a finite difference model which utilizes iterative technique for solution. In order to run the model, the pressure distributions of 12-hour interval weather charts for the period of wave measurement at the Maldo (Nov. 7–Nov. 10, 1991) were read, and they were interpolated to make 3-hour interval data. The sea level pressure and land surface temperature were also read from the same weather charts, and monthly mean sea surface temperatures were used for this period. The irregular data such as air pressure, air temperature, etc., were rearranged to a regular grid field by using an objective analysis technique (BARNSE, 1964).

A modified tidal current model from FLATHER and HEAPS (1975) was used to obtain tidal current fields for the measurement period. The tidal model is a finite difference depth-averaged

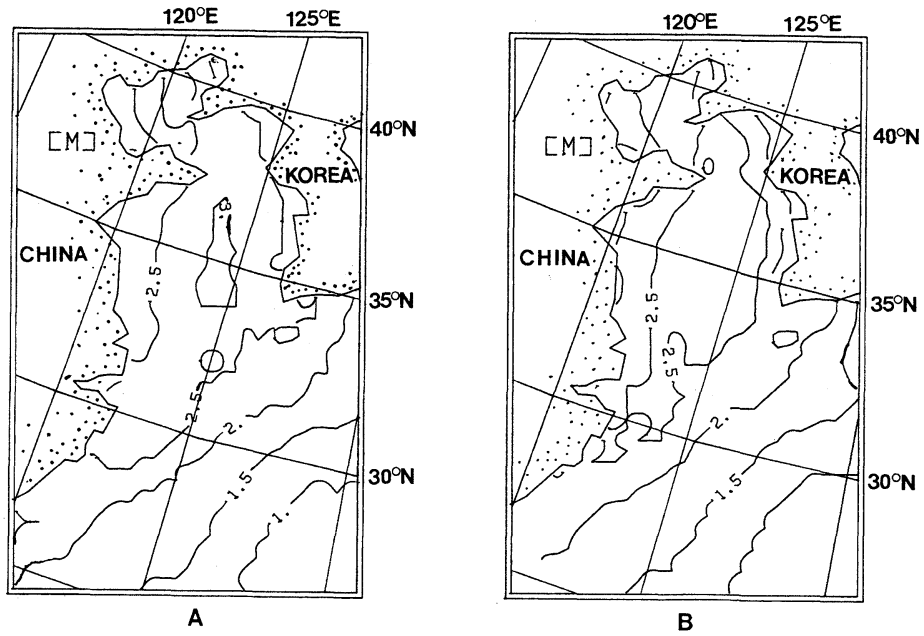

Fig. 9. Computed wave height contours with counter-directional tidal current (a) for the area near the Maldo, and without tidal current (b) at near the peak time of the measured wave energy.

model. For the open boundaries, the tidal phases and elevations of OGURA (1933, See CHOI, 1980) were used. From this model, 3-hour interval tidal currents and elevations of the M_2 component are obtained for the present wave-current interaction calculations.

c. Comparisons of waves with and without currents

The computed 3-hour interval winds and tidal currents from the SSW model and tidal current model were supplied to run the SWW model in order to see the effects of tidal currents on wind wave field. We ran the SWW model more than 144 hours.

The upper part of Fig.7 shows computed wind speeds over the Maldo area for the whole measurement period (Nov. 7 to Nov. 10, 1990). The lower part of Fig. 7 shows the observed and computed wave heights for the period. The time series of the wind speed and wave heights show a good agreement in a general tendency. Considerable discrepancy between the observed and calculated wave heights as much as 65 cm, however, appeared at the 90th hour. This discrepancy may be due to the deviation of the pressure measurements at the sea bottom in the presence of current from those of no-wind (See JONSSON *et al.*, 1970; DRAPER, 1957; PERIGRINE, 1976). Following is Perigrine's derivation. If a Fourier component of a pressure fluctuation at a bottom $z=-h$ has amplitude $p(\omega)$, then the corresponding surface amplitude component is

$$a(\omega)=p(\omega)\cosh(kh)/\rho g \tag{17}$$

The maximum errors will clearly occur when wave direction is parallel or antiparallel to a current. He also derived the following relationship: the ratio of the corrected amplitude a_2 to the computed amplitude a_1

$$\frac{a_2}{a_1}=\frac{\cosh(r)}{\cosh(q)} \tag{18}$$

where q and r are kh for the case of no-current and that for the case of current speed U, respectively. Fig. 8 shows the relative error $(a_2-a_1)/a_1$. It is easy to find from the figure that adverse currents have greater effects.

The computed wave height distribution with counter-current is shown in Fig. 9(a) and that without tidal current in Fig. 9(b) at nearly the time of energy peak when the SWW model ran for 117 hours. The area where we have interests

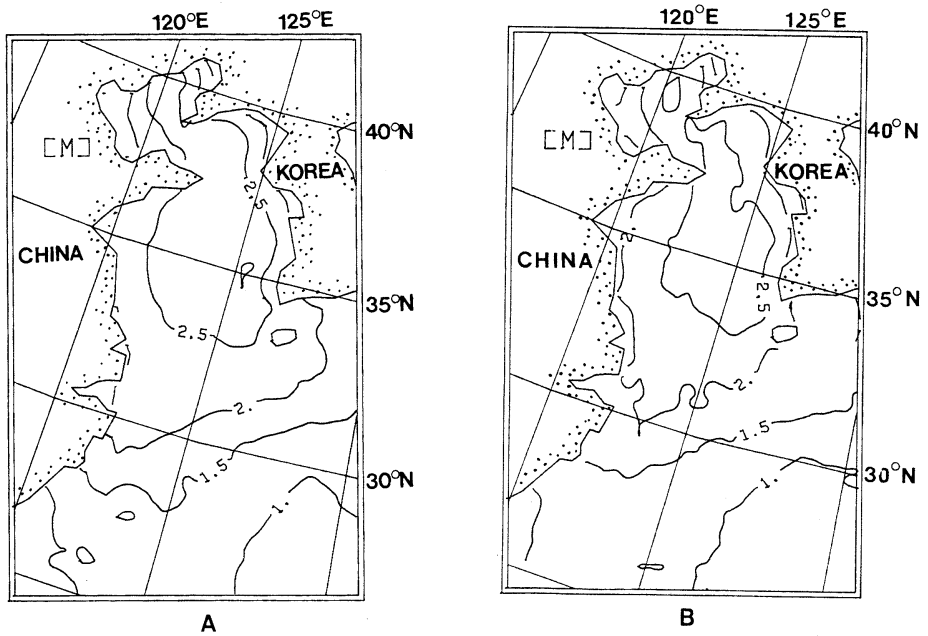

Fig. 10. Computed wave height contours with co-directional tidal current (a) for the area near the Maldo, and without tidal current (b) at nearly the peak time of the measured wave energy.

is the sea around the Maldo Island. We chose a moment when the directions of dominant tidal current and wind are the same as the direction of the significant wave propagation. The area which has wave height of 3.0 m or higher is widened when current effect is included. The general pattern, however, is similar in both cases.

The computed wave height distribution with co-current is shown in Fig. 10(a) and that without tidal current in Fig. 10(b) at nearly the time of energy peak. Similarly to Fig. 9., the area where the wave height is 2.9 m or higher is widened in the southwest of the Korean Peninsula when current effect is included. But, the area of 2.7 m or higher waveheight is shrinked. The general patterns for the both cases, however, are similar.

Fig. 11 shows the directional spectra of wave energy at the Maldo with co-currents (a) and without tidal currents (b). We notice that the dominant direction of wave is not changed but the concentration of wave energy with co-current is much more effective than that with no-current. Fig. 11(c) shows their frequency spectra. We also see the differences in spectral density of wave energy at peak frequency. Fig. 12 shows the directional spectra of wave energy at the Maldo with counter-currents (a) and without tidal currents (b), and frequency spectrum (c). Similarly to Fig. 11, the dominant direction of wave is not changed but the concentration of wave energy with counter-current is much more effective than that with no-current. We also see the considerable differences in spectral density of wave enrgy at peak frequency. Comparing the energy density spectra with co- and counter- currents, we could easily find that there exists more significant difference in the case of counter-current. From this, we can find that the wave height with tidal currents shows 7–12 % difference from the wave height without considering tidal currents.

4. Summary

The influences of steady current on a wave field are reexamined in a theoretical point of view in the first half of this paper. In the next half, we compared the observed wave heights with the computed wave heights with tidal currents. The Shallow Water Wave model is used for the computations. We also compared the wave spectra with and without tidal currents.

The results are summarized as follows.

i) Wave fields are influenced by the current

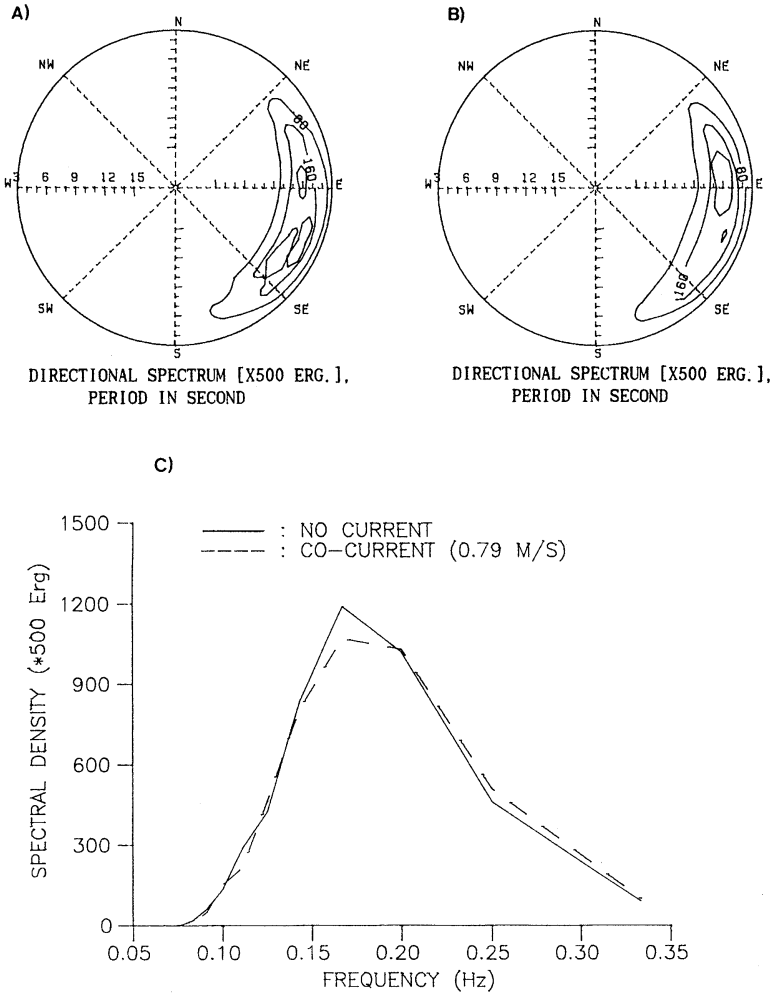

Fig. 11. Directional energy spectrum with counter-directional tidal current (a), spectum without tides (b), and frequency spectrum (c) of the Maldo area at nearly the peak time of the measured wave energy.

direction as well as magnitude. The direction and magnitude of tidal current of the Yellow Sea change in the time scale of the order of an hour; thus the wave field should be influenced by the current variations.

ii) In the typical range of tidal currents and elevation of the Maldo area, the influence of tidal currents on waves is larger than that of tidal elevations, i.e., water depth changes of the ranges.

iii) If there exists an opposing current to the wave propagation, two different wave groups can be excited. The wave numbers of the two group converges to the critical wave number as the current increases.

iv) If the current direction agrees with the wave direction, only one wave group is excited and the wave number and corresponding frequency are always smaller than those of no-current.

v) For the Maldo area, the computed spectra with tidal currents are considerably different from those without currents. The differences may be larger in some areas where tidal currents are strong.

vi) The energy density spectra with counter-currents, compared with those of no-currents, show more significant differences than the spectra with co-currents.

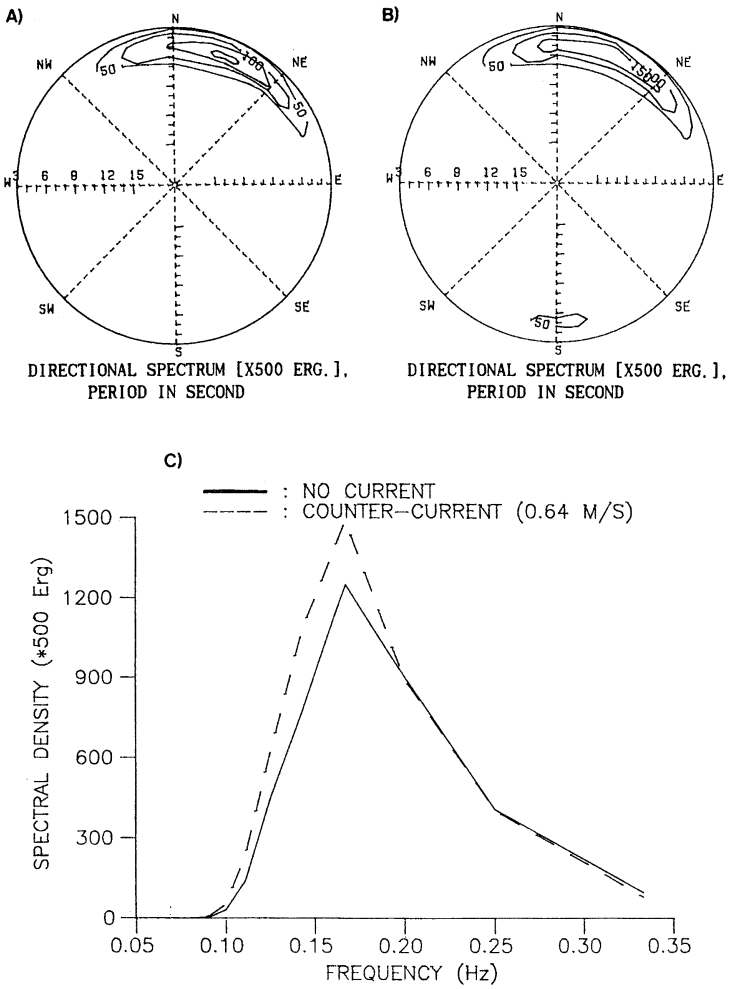

Fig. 12. Directional energy spectrum with co-directional tidal current (a), spectrum without tides (b), and frequency spectrum (c) of the Maldo area at nearly the peak time of the measured wave energy.

vii) Model calculations show 7–12% difference in the wave heights with and without currents in the model.

Acknowledgements

This study was supported by the Korea Science and Engineering Foundation through grants of 1990/1991. The authors would like to thank two anonymous reviewers who made several helpful comments and critics.

References

BARNSE, S.L. (1964): A technique for maximizing details in numerical weather map analysis. J. Meteor., **3**, 396–409.

BONG, J.H., J.B. CHOI, I.S. OH, I.S. KANG (1987): The study of meteorological characteristics and marine forecasting over the seas around Korea (I). Korea Meteorological Service, Meteorol. Res. Inst., Report 220 pp.

BONG, J.H., J.B. CHOI, I.S. OH, I.S. KANG, (1988): The study of meteorological characteristics and marine forecasting over the seas around Korea (II). Korea Meteorological Service, Meteorol. Res. Inst., Report 323 pp.

BONG, J.H., J.B. CHOI, I.S. OH, I.S. KANG, (1989): The study of meteorological characteristics and marine forecasting over the seas around Korea (III). Korea Meteorological Service,

Meteorol. Res. Inst., Report 355 pp.

BONG, J.H., J.B. CHOI, I.S. OH, I.S. KANG, (1990): The study of meteorological characteristics and marine forecasting over the seas around Korea (IV). Korea Meteorological Service, Meteorol. Res. Inst., Report 373 pp.

CARDONE, V. J. (1969): Specification of the wind distribution in the marine boundary layer for wave forecasting, New York Univ. School of Engineering and Science, Report GSL-TR 69-1, 181 pp.

CARDONE, V. J. (1978): Specification and prediction of the vector wind on the United States continental shelf for application to an oil slick trajectory forecast program. New York Univ., Institutes of Marine and Atmospheric Science, Contract T-35430.

CHOI, B. H. (1980): A tidal model of the Yellow Sea and the Eastern China Sea. KORDI Report BSPI 00019(3)-36-2.

COLLINS, J. I. (1972): Prediction of shallow water wave spectra. J. Geophys. Res., **86(C11)**, 2693-2707.

DRAPER, L. (1957): Attenuation of sea waves with depth. La Houille Blanche, **12**, 926-931.

FLATHER, R. A. and N. S. HEAPS (1975): Tidal computation for Morecamble Bay. Geophys. J. R. Astr. Soc., **42**, 489-517.

GELCI, R., and E. DEVILLAZ (1975): Le calcul numérique de l'état de la mer. La Météorologie, VI ème série, No. 2.

HASSELMANN, K. (1960): Grundleichungen der Seegangsveraussage. Schiffstechnik, 7, 191-195.

HUANG, N. E., D. T. HUANG, C.-C. TUNG, and J. R. SMITH (1972): Interactions between steady non uniform currents and gravity waves with applications for current measurements. J. Phys. Oceanogr., **2**, 420-431.

JONSSON, I. G., C. SKOUGAARD and J. D. WANG (1970): Interaction between waves and currents. Proc. 12th Coastal Engrg. Conf. **1**, 489-507.

LAI, R. J., S. R. LONG, and N. E. HUANG (1989): Laboratory studies of wave-current interaction; Kinematics of the strong interaction. J. Geophys. Res., **94**, 16201-16214.

LAMBRAKOS, K. F. (1981): Wave-current interaction effects on water velocity and surface wave spectra. J. Geophys. Res., **86**, 10955-10960.

LONGUET-HIGGINS, M. S. and R. W. STEWART (1960): Changes in the form of short gravity waves on long waves and tidal currents. J. Fluid Mech., **8**, 565-583.

LONGUET-HIGGINS, M. S. and R. W. STEWART (1961): The changes in amplitude of short gravity waves on steady non-uniform currents. J. Fluid Mech., **10**, 529-549.

LONGUET-HIGGINS, M. S. and R. W. STEWART (1964): Radiation stress in water waves ; A physical discussion, with application. J. Fluid Mech., **11**, 529-562.

OH, I. S., T.-R. KIM, C. Y. CHUNG, and J. H. BONG (1990): A study on the development of shallow water wave model. J. Korea Meteorol. Society, **26**, 139-155.

OGURA, S. (1933): The tides in the seas adjacent to Japan. Hydrogr. Bull. Dept. Imp. Jap. Navy, **7**, 1-189.

PEREGRINE, D. H. (1976): Interaction of water waves and currents. Adv. Appl. Mech., **16**, 9-117.

PHILLIPS, O. M. (1969): The dynamics of the upper ocean, 1st ed., Cambridge University Press, 261 pp.

THOMAS, G. P. (1981): Wave-current interactions; an experimental and numerical study. Part 1. Linear waves. J. Fluid Mech., **110**, 457-474.

TOLMAN, H. L. (1990): The influence of unsteady depths and currents of tides on wind-wave propagation in shelf seas. J. Phys. Oceanogr., **20**, 1166-1174.

YOUNG, I. R. (1988): A shallow water spectral wave model. J. Geophys. Res., **93(C5)**, 5113-5129.

VINCENT, C. E. (1979): The interaction of wind generated sea waves with tidal currents. J. Phys. Oceanogr., **9**, 748-753.

WANG, H. and W.-C. YANG (1981): Wave spectral transformation measurement at Sylt, North Sea. Coastal Engrg, **5**, 1-34.

WHITHAM, G. B. (1962): Mass, momentum and energy flux in water waves. J. Fluid Mech., **12**, 135-147.

La mer 30: 287–296, 1992
Société franco-japonaise d'océanographie, Tokyo

Mesoscale coherent structures in the surface wind field during cold air outbreaks over the Far Eastern seas from the satellite side looking radar

Leonid M. MITNIK*

Abstract: Winter monsoon over the Far Eastern seas is followed by regular cold air outbreaks from Asia. Convection developed in the process manifests itself in a form of cloudiness on the satellite optical images and often shows the diverse mesoscale coherent structures: rolls, open and closed cells, vortex and chains of vortices. In such situations a peak appears between turbulent and synoptic peaks in a horizontal wind speed power spectrum. The mesoscale organized structures are also revealed in the sea surface wind W (surface roughness) field, which is observed from analysis of the images, obtained by the side looking radar from "Okean" series satellites. In the present paper the normalized radar cross section (NRCS) is calculated for two-scale model of W distribution in open and closed cells with variations of synoptic and mesoscale wind, the angle between a radar sensing plane and a synoptic wind vector, etc. The model distributions of the NRCS are in good agreement with the brightness variations within the cells on the radar images. The probable detection of the mesoscale organized structures in the subsurface layer of the ocean as a reseponse to quasiperiodic atmosphieric forcing will have a special importance in future experiments.

1. Introduction

During the winter monsoon, the cold air outbreaks are the typical features of the meteorological regime of the Far Eastern seas. These outbreaks are the most severe in the world. The passage of cold, low-humidity air over the warm waters induces strong latent, sensible, and radiative heat fluxes at the air-sea interface reaching 1000–12000 W/m^2 at high wind speeds and clear skies (AGEE, 1987).

During such outbreaks characteristics of the ocean and atmosphere change significantly: surface waters cool down and become more saline and the boundary layer of the atmosphere gets warm and loses its stability (HUH *et al.*, 1984). As a result, the mesoscale organized convective motions are formed in the atmosphere. They are manifested, in particular, in the surface wind field.

* Pacific Oceanological Institute, Far Eastern Branch, Russian Academy of Sciences, 43 Baltiyskaya Street, 690041 Vladivostok, Russia

It is known that mesoscale variabilities of the surface wind and derived surface fluxes may be important in predicting and explaining the rapid development of marine cyclones and the associated large flux variations (NUSS and BROWN, 1987). The mesoscale wind variations can change a structure of the ocean upper layer significantly. Using measurements from the system of moored buoys, TRUMP *et al.* (1982) found out that ocean temperature and current fluctuations at a depth of 20 m are significantly correlated with mesoscale atmospheric structures associated with the passage of well developed cells. As discussed by FEDOROV and GINSBURRG (1984), it is impossible to explain this correlation by using experimental meteorological data by TRUMP *et al.* (1982) and model calculations. On the other hand, ORLANSKI and POLINSKY (1983), using their model, determined that mesoscale atmospheric forcing is potentially an important source for the observed 100 km-scale variability in the ocean. As suggested by MONIN *et al.* (1987), coherent structures in the atmospheric boundary layer may account

for the horizontal mesostructures in the main thermocline. The necessity of considering the mesoscale wind variability follows also from a work by D'ASARO (1988).

Clouds are the obvious products of the large fluxes from the ocean to the atmosphere during cold air outbreaks. At first they have a shape of cloud rolls and then they are converted gradually to cells. Cloud patterns on the visible and infrared (IR) satellite images show synoptic, subsynoptic and mesoscale structures, and, together with the brightness temperature of cloudiness and cloudless regions of the ocean, give a certain representation about conditions on the upper boundary and inside the convective marine boundary layer.

Since September 1983 when the first satellite with a side-looking radar (SLR) was launched (MITNIK and VIKTOROV, 1990), the opportunities to investigate processes in the marine boundary layer have broadened because the surface wind field can be estimated from radar data. Such radars were installed on the Okean series satellites (Kosmos-1500, Kosmos-1766, Okean and others). They operate at wavelength of 3.15cm with vertical polarization. A ground resolution is 2.1–2.8 km (in flight direction) by 0.8–3 km (normal to flight) at 650 km altitude. A swath width is about 460 km. The angle of incidence changes from 21° to 46° within the swath.

The purpose of this study is to evaluate the possibility of the satellite SLR images of the ocean for representing the mesoscale structures in the surface wind field. The main evidence on horizontal wind variations during mesoscale cellular convection is described in section 2. Coupling of the brightness distribution within open and closed cells on the radar images with the sea surface wind characteristics is considered in section 3. Conclusion and proposal on a special experiment to study the mesoscale processes in the air-sea system are presented in section 4.

2. Mesoscale horizontal wind variations

Fig. 1 shows visible and radar images of the Sea of Okhotsk and an area south off the Kuril Islands obtained by Kosmos-1766 satellite. Cloud field (Fig. 1a) of Meteor-2 visible image is an indicator of organized convection, which takes the form of streaks (area 1), open cells (area 2), chains of vortices (areas 3 and 4). Such forms of the convection are typical in winter monsoon period when cold air masses from Asia move over the warmer Pacific Ocean surface (TRUMP *et al.*, 1982; AGEE, 1987; MITNIK and VIKTOROV, 1990).

The radar sensing of the ocean (Fig. 1b) had been carried out half an hour before the visible survey (Fig. 1a). Swath boundaries of the SLR are depicted in Fig. 1a by solid lines. The main cause of changes in brightness is the sea surface roughness (surface wind) variability. The increase of the sea surface wind results in the increase of the radar image brightness. Brightness distribution suggests that there should be a tight correlation between roughness and cloudiness, between processes on lower and upper boundaries of the boundary layer of the atmosphere. For example, bands of alternating brightness in area 1 (Fig. 1b) have the same orientation as cloud streaks in Fig. 1a. The mesoscale brightness variations caused by air circulation inside individual cells are well visible in area 2. Similar formations are prominent in zone 5 with weak winds. Bands join cyclonic vortex of chain 3. Maximum wind speed (about 10–15 m/s in accordance with surface weather map) is observed in the area where clouds are denser and brighter. Zone with maximum wind speed is located under the cloud spiral near its internal boundary, and has a width of about 30–35 km. To the north of the cloud vortex wind speed is markedly lower.

In the region of chain 4 speed of northwest wind was 7–10 m/s by ship data. Dimensions of individual vortices in the chain and distances between their centers are 30–35 km. The southwest boundary of the vortices has prominent radar contrast against the background (area 6 with low wind speed located to the south). The boundary of radar contrast corresponds to the northeast edge of the cloud vortices. Their dimensions increase downwind. Thus, from the analysis of this radar image it follows that the diverse mesoscale organized structures are observed in the sea surface wind.

Taking into account the spatial resolution of the SLR, the primary attention will be given to the domain of atmospheric motions with spatial

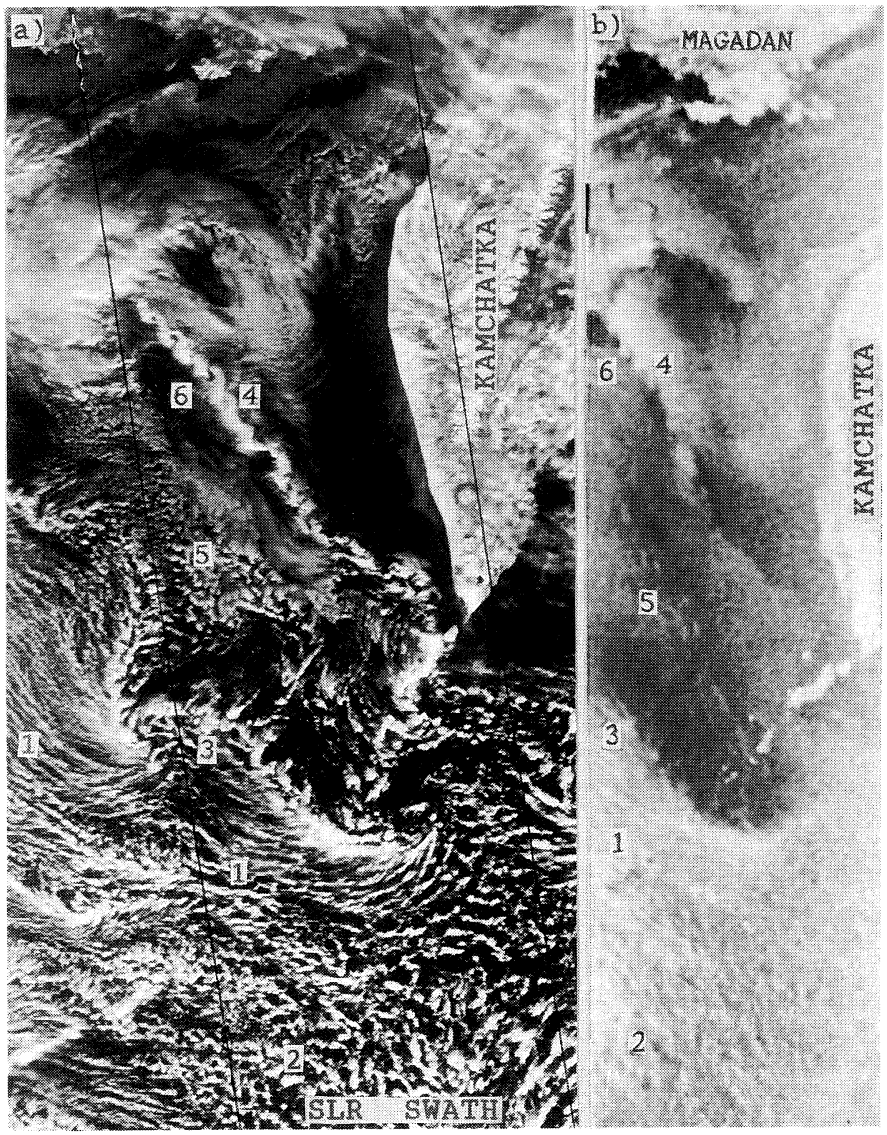

Fig. 1. (a) Meteor-2 visible image and (b) Kosmos-1500 SLR image (3 Jan. 1985, about 0100 GMT) of the Sea of Okhotsk and the Pacific Ocean south of Kuril Islands.

scales L between 1–3 and 100 km and time scales T of minutes to hours. At higher frequencies f ($=1/T$) Kolmogorov turbulence takes place, and at lower ones the synoptic scale motions including fronts and depressions take place. These large-scale structures can be investigated by both scatterometer and SLR.

Our ability to resolve the mesoscale wind variability in the marine boundary layer remains limited by the insufficient temporal and spatial resolution and accuracy of data. A study by NUSS and BROWN (1987) indicates that in data-rich regions, routine surface observations are separated by roughly 400 km on the average and by even greater distances in data-sparse regions. The major sources of the observations are wind reports from ships of opportunity. However, a comparison of wind data from ships and buoys revealed the poor quality and unreliability of wind reports by ships (PIERSON,

1990). Eventually, satellite instruments such as scatterometers and microwave radiometers may provide an observational base for more detailed and accurate surface data for scales larger than 20–50 km. The wind variations with smaller scales will be spatially integrated in the footprint of a satellite sensor. As a result of smoothing, additional errors in the surface wind estimation can arise, which would, in turn, produce poor quality of weather and wave forecasts (PIERSON, 1983, 1990).

The spatial resolution of the satellite SLR permits us to investigate the surface wind variability with scales of 2–50 km. It is of particular importance because the characteristic scales of a major part of coherent motions in the atmosphere are in these limits (AMBROZI *et al.*, 1973; VETLOV and VEL'TISHCHEV, 1982; MITNIKand V IKTOROV, 1990).

Let us summarize briefly the data on the horizontal wind spectrum. As was first shown by VAN der HOVEN (1957), there is a so-called "spectral gap" between turbulent and synoptic peaks in the wind speed power spectrum over land. Then the existence of the gap was revealed in spectra of marine winds (ISHIDA *et al.*, 1984; ISHIDA, 1989; CHAMPAGNE-PHILIPPE, 1989). The existence of the low, flat energy area of spectral gap denotes that energy sources in the corresponding frequency range were lacking during measurements.

A different situation arises when organized convective mesoscale patterns such as rolls, open and closed cells are observed in the atmosphere. Spectrum form changes: secondary peaks may be observed in the gap region between 0.5 and 1.5 hours. In particular, such peaks were found in the wind spectra, obtained from buoys moored in the East-China Sea during the Air Mass Transformation Experiment (AMTEX '75) (BURT and AGEE, 1977; TRUMP *et al.*, 1982; ISHIDA *et al.*, 1984). The meteorological measurements were performed at the height of 4.3 m. Fig. 2 shows two wind spectra, averaged from six buoys. The vertical axis is a frequency multiplied by energy density and the horizontal one is a frequency in logarithmic scale. The lower curve characterizes a typical situation with the spectral gap and the upper one represents a spectrum in the passage of the closed mesoscale

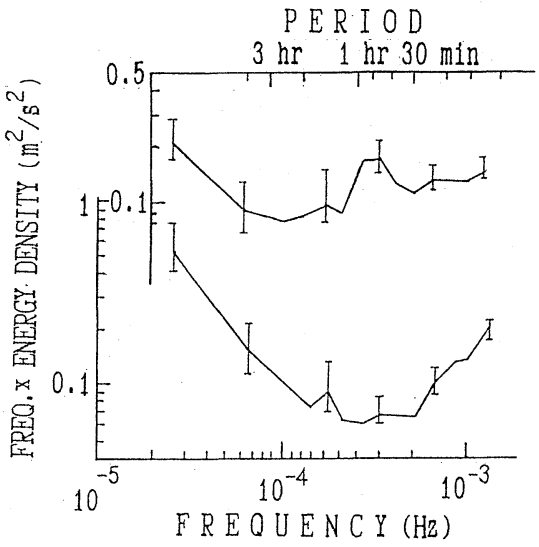

Fig. 2. The averaged spectra of wind speed for six buoys for periods of the well organized MCC (0840 GMT, 16 Feb. – 0555 GMT, 17 Feb. 1975) (upper curve) and of dissipating MCC and without cells, 1150 GMT 17 Feb. – 0955 GMT 18 Feb. 1975) (lower curve) (ISHIDA et al., 1984).

convective cells with average diameter of 24–30 km. A peak at $T = 1$ hr is marked well. Bars correspond to 80 % confidence interval (ISHIDA *et al.*, 1982). Processing of data from buoys located in the triangle apices showed the existence of divergent and convergent air flows corresponding to closed circulation system; downward motion and clear skies in the cell periphery with upward motion and clouds at its center (ISHIDA *et al.*, 1984). A model of the representative closed cell based on the data for 30 hrs period of strong cellular development was characterized by fluctuations in air temperature (±0.2℃), humidity (±0.2 g/kg), and horizontal wind speed (±0.5 m/s relative to the average value of 8 m/s) (TRUMP *et al.*, 1982).

High coherence (0.9) between wind speed and air temperature with the phase difference of about 170° was also revealed by ISHIDA (1989) when significant peaks in their spectra occurred simultaneously in the mesoscale range at a period of 30–40 min (Fig. 3). The data were obtained from an array of buoys during the JASIN-1978 field experiment in the northwest of Scotland. The coherence and phase shift may have been caused by some form of mesoscale

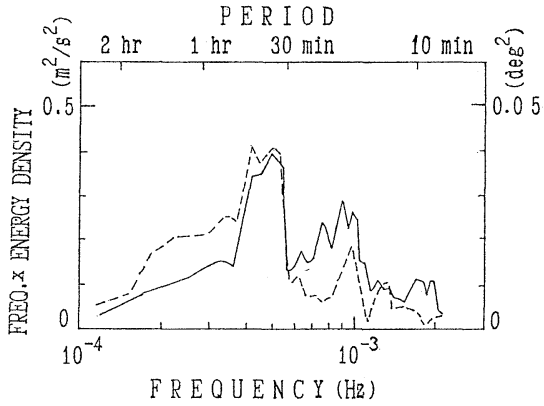

Fig. 3. Spectra of wind speed (solid line) and air temperature (dotted curve) from buoy B3 for 14 21.5 GMT on Aug. 1978 (ISHIDA, 1989).

convective structures.

The spectrum of the horizontal wind measured on the coast during cold air outbreak also showed a somewhat significant peak of energy centered around 0.5–1hr. Wind had been observed for 53 hrs when cumulus and cumulonimbus clouds were numerous and, most of the time, were organized in open mesoscale cells (CHAMPAGNE-PHILIPPE, 1989).

The mesoscale convective cells (MCC) have typical diameters of 10–100 km. Magnitude of the sea surface wind variations may be much larger than the average value reported by TRUMP *et al.* (1982). For example, wind fluctuations up to ±3–4 m/s were registered by onboard sensors, when an aircraft crossed a cellular convection area over the Pacific Ocean at low levels (50 and 90m) (OVERLAND and WILSON, 1984). Wind speed of mesoscale circulation within the large open convective cells may reach 10 m/s and more at their formation (AMBROZI *et al.*, 1973). The average wind speed during mesoscale convection over the Pacific Ocean obtained from the analysis of the satellite cloud images and ship reports was 8.6 m/s at closed cells, 14.3 m/s at open cells, and 17.6 m/s in the case when the cells have crescent shape (POKHIL, 1985).

3. Manifestation of mesoscale cellular convection on radar images of the ocean

The analysis of satellite optical and radar images shows that the mesoscale convective cells

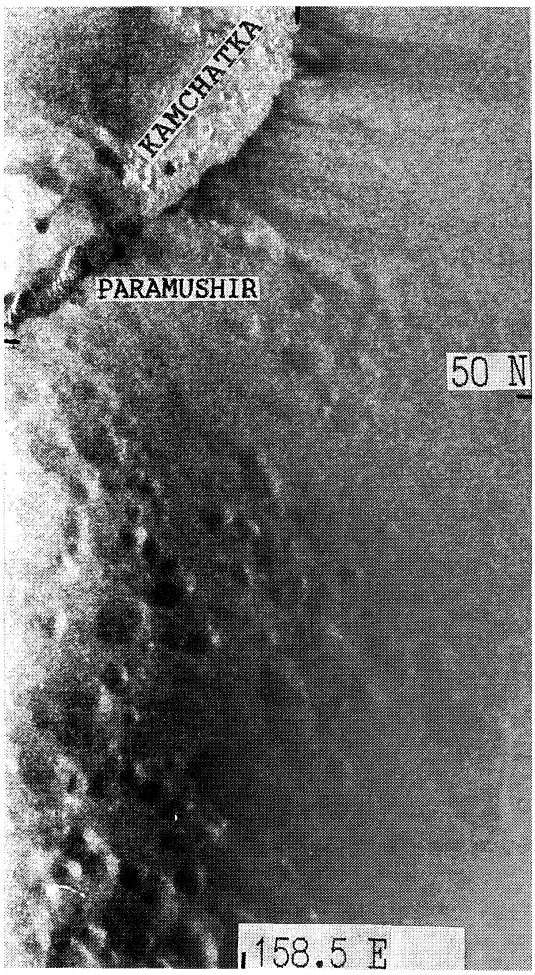

Fig. 4. Okean SLR image of the Pacific Ocean south of Kamchatka for 1940 GMT, 16 Nov. 1988.

are the most popular organized structures in the atmosphere over the ocean in winter period. By means of buoy, ship and aircraft measurements it is difficult or impossible to study the mesoscale spatial structures of wind field in detail. At the same time, the sea surface wind distribution is reflected distinctly on the radar images.

The individual convective cells are well seen in the brightness (roughness) field on the radar image in Fig. 4. During radar survey a synoptic situation was characterized by a deep cyclone with a minimum pressure of 985 mb. Its center was located over the northeastern part of the Sea of Okhotsk outside the swath. A northwest

and west wind speed ranged between 5 and 17 m/s. The surface imprints of the individual cells have mainly circular form. Their diameters change from 10 to 40 km. At higher wind speed these imprints take an stretched form. The effect of air circulation within the cell appears as dark and light zones. A number of cells have crescent brightness distribution: a dark patch surrounded by light sickle. As a result, outlines of the cell have positive, negative or close to zero contrast against the background.

To explain these features the model calculations of the normalized radar cross section (NRCS) σ° of the sea surface have been carried out for horizontal wind distributions in open and closed cells. The brightness of the radar image is proportional to σ°. The value of NRCS is a characteristics of scattered signal power and related to the wind speed W by power law (MOORE and FUNG, 1979; MASUKO *et al.*, 1986).

$$\sigma^\circ(\lambda, p, \theta, \phi) = 10[G(\lambda, p, \theta, \phi) + H(\lambda, p, \theta, \phi)\lg W], \quad (1)$$

where λ is radar wavelength, p polarization of signal, θ angle of incidence, ϕ azimuthal angle (angle between the plane of radar signal propagation and the direction opposite to the wind vector), G coefficient and H wind speed exponent. With the increase of θ the values of σ° decrease.

Azimuthal relationship is approximated well by the cosine expansion regression:

$$\sigma^\circ = A_0 + A_1 \cos\phi + A_2 \cos 2\phi . \quad (2)$$

Empirical approximate coefficients $G(\theta, \phi)$, $H(\theta, \phi)$, A_0, A_1 and A_2 for $\lambda = 3$ cm obtained by MASUKO *et al.* (1986) have been used in subsequent calculations of σ° at vertical polarization.

The features of NRCS distribution within the MCC are explained by using a simple two-component model for horizntal wind pattern (MITNIK and VIKTOROV, 1990). There is a synoptic (background) flow with constant wind speed W_s and regular mesoscale cellular circulation imposed on it. The circulation in cells is axisymmetrical with magnitude W_c. The function $W_c(r)$ describing dependence of wind speed on the distance r from the center of a cell is

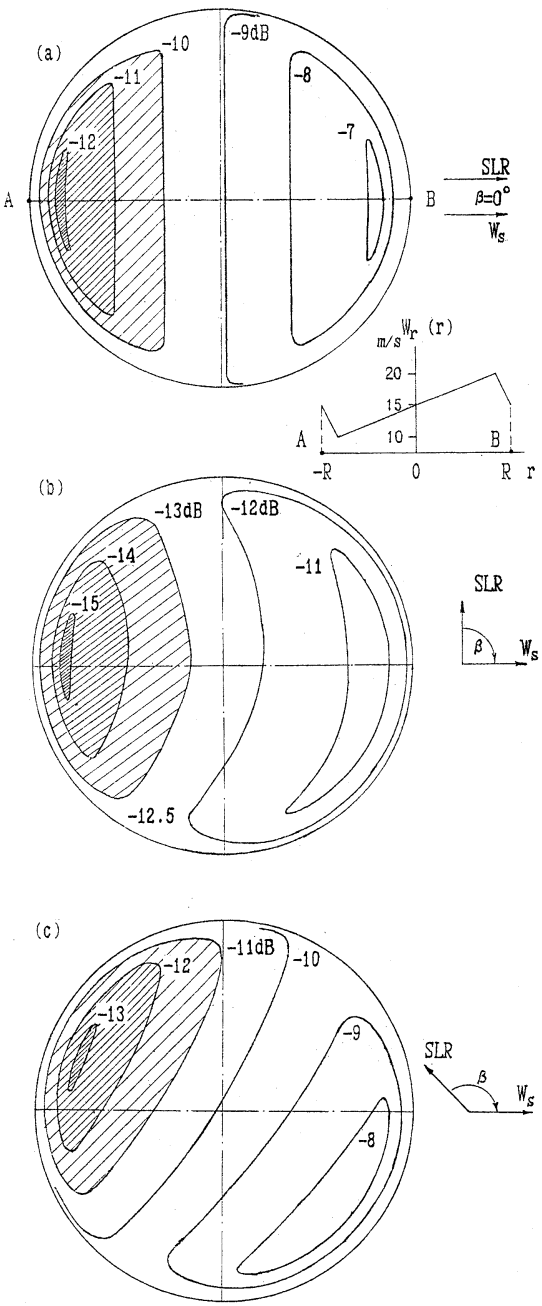

Fig. 5. Distributions of NRCS (in dB) inside open cell for $W_s = 15$ m/s, $W_c = 5$ m/s, $\theta = 30°$: (a) $\beta = 0°$, (b) $\beta = 90°$, and (c) $\beta = 135°$.

specified analytically or numerically. Resulting wind speed $W_r(r)$ and the angle $\phi(r)$ in any point within the cell are determined from given

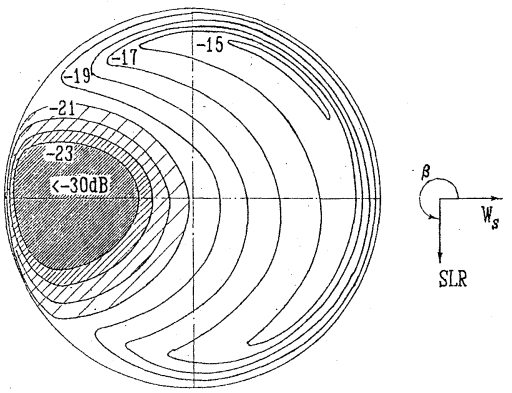

Fig. 6. Distributions of NRCS (in dB) inside open cell for $W_s=5$ m/s, $W_c=5$ m/s, $\theta=30°$, $\beta=270°$.

values of W_s, $W_c(r)$, and β (angle between W_s and the radar signal plane). Angle θ is found from the known position of the cell inside the SLR swath. It allows us to use relationships (1) and (2).

The model calculations of $\sigma°$ distribution have been carried out at wavelength of 3 cm with vertical polarization for $W_s=0-15$ m/s, $\beta=0-360°$, $\theta=30-40°$ and different $W_c(r)$ functions.

For the open cell (upward motion in the cell periphery with downward motion at the center) horizontal wind speed is directed from the center toward the periphery and given by a function

$$W_c(r)=\begin{cases}(|r|/R)W_c, & 0<r<r_0,\\ [(R-|r|)/(R-r_0)]W_c, & r_0<r<R,\end{cases}$$

where $W_c=0.5-5$ m/s, $r_0=5R/6$, and R is the radius of the cell. The origin is at the cell center.

For cell with $R<10$ km change of an angle θ within the cell is small and can be neglected. For such cells the values of $\sigma°$ at the center and the cell edge are equal to each other and determined by parameters of W_s, β and θ.

Radar patterns of the open MCC are shown in Figs. 5 and 6. The extremes of the NRCS are located at a distance of $r=r_0$. Here the resulting wind approaches the extremal values W_{ext} in those points where a mesoscale flow is added with synoptic one or subtracted from it, as shown for A–B section in Fig. 5a. A position of the NRCS extremes may, however, differ from the points of W_{ext} due to the impact of azimuthal dependence (2) (Fig. 5). Amplification of mesoscale circulation (growth of W_c) at W_s=const. will increase the radar contrast between different parts of the cell.

The radar patterns of the MCC significantly depend on the orientation of the radar sensing plane relative to background flow (on angle β). In particular, isolines of $\sigma°$ are of a concave shape when β is near $\pm 90°$ (Fig. 5b). In such cases the radar images of the MCC take crescent shape (KALMYKOV *et el.*, 1985; MITNIK and VIKTOROV, 1990). At other values of β the concavity is small, if any (Figs. 5a and 5c).

As the speed of synoptic flow decreases the values of $\sigma°$ decrease, too, and the radar patterns of the MCC are transformed. The edges of sickles are twisted towards the wind (Fig. 6). In real conditions differencies in the brightness inside the cell may be even greater, when the resulting wind speed will be lower than a threshold value W_0 (which depends on the sea surface temperature). At $W_r<W_0$ capillary-gravity waves on which the radar signals are scattered are not formed (DONELAN and PIERSON, 1987) and appropriate parts of the cells become dark. The dark patches in windward parts of the open cells give a higher radar contrast of leeward ones where synoptic and mesoscale flows are added (Fig. 4).

The mesoscale circulation in the closed cell was described by a harmonic function (TRUMP *et al.*, 1982)

$$W_c(r)=-W_c\sin(\pi r/R).$$

Horizontal wind speed is directed from the cell periphery toward its center. The origin is again at the cell center.

Distributions of NRCS for the closed MCC with $W_c=5$ m/s are presented in Fig. 7. Vector diagrams give an indication of resulting horizontal wind vector for four points located at a distance of $r=R/2$ where $W_c(r)$ has a maximum. Inside the closed cell there are areas having positive and negative radar contrast against the background. The contrast magnitude and radar patterns of the cell depend significantly on the relationship between W_s, W_c and β, and also on a number of other parameters.

For large MCC ($R>10$ km) the change of an angle θ within the cell must be allowed for in model calculations. To illustrate, the additional

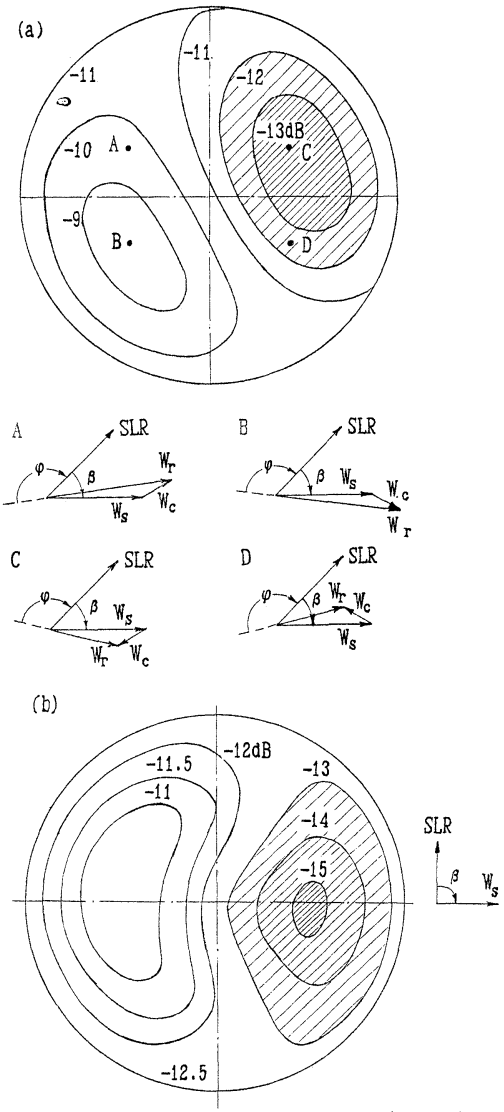

Fig. 7. Distributions of NRCS (in dB) inside closed cell for W_s=15 m/s, W_c=5 m/s, θ =30°: (a) β =45°, (b) β =90°.

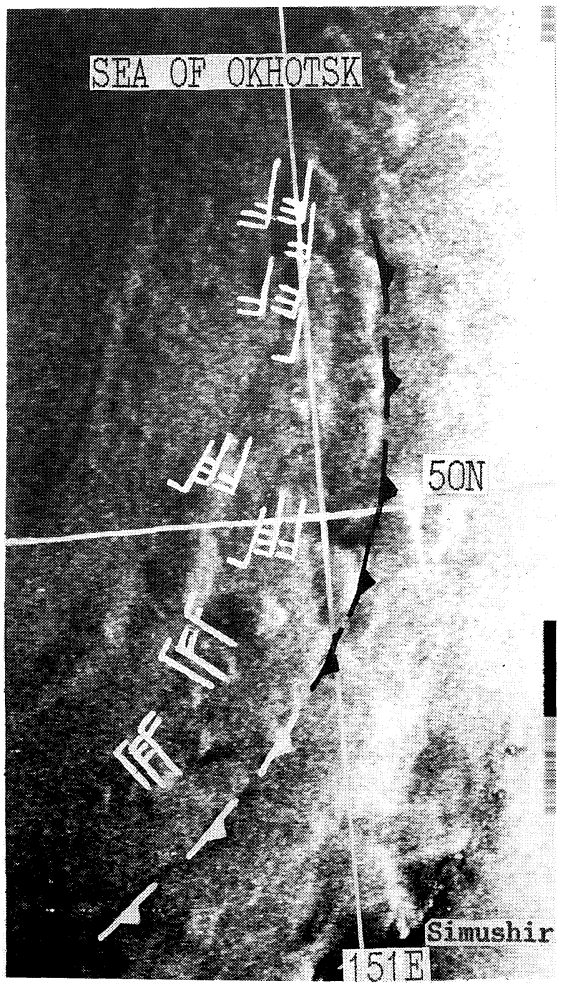

Fig. 8. Okean SLR image of the central part of the Sea of Okhotsk for 1245 GMT, 14 Oct. 1988, and the retrieved average and extremal values of the surface wind vector in a cell area (Bukharov et al., 1991).

decrease of σ° value of remote (from the SLR) portion of the cell relative to near one will be 1.0–1.6 dB for cells with R=20 km at θ =30–40° (MITNIK and VIKTOROV, 1990).

Let us correlate the results of model calculation with the features of the brightness (surface wind) distribution in areas of cell convection on the radar images. An algorithm of wind speed determination by radar image was described by MITNIK and VIKTOROV (1990). This algorithm takes into account the information on radar system, calibration of a transmitter power, altitude of the satellite, wind direction (from surface weather maps), values of an angle of incidence for the ocean area under investigation, etc. Let us analyze the radar image of the south part of the Sea of Okhotsk obtained by "Okean" satellite (Fig. 8a, BUKHAROV *et al.*, 1991). By the time of the radar survey this area had been influenced by the secondary cold front which was formed in the rear of the occluded cyclone. This front moved rapidly to the east with a

speed of 6 m/s in the northern part and 11 m/s in more active southern one. The air temperature near the sea surface behind the cold front was 1.5–2℃ lower than before it.

The larger part of the cells is organized in a form of chains stretched northeastward (lower part of the image) and northward (upper one) along the front line. The cells form is nearly circular, but their dimensions are distinguished significantly (from 12 to 70 km) even for adjacent cells. The light parts of the cells (with the higher wind speed) are noticeably brighter than the surrounding sea surface (background) and have a form of patches, narrow bands along the cell edges, patches coupled with bands, or sickles. Their width is about 20–50 % of the cell size. The radar contrasts are about 3.5–5.5 dB between light and dark parts of the cells, and 2–3.5 dB between light parts and background. These estimations are in good agreement with calculations for W_s=10–15 m/s and W_c=3–5 m/s (Fig. 5). BUKHAROV *et al.* (1991) carried out model calculations of the radar contrasts between various areas of the cell to estimate values of W_c/W_s and angle β. The results of wind retrieval are given in Fig. 8. The wind characteristics on the other radar images were estimated in a similar way.

As noted above, the enhanced heat fluxes in the areas with the MCC favour to the cyclogenesis. During the radar survey cloudiness field reflected the origin stage of the cyclonic vortex on the secondary cold front. The vortex reached the stage of maximum development in 7 hrs.

4. Conclusion

The analysis of the radar images obtained by the satellite SLR during winter monsoon over the Far Eastern seas confirmed that there are diverse organized structures in horizontal wind field. The most popular structures are connected with the MCC.

Brightness (NRCS) variations of the radar images of the sea surface areas over which the MCC are observed can be explained by means of a simple model of W distribution containing constant synoptic and variable mesoscale components. The mesoscale circulation inside the cells is axisymmetrical; wind is directed to the center from the cell periphery for the closed cell and vice versa for the open cell.

The model patterns of NRCS are consistent with the brightness distribution of areas with the MCC on the radar images. It follows from calculations that the patterns of the NRCS are governed by the relation between mesoscale and synoptic flows by an angle between synoptic wind direction and a radar sensing plane. It can be used to estimate the sea surface wind characteristics (MITNIK and VIKTOROV, 1990; BUKHAROV *et al.*, 1991).

The combination of visible, infrared and radar images with contact measurements provides new opportunities to study processes in the boundary layers of the atmosphere and ocean during cold air outbreaks from Asia. These layers play an important part in formation of the daily and seasonal patterns of weather and climate of the Far Eastern seas. Special experiments are necessary to study the air-sea system behavior during these processes. The comprehensive investigation of the response of the subsurface layer of the ocean to the quasiperiodic atmospheric disturbances is of primary importance.

Acknowledgments

The author wishes to thank Dr. M.V. BUKHAROV of the Russian Hydrometeorological Scientific Research Center for his valuable discussion of radar sensing of the ocean in areas with the mesoscale sea surface wind variability, and the anonymous reviewers for their careful examination and suggestions for improving the manuscript.

References

AGEE, E. M. (1987): Mesoscale cellular convection over the oceans. Dyn. Atmos. Oceans, **10**, 317–341.

AMBROZI, P., N. V. VEL'TISHCHEV, G. GOTZ. (1973): Utilization of evidence on mesoscale features of cloudiness in weather analysis. Gidrometeoizdat, Leningrad, 151 pp. (in Russian).

BUKHAROV, M. V., T. V. ZAKHAROVA and G. M. OZEROVA (1991): The reconstruction of near water wind in the regions with atmospheric convection based on a side looking radar imagery. Issledovanie Zemli iz Kosmosa, N 3, 26–32 (in Russian).

BURT, W. J. and E. M. AGEE (1977): Buoy and satellite observations of mesoscale cellular convection during AMTEX'75. Boundary-Layer Meteorol., **12**, 3–24.

CHAMPAGNE-PHILIPPE, M. (1989): Coastal wind in the transition from turbulence to mesoscale. J. Geophys. Res., **94**, 8055–8074.

D'ASARO, E. A. (1989): The decay of wind-forced mixed layer internal oscillations due to the β effect. J. Geophys. Res., **94**, 2045–2056.

DONELAN, M. A. and W. J. PIERSON (1987): Radar scattering and equilibrium ranges in wind generated waves with application to scatterometry. J. Geophys. Res., **92**, 4971–5029.

FEDOROV, K. N. and A.I. GINSBURG (1988): The Subsurface Layer of the Ocean Gidrometeoizdat, Leningrad, 304 pp. (in Russian).

HUH, O. K., L. I. ROUSE, Jr and N. D. WALKER (1984): Cold air outbreaks over the Northwest Florida continental shelf, heat flux processes and hydrographic changes. J. Geophys. Res., **89**, 717–726.

ISHIDA, H. (1989): Spectra of surface wind speed and air temperature over the ocean in the mesoscale frequency range in JASIN–1978. Boundary-Layer Meteorol., **47**, 75–84.

ISHIDA, H., W.V. BURT and V. MITSUTA (1984): The effects of mesoscale convective cells on the surface wind fields over the ocean. Boundary-Layer Meteorol., **29**, 75–84.

KALMYKOV, A. I., M. NAZIROV, P. A. NIKITIN and YU. G. SPIRIDONOV (1985): On regulated mesoscale structures on the ocean surface revealed by radar surveys from space. Issledovanie Zemli iz Kosmosa, (3), 41–47 (in Russian).

MASUKO, H., K. OKAMOTO, M. SHIMADA and S. NIWA (1986): Measurement of microwave backscattering signatures of the oceane surface using X band and Ka band airborne scatterometers. J. Geophys. Res., **91**, 13065–13085.

MITNIK, L. M. and S.V. VIKTOROV (editors) (1990): Radar Sensing of the Earth's Surface from Space. Gidrometeoizdat, Leningrad, 200 pp. (in Russian).

MONIN, A. S., R. V. OZMIDOV and V. T. PAKA (1987): On horizontal mesostructure of the main thermocline. Dokl. AN SSSR, **297**, 1469–1472 (in Russian).

MOORE, R. K. and A.K. FUNG (1979): Radar sensing wind over the ocean. Proc. IEEE, **67**, 1504–1521.

NUSS, W. A. and R. A. BROWN (1987): Evaluation of surface wind and flux analysis techniques using conventional data in marine cyclones. Dyn. Atmos. Oceans, **10**, 291–315.

ORLANSKI, I. and L. J. POLINSKY (1983): Ocean response to mesoscale atmospheric forcing. Tellus, **35**, 296–323.

OVERLAND, J. E. and J. G. WILSON (1984): Mesoscale variability in marine winds at midlatitude. J. Geophys. Res., **89**, 10599–10614.

PIERSON, W. J. (1983): The measurement of the synoptic scale wind over the ocean. J. Geophys. Res., **88**, 1683–1708.

PIERSON, W. J. (1990): Examples of, reason for, and consequences of the poor quality of wind data from ships for the marine boundary layer: Implications for remote sensing. J. Geophys. Res., **95**, 13313–13340.

POKHIL, A. E. (1985): On the indentification of storm wave conditions and calm zones in the Pacific Ocean from satellite cloud imagery. Meteorologiya and Gidrologiya, (12), 68–76 (in Russian).

TRUMP, C. L., S. J. NESHYBA and W. V. BURT (1982): Effects of mesoscale atmospheric convection cells on the waters of the East-China Sea. Boundary Layer Meteorol., **24**, 15–34.

VAN der HOVEN, I. (1957): Power spectrum of horizontal wind speed in the frequency range from 0.0007 to 900 cycles per hour. J. Meteorol., **14**, 160–164.

VETLOV, I. P. and N.F. VEL'TISHCHEV (editors) (1982): Manual by usage of satellite data in weather analysis and forecast. Gidrometeoizdat, Leningrad, 300 pp. (in Russian).

La mer 30: 297–314, 1992
Société franco-japonaise d'océanographie, Tokyo

Lagrangian flow observations in the East China, Yellow and Japan Seas

Robert C. BEARDSLEY*, Richard LIMEBURNER,* Kuh KIM**
and Julio CANDELA***

Abstract: Satellite-tracked drifters with drogues centered at 10 and 40 m were deployed in the Yellow and East China Seas in January and July 1986. Two drifters launched in January returned useful data for about 60 days. Both drifters exhibited weak mean velocities of 2–3 cm/s but larger subtidal variability (eddy kinetic energy 31–35 cm^2/s^2). All ten drifters launched in July returned useful data for at least 90 days. The resulting trajectories of five drifters deployed in the Yellow Sea describe a weak basin-scale cyclonic gyre in the surface waters of the Yellow Sea in late summer. The center of the gyre was located near 35.6° N, 123.8° E, and the mean velocities along the Korean and Chinese coasts varied from 2 to 6 cm/s. Within the Yellow Sea, the distribution of eddy kinetic energy was relatively uniform spatially at 30–50 cm^2/s^2 except with an increase to about 80 cm^2/s^2 near the Korean coast and higher near the southeast entrance of the Yellow Sea.

Drifter trajectories in the East China Sea describe a strong inflow of Kuroshio and shelf water in late summer into the Korea Strait through both western and eastern channels. While two drifters continued to move slowly southeastward along the Chinese coast, no drifters entered the Yellow Sea, suggesting that the Yellow Sea Warm Current may not be a coherent and continuous current in summer. The mean eddy kinetic energy in the East China Sea was 112 ± 43 cm^2/s^2. Three drifters entered the Japan Sea and followed quite different paths, suggesting that the Tsushima Current may not simply split into several semi-permanent branches as it leaves the Korea Strait. One drifter entered a cyclonic mesoscale eddy near 37° N, 133° E and made three complete loops with a mean speed and radius of 26 ± 14 cm/s and 35 ± 14 km before exiting. The mean eddy kinetic energy in the Japan Sea west of 138° E was 415 ± 91 cm^2/s^2. One drifter was deployed in the Ohsumi branch of the Kuroshio and carried eastward in the Kuroshio and Kuroshio Extension to about 160° E before drifting to the south in the recirculation. While in the Kuroshio and Kuroshio Extension, the drifter had a mean and eddy kinetic energy of 0.29 and 0.38 m^2/s^2.

1. Introduction

It is generally believed from the early work of UDA (1934) and others that some warm water from the Kuroshio flows northward across the East China Sea continental shelf and into the Japan and Yellow Seas via two branches, the Tsushima Current and the Yellow Sea Warm Current, respectively (Fig.1). The Tsushima Current has an annual mean geostrophic transport of about 1.3 Sv (YI, 1966), and carries Kuroshio water of high temperature and high salinity through the Korea Strait into the Japan Sea where it strongly influences water structure within this semi-enclosed basin (SVERDRUP *et al.*, 1942: page 734; MORIYASU, 1972; KOLPACK, 1982). The Tsushima Current has a minimum geostrophic transport of about 0.5 Sv in January to May increasing rapidly to a summer-fall maximum of about 2.2 Sv in July to November. Much less is known about the path, magnitude and seasonal variation of the Yellow Sea Warm Current, although its transport is thought to be less than that of the Tsushima Current. The

*Department of Physical Oceanography, Woods Hole Oceanographic Institution, Woods Hole, MA 02543, USA
**Department of Oceanography, Seoul National University, Seoul 151–742, Korea
***Departamento de Oceanografía, Centro de Investigación Científica, y de Educación Superior de Ensenada (CICEE), Ensenada, Baja California, México

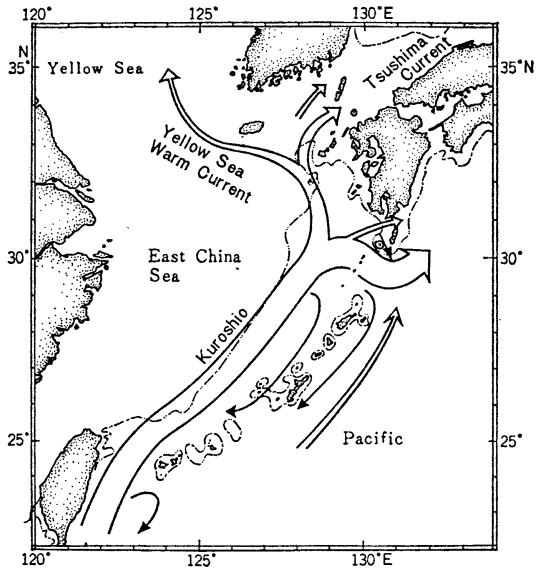

Fig. 1. Schematic representation of the current system in the East China Sea. From Nitani (1972).

Yellow Sea Warm Current is generally thought to flow northward up the deep central channel toward the Gulf of Bohai, with some flow turning westward and feeding a large basin-wide cyclonic gyre in the Yellow Sea.

While there has been little disagreement on this general description of the branching of the Kuroshio in the East China Sea, recent observations question the historical ideas about the path and strength of the Yellow Sea Warm Current in the Yellow Sea, the formation region of the Tsushima Current in the eastern East China Sea, and the subsequent path of the Tsushima Current in the Japan Sea. As part of a cooperative US – Korea – China research program, satellite-tracked drifters were deployed in the East China and Yellow Seas in January and July 1986. The resulting drifter trajectories provide the first long quasi-Lagrangian current measurements in this region, which in turn provide insight into the questions raised about the Yellow Sea Warm Current and Tsushima Current. This paper presents a simple description of the drifter trajectories and some initial conclusions, which are summarized in the discussion, based primarily on this small but unique data set. The drifters were deployed during regional hydrographic surveys so that the initial water masses into which drifters were deployed have been identified by standard and cluster analysis of the temperature-salinity data. Detailed descriptions of the hydrographic data and the results of moored current meter and shipboard acoustic Doppler current meter measurements made in the 1986 cooperative experiment are presented elsewhere by KIM *et al.* (1991), CHEN *et al.* (1992, 1993), HSUEH and PANG (1988), HSUEH (1989), and CANDELA *et al.* (1992), respectively.

2. The Drifter Experiment

Between January 8–February 2, 1986, we deployed one Technocean Associates Tristar (NILLER *et al.*, 1987) and seven ORE (Ocean Research Equipment, Inc.) satellite-tracked drifting buoys in the Yellow and East China Seas from the R/V Thompson during a regional scale CTD/ADCP survey. Six additional ORE drifters were deployed from the Korean R/V Pusan 801 and the Chinese R/V Venus 2 during mooring recovery cruises in April. These were prototype drifters consisting of a surface drifter housing an ARGOS platform transmitter and a Tristar drogue centered at 10 m depth. The ORE drifter and drogue design was patterned after the Tristar. All these drifters had a drag ratio of the drogue to all other components of the drifter of about 28, so that the downwind slip velocities estimated from field tests were about 2.5 and 4.3 cm/s at wind speeds of 10 and 20 m/s, respectively (P. RICHARDSON, personal communication). Data return from the drifters was extremely poor, with only two ORE drifters deployed in January returning useful data for up to about 60 days (Table 1).

Between July 6–18, we deployed ten Draper Laboratory satellite-tracked Low-Cost Drifters (LCDs) in the Yellow and East China Seas during a regional CTD survey aboard the R/V Washington. These ARGOS-tracked drifters featured a surface float attached to a holey sock drogue centered at either 10 or 40 m depth (DAHLEN, 1985). The 10 m LCDs had a drag ratio of 36, giving an estimated downwind slip velocity of about 2.2 and 3.8 cm/s for wind speeds of 10 and 20 m/s, while the 40 m LCDs had a drag ratio of only about 18, giving an estimated downwind slip velocity of about 4.0 and

Table 1. Summary of satellite-track drifters deployed in Yellow and East China Seas during 1986. The two winter drifters were ORE drifters with Tristar drogues, while the summer drifters were made by Draper Laboratory with holey-sock drogues. Listed are the drifter identification number (ID), drogue depth, area deployed, and the initial location, start time, and length of the low-passed drifter position time series.

Drifter ID	Drogue Depth (m)	Area Deployed	Latitude (°N)	Longitude (°E)	Start Date (yd)	Record Length (days)
Winter						
6970	10	C Yellow Sea	34.91	124.62	22	43
6975	10	Cheju Island	32.94	125.74	26	56
Summer						
5843	10	C Yellow Sea	35.13	123.29	194	114
6971	10	W Yellow Sea	35.18	121.50	193	280
6974	10	Kuroshio	30.32	129.62	202	180
6978	10	Cheju Island	33.12	125.47	197	15
6983	10	Tsushima Strait	32.69	128.04	199	49
6984	10	E Yellow Sea	35.06	125.47	194	25
6985	10	NC Yellow Sea	36.84	123.15	190	112
6986	10	Yangtze River	31.70	123.03	198	148
6987	10	NC East China Sea	33.01	123.01	196	88
6988	10	Cheju Island	33.05	125.52	197	188

6.0 cm/s, respectively (P. RICHARDSON, personal communication). All LCDs returned useful data for over 90 days, some much longer (Table 1). For both January and July deployments, each drifter obtained about 4–6 fixes per day on average with a nominal accuracy per fix of about 300 m.

The drifter raw position data were first linearly interpolated to a uniform 6-hour time series of latitude and longitude. Then these series were low-pass filtered with a parabolic-linear filter with a 33-hour half-amplitude period (FLAGG *et al.*, 1976) to eliminate tidal and inertial motions. Drifter velocities were then computed by simple backward difference. To examine the influence of wind on the low-passed drifter velocities, values of the 10 m wind at the drifter positions were extracted by linear interpolation in time and space from the ECMWF/WCRP Level III-A global atmospheric surface data set, which has a 12-hour, 2.5° resolution. The drifter wind time series were then converted into wind stress time series using the neutral drag law of LARGE and POND (1981). Time is expressed here in GMT year days (yd) for 1986 to simplify comparison between drifters. Drifter deployment areas and initial position, start time and record length of the low-passed drifter position time series are summarized in

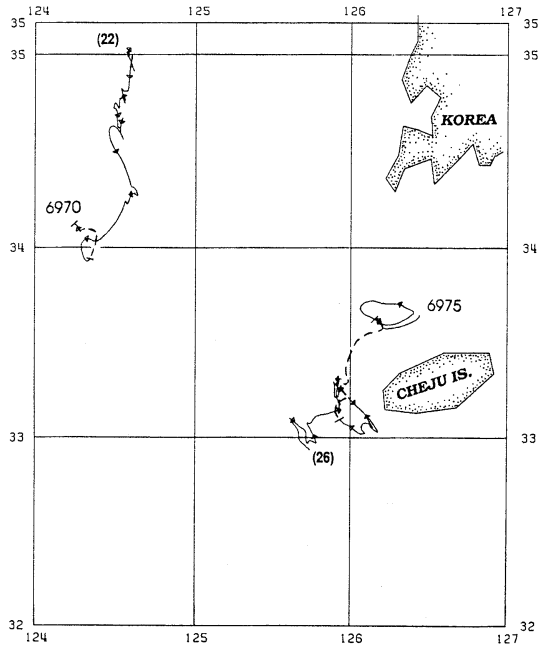

Fig. 2. Drifter trajectories from winter 1986 deployment. Starting date of trajectory in yearday is shown in parenthesis at beginning of each trajectory. Arrows showing direction of motion are placed along each trajectory every five days from yd 1. The drifter trajectory during the spring transition (yd 62–70) is indicated by the dashed path.

Table 2. Statistics for drifters 6970 and 6975 for a 39-day common period starting on yd 26.75. The mean (m), standard deviation (sd), standard error (se), minimum (min) and maximum (max) values and decorrelation time scales are listed for drifter east (U), north (V), and speed (S) in cm/s and wind stress east (E) and north (N) components in dyne/cm^2. The decorrelation time scale t_{dc} is one-half the zero crossing estimated from the auto-correlation function, and the standard error is the standard deviation divided by the square root of the record length divided by the decorrelation time scale following Kundu and Allen (1976). The initial drifter position, start time in yd and length of averaging period in days is listed at the top for each drifter.

	m	sd	se	min	max	t_{dc}
6970: 35.00° N, 124.60° E, yd 26.75, 39 d						
U	−1.0	3.9	0.6	−12.8	7.6	1
V	−2.8	6.8	1.1	−15.4	19.0	1
S	7.1	4.5	−	0.8	19.8	−
E	.25	.34	.07	− 6.5	1.55	1.5
N	−.58	.53	.10	−2.28	.47	1.5
6975: 32.94° N, 125.74° E, yd 26.75, 39 d						
U	0.6	5.4	.9	−11.7	15.5	1
V	1.1	6.4	1.0	−14.9	12.9	1
S	7.4	4.1	−	0	21.2	−
E	.29	.36	.07	− .94	1.61	1.5
N	−.60	.45	.10	−1.69	.43	1.5

Table 1.

3. Results

A. Winter 1986 deployment

Two drifters (6970 and 6975) deployed in mid-to-late January 1986 returned useful velocity data. Drifter 6970 was launched into Yellow Sea Cold Water (group 3 in Figures 3 and 5 of KIM *et al.*, 1991) near the central Yellow Sea (water depth 94 m) and generally moved toward the south and southwest with a mean velocity of about 3 cm/s during the interval yd 22–66 (Fig. 2). Drifter 6975 was launched southwest of Cheju into a mixture of shelf and Kuroshio water called East China Sea Water (group 4)(water depth 91 m) and moved north and northeastward with a mean velocity of about 2 cm/s during the interval yd 27–83. Both drifters exhibited significant subtidal variability, with mean and maximum speeds of 7–8 and 19–22 c m/s (eddy kinetic energy 31–35 cm^2/s^2). Winds during this late winter period between launch and early March were predominately oriented toward the southeast with mean and maximum wind speeds of about 6 and 12 m/s, respectively. During yd 62–70 (March 3–11), a large-scale "spring transition" occurred in the wind field over the Yellow Sea, with winds generally

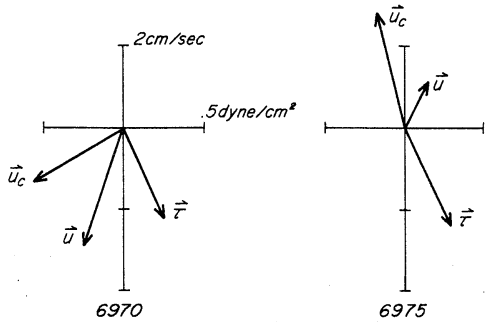

Fig. 3. Mean drifter velocity and wind stress for 6970 and 6975 during common time yd 27–66. Also shown is drifter velocity corrected for windage.

weakening and becoming more variable in direction. HSUEH (1988) shows that accompanying this spring transition is a reversal of the north-south surface pressure gradient in the Yellow Sea from a mean setup toward the south (driven by the predominant southeastward winds) to a mean northward setup. During the later half of this transition (yd 66–70), 6975 moved swiftly northward with mean and maximum speeds of 14 and 23 cm/s, respectively, moving a net distance of about 40 km.

To allow comparison over a common time period, statistics for 6970 and 6975 were computed over the 39-day interval yd 27–66 (Table 2).

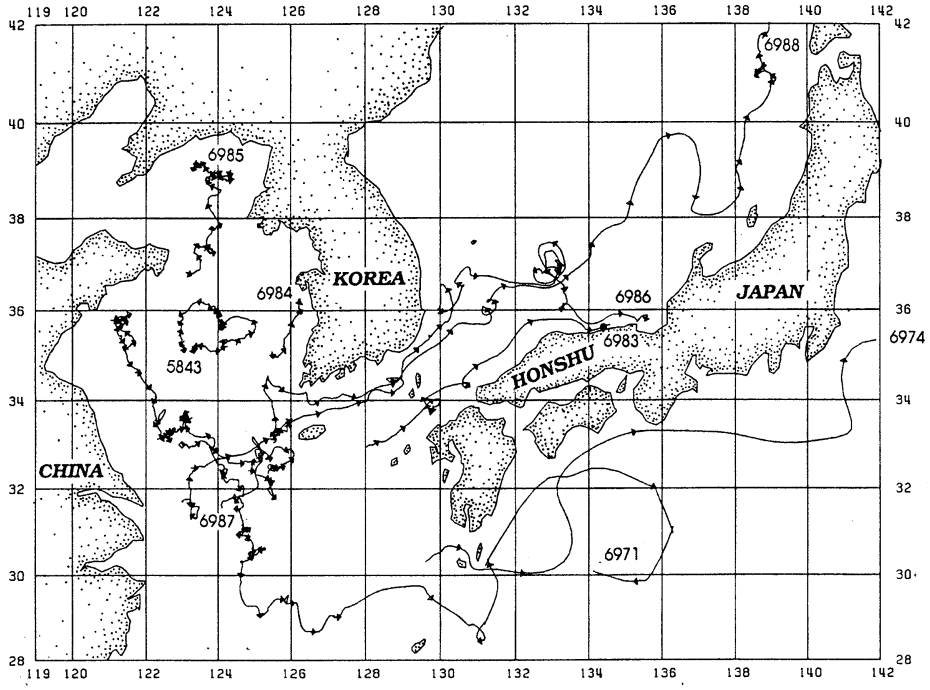

Fig. 4. Drifter trajectories from summer 1986 deployment. The drifter identification number is printed at end of trajectory. Arrows showing direction of motion are placed along each trajectory every five days from yd 1. All drifter trajectories start within a 12-day period (yd 190–202).

This common period ends during the beginning of the spring transition, so the statistics represent late winter conditions. Fig. 3 illustrates the mean drifter velocity and wind stress components: 6970 moved at about a 45° angle to the right of the wind stress while 6975 clearly moved to the left and against the mean wind stress. Also plotted in Fig. 3 are the mean drifter velocities "corrected" for downwind slippage using the drifter drag ratio and empirical slippage curves supplied by RICHARDSON (personal communication). While the uncertainty in this correction may be large, the resulting mean velocity of 6970 is closer to 90° to the right of the wind stress in the correct sense for a surface mixed layer while 6975 moved more directly against the mean wind stress. CTD data collected at deployment showed that the surface mixed layer in late winter was significantly deeper than the drogues which were centered at 10 m. Complex vector correlations computed between drifter velocities and wind stresses indicate that while both drifters essentially experienced the same wind field during the common time period, 6970 and 6975 velocity fluctuations were not correlated in time, and only 6970 exhibited partial wind-driving. Perhaps more importantly, Fig. 3 illustrates the need for higher drag ratios to reduce the relative effects of windage in future drifter experiments in this region.

B. Summer 1986 deployment

Ten drifters were deployed in mid-July 1986 and all returned useful data (Table 1, Fig. 4). Five drifters (5843, 6971, 6984, 6985, and 6987) were deployed with drogues centered at 10 m in the Yellow Sea; with the exception of 6984, which became stuck (perhaps caught in fishing gear) off Korea after about 30 days, the remaining four drifters returned low-pass data for periods ranging from 88 to 280 days. Four drifters (6978, 6983, 6986, and 6988) were deployed in the East China Sea. Drifters 6978 and 6988 were set as a pair with drogues centered at 40 and 10 m, respectively, to examine vertical shear near Cheju Island; 6978 was recovered about 17 days after launch by a fisherman from Cheju. Drifter

Table 3. Statistics for drifters deployed in July, 1986. The mean (m), atandard deviation (sd), standard error (se), minimum (min) and maximum (max) values and decorrelation time scales are listed for drifter east (U), north (V), and speed (S) in cm/s and wind stress east (E) and north (N) components in dyne/cm^2. The decorrelation time scale (t_{dc}) is one-half the zero crossing estimated from the auto-correlation function, and the standard error is the standard deviation divided by the square root of the record length divided by the decorrelation time scale following Kundu and Allen (1976). The initial drifter position, start time in yd and length of averaging period in days is listed at the top for each drifter.

	m	sd	se	min	max	t_{dc}
5843 : 35.13°N, 123.29°E, yd194.0(July 13), 19d						
U	4.5	5.1	···	−4.6	17.2	···
V	.2	4.6	···	−10.3	12.9	···
S	7.2	3.9	···	0	18.1	···
E	0.03	0.11	···	−.28	.40	···
N	0.07	0.21	···	−.60	.81	···
35.16°N, 124.12°E, yd213(August 1), 31d						
U	−.1	10.7	3.3	−45.5	19.3	3
V	2.1	6.7	1.2	−31.4	11.3	1
S	9.5	8.6	···	.7	48.4	···
E	.11	1.05	.19	−3.13	9.03	1
N	−.39	.93	.20	−5.64	.90	1.5
35.65°N, 124.07°E, yd244(September 1), 30d						
U	−1.0	3.8	0.7	−12.1	7.9	1
V	1.8	4.9	0.9	−13.4	15.4	1
S	5.5	3.4	···	.4	15.6	···
E	.02	.17	.03	−.68	.60	1
N	−.21	.27	.05	−1.27	.54	1
36.06°N, 123.78°E, yd274(October 1), 31d						
U	−2.4	5.9	1.1	−16.6	10.5	1
V	−3.6	6.1	1.1	−22.1	7.2	1
S	8.1	5.0	···	1.0	23.1	···
E	.05	.22	.04	−.71	.82	1
N	−.30	.49	.09	−2.29	.57	1
35.18°N, 123.05°E, yd305(November 1), 3d						
U	1.3	2.7	···	−2.9	5.9	···
V	−4.6	9.2	···	−19.0	11.3	···
S	9.1	5.2	···	2.1	19.3	···
E	.10	.16	···	−.08	.40	···
N	−.20	.41	···	−.93	.35	···
6971 : 35.18°N, 121.50°E, yd193.5(July 12), 19.5d						
U	−.8	6.0	···	−14.3	10.1	···
V	4.4	2.4	···	−.5	13.4	···
S	7.0	3.5	···	0	18.5	···
E	.01	.09	···	−.37	.19	···
N	.07	.17	···	−.40	.51	···
35.85°N, 121.34°E, yd213(August 1), 31d						
U	−.2	5.9	1.1	−22.1	11.7	1
V	−1.7	4.9	0.9	−18.0	6.2	1
S	6.4	4.5	···	0	23.3	···
E	.04	.39	.07	−1.20	3.24	1
N	−.31	.86	.16	−4.88	.51	1
35.44°N, 121.29°E, yd244(September 1), 30d						
U	3.4	4.5	0.8	−9.8	13.2	1
V	−7.0	4.3	0.8	−18.5	2.6	1
S	9.0	4.4	···	1.4	21.4	···
E	−.02	.14	.02	−.43	.42	1
N	−.16	.24	.04	−.90	.51	1
33.79°N, 122.24°E, yd274(October 1), 31d						
U	1.6	6.2	1.1	−21.9	15.4	1
V	−2.1	11.0	2.0	−26.3	22.7	1
S	10.8	7.1	···	.7	29.2	···
E	.00	.34	.06	−1.18	1.09	1
N	−.28	.41	.07	−1.35	.53	1
33.32°N, 122.68°E, yd305(November 1), 30d						
U	1.6	5.4	1.0	−11.6	14.2	1
V	1.5	7.5	1.4	−18.0	17.5	1
S	8.4	4.4	···	.7	19.0	···
E	−.05	.29	.05	−.90	.65	1
N	−.50	.66	.12	−3.09	.77	1
6971 : 33.67°N, 123.13°E, yd335(December 1), 31d						
U	5.0	8.9	1.6	−9.1	34.5	1
V	−6.8	10.4	1.9	−36.0	16.0	1
S	13.7	8.4	···	2.1	36.1	···
E	.25	.56	.10	−.54	2.37	1
N	−.54	.71	.13	−2.39	1.09	1
32.01°N, 124.57°E, yd366(January 1), 31d						
U	.9	7.6	1.4	−17.6	17.0	1
V	−4.7	10.2	1.8	−39.1	14.4	1
S	11.7	7.0	···	1.0	40.6	···
E	.13	.60	.11	−.86	2.66	1
N	−.71	.83	.15	−3.14	0.93	1
30.88°N, 124.83°E, yd397(February 1), 28d						
U	0.8	11.8	2.2	−24.9	37.7	1.5
V	−7.2	14.2	2.7	−53.0	11.8	1
S	15.9	11.9	···	.9	55.7	···
E	.28	.65	.12	−.86	3.44	1
N	−.71	1.13	.21	−4.10	1.60	1
29.28°N, 125.04°E, yd425(March 1), 31d						
U	22.0	25.3	4.5	−32.6	123.4	1.5
V	−3.4	22.8	4.1	−49.9	48.5	1
S	33.0	23.7	···	2.1	124.3	···
E	.18	0.46	.08	−1.20	2.52	1
N	−.42	.66	.12	−2.76	1.16	1
28.46°N, 131.08°E, yd456(April 1), 17.75d						
U	17.7	70.0	···	−86.5	198.0	···
V	11.6	84.1	···	−185.8	314.0	···
S	83.1	73.6	···	6.4	371.2	···
E	−.19	.44	···	−1.25	.77	···
N	−.11	.32	···	−.75	.63	···

	m	sd	se	min	max	t_{dc}
6974 : 30.32°N, 129.62°E, yd202(July 21), 11d						
U	37.9	38.4	···	−34.8	138.2	···
V	10.5	40.5	···	−42.7	129.2	···
S	53.4	42.1	···	0	139.3	···
E	.04	.40	···	−.77	1.06	···
N	−.14	.09	···	−.31	.15	···
31.23°N, 133.45°E, yd213(August 1), 31d						
U	83.4	60.5	15.4	−54.5	217.8	2
V	9.6	60.4	13.3	−110.0	193.1	1.5
S	108.5	50.4	···	13.5	217.8	···
E	−.19	.57	.10	−2.02	2.44	1
N	−.28	.50	.14	−2.20	0.50	2
33.31°N, 157.93°E, yd244(September 1), 30d						
U	5.5	29.1	8.4	−27.6	131.7	2.5
V	−13.2	29.4	8.5	−96.8	35.2	2.5
S	33.1	28.4	···	.96	136.3	···
E	−.07	.44	.06	−1.59	.69	1
N	−.03	.33	.05	−1.13	.71	1
30.12°N, 159.20°E, yd274(October 1), 31d						
U	8.1	14.0	4.0	−25.4	39.0	2.5
V	4.2	12.1	3.4	−22.1	26.8	2.5
S	17.5	10.8	···	1.1	39.7	···
E	−.02	.34	.05	−1.26	1.09	1
N	−.16	.45	.06	−2.63	.76	1
31.13°N, 161.54°E, yd305(November 1), 30d						
U	9.3	8.8	2.5	−11.9	26.8	2.5
V	6.6	6.8	2.0	−10.8	22.1	2.5
S	14.6	6.3	···	1.8	27.0	···
E	.06	.33	.05	−.58	1.28	1
N	−.10	.25	.04	−.78	.98	1
6974 : 32.68°N, 164.13°E, yd335(December 1), 31d						
U	4.4	8.8	2.5	−15.0	22.7	2.5
V	−11.6	8.8	2.5	−29.4	6.7	2.5
S	15.8	7.7	···	1.1	31.8	···
E	.30	.40	.07	−.31	1.72	1
N	−.08	.43	.08	−1.25	2.12	1
29.87°N, 165.36°E, yd366(January 1), 15.75d						
U	4.2	6.6	···	−10.3	18.3	···
V	−4.3	3.5	···	−12.9	2.6	···
S	7.9	5.4	···	2.1	20.8	···
E	.44	.58	···	−.50	3.50	···
N	−.11	.37	···	−1.26	.75	···
6978 : 33.12°N, 125.47°E, yd197.5(July 16), 14.75d						
U	4.1	4.3	···	−4.3	14.2	···
V	4.0	3.3	···	−4.1	9.8	···
S	7.3	3.0	···	0	14.2	···
E	.10	.15	···	−.14	.55	···
N	.05	.17	···	−.29	.49	···
6983 : 32.96°N, 128.04°E, yd199.25(July 18), 13.5d						
U	10.7	10.2	···	−15.8	26.9	···
V	5.6	10.5	···	−19.6	27.3	···
S	17.4	7.3	···	0	36.0	···
E	.08	.18	···	−.27	.69	···
N	−.00	.19	···	−.78	.70	···
34.01°N, 129.55°E, yd226(August 14), 22d						
U	22.7	20.0	···	−10.6	67.6	···
V	9.4	16.1	···	−27.3	65.9	···
S	29.4	19.8	···	2.2	82.4	···
E	−.09	.36	···	−1.39	.72	···
N	.02	.48	···	−.70	2.14	···
6984 : 35.06°N, 125.47°E, yd194.5(July 13), 18.5d						
U	4.4	7.2	···	−14.6	21.3	···
V	8.2	8.8	···	−8.8	26.3	···
S	12.3	7.9	···	0	29.1	···
E	.06	.10	···	−.27	.34	···
N	.06	.14	···	−.29	.46	···
36.25°N, 126.26°E, yd213(August 1), 6.75d						
U	.4	5.7	···	−9.1	13.8	···
V	−5.3	9.4	···	−21.1	12.4	···
S	10.9	5.2	···	1.3	21.1	···
E	.05	.15	···	−0.07	.59	···
N	−.18	.25	···	−1.00	.10	···
6985 : 36.84°N, 123.15°E, yd190.25(July 9), 22.75d						
U	3.2	5.7	···	−16.0	15.7	···
V	2.5	6.5	···	−8.2	17.0	···
S	8.4	4.4	···	0	18.4	···
E	.03	.11	···	−.37	.35	···
N	.04	.20	···	−.44	.75	···
37.28°N, 123.88°E, yd213(August 1), 31d						
U	−.6	7.7	1.4	−18.9	18.9	1
V	6.4	7.1	1.3	−11.8	25.2	1
S	10.8	5.8	···	.7	25.5	···
E	.09	.43	.08	−1.34	3.31	1
N	−.27	.84	.15	−7.53	0.55	1
38.83°N, 123.67°E, yd244(September 1), 30d						
U	.8	5.8	1.0	−8.0	16.4	1
V	.6	5.3	1.0	−9.3	15.4	1
S	7.0	3.8	···	1.2	16.4	···
E	.01	.09	.02	−.33	.26	1
N	−.08	.15	.03	−.72	.19	1
6985 : 38.95°N, 123.90°E, yd274(October 1), 28.75d						
U	−2.0	3.5	···	−9.2	6.8	···
V	.5	3.9	···	−9.3	7.7	···
S	5.1	2.3	···	.5	12.2	···
E	.01	.08	···	−.33	.16	···
N	−.17	.28	···	−1.37	.33	···
6986 : 31.70°N, 123.03°E, 198.25yd(July 17), 14.75d						
U	1.7	9.5	···	−11.4	28.5	···
V	−.2	11.1	···	−17.5	27.3	···
S	12.9	6.8	···	0	29.2	···
E	−.02	.18	···	−.32	.71	···
N	.21	.23	···	−.19	.83	···
31.68°N, 123.26°E, yd213(August 1), 31d						
U	7.7	12.5	2.3	−27.3	35.1	1
V	11.2	10.8	2.7	−24.2	35.0	2
S	19.8	8.1	···	4.4	42.4	···
E	−.01	.80	.13	−2.96	6.08	1
N	−.21	.42	.08	−1.66	.79	1

	m	sd	se	min	max	t_{dc}
	34.36°N, 125.50°E, yd244(September 1), 30d					
U	14.9	15.2	3.4	−50.5	42.6	1.5
V	4.6	12.9	2.4	−35.0	27.3	1
S	23.4	9.6	···	3.7	50.5	···
E	−.08	.26	.05	−.92	.81	1
N	−.15	.23	.04	−.95	.61	1
	35.46°N, 129.71°E, yd274(October 1), 31d					
U	9.8	21.8	4.8	−30.4	66.6	1.5
V	5.9	19.8	3.6	−43.2	56.1	1.0
S	27.0	16.2	···	3.9	67.5	···
E	.05	.26	.04	−.59	.76	1
N	−.15	.30	.06	−1.80	.62	1
6986 :	36.88°N, 132.67°E, yd305(November 1), 30d					
U	2.1	16.7	3.7	−33.1	45.8	1.5
V	−3.3	21.1	4.7	−55.1	37.1	1.5
S	24.2	12.4	···	3.5	65.9	···
E	.22	.48	.09	−1.30	1.63	1
N	−.10	.29	.05	−1.05	.53	1
	36.08°N, 133.29°E, yd335(December1), 11.75d					
U	19.8	23.3	···	−12.5	70.5	···
V	−3.5	17.8	···	−45.8	34.5	···
S	28.0	21.7	···	0	71.0	···
E	.21	.30	···	−.26	1.10	···
N	−.03	.25	···	−.66	.64	···
6987 :	33.01°N, 123.01°E, yd196(July 15), 17d					
U	11.7	7.1	···	−3.9	28.5	···
V	−2.8	7.9	···	−20.6	15.4	···
S	14.4	7.0	···	0	32.4	···
E	.01	.14	···	−.29	.55	···
N	.10	.22	···	−.58	.65	···
	32.63°N, 124.87°E, yd213(August 1), 31d					
U	2.7	10.3	1.9	−25.3	37.3	1
V	−.3	13.6	2.4	−17.5	70.5	1
S	12.3	12.0	···	1.0	71.8	···
E	−.20	1.19	.21	−5.92	2.46	1
N	−.36	.82	.15	−4.54	1.60	1
	32.56°N, 125.60°E, yd244(September 1), 30d					
U	−2.4	10.6	1.9	−29.0	14.7	1
V	2.7	10.8	2.0	−30.4	29.3	1
S	12.7	9.0	···	1.3	35.3	···
E	−.03	.25	.04	−.82	1.32	1
N	−.30	.36	.06	−1.70	.30	1
6987 :	33.18°N, 124.94°E, yd274(October 1), 9.75d					
U	−9.3	19.4	···	−53.8	19.9	···
V	−20.9	12.6	···	−40.7	.5	···
S	30.1	12.1	···	6.4	59.2	···
E	.10	.34	···	−.35	1.16	···
N	−.36	.30	···	−1.35	0.04	···
6988 :	33.05°N, 125.52°E, yd197(July 16), 16d					
U	10.3	8.4	···	−6.5	24.4	···
V	6.1	4.1	···	−4.1	14.4	···
S	13.8	6.1	···	0	24.7	···
E	.09	.15	···	−.15	.56	···
N	.06	.16	···	−.28	.46	···
	33.82°N, 127.08°E, yd213(August 1), 31d					
U	18.9	16.9	3.7	−26.6	64.9	1.5
V	11.0	15.1	3.8	−19.6	53.1	2
S	28.4	13.6	···	2.4	83.2	···
E	.00	.39	.07	−1.76	1.39	1
N	.08	.46	.08	−.88	2.47	1
	36.49°N, 132.65°E, yd244(September 1), 30d					
U	18.3	16.2	3.6	−18.2	50.3	1.5
V	10.6	28.4	7.3	−75.7	64.9	2
S	36.2	14.2	···	8.1	75.7	···
E	.07	.46	.09	−.55	2.45	1
N	−.05	.38	.07	−.86	3.14	1
6988 :	39.00°N, 138.02°E, yd274(October 1), 31d					
U	2.3	8.3	1.5	−19.0	24.7	1
V	8.7	10.7	1.9	−12.9	35.0	1
S	13.4	9.2	···	.5	35.0	···
E	.15	.43	.08	−1.20	1.08	1
N	−.14	.51	.09	−3.08	1.01	1
	41.09°N, 138.77°E, yd305(November 1), 30d					
U	−.1	7.5	1.4	−14.0	19.9	1
V	8.1	9.8	1.8	−13.9	35.5	1
S	12.9	7.1	···	1.6	35.5	···
E	.76	.75	.13	−.29	3.64	1
N	−.25	.64	.11	−2.48	1.07	1
	42.99°N, 138.71°E, yd335(December 1), 31d					
U	2.1	9.9	1.8	−14.2	38.1	1
V	5.4	7.4	1.3	−10.3	20.6	1
S	11.6	7.3	···	1.2	41.0	···
E	.59	.70	.13	−.54	3.46	1
N	−.54	.78	.14	−5.17	.99	1
	44.31°N, 139.41°E, yd366(January 1), 19.25d					
U	1.5	6.6	···	−15.2	18.4	···
V	−2.5	7.1	···	−19.6	19.0	···
S	8.7	5.0	···	1.5	19.7	···
E	.71	.80	···	−.75	2.67	···
N	−.59	.70	···	−2.56	1.11	···

6983 went ashore in the lee of Iki Island in the eastern channel of the Korea Strait at 33.7° N, 129.8° E about 18 days after launch, was redeployed about 10 days later nearby to the north at 34° N, 129.6° E, and went ashore on Honshu near 35.6° N, 134.3° E about 22 days after re-launch. Drifters 6986 and 6988 returned low-pass data for 148 and 188 days, respectively. The tenth drifter (6974) was deployed in the core of the Kuroshio with a drogue at 40 m and returned low-pass data for 180 days.

To facilitate comparison over common time periods, statistics of drifter velocity and wind stress computed by calendar month are given in

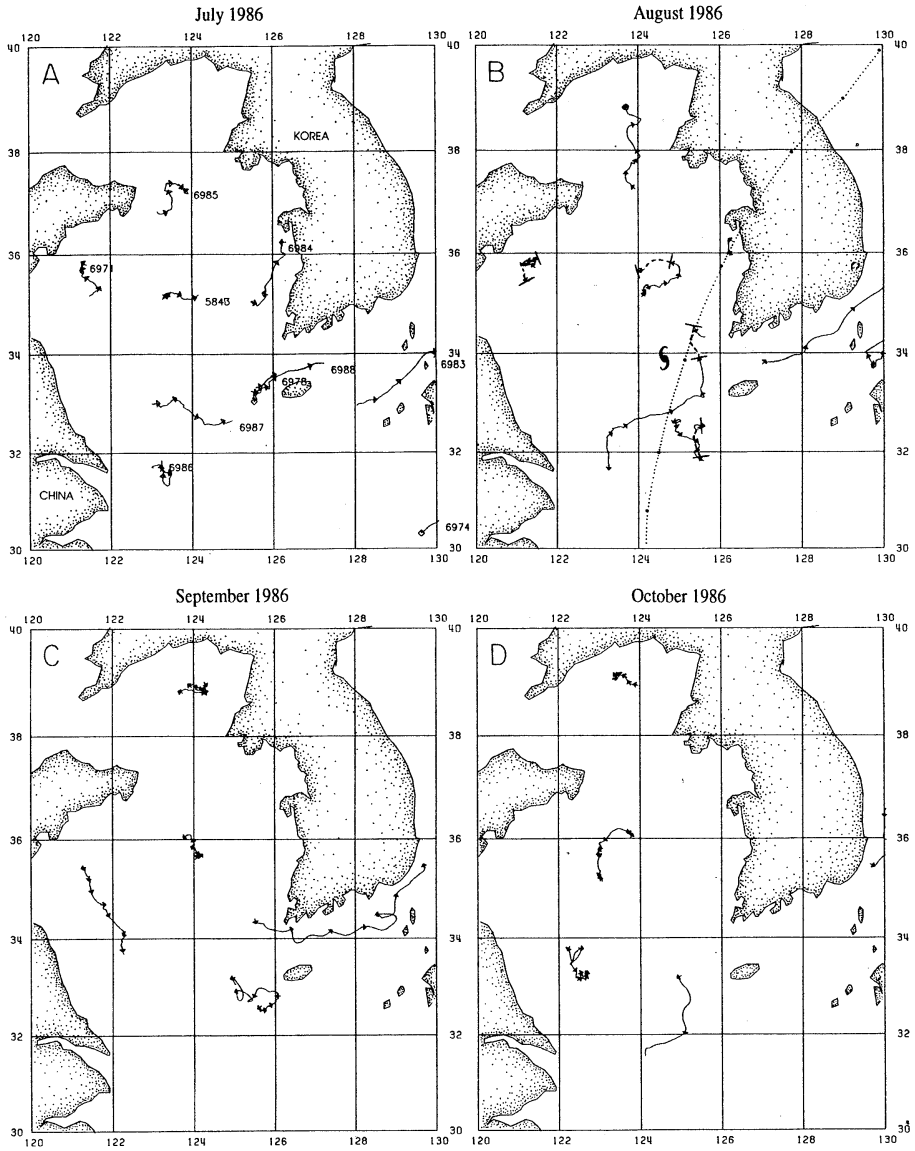

Fig. 5. Drifter trajectories in Yellow and East China Sea for July (A), August (B), September (C), and October (D). Drifter number is printed at the end of each trajectory in panel A. Arrows are placed along each trajectory every five days from first day in each month. The path of typhoon Vera during August 27–28 (yd 239–240) is shown in panel B; the location of the eye of Vera at 00 GMT August 28 (yd 240) is indicated by the typhoon symbol. The drifter trajectories during the three-day period yd 239–241 surrounding the passage of typhoon Vera are indicated by the dashed paths in panel B. (See Appendix for maps of the wind field and individual drifter trajectories during Vera.)

Table 3. When drifter data is available for a complete month, crude estimates of decorrelation time scales for east and north velocity and wind stress components were made from auto-correlation functions and standard errors computed following KUNDU and ALLEN (1976). Winds over the East China and Yellow Seas during late summer 1986 were generally light and variable in direction with mean wind speeds of about 4 ± 2 m/s with one major

exception. On yd 237–238 (August 25–26), typhoon Vera swept west over the Ryukyu Islands into the East China Sea (DEANGELIS, 1987). Vera then started to weaken and curved north and moved across the East China Sea at an average speed of 6 m/s before crossing Korea on yd 240 (August 28) as a tropical storm and dying in the Japan Sea (see Appendix for maps of the surface wind field). Vera was a major typhoon, maintaining typhoon intensity from yd 231 through yd 240 and reaching super typhoon intensity on yd 235 with peak wind speed 67 m/s. The ECMWF/WCRP Level III-A surface analysis reported that Vera produced maximum 10 m wind speeds of about 24 m/s in the East China and Yellow Seas on yd 239. Beginning about yd 280 (October 6), a large-scale "fall transition" occurred in the wind field over the Yellow Sea with the onset of winter storms and an increase in the mean southeastward winds.

1. Yellow Sea

The trajectories of the five drifters deployed in the Yellow Sea are shown by month for July –October in Fig. 5. Drifter 6984 was launched in Yellow Sea surface water (YSsw) (groups 9 and 10 in Fig. 4 of KIM *et al.*, 1991) with its drogue in the base of the surface layer (water depth 78 m) just off the southwest Korean coast and generally moved north and eastward toward the Korean coast in July with a mean (vector) velocity and (scalar) speed of about 9 and 12 cm/s, respectively. In early August, 6984 became stuck near 36° N, 126.3° E. Drifter 6985 was launched in YSsw with its drogue in the upper pycnocline (water depth 30 m) just east of the Shangdong peninsula and moved slowly toward the northeast at a mean velocity of 4 cm/s in July, and then moved more quickly northward into the Gulf of Bohai with a mean velocity of 6 cm/s in August. Drifter 6985 then slowed down and moved east then west during September and toward the northwest in October. The mean and maximum speeds of 6985 increased from about 8 and 15–18 cm/s in July, to 11 and 20–25 in August, and then decreased to 5–7 and 10–15 cm/s, respectively, in September and October.

Both 6971 and 6987 were launched in YSsw off the central Chinese coast, 6971 with its drogue at the base of the surface layer (water depth 29 m) and 6987 with its drogue in the upper pycnocline (water depth 35 m). Drifter 6971 first moved northward with a mean velocity of 5 cm/s in July, then began to move slowly southward in August with a mean velocity of 2 cm/s. In September, 6971 moved more quickly toward the south-southeast roughly parallel to the Chinese coast and local topography with a mean velocity of 8 cm/s. Drifter 6971 then slowed and moved more southeastward with a mean velocity of 3 cm/s in October, ending close to the launch position of 6987. Drifter 6987 moved quickly eastward following deployment in July with a mean velocity and speed of 12 and 14 cm/s, then made a large loop to the south in August with a mean speed of 12 cm/s, resulting in a mean eastward velocity of only 3 cm/s. Drifter 6987 then turned and meandered northwestward with a mean velocity of 4 cm/s in September before turning and moving quickly toward the south-southwest with a mean velocity of 23 cm/s in early October.

Drifter 5843 was launched in YSsw in the central Yellow Sea with its drogue within the surface layer (water depth 73 m) and moved eastward in July with a mean velocity of 5 cm/s and continued to move eastward until mid-August when 5843 turned to the north and moved westward, resulting in a monthly mean velocity and speed for August of 2 and 10 cm/s, respectively. Drifter 5843 then moved slowly toward the northwest in September with a mean velocity and speed of 2 and 6 cm/s, before turning toward the south in October with a mean velocity and speed of 4 and 8 cm/s.

While vector correlations computed between drifter velocity and wind stress over one month and longer periods suggest that only 5843 and to a lesser extent, 6971 exhibited clear evidence of partial wind-driving during the summer, four of the five drifters deployed in the Yellow Sea (6984 was not working then) showed short but clear responses to typhoon Vera (see Appendix for maps of the individual drifter trajectories during Vera). The character of the response varied with drifter. Drifter 5843 in the center of the Yellow Sea moved rapidly to the right of the wind stress (angle between wind stress and current vectors varying from 50° to 110° as the

wind stress veered counterclockwise) with a peak speed of 48 cm/s occurring on yd 240.25 about six hours before a peak wind stress of 10.8 dyne/cm^2. Both drifter speed and wind stress decreased rapidly on yd 241. Drifter 6987, located near the main channel into the Yellow Sea west of Cheju, also initially moved to the right of the wind stress (angle varying from 100° to 40°) for more than two days while the wind stress with a maximum magnitude of 6.0 dyne/cm^2 veered slightly clockwise. Current speed during this period of active wind forcing increased to about 28 cm/s on yd 238.75, however, as the wind stress then quickly decreased over the next several days, 6987 surged northward (to the north and northeast) for 1.5 days, reaching a peak speed of 72 cm/s on yd 239.5. After the drifter speed had decreased to a minimum of 12 cm/s on yd 240.5, 6987 veered clockwise towards the north with a speed of about 20 cm/s. In the western Yellow Sea, 6971 moved toward the southwest and south to the right of the wind stress (angle varying from 80° to 30° as the wind veered anti-clockwise) with a peak speed of 23 cm/s occurring on yd 239.75 about six hours after a peak wind stress of 5 dyne/cm^2. The drifter speed decreased to about 5 cm/s about 12 hours after the wind stress had rapidly decreased in magnitude. Drifter 6985 exhibited a weak response in the Gulf of Bohai despite a pronounced wind stress event with a maximum stress of 8.2 dyne/cm^2 on yd 240.5. Initially moving northwestward at a mean speed of 15 c m/s, 6985 made a clockwise turning loop over several days before moving northwestward again. The drifter velocity, directed from 30 to 70° to the right of the wind stress during the wind stress event, increased from about 4 to 13 cm/s in magnitude.

2. East China Sea

The initial trajectories of the four drifters deployed in the East China Sea are also shown by month in Figure 5. Drifter 6986 was launched with its drogue just in the base of surface Changjiang dilute water (a mixture of group 9 and 11, water depth 34 m) just northeast of the mouth of the Changjiang, and moved in a small anticyclonic loop in July with a mean speed of 13 cm/s. Drifter 6986 then accelerated and

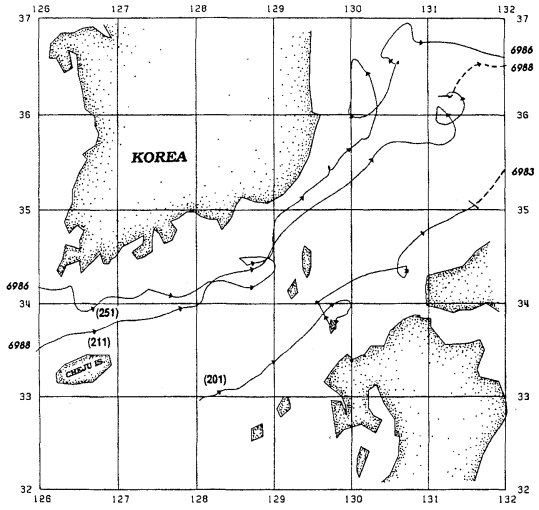

Fig. 6. Drifter trajectories in Korea Strait. Drifter number is printed at beginning and end of each trajectory. Arrows are placed along each trajectory every five days from yd 1, and the time in year-day of the first arrow on each trajectory is shown in parenthesis. The drifter trajectory during the three-day period yd 239–241 bracketing the passage of typhoon Vera is indicated by the dashed path. (See Appendix for expanded maps of 6983 and 6988 trajectories during Vera.)

moved quickly to the north and east in August in the direction of the historical mean surface plume of the Changjiang (BEARDSLEY *et al.*, 1985) with a mean velocity and speed of 14 and 20 cm/s. On yd 242, 6986 abruptly turned south and moved quickly through the western channel of the Korea Strait in September with a mean velocity and speed of 16 and 23 cm/s (with a peak speed of 51 cm/s directed westward in the small cyclonic loop near 34.4° N, 128.6° E) and into the Japan Sea in late September (Fig.6). Drifter 6988 and 6978 were deployed as a pair with drogues centered at 10 and 40 m to examine vertical shear in the main channel (water depth 91 m) west of Cheju Island. At launch, the drogue of 6988 was in the base of the YSsw while the drogue of 6978 was in a thick layer of cold saline water representing a mixture of Yellow Sea Cold Water and Kuroshio water (group 3). Both 6988 and 6978 entered the western channel of the Korea Strait and moved northeastward in July until yd 214 when 6978 was recovered by a

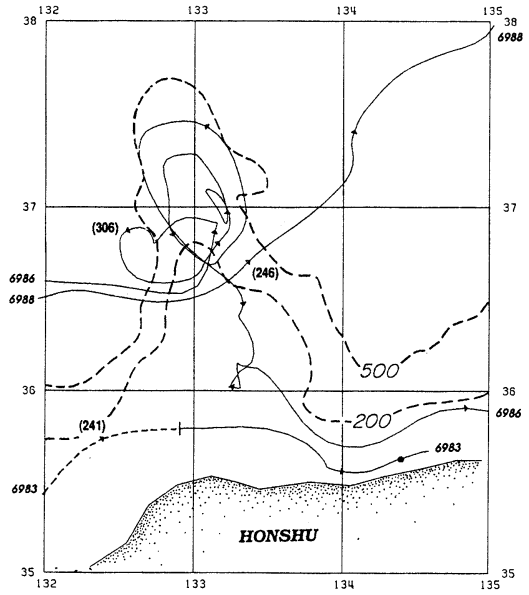

Fig. 7. Drifter trajectories in Japan Sea. Drifter number is printed at beginning and end of each trajectory. Arrows are placed along each trajectory every five days from yd 1, and the time in year-day of the first or second arrow on each trajectory is shown in parenthesis. The trajectory of 6983 during the period yd 240 -241 corresponding to the passage of Vera is indicated by the dashed path. The 200- and 500-m isobaths are shown as long dashed curves.

fisherman. During the 15-day period when both drifters were moving freely, the 10 and 40 m drifter velocities tracked one another about half the time, with a mean velocity and speed at 40 m (6 and 7 cm/s) about half that at 10 m (12 and 14 cm/s). Drifter 6988 then accelerated in August and moved through the Korea Strait with a mean velocity and speed of 22 and 28 cm/s. Drifter 6988 reached a peak speed of 83 cm/s in the narrows between Korea and Tsushima Island before slowing somewhat as it entered the Japan Sea. Drifter 6983 was launched into a surface layer of Kuroshio water mixed with shelf water (group 8)(water depth 166 m) and moved quickly through the eastern channel of the Korea Strait in July with a mean velocity and maximum speed of 12 and 28 cm/s until it went ashore in the lee of Iki Island. After being redeployed back in the center of the eastern channel, 6983 continued to move quickly northeastward through the strait reaching a peak speed of 53 cm/s on yd 227 before slowly entering the Japan Sea.

Drifter 6971 moved slowly toward the northeast in the Yellow Sea with a mean velocity and speed of 2 and 8 cm/s in November (see Figs. 4 and 5), then turned toward the southeast and moved into the East China Sea in December with a mean velocity and speed of 8 and 14 cm/s. Drifter 6971 continued to move toward the south and southeast across the East China Sea with monthly mean velocities and speeds of 5–7 and 12–16 cm/s in January and February 1987 until about yd 83 (1987, Fig. 8) when 6971 began to accelerate sharply and entered the Kuroshio near 29.3° N, 127.7° E. 6971 then remained in the Kuroshio until it stopped operating on yd 109 (1987). While in the Kuroshio, 6971 had a mean and maximum speed of 76±64 and 371 cm/s.

Vector correlations computed between drifter velocity and wind stress over one month and longer periods suggest that of the three drifters which remained in the East China Sea for at least one month, only 6971 exhibited clear evidence of partial wind-driving during the winter (December–January). Drifter 6986, located off the southwest tip of Korea (Fig.5), gave a complex response to typhoon Vera (see Appendix). The eye of the typhoon passed near 6986 so that the wind stress on yd 239.5 had a peak of 3.4 dyne/cm^2 toward the southwest and then veered clockwise to a peak of 6.0 dyne/cm^2 toward the east on yd 240.5. On yd 239, 6986 accelerated to the right of the wind stress (angle varying from 120° to 0°) to a peak speed of 42 cm/s on yd 239.75, then decreased in speed rapidly on yd 240 (moving against and to the left of the wind stress). Then as the wind stress decreased from its peak on yd 240.5, 6986 accelerated rapidly to the north to a peak speed of 36 cm/s on yd 241.75.

3. Japan Sea

Three drifters entered the Japan Sea and followed quite different trajectories (Fig. 4). Drifter 6983 left the eastern channel of the Korea Strait about yd 236 and moved roughly parallel to the coast of Honshu with a mean velocity and speed of 41 and 45 cm/s (peak speed 82 cm/s) until about yd 244 when it moved

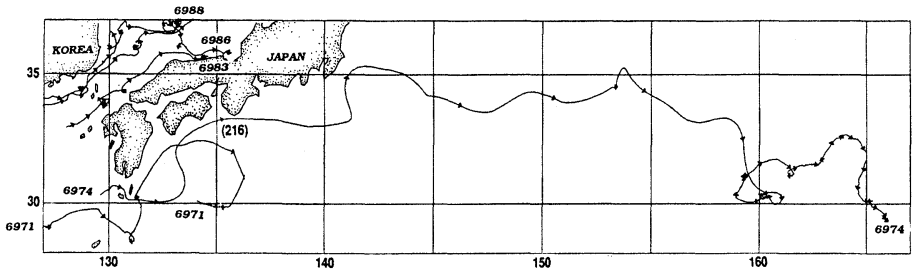

Fig. 8. Drifter trajectories in the Kuroshio and Kuroshio Extension. Drifter number is printed at beginning and end of each trajectory. Arrows are placed along each trajectory every five days from yd 1. The time in year-day of one arrow for 6974 is shown in parenthesis.

quickly close to the coast and became stuck near 35.6° N, 134.3° E four days later. Drifter 6988 left the western channel about yd 230 and began to move quickly toward the northeast, making a small cyclonic loop near 36° N, 131° E before turning east and then northeast and making a larg meander between 38 and 40° N (Fig. 8). During this 35-day period (yd 251–286), 6988 had a mean speed of 32 cm/s, and reached peak speeds of 67 and 76 cm/s in the first northward and southward legs of the large meander. After about yd 286, 6988 slowed on average and drifted generally northward with mean velocities and speeds of 6–9 and 12–13 cm/s. Drifter 6986 left the western channel about yd 276 and moved northeastward, making one cyclonic loop near 36° N, 130° E. On yd 296, 6986 began to accelerate toward the east and made three large and one small cyclonic loops centered near 37° N, 133° E during yd 299–330 (Fig.7). During this period, the mean and maximum speed of 6986 were 26±14 and 68 cm/s, and the average radius of the three large loops was 35±14 km. Then 6986 slowed, drifted southeast and then accelerated and moved quickly along the coast on Honshu with a peak speed of 71 cm/s near 35.9° N, 135° E before slowing and moving onshore and becoming stuck near 35.8° N, 135.6° E on yd 346. The mean drifter eddy kinetic energy in the Japan Sea west of 138° E was 415±91 cm^2/s^2; only 6988 moved east of 138° E where its eddy kinetic energy was only 81±9 cm^2/s^2.

The two drifters in the Japan Sea during tropical storm Vera both exhibited a clear response (see Appendix) but otherwise showed no consistent response to wind forcing based on vector correlations between drifter velocity and wind stress computed over monthly intervals. Drifter 6983 accelerated rapidly toward the northeast to the right of the wind stress (angle varying from about 80° to 30°), reaching a peak speed of 82 cm/s on yd 240.5 even though the wind stress maximum was only 2.4 dyne/cm^2 on yd 240. Drifter 6988 also accelerated rapidly to the northeast to the right of the wind stress (angle varying from about 75° to 30°), reaching a peak speed of 51 cm/s on yd 240.5 about 12 hours after the wind stress reached its maximum of 2.6 dyne/cm^2. For both drifters, the increase in speed over one day from pre-storm speeds was roughly 50 cm/s. Since this acceleration does not seem locally wind-driven, we speculate that the moving wind stress pattern of typhoon Vera forced a strong eastward current pulse through the Korea Strait during yd 240–242.

4. Kuroshio

Drifter 6974 was deployed in Kuroshio surface water (group 7, water depth 1060 m) and moved northeastward at speeds of 20–30 cm/s for several days in July before turning southeastward in the Ohsumi branch of the Kuroshio and continuing eastward (Fig. 8). Drifter 6974 began to accelerate rapidly after passing 130.8° E and joined the core of the Kuroshio by 132° E. Drifter 6974 then moved quickly eastward in the Kuroshio and Kuroshio Extension until about yd 250 when 6974 passed 160° E and slowed dramatically, moving southward on average in the Kuroshio recirculation. Between yd 211–250 when 6974 moved from 132° E to 160° E, 6974 had a mean east velocity and mean speed of 76 and 105 cm/s, reaching a peak speed of 218 cm/s on

yd 217 near 33.3° N, 137° E. The initial path of 6974 in the Kuroshio Extension between 140–152° E illustrates the two quasi-stationary meanders described by QIU *et al.* (1991). While in the Kuroshio and Kuroshio Extension, 6974 had a mean and eddy kinetic energy of 0.29 and 0.38 m^2/s^2; after leaving the Kuroshio Extension at 160° E, its mean and eddy kinetic energy dropped to 13 and 148 cm^2/s^2. This variation of drifter eddy kinetic energy with longitude is generally consistent with the analysis of altimeter data by QIU *et al.* (1991). Neither 6974 nor 6971 after entering the Kuroshio appeared to be wind-driven.

4. Discussion

The trajectories of the five drifters deployed in the Yellow Sea support the historical concept of a large-scale cyclonic gyre in the surface waters of the Yellow Sea during late summer. The center of the gyre was located in 1986 near 35.6° N, 123.8° E based on 5843, and the mean velocities along the Korean and Chinese coasts varied from 2 to 6 cm/s. Within the Yellow Sea, the distribution of eddy kinetic energy was relatively uniform spatially at 30–50 cm^2/s^2 except with an increase to about 80 cm^2/s^2 near the Korean coast and higher near the southeast entrance of the Yellow Sea.

The trajectories of drifters deployed in the East China Sea contradict the historical concept of the Tsushima Current as a simple branch of the Kuroshio (as shown in Fig. 1). Instead, the drifter trajectories clearly demonstrate eastward flow into the Korea Strait through both western and eastern channels in late summer and suggest that shelf water (perhaps including some dilute Changjiang discharge) may be drawn directly into the Tsushima Current through the Cheju Strait so that the Tsushima Current may represent a mixture of varying amounts of Kuroshio and shelf water. This idea is supported by direct current measurements made in Cheju Strait by CHANG (1984) which indicate eastward flow with mean speeds of 5–10 cm/s. CHO (1988) argues that this eastward flow through Cheju Strait may contribute as much as one-third of the total Tsushima Current. Although we cannot rule out the possibility that subsurface currents in the western channel of the Korea Strait may originate from the Kuroshio, it is unlikely that the surface current in the western channel comes from the Kuroshio exclusively as indicated by UDA (1934) and NITANI (1972). These drifter trajectories also question the existence of the Yellow Sea Warm Current as a coherent and continuous current in summer, since such a current would have to cross the near-surface currents flowing eastward into Cheju Strait. In winter, the continued drift of 6987 and 6971 toward the south and southeast along the Chinese coast supports the idea of a weak flow of shelf water across the shelf break into the Kuroshio in the East China Sea.

The trajectories of drifters entering the Japan Sea do not support the simple model of branching of the Tsushima Current originally introduced by SUDA and HIDAKA (1932) and UDA (1934). They proposed that the Tsushima Current splits into several branches as it leaves the Korea Strait, and UDA (1934) named the branch along Honshu the Tsushima Warm Current (TWC) and the branch along the east coast of Korea the East Korean Warm Current (EKWC). The concept of branching of the Tsushima Current has been widely accepted, motivating YOON (1982a,b,c) and KAWABE (1982) to simulate it numerically in a model of the Japan Sea with inflow and outflow. In particular, KAWABE (1982) concluded that three branches develop; two branches corresponding to the EKWC and TWC are permanent due to the planetary beta-effect and stratification on the continental shelf, and a third branch located between the two permanent branches is transient, occurring only when the inflow through the Korea Strait increases in summer as shown by MIYAZAKI (1952) and YI (1966).

However, KIM and CHUNG (1984) conducted an intensive hydrographic survey in an area of the Korea Strait where the incipient stage of branching was anticipated, and found that branching did not occur in September 1981. Later KIM and LEGECKIS (1986) analyzed satellite infrared and additional hydrographic data for the period 1981–83 and confirmed that the EKWC did not develop at all in 1981. Instead, abnormally cold water prevailed in the southwestern part of the Japan Sea in 1981, and the

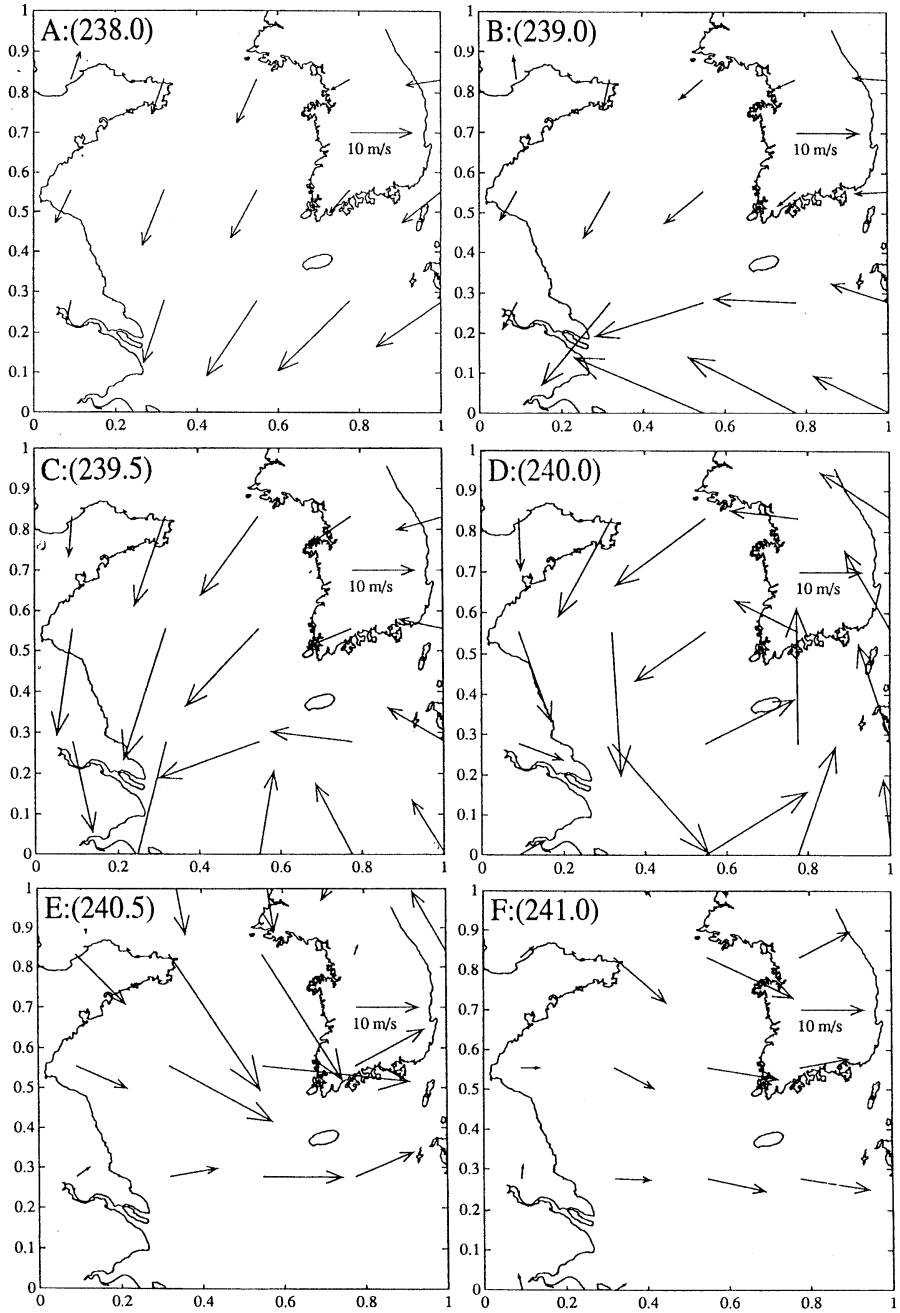

Fig. A1. ECMWF/WCRP-derived surface winds over the Yellow and East China Seas during the passage of typhoon Vera. Panels A-F correspond to a sequence of wind maps starting at 00 GMT August 26 (yd 238.0) through 00 GMT August 29 (yd 241.0). The time of each panel in year-day is given in parenthesis in the upper left of each panel. The horizontal scale in each panel is 1000 km.

entire Tsushima Current flowed along Honshu with no branching. In 1982 and 1983, the EKWC formed in April but was much weaker in 1983.

In summer 1986, we may consider 6983 to be in the TWC but neither drifter exiting the western channel (6986 and 6988) followed the proposed

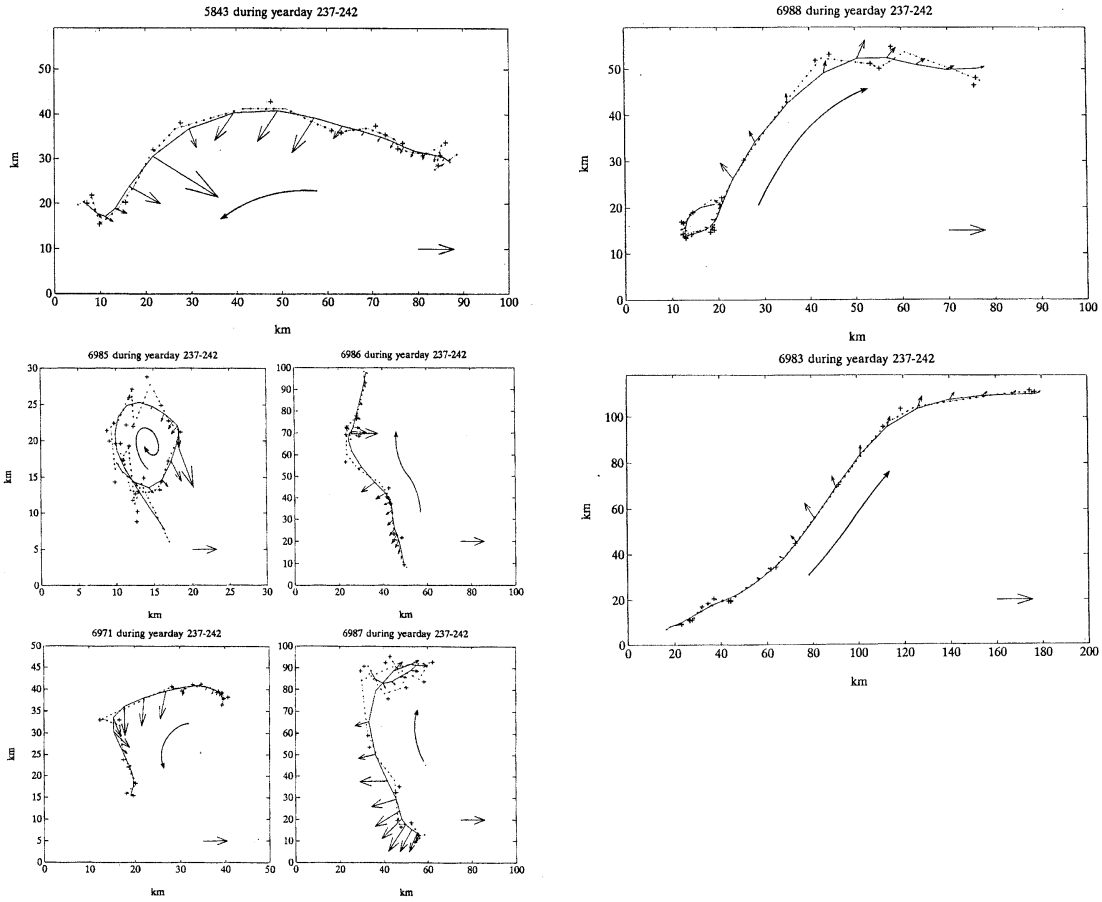

Fig. A2. Drifter trajectories during the five-day period yd 237–242 bracketing the passage of typhoon Vera. Each panel shows the raw drifter positions (crosses), the six-hour interpolated positions (dotted line), and the low-pass filtered trajectory (solid line). The wind stress is superimposed on the low-pass drifter position every six hours. The wind stress vector in the lower right of each panel corresponds to 5 dynes/cm^2.

path of the EKWC. These direct current measurements, plus the recent examination of sea surface temperature variability using synoptic satellite infrared imagery by KIM and LEGECKIS (1986), demonstrate that the behavior of the Tsushima Current in the Japan Sea is quite complex both spatially and temporally.

Acknowledgments

This work was supported by the U. S. National Science Foundation (NSF) and the Korean Science and Engineering Foundation (KOSEF). The drifter observations were made under NSF grants OCE 85–01366 and OCE 86 16937 and analysis was covered by NSF grants OCE 87 – 13988 and OCE 91 – 01034 for LIMEBURNER, BEARDSLEY, and CANDELA and a grant from KOSEF for KIM. J. CHURCHILL, T. ICHIYE, H. ICHIKAWA, B. QIU and P. RICHARDSON provided helpful input into this study and A. -M. MICHAEL, T. McKEE, and T. TURNER helped with the final preparation of the manuscript, tables and figures. We also acknowledge the support of the European Centre for Medium-Range Weather Forecasting (ECMWF) in providing the 1986–87 surface wind data from the ECMWF/WCRP Level III-A global atmospheric data archive used in this analysis. This is Woods Hole Oceanographic Institution Contribution No. 7908.

Appendix

Typhoon Vera passed across the East China Sea on August 28, 1986 (yd 240). While the primary focus of this paper is on the long-term behavior of each drifter, a brief description of the response of individual drifters to typhoon Vera is given in the text. In this appendix we complete this description by presenting maps of the surface wind field during the passage of Vera (Fig. A1) and maps of the individual drifter trajectories during the five day period August 25 30 (yd 237–242) bracketing the passage of Vera (Fig.A2). The wind field maps show the 10 m gridded winds produced by the ECMWF/WCRP Level III-A surface analysis. The drifter trajectory maps show the raw dirfter positions (which are irregularly spaced in time), the six-hour interpolated positions and the six-hour low-pass filtered positions, in part to illustrate the density of raw position data and how well the interpolation and filtering procedure works to create a smoothed drifter trajectory without tidal and inertial variability. A close look at the raw position data from drifter 6985 in the Gulf of Bohai indicates a significant north-south semidiurnal excursion which is eliminated in the low-pass drifter path. In general, however, the temporal spacing of the raw drifter position data were inadequate to clearly identify significant tidal or inertial motion. Superimposed on the low-pass drifter trajectories is the surface wind stress, computed from the 10 m winds interpolated in space and time to the drifter position from the ECMWF/WCRP Level III-A surface analysis wind field. A wind stress of 5 dyne/cm^2 directed eastward is shown in each map to provide a common scale for the drifter wind stress time series. The speed of a drifter is indicated by the relative length of the trajectory or spacing between the six hourly wind stress vectors.

References

BEARDSLEY, R. C., R. LIMEBURNER, H. YU, and G. A. CANNON (1985): Discharge of the Changjiang (Yangtze River) into the East China Sea. Continental Shelf Research, **4**, 57–76.

CANDELA, J., R. C. BEARDSLEY, and R. LIMEBURNER (1992): Separation of tidal and subtidal currents in ship-mounted acoustic Doppler current profiler (ADCP) observations. J. Geophy. Res., **97**, 769–788.

CHANG, K. I. (1984): The structure of currents and flow dynamics of the Jeju Strait. M. S. Thesis, Seoul National University, 62 pp.

CHEN, C., R. C. BEARDSLEY, and R. LIMEBURNER (1992): The structure of the Kuroshio Southwest of Kyushu: velocity, transport, and potential vorticity fields. Deep-Sea Res., **39**, 245–268.

CHEN, C., R. C. BEARDSLEY, R. LIMEBURNER, and K. KIM (1993): Comparison of winter and summer hydrographic observations in the Kuroshio and adjacent East China Sea during 1986. Continental Shelf Research (in press).

CHO, Y. K. (1988): A study on the bottom water and transport in the South Sea, Korea. M.S. Thesis, Seoul National University, 55 pp.

DAHLEN, J. M. (1985): The Low-Cost Drifter (LCD) design description and early test results. The Charles Stark Draper Laboratory Report P-2024, Cambridge, MA.

DEANGELIS, R., (Ed.) (1987): Mriners Weather Log (Winter 1987), **31**, 54.

FLAGG, C. N., J. A. VERMERSCH and R. C. BEARDSLEY (1976): 1974 MIT New England Shelf Dynamics Experiment (March, 1974). Data Report, Part II : The Moored Array. MIT Report 76-1.

HSUEH, Y. (1988): Recent current observations in the Eastern Yellow Sea. J. Geophy. Res., **93**, 6875–6884.

HSUEH, Y. and I. PANG (1989): Coastal trapped long waves in the Yellow Sea. J. Phys. Oceanogr., **19**, 612–625.

KAWABE, M. (1982): Branching of the Tsushima Current in the Japan Sea, Part II. Numerical Experiment. J. Oceanogr. Soc. Japan, **38**, 183–192.

KIM, K. and J. Y. CHUNG (1984): On the salinity minimum and dissolved oxygen-maximum layer in the East Sea (Sea of Japan). *In*: Ocean Hydrodynamics of the Japan and East China Seas, (ed. T. ICHIYE), Elsevier Science Publishers, Amsterdam, 55–65.

KIM, K. and R. LEGECKIS (1986): Branching of the Tsushima Current in 1981–83. Progress in Oceanography, **17**, 265–276.

KIM, K., K.-R. KIM, T. S. RHEE, H. K. RHO, R. LIMEBURNER and R. C. BEARDSLEY (1991): Identification of water masses in the Yellow Sea and the East China Sea by cluster analysis. *In*: Oceanography of Asian Marginal Seas, (ed. K. TAKANO), Elsevier Oceanography

Series, **54**, 253–267.

KOLPACK, R. L. (1982): Temperature and salinity changes in the Tsushima Current. La Mer, **20**, 199–209.

KUNDU, P. K. and J. S. ALLEN (1976): Some three-dimensional characteristics of low-frequency current fluctuations near the Oregon coast. J. Phys. Oceanogr., **6**, 181–199.

LARGE, W. S. and S. POND (1981): Open ocean momentum flux measurements in moderate to strong winds. J. Phys. Oceanogr., **11**, 324–336.

MIYAZAKI, M. (1952): The heat budget in the Japan Sea. Bulletin Hokkaido Registry of Fisheries Research Lab., **4**, 1–45 (in Japanese).

MORIYASU, S. (1972): The Tsushima Current. *In*: Kuroshio (eds. H. STOMMEL and K. YOSHIDA), University of Washington Press, pp. 353–369.

NIILER, P. P., R. E. DAVIS and H. J. WHITE (1987): Water-following characteristics of a mixed layer drifter. Deep-Sea Res., **34**, 1867–1881.

NITANI, H. (1972): Beginning of the Kuroshio. *In*: Kuroshio (eds. H. STOMMEL and K. YOSHIDA), University of Washington Press, pp. 129–164.

QIU, B., K. KELLY and T. JOYCE (1991): Mean flow and variability in the Kuroshio Extension from Geosat altimetry data. J. of Geophys. Res., **96**, 18491–18507.

SUDA, K. and K. HIDAKA (1932): The result of the oceanographical observations on board R. M. S. Syunpu Maru in the southern part of the Japan Sea in the Summer of 1929, Part I. J. Oceanogr. Imperial Marine Observations, **3**, 291–375. (in Japanese).

SVERDRUP, H. U., M. W. JOHNSON and R. H. FLEMING (1942): The Oceans. Prentice-Hall, Englewood Cliffs, NJ, 1087 pp.

UDA, M. (1934): The results of simultaneous oceanographical investigations in the Japan Sea and its adjacent waters in May and June, 1932. J. Imperial Fishery Experimental Station, **5**, 57–190 (in Japanese).

YI, S. U. (1966): Seasonal and secular variations of the water volume transport across the Korea Strait. J. Oceanolog. Soc. Korea, **1**, 7–13.

YOON, J. H. (1982a): Numerical experiment on the circulation in the Japan Sea, Part I: Formation of the East Korean Warm Current. J. Oceanogr. Soc. Japan, **38**, 43–51.

YOON, J. H. (1982b): Numerical experiment on the circulation in the Japan Sea, Part II: Influence of seasonal variations in atmospheric conditions on the Tsushima Current. J. Oceanogr. Soc. Japan, **38**, 81–94.

YOON, J. H. (1982c): Numerical experiment on the circulation in the Japan Sea, Part III: Formation of the nearshore branch of the Tsushima Current. J. Oceanogr. Soc. Japan, **38**, 119–124.

スライド式高速曳航体 JAMSTEC TSK方式

Underwater Sliding Vehicle System (USV)

○本システムは海洋科学技術センター殿の御指導によって開発されました。
○USVは小型かつ軽量で極めて優れた水中運動性能を有しております。
○電磁誘導伝送方式を使うことにより船上からのUSVの昇降運動制御及びリアルタイム信号モニターリングを行うことができます。
○取得データはFD及びハードディスクに記録し２次電算機処理に供します。

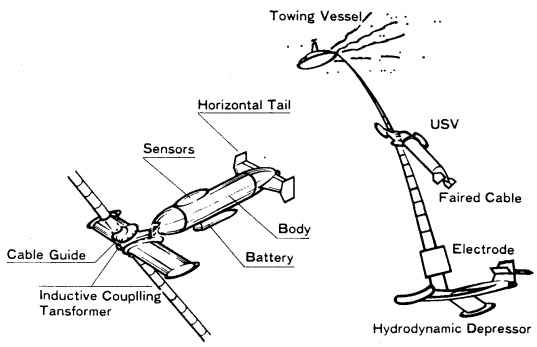

The USV system

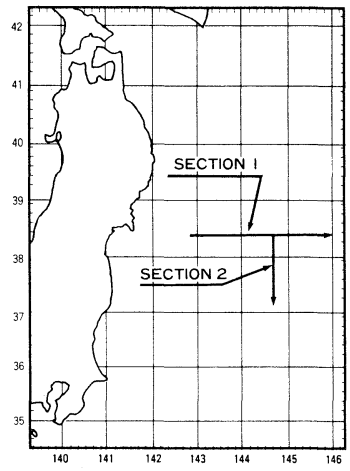

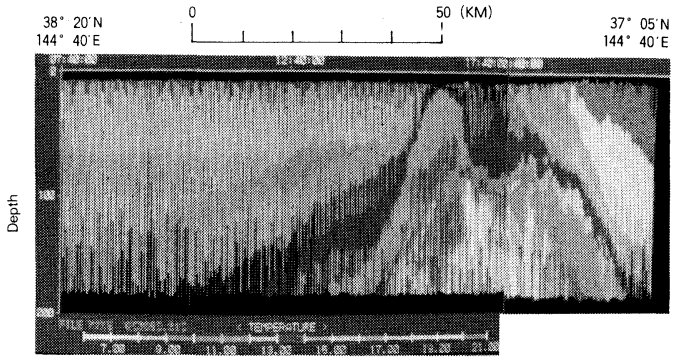

T.Sスライド式高速曳航体によって得られた三陸沖の水温鉛直分布のカラー画像。
（海洋科学技術センター殿から資料を御提供頂きました。）

SPECIFICATIONS

Towing Speed	:0～8knots	
Operation Dapth	:Max.400m	
Tow Cable	:8mm hydrodynamically fared stainless steel wire rope with polyurethane coating	
Sensor	Range	Accuracy
Conductivity	20～70ms	±0.05ms
Temperatune	−2～35℃	±0.05℃
Depth	0～400dbar	0.5%FS
Data Transport	:Inductive Coupling Data Communication System	
Sempling Rate	:5times per second	
Sensor Battery Life	:50hours	

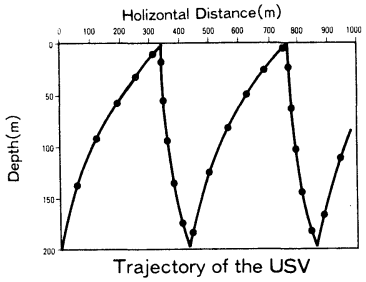

Trajectory of the USV

T.S.K

株式会社鶴見精機

本　　社　〒230 神奈川県横浜市鶴見区鶴見中央2-2-20
TEL.(045)521-5252　FAX.(045)521-1717
白河工場　〒969-03 福島県西白河郡大信村大字中新城字弥平田
TEL.(0248)46-3131　FAX.(0248)46-2288

TSK AMERICA INC.
828 MILLS PL.N.E. NORTH BEND, WA. 98045, U.S.A.
TEL.206-888-3404 TLX.230754235 TSKA SEA UD

賛　助　会　員

旭化成工業株式会社	東京都千代田区有楽町 1-1-2　三井ビル
株式会社旭潜研	東京都北区栄町 9-2
阿部嘉方	東京都練馬区春日町 2-15-6
株式会社 内田老鶴圃 内田悟	東京都文京区大塚 3-34-3
有限会社 英和出版印刷社	東京都北区中里 2-7-7
株式会社カイジョウ	東京都西多摩郡羽村町栄町 3-1-5
㈶海洋生物環境研究所	東京都千代田区内神田 1-18-12　北原ビル内
株式会社川合海苔店	東京都大田区大森本町 2-31-8
三信船舶電具株式会社	東京都千代田区神田 1-16-8
株式会社 自然・情報環境研究所	横浜市栄区桂町 1-1，3-401
昭和電装株式会社	高松市寺井町 1079
新日本気象海洋株式会社	東京都世田谷区玉川 3-14-5
全日本爬虫類皮革産業連合会	東京都足立区梅田 4-3-18
株式会社高岡屋	東京都台東区上野 6-7-22
株式会社鶴見精機	横浜市鶴見区鶴見中央 2-2-20
株式会社東京久栄技術センター	埼玉県川口市芝鶴ケ丸 6906-10
株式会社 東急フーズミート	東京都品川区東品川 4-10-21
株式会社西日本流体技研	長崎県佐世保市棚方町 283
日本アクアラング株式会社	神奈川県厚木市温水 2229-4
株式会社 日立造船技術研究所 バイオ研究センター	大阪市此花区桜島1-3-22
宮本悟	東京都中央区かきどき 3-3-5　かちどきビル　㈱本地郷
株式会社読売広告社	東京都中央区銀座 1-8-14
渡辺機開工業株式会社	愛知県渥美郡田原町神戸大坪 230
株式会社 渡部計器製作所	東京都文京区向丘 1-7-17

応援します。
良い海苔づくり—

生海苔活性調整機

RS-2型

海苔の等級が数段あがる

※生海苔を活性化し、海苔製品の表面をなめらかに光沢よく仕上げます。

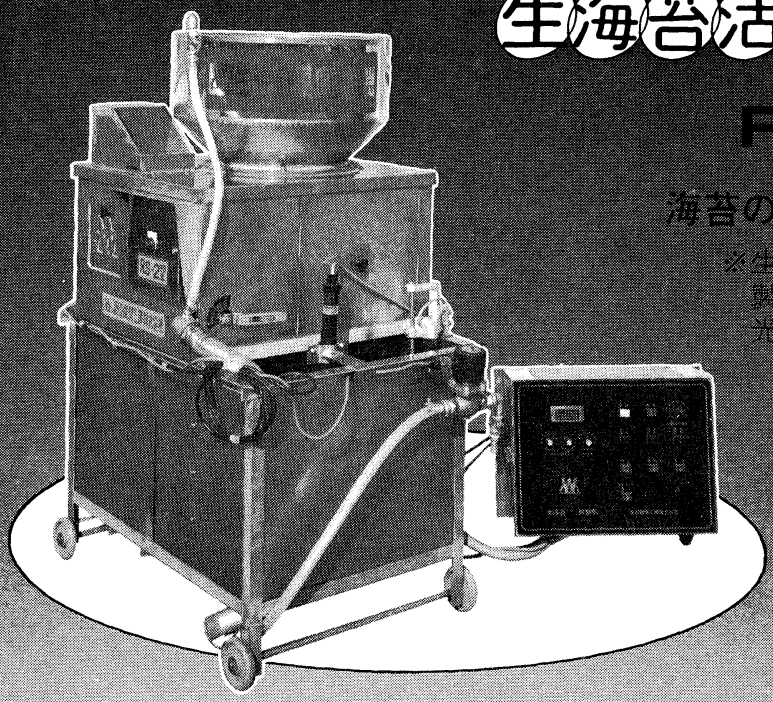

	RS-1型	RS-2型
本体	770㎜	1,080㎜
幅	960㎜	960㎜
横	680㎜	780㎜
電源	60Hz	180kg
モートル	40W 1台 100W 1台	40W 2台 60W 1台 100W 1台 150W 1台

渡辺機開工業株式会社

愛知県渥美郡田原町神戸大坪230

電話 05312(2)1121(代表)

日仏海洋学会入会申込書

（正　会　員）

	年度より入会	年　月　日申込
氏　名 ローマ字		年　月　日生
住　所　〒 勤務先　機関名 電　話		
自　宅　住　所　〒 電　話		
紹介会員氏名		
送付金額　円	送金方法	
会誌の送り先（希望する方に○をつける）	勤務先　自　宅	

（以下は学会事務局用）

受付	名簿 原簿	会費 原簿	あて名 カード	学会 記事

入会申込書送付先：　〒101　東京都千代田区神田駿河台 2-3

（財）日仏会館内

日仏海洋学会

郵便振替番号：　東京 5-96503

投稿の手引

1. 「うみ」(日仏海洋学会機関誌; 欧文誌名 **La mer**) は，日仏海洋学会正会員およびそれに準ずる非会員からの投稿 (依頼稿を含む) を，委員会の審査により掲載する。
2. 原稿は海洋学および水産学両分野の原著論文，原著短報，総説，書評，資料などとする。すべての投稿は，本文，原図とも正副2通とする。副本は複写でよい。本文原稿用紙はすべてA4判とし，400 字詰原稿用紙 (和文) に，または厚手白紙にダブル・スペース (和文ワープロでは相当間隔) で記入する。表原稿および図説明原稿は，それぞれ本文原稿とは別紙とする。
3. 用語は日，仏，英3カ国語の何れかとする。ただし，表および図説明の用語は仏文または英文に限る。原著論文 (前項) には約 200 語の英文または仏文の要旨を，別紙として必ず添える。なお，欧文論文には，上記要旨の外に，約 500 字の和文要旨をも添える。ただし，日本語圏外からの投稿の和文要旨については編集委員会の責任とする。
4. 投稿原稿の体裁形式は最近号掲載記事のそれに従う。著者名は略記しない。記号略号の表記は委員会の基準に従う。引用文献の提示形式は，雑誌論文，単行本分載論文(単行本の一部引用を含む)，単行本などの別による基準に従う。
5. 原図は版下用として鮮明で，縮尺 (版幅または1/2版幅) に耐えられるものとする。
6. 初校に限り著者の校正を受ける。
7. 正会員に対しては7印刷ページまでの掲載を無料とする。ただし，この範囲内であっても色彩印刷を含む場合などには，別に所定の費用を著者負担とすることがある。正会員の投稿で上記限度を超える分および非会員投稿の印刷実費はすべて著者負担とする。
8. すべての投稿記事について，1篇あたり別刷 50 部を無料で請求できる。50 部を超える分は請求により，50部単位で作製される。別刷請求用紙は初校と同時に配布される。
9. 原稿の送り先は下記の通り。

〒108 東京都港区港南4-5-7 東京水産大学　村野正昭 気付
日仏海洋学会編集委員会

1992 年 8 月 25 日 印刷
1992 年 8 月 28 日 発行

う　み　　第 30 巻 第 3 号

定価 ¥ 3,200

編集者　村野正昭
発行所　日仏海洋学会
財団法人 日仏会館内
東京都千代田区神田駿河台2-3
郵便番号：101
電話：03(3291)1141
振替番号：東京 5-96503
印刷者　佐藤一二
印刷所　有限会社英和出版印刷社
東京都北区中里2—7—7
郵便番号：114
電話：03(5394)4856

Tome 30 N° 3

SOMMAIRE

Proceedings of the Sixth Japan and East China Seas Study Workshop, 22–27 April 1991, Fukuoka, Japan